Development of a new design method for the cross-section capacity of steel open sections at high temperatures

Mémoire

Jeanne Paquet

Maîtrise en génie civil - avec mémoire
Maître ès sciences (M. Sc.)

Québec, Canada

Development of a new design method for the cross-section capacity of steel open sections at high temperatures

Mémoire

Jeanne Paquet

Sous la direction de :

Nicolas Boissonnade, Directeur de recherche

Résumé

À hautes températures, les propriétés de l'acier sont affectées et sa résistance est donc moindre que sa résistance à température ambiante. Des méthodes de calculs différentes doivent donc être utilisées pour prédire la résistance dans la situation exceptionnelle d'incendie. Les normes actuelles proposent des méthodes simplifiées pour prédire la résistance de l'acier à haute température. Toutefois, ces méthodes sont inspirées des méthodes de dimensionnement à froid et ne sont donc généralement pas adéquates pour prédire de façon précise la résistance des éléments en situations d'incendie.

Ce mémoire présente les recherches effectuées pour la proposition d'une nouvelle méthode de calcul pour les sections d'acier ouvertes soumises à de hautes températures en utilisant l'Overall Interaction Concept (O.I.C). Cette méthode est basée sur l'interaction entre la résistance et la stabilité et permet de considérer les imperfections géométriques et matérielles. Entre autres choses, l'avantage de cette nouvelle méthode est qu'elle permet d'obtenir des résultats précis et de conserver une continuité entre les prédictions.

Un modèle numérique a été utilisé pour prédire la résistance de l'acier à hautes températures. Ce modèle a été validé en comparant les résultats avec des résultats expérimentaux. À la suite de la validation, le modèle a été utilisé pour conduire des simulations dans lesquelles plusieurs géométries, températures, limites élastiques et cas de chargement ont été considérés. Les résultats ont ensuite été utilisés pour proposer de nouvelles équations dans le format O.I.C.

La performance de la nouvelle proposition a été évaluée et comparée avec la performance de normes existantes. Cette évaluation a permis de conclure que la proposition donne des résultats beaucoup plus précis.

Finalement, l'évolution du comportement de l'acier entre la température ambiante et les hautes températures a brièvement été analysé. Puisque ce point est abordé de façon sommaire, il ouvre la porte vers de futures études sur le sujet.

Abstract

At high temperatures, steel suffers from great losses in strength and stiffness. Different design methods must therefore be considered to predict the resistance of steel in the exceptional situation of fire. Current standards propose simplified methods to predict the resistance of steel at high temperatures. However, these methods are inspired by steel design equations used at room temperature and are therefore generally not suitable to predict accurately the resistance of steel elements in fire situation.

This thesis presents research investigations pursued to propose a new design method for open steel cross-sections subjected to high temperatures by means of the Overall Interaction Concept (O.I.C.). This calculation method is based on the interaction between resistance and stability and allows to consider geometrical and material imperfections. The advantage of this new calculation method is that it allows to obtain precise results and to keep continuity between predictions contrarily to standards that use the cross-section classification.

A numerical model, initially developed for open steel cross-sections at ambient temperature, was improved to predict the resistance of steel at high temperatures. It was then verified against experimental test results to ensure its accuracy. After validation, the numerical model was used to conduct simulations using different geometries, temperatures, yield limits and load cases. Results were then used to formulate new design proposals for cross-sections at high temperatures in the O.I.C. format.

The performance of the new proposal was then evaluated et compared with the performance of existing standards. This evaluation allowed to conclude that the proposition is much more accurate than existing standards.

Finally, the evolution of the behaviour of steel between cold and high temperature was briefly analysed. As this point was only briefly discussed, it opens the door for future studies on the subject.

Table of Contents

List of figures

List of Tables

Notations

Abbreviations

AISC	American Institute of Steel Construction
ASCE	American Society of Civil Engineering
CSA	Canadian Standards Association
E.W.M.	Effective Width Method
EC3	Eurocode 3
ECCS	European Convention for Constructional Steelwork
F.E.	Finite Element
G.M.N.A.	Geometrically and Materially Non-linear Analysis
G.M.N.I.A.	Geometrically and Materially Non-linear with Imperfections Analysis
L.B.A.	Linear Buckling Analysis
NFPA	National Fire Protection Association
M.N.A.	Materially Non-linear Analysis
O.I.C.	Overall Interaction Concept
SFRM	Spray-on fire resistive materials

Latin letters

A	Area
a_{avg}	Average buckling length
A_e	Effective area
A_{eff}	Effective area
A_f	Flange area
a_f	Buckling length of the flanges
A_g	Gross area
A_w	Web area
a_w	Buckling length of the web
b	Flange width
b_e	Effective flange width
b_{eff}	Effective width
$b_{eff,\theta}$	Effective width at elevated temperatures

b_{el}	Width of compression element (S16-14)
C_b	Lateral-torsional buckling modification factor (AISC)
C_f	Compression load (S16-14)
$C_r(T)$	Resistance to compression at elevated temperatures (S16-14)
C_w	Warping torsional constant (S16-14/AISC)
$C_y(T)$	Axial compression load at yielding at elevated temperatures (S16-14)
E	Young's modulus of elasticity
$E(T)$	Young's modulus of elasticity at elevated temperatures
$E_{a,\theta}$	Young's modulus of elasticity at elevated temperatures
e_y	Eccentricity on y axis
e_z	Eccentricity on z- axis
$f_{0,2p,\theta}$	0.2% proof strength at elevated temperatures (Eurocode 3)
$F_{cr}(T)$	Local buckling stress at elevated temperatures (AISC)
$F_e(T)$	Elastic buckling stress at elevated temperatures (AISC)
$F_L(T)$	Nominal compressive strength above which the inelastic buckling limit states apply at elevates temperatures (AISC)
$f_{L/G}$	Coupling factor
$f_{p,\theta}$	Proportional limit at elevated temperatures (Eurocode 3)
$f_{u,\theta}$	Ultimate strength at elevated temperatures (Eurocode 3)
F_y	Yield strength
f_y	Yield strength (Eurocode 3)
$F_y(T)$	Effective yield strength at elevated temperatures (S16-14 / AISC)
$f_{y,\theta}$	Effective yield strength at elevated temperatures (Eurocode 3)
f_{yk}	Yield limit
G	Shear modulus
$G(T)$	Shear modulus at elevated temperatures (S16-14/AISC)
h	Height of cross-section
h_0	Distance between the flange centroids
h_{eff}	Effective web height
h_w	Height of web
I	Moment of inertia
I_t	St. Venant torsional constant (Eurocode 3)
I_w	Warping torsional constant (Eurocode 3)

I_x	Moment of inertia, x-x axis
I_y	Moment of inertia, y-y axis
I_z	Moment of inertia, z-z axis
J	St. Venant torsional constant (S16-14/AISC)
K	Effective length factor
k	Coefficient for plate buckling
$k_{0,2p,\theta}$	Reduction factor for the 0.2% proof strength (Eurocode 3)
k_E	Reduction factor for the Young's modulus of elasticity (S16-14/AISC)
$k_{E,\theta}$	Reduction factor for the Young's modulus of elasticity (Eurocode 3)
k_{LT}	Interaction factor (Eurocode 3)
k_p	Reduction factor for the proportionality limit (S16-14/AISC)
$k_{p,\theta}$	Reduction factor for the proportionality limit (Eurocode 3)
k_y	Interaction factor (Eurocode 3) / Reduction factor for the yield strength (S16-14/AISC)
$k_{y,\theta}$	Reduction factor for the yield strength (Eurocode 3)
k_z	Interaction factor (Eurocode 3)
$k_{\sigma,f}$	Flange buckling coefficient
$k_{\sigma,w}$	Web buckling coefficient
L	Length
L_b	Unsupported length
$L_p(T)$	Limiting laterally unbraced length for the limit state of yielding at elevated temperatures (AISC)
$L_r(T)$	Limiting laterally unbraced length for the limit state of inelastic lateral-torsional buckling at elevated temperatures (AISC)
$M_c(T)$	Available flexural strength at elevated temperatures (AISC)
$M_c(T)$	Available resistance to bending at elevated temperatures (AISC)
M_{cr}	Critical elastic moment of laterally unbraced frames (Eurocode 3)
$M_{cx}(T)$	Available resistance to bending at elevated temperatures, x-x axis (AISC)
$M_{cy}(T)$	Available resistance to bending at elevated temperatures, y-y axis (AISC)
$M_{ep,fi,\theta,Rd}$	Partial plastic resistance to bending moment at elevated temperatures (Eurocode 3)
M_f	Bending moments load (S16-14)
$M_{fi,Ed}$	Bending moments load at elevated temperatures (Eurocode 3)
$M_{fi,\theta,Rd}$	Resistance to bending moments at elevated temperatures (Eurocode 3)

M_{fx}	Bending moment load, x-x axis (S16-14)
M_{fy}	Bending moment load, y-y axis (S16-14)
$M_n(T)$	Nominal flexural strength at elevated temperatures (AISC)
$M_{N,fi,Rd}$	Reduced plastic moment due to the axial load at elevated temperature (Eurocode 3)
$M_{N,y,fi,Rd}$	Reduced plastic moment due to the axial load at elevated temperature, y-y axis (Eurocode 3)
$M_{N,z,fi,Rd}$	Reduced plastic moment due to the axial load at elevated temperature, z-z axis (Eurocode 3)
$M_p(T)$	Plastic resistance to bending at elevated temperatures (S16-14/AISC)
$M_{pl,fi,\theta,Rd}$	Plastic resistance to bending moment at elevated temperatures (Eurocode 3)
$M_{pl,y,fi,Rd}$	Plastic resistance to bending moment at elevated temperatures, y-y axis (Eurocode 3)
$M_{pl,z,fi,Rd}$	Plastic resistance to bending moment at elevated temperatures, z-z axis (Eurocode 3)
$M_r(T)$	Required flexural strength (AISC)
$M_r(T)$	Resistance to bending at elevated temperatures (S16-14)
M_{rx}	Required resistance to bending at elevated temperatures, x-x axis (AISC)
$M_{rx}(T)$	Resistance to bending at elevated temperatures, x-x axis (S16-14)
M_{ry}	Required resistance to bending at elevated temperatures, y-y axis (AISC)
$M_{ry}(T)$	Resistance to bending at elevated temperatures, y-y axis (S16-14)
$M_u(T)$	Critical elastic moment of laterally unbraced frames at elevated temperatures (S16-14)
m_y	Ratio of design major-axis bending moment to design plastic resistance to major-axis bending
M_y	Major-axis bending load
$M_y(T)$	Elastic resistance to bending moment at elevated temperatures (S16-14)
$M_{y,fi,Ed}$	Bending moment load at elevated temperatures, y-y axis (Eurocode 3)
$M_{y,fi,\theta,Rd}$	Resistance to bending moment at elevated temperatures, y-y axis (Eurocode 3)
$M_{yc}(T)$	Yield moment in the compression flange (AISC)
m_z	Ratio of design minor-axis bending moment to design plastic resistance to minor-axis bending
M_z	Minor-axis bending load

$M_{z,fi,Ed}$	Bending moment load at elevated temperatures, z-z axis (Eurocode 3)
$M_{z,fi,\theta,Rd}$	Resistance to bending moment at elevated temperatures, z-z axis (Eurocode 3)
n	Ratio of design axial force to design plastic resistance to axial force
N	Compression load
$N_{b,fi,\theta,Rd}$	Buckling resistance in compression at elevated temperatures (Eurocode 3)
$\overline{N}$	Buckling reduction factor
N_{cr}	Critical compression load
$N_{fi,Ed}$	Compression load at elevated temperature (Eurocode 3)
N_{max}	Ultimate axial load
$N_{pl,fi,Rd}$	Plastic resistance in compression at elevated temperatures (Eurocode 3)
$P_c(T)$	Available axial strength at elevated temperatures (AISC)
$P_n(T)$	Nominal axial strength at elevated temperatures (AISC)
$P_r(T)$	Required axial strength (AISC)
r	radius of hot-rolled section / radius of gyration (S16-14/AISC)
R_b	Ultimate multiplier
$R_{b,L}$	Local ultimate multiplier
$R_{b,L+G}$	Global ultimate multiplier
R_{cr}	Critical multiplier
$R_{cr,g}$	Global critical multiplier
$R_{cr,L}$	Local critical multiplier
R_{pc}	Web plastification factor (AISC)
R_{pg}	Bending strength reduction factor (AISC)
R_{pl}	Plastic multiplier
S	Section’s elastic modulus (S16-14/AISC)
S_{eff}	Effective section’s modulus (S16-14/AISC)
S_x	Section’s elastic modulus, x-x axis (S16-14/AISC)
S_{xc}	Section's elastic modulus referred to compression flange, x-x axis (AISC)
S_y	Section’s elastic modulus, y-y axis (S16-14/AISC)
t	Plate thickness
t_f	Flange thickness
t_w	Web thickness

U_1	Factor to account for moment gradient and second-order effects of axial load force acting on the deformed member
w	Deflection
W	Section modulus (Eurocode 3)
$W_{eff,y}$	Effective section modulus, y-y axis (Eurocode 3)
$W_{el,y}$	Elastic section modulus, y-y axis (Eurocode 3)
$W_{el,z}$	Elastic section modulus, z-z axis (Eurocode 3)
W_{ep}	Partial plastic section modulus (Eurocode 3)
$W_{ep,y}$	Partial plastic section modulus, y-y axis (Eurocode 3)
$W_{ep,z}$	Partial plastic section modulus, z-z axis (Eurocode 3)
W_{pl}	Plastic section modulus (Eurocode 3)
$W_{pl,y}$	Plastic section modulus, y-y axis (Eurocode 3)
$W_{pl,z}$	Plastic section modulus, z-z axis (Eurocode 3)
W_y	Section modulus, y-y axis (Eurocode 3)
W_z	Section modulus, z-z axis (Eurocode 3)
Z	Section's plastic modulus (S16-14/AISC)
z	Position of neutral axis
Z_x	Section's plastic modulus, x-x axis (S16-14/AISC)
Z_y	Section's plastic modulus, y-y axis (S16-14/AISC)

Greek letters

α	Imperfection factor
α_L	Parameter to account for imperfections
$\beta_{ep,y}$	Interpolation factor for bending about y-y (Eurocode 3)
$\beta_{ep,z}$	Interpolation factor for bending about z-z (Eurocode 3)
γ	Leading parameter for hot-rolled sections
$\gamma_{M,fi}$	Safety factor (Eurocode 3)
δ	Parameter to account for the post buckling resistance
ΔR_1	Last positive increment
ΔR_2	First negative increment
ε	Strain / Material parameter (Eurocode 3)
$\varepsilon_{p,\theta}$	Strain at proportional limit at elevated temperatures
$\varepsilon_{t,\theta}$	Limiting strain for yield strength at elevated temperatures

$\varepsilon_{u,\theta}$	Ultimate strain at elevated temperatures
$\varepsilon_{y,\theta}$	Yield strain at elevated temperatures
ε_{θ}	Strain at elevated temperatures / Material parameter at elevated temperatures (Eurocode 3)
ζ	Restraint coefficient
η	Leading parameter for welded sections
θ	Angle that defines the degree of moment biaxiality
θ_a	Temperature (Eurocode 3)
$\lambda(T)$	Non-dimensional slenderness at elevated temperatures (S16-14)
λ_0	End of plastic plateau
$\overline{\lambda}$	Relative slenderness (Eurocode 3)
$\overline{\lambda}_{LT}$	Relative slenderness for lateral-torsional buckling (Eurocode 3)
$\overline{\lambda}_{LT,\theta}$	Relative slenderness for lateral-torsional buckling at elevated temperatures (Eurocode 3)
$\overline{\lambda}_p$	Plate slenderness
$\overline{\lambda}_{\theta}$	Relative slenderness at elevated temperature (Eurocode 3)
$\lambda_{c,T}$	Relative slenderness
λ_G	Global relative slenderness
λ_L	Local relative slenderness
λ_{pf}	Limiting slenderness for a compact flange (AISC)
λ_r	Euler slenderness
λ_{rel}	Relative slenderness
λ_{rf}	Limiting slenderness for a noncompact flange (AISC)
ν	Poisson's ratio
ρ	Plate reduction factor
ρ_{θ}	Plate reduction factor at elevated temperatures
σ	Stress
σ_c	Compression stress
σ_{cr}	Critical plate buckling stress
$\sigma_{cr,\theta}$	Critical plate buckling stress at elevated temperatures
σ_t	Tension stress

ϕ	Value to determine de reduction factor χ / Angle that defines the degree of compression
ϕ_{θ}	Value to determine de reduction factor χ_{fi} (Eurocode 3)
χ	Ultimate reduction factor
χ_{fi}	Buckling reduction factor at elevated temperatures (Eurocode 3)
$\chi_{fi,y}$	Buckling reduction factor at elevated temperatures, y-y axis (Eurocode 3)
$\chi_{fi,z}$	Buckling reduction factor at elevated temperatures, z-z axis (Eurocode 3)
χ_G	Global reduction factor
χ_L	Cross-section reduction factor
$\chi_{LT,fi}$	Reduction factor for lateral-torsional buckling in the fire design situation (Eurocode 3)
$\chi_{min,fi}$	Minimum between $\chi_{y,fi}$ and $\chi_{z,fi}$ (Eurocode 3)
ψ	Stress ratio
ω_2	Coefficient to account for increased moment resistance of a laterally unsupported doubly symmetric beam segment when subjected to a moment gradient (S16-14)

À mes parents, Martine et Marc
Et à mon conjoint, Serge

Remerciements

J'aimerais d'abord remercier mon directeur de recherche Nicolas Boissonnade pour son aide et sa grande disponibilité tout au long de ma maîtrise. Merci de m'avoir appris tant de choses qui me seront forcément utiles dans ma carrière d'ingénieur et de m'avoir guidé au travers de mon projet. Je remercie aussi le chercheur Carlos Couto pour sa grande aide sur tous les aspects en lien avec l'acier à haute température.

J'aimerais également remercier mes collègues du groupe O.I.C. avec qui j'ai beaucoup aimé travailler. Un merci tout spécial à Liya pour sa grande contribution à ma maîtrise avec ses outils et pour son aide qui m'a permis de pousser ma recherche encore plus loin.

Je remercie aussi mon employeur, John Cafarelli chez Tetra Tech qui m'a encouragé à poursuivre mes études tout en me permettant de continuer à travailler dans une équipe dynamique.

Finalement, je remercie ma famille et mon conjoint qui m'ont encouragée dans ce projet et qui ont toujours été là pour moi.

Introduction

Use of steel in structures

Steel is a material that is widely used in buildings and infrastructures. It can be used to construct houses and small buildings as well as very high skyscrapers, bridges and tunnels. The main advantages of steel use are as follow:

- It is a strong material which allows to use small cross-sections and provides wide open spaces in buildings;
- It makes light structures that require reduced foundations;
- It can easily be used for prefabricated building which leads to very fast constructions;
- It can easily be combined with other materials;
- Due to its ductility, it is a good choice for buildings in seismic areas;
- Its ductility also makes it a good material in fire situations as it allows for a progressive collapse of the structure.

Those advantages explain why engineers and architects choose steel when designing buildings and bridges. However, improvements still need to be made regarding design for fire situations; which is the focus of the present study. Effectively, guidelines provided in actual codes are known to lack accuracy and are therefore not appropriate for the design in fire situations.

Steel in fire situations

During a fire, temperatures as high as 1000°C can often be reached. As steel sections are usually made of thin plates, they heat rapidly in such situation. When steel is subjected to heat, further to experiencing thermal elongation, it rapidly loses in strength and stiffness. Moreover, strength and stiffness do not decrease at the same rate when the temperature increases. Therefore, design methods used at ambient temperature cannot be used for the design in the case of fire. However, buildings must absolutely be designed by taking into consideration the fire situation as it could otherwise lead to the collapse of the structure if a fire occurs. As user safety is the most important criterion when designing any structure, the fire situation must not be disregarded. Moreover, the fire situation most be considered in the design process as it can be decisive for member selection.

Actual practice in fire design

Both active and passive fire protection measures are often used in buildings. Active protection measures include fire alarms and sprinklers and are used to control the fire spread. Passive protection measures, on the other hand, provide fire resistance to the structure. These include adequate design of the structure (materials and dimensions), compartmentation and fire protection materials; they are used to ensure the structural stability and integrity of the structure during specific time periods prescribed by building codes. Theses time periods are based on the fire safety objectives and on the type of occupancy in the building [1].

In actual practice, steel structures are rarely designed by considering the properties at high temperature. Effectively, most buildings code have a prescriptive approach. This means that compartmentation and protection materials are mostly used as passive protection measures and that the protection materials are chosen from a wide range of products for which the resistance to fire has been proven following specific testing procedures. In the case of steel structures, theses protection materials include, but are not limited to, spray-on fire resistive materials (SFRM), intumescent coatings and enclosures of gypsum boards [1].

The use of fire protection materials does ensure the structural integrity of the structure in case of fire. It however greatly increases the cost of construction of a building. For example, according to a report made by the National Fire Protection Association (NFPA), in the United States, the cost of fire protection for a commercial building can represent up to 12% of the value of the building [2]. New methods most therefore be considered to ensure more economical design.

In the past years, more buildings codes have switched to a performance-based approach to fire safety. This means that designers can choose the strategy they want to provide fire safety as long the level of performance required is proven to be met [1]. They can therefore incorporate fire considerations directly in the design process of steel structures which could lead to large money savings without jeopardizing user safety. Most design standards do provide simplified methods of analysis that can be used when the design involves structural members that do not act as a system. Those methods mostly consist in using the equations at room temperature with a few modifications and reduced mechanical properties. However, the behaviour of steel at high temperature is very different than its behaviour at room temperature, and the guidelines thus often lack in precision and accuracy. Moreover, most standards resort to the cross-section classification which can lead to a lack in continuity and often use tedious calculation methods. Standards therefore need to be improved to accurately consider steel properties at high temperatures, to ensure safe designs and to increase the precision and the simplicity of the calculation methods.

Overall Interaction Concept

The need for more accurate and simpler design rules led to a new design method: the Overall Interaction (O.I.C). This new design method as been in development since 2012. It is based on the interaction between the main factors influencing the load bearing capacity of a member which are resistance and instability. One of the main advantages of the O.I.C. concept is that resistance predictions are no longer based on cross-section classification responsible for non-continuous transitions in the design. The use of the O.I.C. is also much simpler than the actual calculation methods used in standards.

To explain the background and the concept of the O.I.C., it is possible to recall the case of a simple column subjected to compression. Figure 1 shows the column and a graph of the resistance of the column as a function of its length.

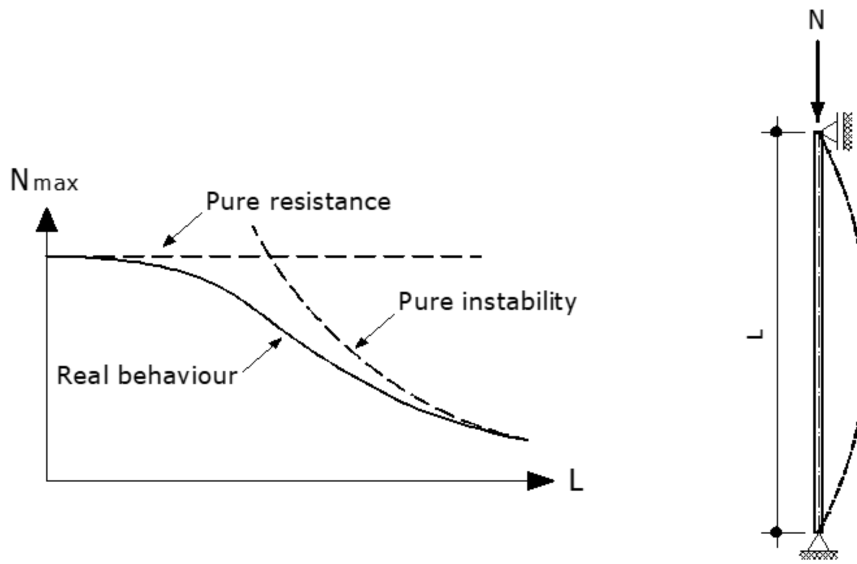

Figure 1 : Resistance of a simple column under pure compression

The graph shows that for very short columns, resistance is governed by the plastic capacity while for long members, resistance in governed by instability. The resistance of members of intermediate lengths is affected by imperfections and the resistance follows the "Real behaviour" curve which is a so-called buckling curve.

The O.I.C. concept uses similar graphs and buckling curves. However, the curves used by the O.I.C. rely on dimensionless relative slenderness. These dimensionless parameters allow use the same buckling curves for elements with different shapes and properties.

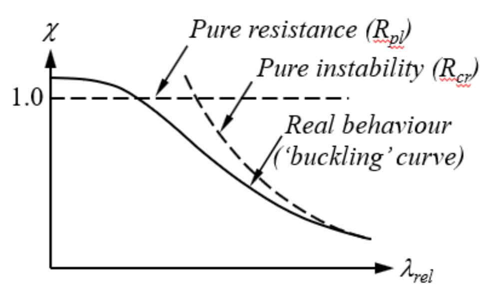

Figure 2 : O.I.C. buckling curves

Figure 3 presents the general O.I.C. chart with the steps that need to be followed to determine the resistance according to the O.I.C. concept. The O.I.C. approach concerns both the *local* (cross-section level) and the *global* (member level) capacity. Although the present study focuses on the local resistance, all steps will be discussed.

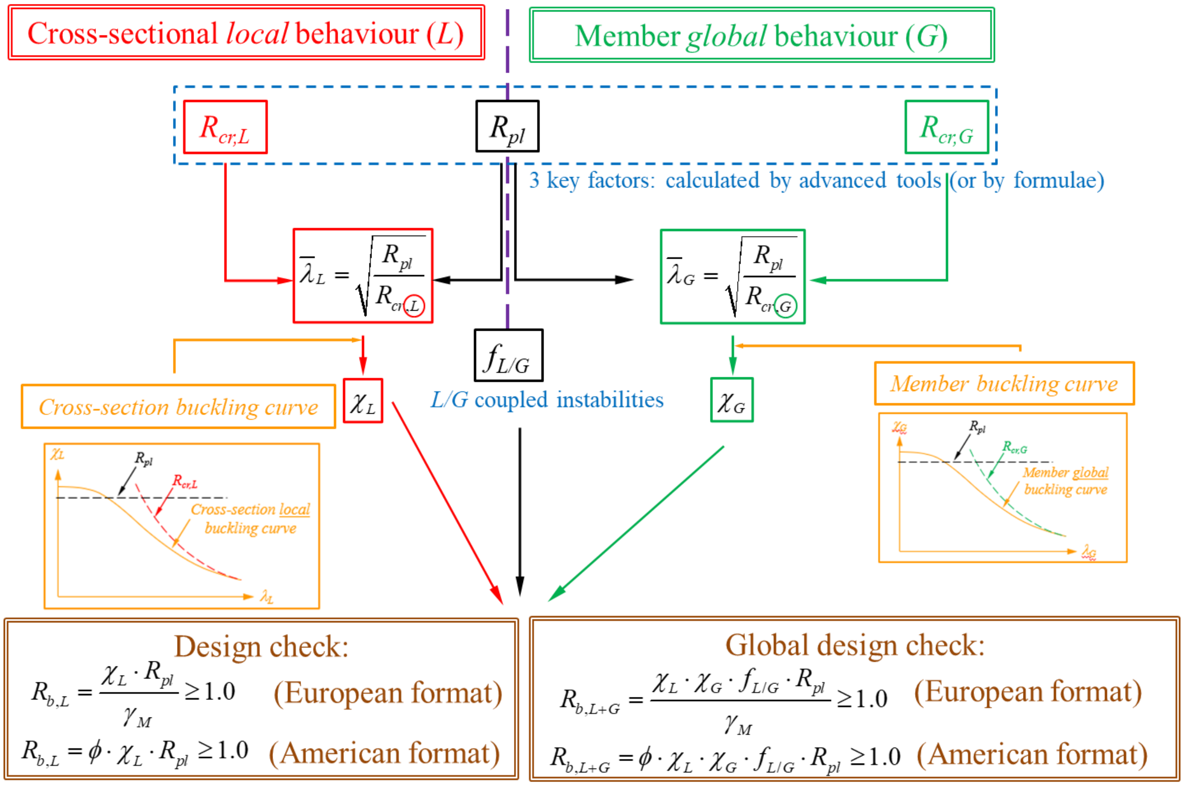

Figure 3 : Principles and application steps of the Overall Interaction Concept

The O.I.C. uses 3 key factors which are load multipliers. $R_{cr,L}$ and $R_{cr,G}$ are respectively the local and the global critical load multipliers. They are calculated by dividing the critical load (either local or global) by the initial load applied to the member. Both critical loads can be obtained by performing Linear Buckling Analysis (L.B.A.). To obtain the local critical load, the length of the member used in the F.E. numerical model must be very short to prevent global effects. R_{pl} is the plastic multiplier. It is obtained by dividing the plastic resistance by the initial load. The plastic resistance is determined with the use of a MATLAB tool. The initial load used to calculate the multipliers must be the same for all multipliers so that they can combined in the O.I.C. process.

The main objective of the studies made on the O.I.C. is to determine the buckling curves that will later be used by designers following the approach presented on Figure 3. Different sets of curves must be developed for local and global behaviour. To determine the buckling curves that will later on be used by the designers, the following steps must first be followed by the researcher for the local behaviour:

1) The local relative slenderness must first be calculated with the following equation:

$$\lambda_L = \sqrt{\frac{R_{pl}}{R_{cr,L}}} \tag{1}$$

2) Geometrically and Materially Non-linear with Imperfections Analysis (G.M.N.I.A.) are then performed to determine the ultimate load multiplier $R_{b,L}$. As only the local resistance is of interest, the length of the member in the numerical model must be short enough so that no global effects occur. The initial load used to determine the ultimate load multiplier must be the same as the one used to calculate the critical and plastic multipliers;
3) The local reduction factor must be calculated using the following equation:

$$\chi_L = \frac{R_{b,L}}{R_{pl}} \tag{2}$$

4) Design curves can then be determined based on results obtained in steps 1-3 for various cases.

The following steps must then be followed by the researcher for the global behaviour:

1) The local relative slenderness must first be calculated with the following equation:

$$\lambda_G = \sqrt{\frac{R_{pl}}{R_{cr,G}}} \tag{3}$$

2) Geometrically and Materially Non-linear with Imperfections Analysis (G.M.N.I.A.) are then be performed to determine the ultimate load multiplier $R_{b,L+G}$. The ultimate resistance accounts for both local and global behaviour. The initial load used to determine the ultimate load multiplier must be the same as the one used to calculate the critical and plastic multipliers.
3) The function used to calculate the $f_{L/G}$ coupling factor must then be determined. This function is based on the difference between non-linear analysis in which both local

and global buckling is considered and non-linear analysis free of local instabilities. The $f_{L/G}$ coupling factor accounts for [3]:

- The influence of local behaviour which diminishes with the increase in length;
- The second-order effects that can precipitate the local buckling of the cross-section;
- The local second-order effects that can cause a loss in stiffness and load redistribution.

4) The local reduction factor must be calculated using the following equation:

$$\chi_G = \frac{R_{b,L+G}}{R_{pl} \cdot f_{L/G} \cdot \chi_L} \tag{4}$$

5) Design curves can be determined based on results obtained in steps 1-4 for various cases.

Once the design buckling curves have been developed, the O.I.C. approach from Figure 3 can be followed by a designer. In this approach, the local and global slenderness are calculated using Equations (1) and (3) presented previously. Then, χ_L and χ_G are determined with the use of the buckling curves. Finally, the coupling factor $f_{L/G}$ is calculated. Finally, the ultimate multiplier, $R_{b,L}$ or $R_{b,L+G}$, can be calculated with the equation presented on Figure 3. An ultimate multiplier over 1.0 means that the initial applied load must be multiply by a value over 1.0 for failure to be reached and therefore that the resistance is sufficient.

Objectives of the Master's thesis

The objective of this Master's thesis is to extend the O.I.C. for open I and H cross-sections shapes at elevated temperatures. In all studied cases, the temperature is considered to be uniform throughout the section. Only doubly-symmetric sections are studied and only the local resistance of those cross-sections is assessed in this thesis. Various shapes of hot-rolled and welded cross-sections are chosen to accurately represent the behaviour of compact to slender cross-sections in fire situations. Numerical simulations are also performed using different values of temperature, yield limit and load cases.

Methodology

Chapter 1 of this thesis presents the State-of-the-Art realised at the beginning of the master. The aim of this literature review is to review previous work done on important subjects such as steel behaviour at high temperature, plastic resistance in fire conditions, local buckling and imperfections which will be useful and needed for the realisation of this thesis. Actual design methods in European, Canadian and American codes are also studied and are presented in this chapter.

Chapter 2 presents a description of the finite element (F.E.) models used throughout the research. All parameters used in the model are described and sub-studies regarding the mesh density and the introduction of residual stresses are also presented. A validation study of the model against experimental results is also presented.

Chapter 3 addresses the different parameters considered in the parametric study. In this chapter, all the cases studied are presented, discussed and analysed.

Chapter 4 concerns the identification of the leading parameters. A leading parameter is a parameter that influences the resistance. Identification of leading parameters is mandatory to be able to define a series of buckling curves that can accurately predict the resistance. In this chapter, relevant parameters studied are presented and the chosen leading parameter are presented.

Chapter 5 presents the proposed design curves based on the numerical study. Two different proposals are made: one proposal for welded sections and one proposal for hot-rolled sections. The performance of the proposals is then compared to finite element predictions and the influence of different parameters on the performance is studied.

Chapter 6 proposes a comparison of the performances of the O.I.C. proposals and of existing standards. The intent of this chapter is to show that the O.I.C. proposals lead to more accurate results and are therefore an improvement over the current design methods.

Chapter 7 presents worked examples that shows the efficiency of the O.I.C. proposals compared to the actual calculation methods used in standards.

Chapter 8 briefly discusses observations on the influence of increasing temperature on section capacity and explains what is left to study.

Chapter 1 : State of the art

1.1 Steel behaviour at high temperature

When subjected to fire, the heat of steel increases rapidly due to the good thermal capacity of steel. Steel elements also usually have high section factors *A/V*, the ratio between the area of the member in contact with the heat and the volume of the member, which also increases the rate at which steel heats [4]. In a fire, a steel element is rarely exposed equally to the heat on all its side. This leads to temperature gradients in the steel elements. When doing a simplified mechanical analysis, the temperature is often considered constant throughout the section and the higher temperature is kept as the uniform temperature.

The heating of steel causes a decrease in both strength and stiffness that need to be accounted for when trying to predict the resistance of steel at high temperatures. Many experimental tests have been conducted over the years to determine the mechanical properties of steel at high temperatures. Those tests can either be transient-state tests or steady-state tests. When performing transient-state tests, the load is applied on the specimen at ambient temperature and then the temperature is increased at a constant rate. In steady-state tests, the specimen is first heated at a specific temperature and then load is applied and increased. Both methods can lead to differences in results [5]. When performing numerical simulations with finite element software, it is easier to use steady-state procedures. Effectively, in this method, material properties are adjusted to fit the desire temperature and the load is then progressively increased as it would be for a regular static numerical simulation at normal temperature.

Figure 4 and Figure 5, extracted from Kodur et al. [5], show how the elastic modulus and the yield strength evolve with the increase in temperature. In those graphs, data from different models and tests are presented.

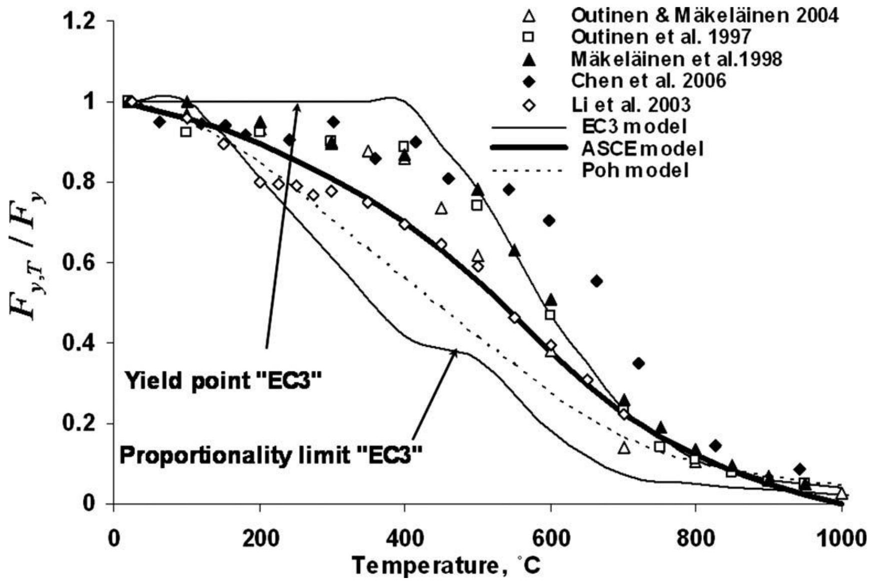

Figure 4 : Influence of the temperature on the yield limit of steel [5]

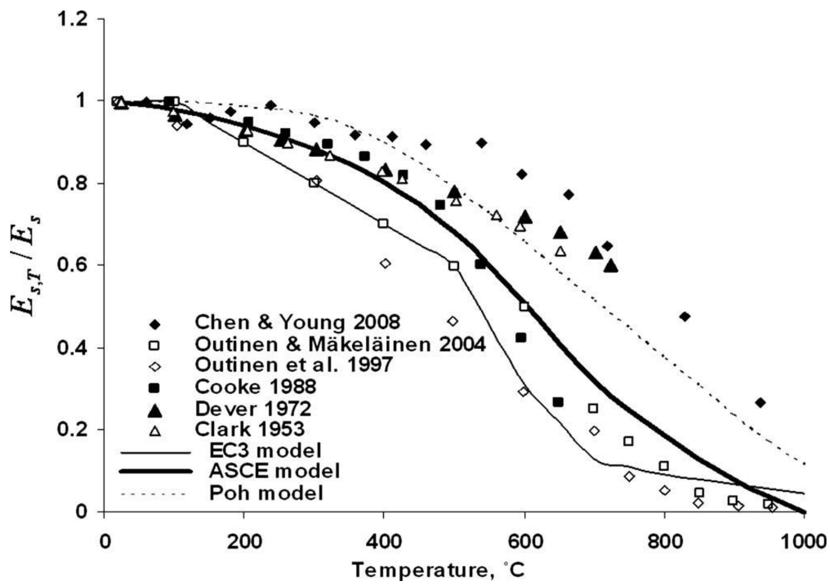

Figure 5 : Influence of the temperature on the elastic modulus of steel [5]

Graphs show that both the yield limit and the elastic modulus decrease with an increase in temperature. This can be explained by the fact that, when steel temperature increases, the nucleus of the iron atoms in steel move apart. This leads to weakened bonds and thus reduces both the yield strength and the elastic modulus of steel [5]. Both figures also show that the results from one study to the other can be very different. This can be explained by different test procedures, but also by the influence of the heat rate and of the rate of loading on the material properties.

Moreover, the typical linear stress-strain relationship used for steel is no longer accurate at high temperature. Effectively, the stress-strain relationship becomes drastically non-linear [6]. Because of the non-linearity, larger strains are needed to reach high stresses. According to Knobloch et al. [7], the stress-strain relationship can be classified in three temperature ranges :

- For temperatures below 300°C, there is a linear elastic branch, a clearly defined yield point, a yield plateau and strain hardening is present at high strains;
- For temperatures between 300°C and 600°C, the linear elastic branch becomes shorter and the stiffness is lower. No clear yield point can be noticed. However, the plastic behaviour remains governed by strain hardening;
- For temperature over 600°C, the elastic branch is even shorter and the range for strain hardening is less pronounced.

Figure 6 shows the stress-strain relationship at different temperatures obtained from tensile tests [8]. This figure is from a study from Knobloch et al. [8] on the influence of strain-rate. Among other things, it shows that higher strain rates lead to higher material properties (modulus of elasticity, proportional limits and yield strength). The difference is especially important for higher temperatures such as 550°C and 700°C.

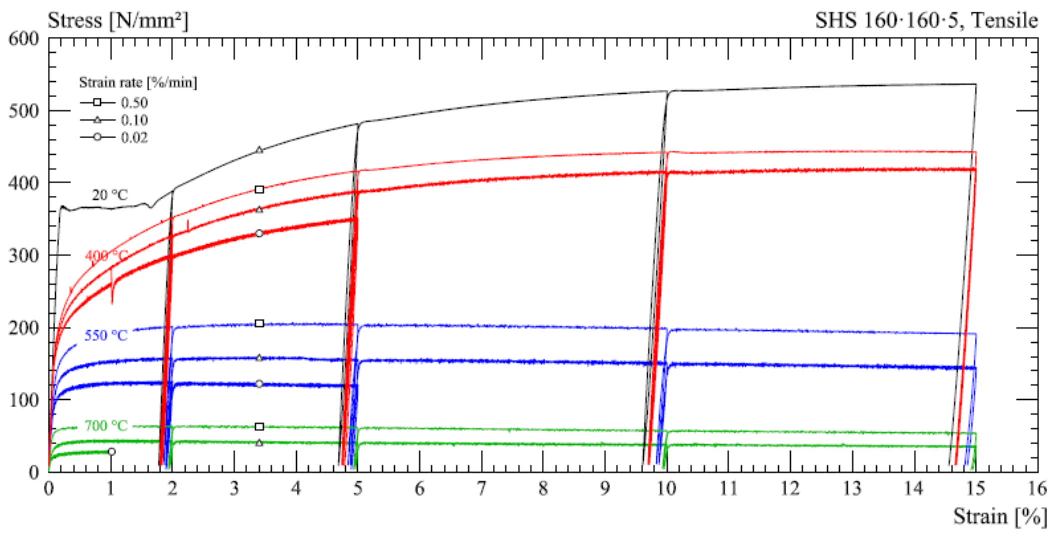

Figure 6 : Stress-strain relationships at various temperature based on tensile tests [8]

As the material law greatly depends on the strain rate and between different tests, Part 1-2 of Eurocode 3 (EC3) [9], which is the European standards for the design of steel, gives recommendations regarding the material law that can be used when performing numerical simulations. Figure 7 shows the recommended stress-strain relationship.

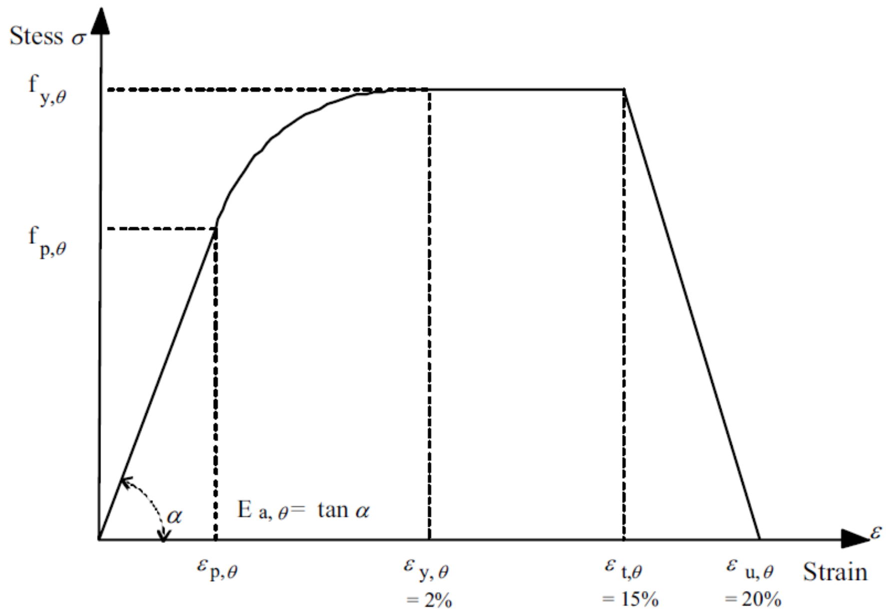

Figure 7 : Steel material law at high temperatures recommended by Eurocode 3 [9]

The standards also provide all the information to calculate the different parameters presented on the figure. The standards also allow to consider strain hardening in some cases. Figure 8 shows the recommended stress-strain relationship with strain hardening.

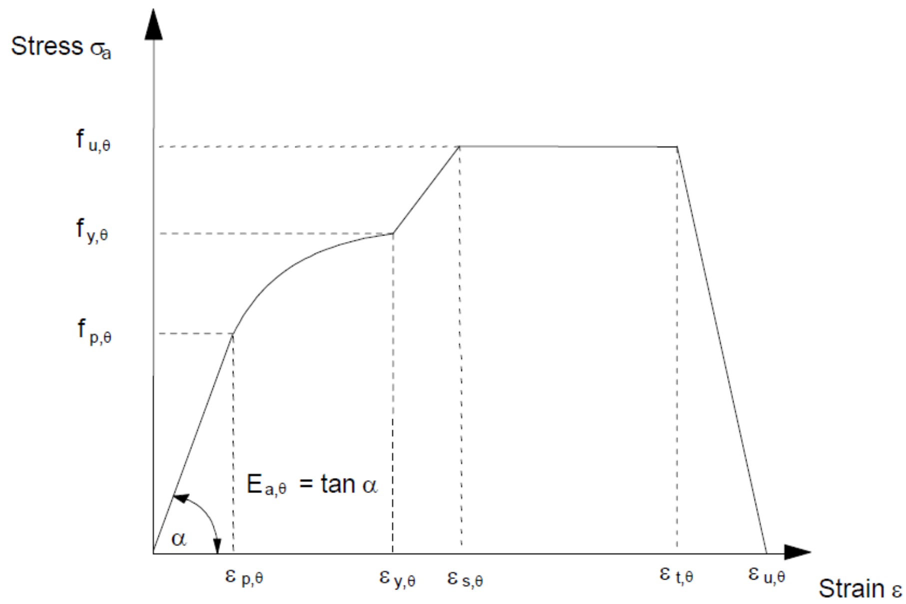

Figure 8 : Steel material law at high temperatures with strain hardening recommended by Eurocode 3[9]

This material law is only valid for temperatures below 400°C. However, the material law recommended by the standards is the one without strain-hardening shown on Figure 7. The second one from Figure 8 is presented as an alternative.

At high temperatures, the loss in stiffness, shown in Figure 5, combined with the large strains needed to reach high resistance, due to the non-linearity of the material law shown on Figure 7 and Figure 8, lead to significantly lower stability. Therefore, more cross-sections are subjected to local buckling at high temperatures than at ambient temperature. As for the loss in strength, shown on Figure 4, it has a direct impact on the resistance at high temperatures. The loss in resistance and stability increases as the temperature increases. As an example, Knobloch et al. [10] conducted an experimental study in which stub columns HEA shapes were loaded at different temperatures. The ultimate strength measured at 400°C, 550°C and 700°C were respectively reduced to 89%, 45% and 14% of the ultimate resistance at ambient temperature. Moreover, a study conducted by Wang et al. [11] concluded that the degradation in resistance of high strength elements is much more rapid than in mild steel elements. This could be explained by the fact that, even at ambient temperature, high strength elements are more subjected to instabilities. Moreover, for different steel grades, the rates at which the material respectively loses its resistance and its rigidity may be different, therefore affecting the behaviour.

In addition, creep, which is not significant at ambient temperature, has a significant impact on the resistance of steel structures at high temperatures. Effectively, at elevated temperatures, deformations caused by creep accelerate and affect the response of the structure. Creep effects are noticeable at temperatures higher than 400°C [5].

1.2 Plastic resistance in fire conditions

As explained previously, when the temperature increases, the stress-strain relationship of steel is no longer linear. As a result, at high temperatures, there is no clearly defined yield point. Therefore, the plastic resistance cannot be defined at high temperature as at room temperature. In some standards (Eurocode 3, CSA-S16, AISC), the stress at 2% total strain is used as the yield limit to calculate the plastic capacity. It is however an approximation as this stress does not correspond to a plateau such as in the material law at ambient temperature.

Moreover, larger strains are necessary to reach higher stresses. A numerical study was conducted by Knobloch et al. [12] to understand the cross-section behaviour of steel sections at high temperatures. In this study, various cross-sections with different yield strengths were studied at ambient temperature and at multiple high temperatures. Results of the study confirmed that compact cross-sections were able to reach resistance higher than the plastic resistance at ambient temperature before failure du to strain-hardening effects. However, those same cross-sections, even those that were very compact, were not able to reach their full plastic capacity at higher temperature. Effectively, as larger strains need to be reached to increase the resistance, instabilities can develop before the plastic resistance is reached. Other studies have shown that, at the ultimate capacity, the strain reached by very stocky cross-sections is smaller than 2% [13]. The use of the stress at 2% total strain in standards can therefore lead to unrealistic and unconservative results and, consequently, calculation methods must be improved.

1.3 Local buckling

Local instability can have a significant impact on a cross-section’s resistance. The impact of instability increases as the slenderness of the cross-section increases. Instabilities occurs when compression stresses are applied to plates. A review on local buckling at ambient and at elevated temperatures is made in the following sections.

1.3.1 Ambient temperature

1.3.1.1 Brief historical review on buckling

Euler was the first to contribute to buckling investigations. After accepting the theory proposed by Bernouilli stating that “the curvature of an elastic beam at any point is proportional to the bending moment at that point”, he studied the shape of a slender elastic bar under different loading conditions [14]. He then derived a first equation to predict load at which buckling occurs on a straight column without any imperfections made of a purely elastic material. The well-known form of the formulae (see Equation (5)) was proposed in 1759 [15].

$$P_{cr} = \frac{\pi^2 \cdot E \cdot I}{L^2} \tag{5}$$

In this equation, the parameter E was introduced as the *modulus of extension* which characterizes the elastic material response [15]. This last formulation does not however consider the fact that real columns are imperfect [16].

According to the summary made by Maquoi et al. [16], the studies conducted on buckling after Euler followed two distinct branches. First, the definition of the elasticity modulus was reviewed to consider inelastic behaviour of a column without any imperfections. Engesser [17] first proposed the use of a tangent modulus while Considere [18] and Jasinski [19] introduced a reduced modulus. In 1947, Shanley [20] demonstrated that the difference between both models reside in the fact that imperfections are not considered. The reduced modulus approach can adequately predict the buckling load of a perfect column. However, the buckling load of real columns is closer to the load predicted using the tangent modulus.

Other researchers focused their study on applying the theory proposed for perfect column to real column with imperfections. Young [21] was the first to demonstrate in 1807 that the behaviour of columns is affected by geometrical imperfections, load eccentricities and material inhomogeneity.

As for contributions to the understanding of plate buckling, Saint-Venant was the first to contribute by establishing the differential equation of buckling for a plate loaded in its plane in 1870 [22].

1.3.1.2 Concept of stability

Instabilities can have a significant impact on the cross-section's and member's resistance. The effect is particularly present for slender sections. At the cross-section's level, which is the focus of the present thesis, the slenderness of a sections depends on the height-to-width ratio of the plates that compose the cross-section. Local buckling of the plates occurs when the plates are no longer in a stable state of equilibrium.

To explain the principle of stability, Figure 9 presents the three main types of equilibrium with the use of a ball on a surface.

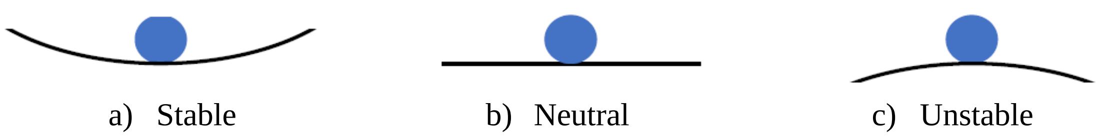

Figure 9 : Types of equilibrium (figure from [23])

The drawing on the left shows a ball that is in a state called stable. If a force is applied to the ball, it will move. However, if the force is removed, the ball will return to its original position. An analogy can be made to a column under a compression load. If a lateral load is applied at the top of the column, it will generate a small displacement. However, if the column is in a stable equilibrium state, it will return to its initial position when the load is removed.

The drawing in the middle shows a ball that is in a state call neutral. If a force is applied to the ball it will move but, contrary to the stable state, it will no go back to its initial position after the removal of the external force. It will however keep its new position which will become its new state of equilibrium. When a column reaches its critical load, the same principle will apply. After the removal of the load, the column will not return to its initial position. However, it will keep its new position as a new state of equilibrium.

Finally, the drawing on the right illustrates a ball in an unstable state of equilibrium. If even a very small force is applied to the ball, it will undergo a large displacement and will not be able to reach a new state of equilibrium by itself. To continue with the analogy, once the critical load has been reached, if a small load increment is applied to the column, it will undergo large deformations and will no longer be able to reach a stable state.

The first form of instability that may occur in a column is instability by bifurcation (Linear Buckling Analysis (L.B.A.)). A bifurcation point is a point when two or more equilibrium states cross path. Instability by bifurcation is shown on Figure 10. This type of instability occurs with a perfect column free of any imperfections.

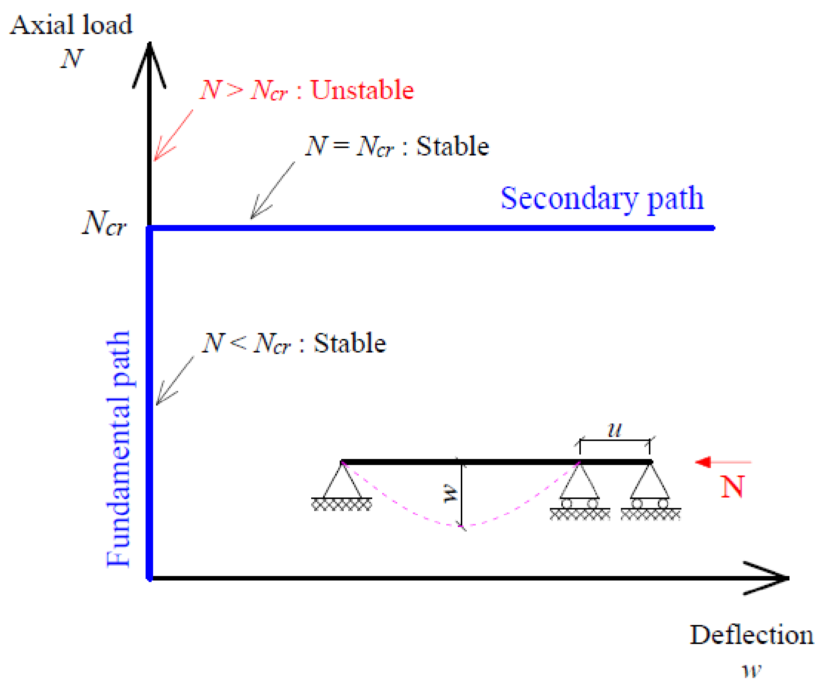

Figure 10 : Instability by bifurcation (figure from [3])

On this figure, it is possible to see that when the applied compressive load (N) is lower than the critical load (N_{cr}), the column undergo limited axial shortening *u* but do not undergo transverse deflection *w*. The column follows what is identify as the fundamental path on

Figure 10 and is considered to be in a stable state of equilibrium. Once the load applied to the column reaches the critical load (N_{cr}), transverse deformations begin to increase and the column can no longer return to its initial shape. It then follows the path identified as the secondary path. Finally, if the load applied is larger then the critical load (N_{cr}), the column is no longer stable.

As no structure is free of any imperfections, instabilities do not occur by bifurcation but by divergence of equilibrium (Geometrically and Materially Non-linear Analysis with or without imperfections (G.M.N.A. or G.M.N.I.A.). This type of instability is shown on Figure 11.

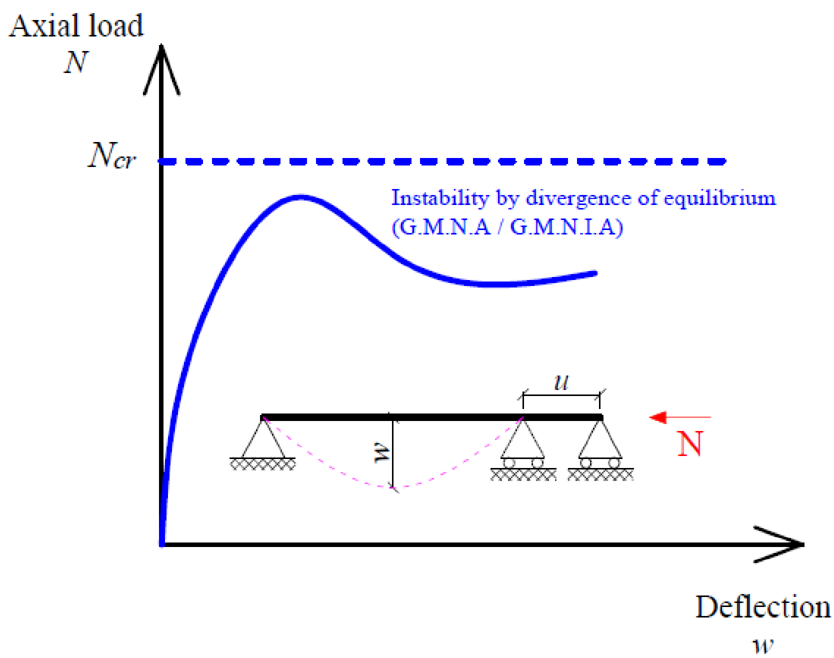

Figure 11 : Instability by divergence of equilibrium (figure from [3])

This figure shows that lateral deflection starts to develop before the attainment of critical load. This is due to the presence of initial imperfections. Moreover, owing to imperfections, the ultimate resistance of the structure will be reached before the applied load reaches the critical load.

1.3.1.3 Characterization of local buckling

Local buckling refers to the buckling of the plates that compose a cross-section. As shown on Figure 12, plates subjected to compression stresses present some buckles. As plates are connected, the buckling of a plate triggers the movement on the adjacent plates.

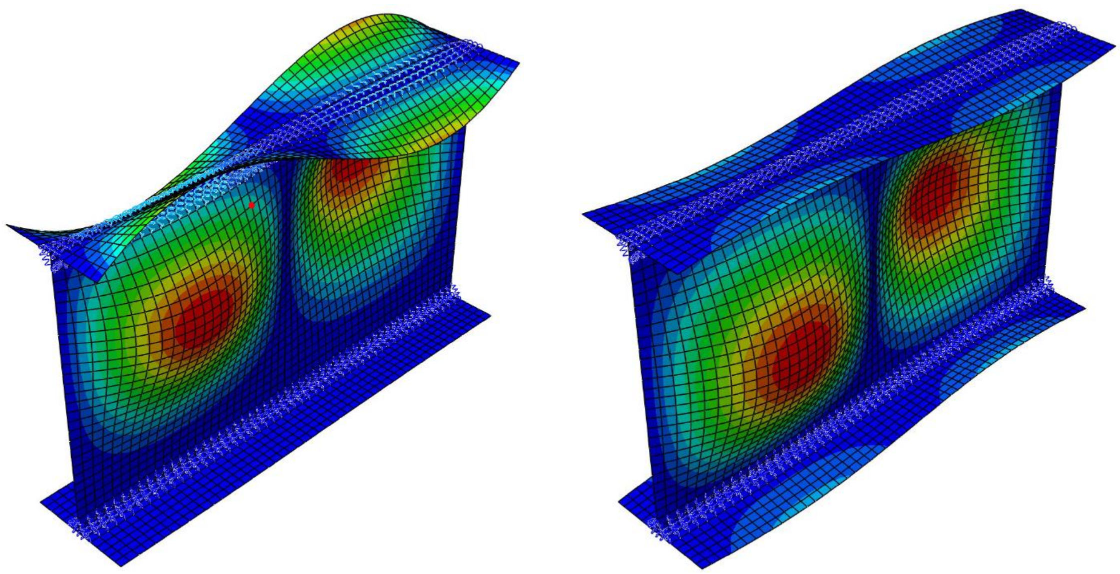

a) b)

Figure 12 : Local buckling of an I-section under: a) Major-axis bending; b) Compression (L.B.A. analysis)

1.3.1.4 Plate buckling

Buckling occurs when plates are loaded with compressive stress in their plane. Figure 13 shows how local buckling develops on a rectangular plate simply supported on all sides.

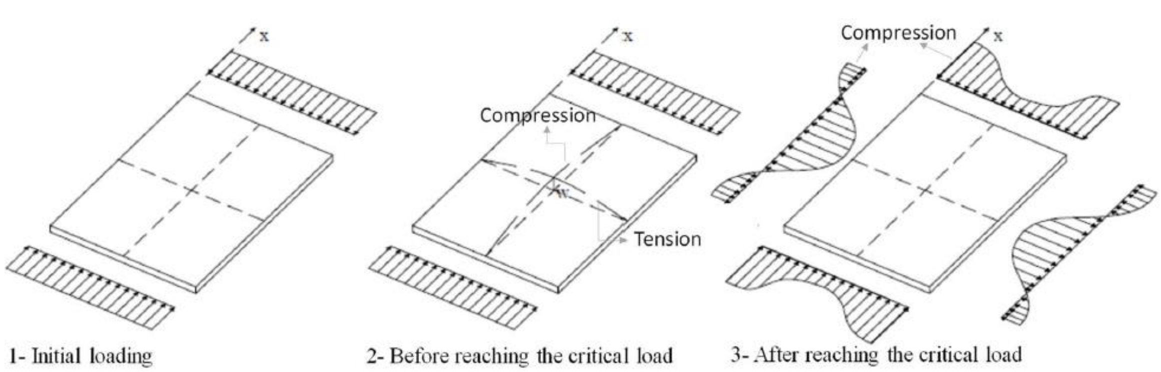

Figure 13 : Development of local buckling (figure from [23])

In this figure, the plate free of imperfections is loaded in only one direction. Initially, the compressive load is uniformly distributed on the side and the plate remains plane. As the load increases, the stress distribution on the side of the plate remains uniform, but the fibers parallel to the load are in compression while the fibers that are perpendicular to the applied load are in tension. When the critical load is reached, the stress distribution is no longer uniform due to the development of buckles. As the edges are stiffer than the middle of the plate, compression stress decreases in the middle of the plate and increases near the edges. The critical stress of a plate, without any imperfections and simply supported on all sides, can be calculated with the following differential Equation [24].

$$\frac{E \cdot t^3}{12 \cdot (1-\nu^3)} \cdot \left(\frac{\partial^4 w}{\partial x^4} + 2 \cdot \frac{\partial^4 w}{\partial x^2 \cdot \partial y^2} + \frac{\partial^4 w}{\partial y^4} \right) = -N_x \cdot \frac{\partial^2 w}{\partial x^2} \quad (6)$$

In this equation, the deflection w can be expressed as the sinusoidal function presented in Equation (7) [24].

$$w(x,y) = \sum_{m=1}^{\infty} \sum_{n=1}^{\infty} A_{mn} \cdot \sin\left(\frac{m \cdot \pi x}{a} \right) \cdot \sin\left(\frac{n \cdot \pi y}{b} \right) \quad (7)$$

The deflection depends on the number of waves in both the x-direction (m) and in the y-direction (n). In this equation, a and b are the dimensions of the plate.

By combining both equations, the critical buckling stress $\sigma_{cr,p}$ is obtained and is defined by the following Equation [25].

$$\sigma_{cr,p} = \left(\frac{m \cdot b}{a} + \frac{a}{b \cdot m} \right)^2 \cdot \frac{\pi^2 \cdot E}{12 \cdot \left(1-\nu^2\right)} \cdot \left(\frac{t}{b} \right)^2 = k \cdot \frac{\pi^2 \cdot E}{12 \cdot \left(1-\nu^2\right)} \cdot \left(\frac{t}{b} \right)^2 \quad (8)$$

In this equation, the buckling factor k depends on the boundary conditions of the plates. If more restraint is provided by the boundary conditions, the value of k is higher which increases the critical stress. The buckling factor also depends on the aspect ratio and on the number of half-waves in both directions.

Figure 14 presents the buckling factor k as a function of the aspect ratio $\alpha = a/b$ and of the number of half-waves m for a simply supported plate subjected to pure compression in one direction. The value of m also indicates the buckling mode considered, i.e. when $m = 1$ the plate is in its first buckling mode and has one half-wave.

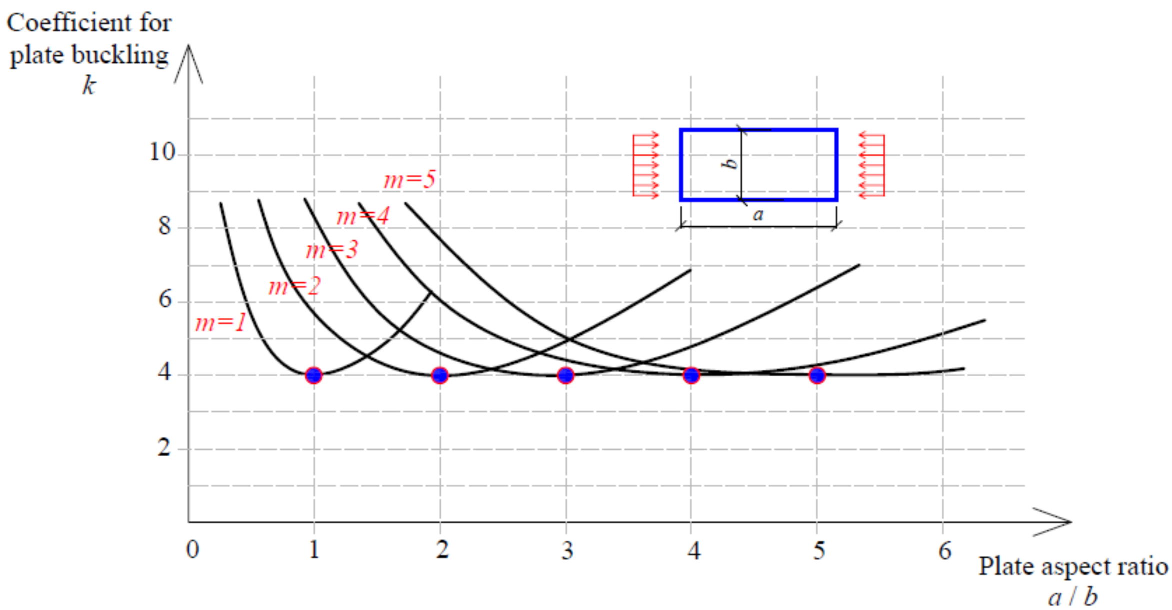

Figure 14 : Factor k as a function of the aspect ratio for a simply supported plate under pure compression (figure from [3])

To determine the critical buckling stress, the minimum value of k must be used. As shown on Figure 14, the critical buckling mode is not the same for all aspect ratios. However, all buckling modes give a minimal value of $k = 4$. Finding the precise value of k for each plate based on its aspect ratio would be long and laborious. Therefore, for a simply supported plate under pure compression, the retained value is $k = 4$ which is conservative.

1.3.1.5 Influence of boundary conditions and stress distribution

As specified previously, the value of k is influenced by the boundary conditions of the plate. It is also influenced by the loading. Effectively, as compressive stresses are the ones that induce buckling, the critical load of a plate under pure compression where a compressive stress is applied uniformly will be lower than the one of a plate under bending where the compressive stress is only applied on a part of the plate. For set of each boundary conditions and load cases, it is possible to obtain a graph similar to the one presented on Figure 14. Again, the minimal value of k is retained.

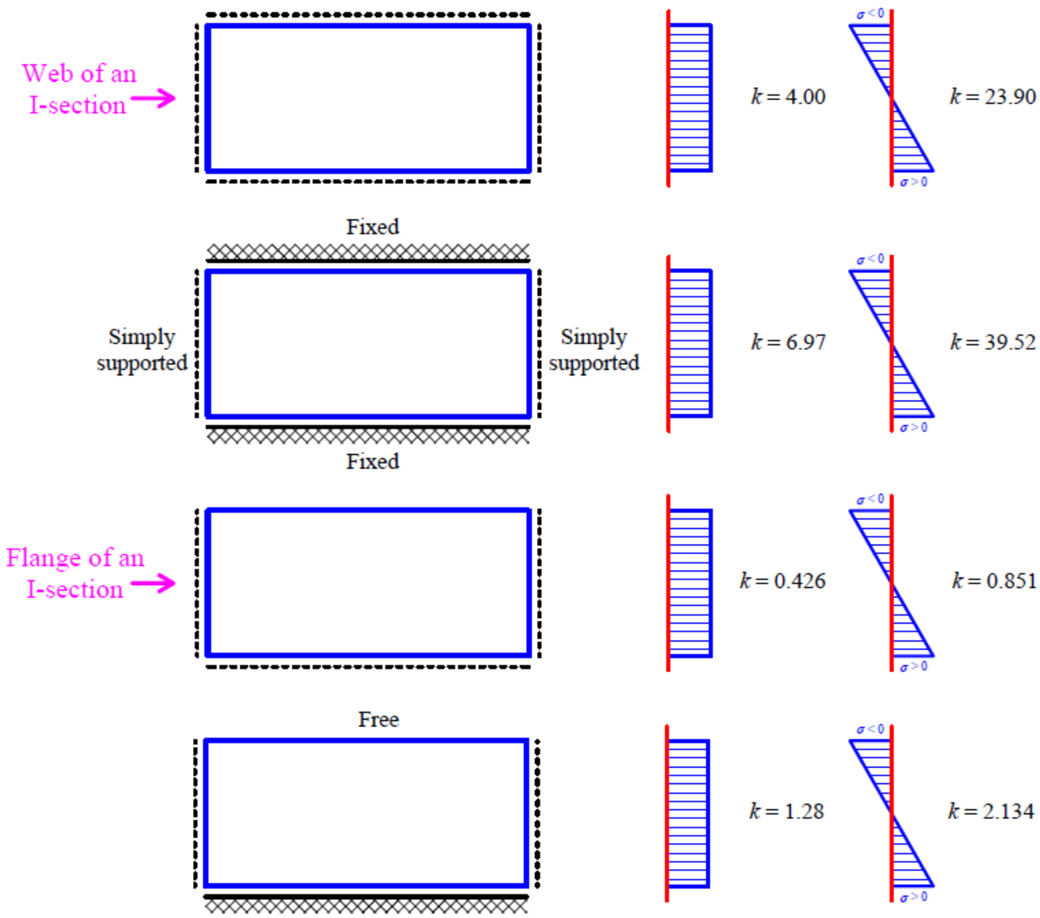

Figure 15 : Value of k for various boundary conditions and stress distributions (figure from [3])

As expected, the figure shows that the buckling factor is higher when more restraint is provided by the boundary conditions and when non-constant compression (e.g. bending) is applied. When computing the critical stress of the plates composing an open-section, the web is often considered as simply supported on all sides while the flanges are considered as simply supported on three sides. These assumptions are however disputable has they do not consider plate interaction. This subject is discussed in the following section.

1.3.1.6 Plate interaction

In many standards (e.g. Eurocode 3 [26], CSA S16 [27] and AISC [28]), plates that constitute a cross-section are considered individually when classifying the section or when determining the critical stress. The most conservative result is then kept and considered for the entire cross-section. As mentioned previously, in the case of I and H-sections, the web is considered as supported on all sides while flanges are considered as simply supported on three sides. These assumptions are conservative and non-realistic as they do not consider restraints provided by adjacent plates. Effectively, elements that are more stable have the capacity to stabilise less stable elements. In an experimental study, Cheng et al. [29] calculated the critical stress for individual plates of open section and compared the results with critical stress of the cross-section as a whole. Results show that the overall critical stress was always higher than the lowest critical stress of the individual plates which confirms that there is an interaction between plates and that plates do provide additional restraints to adjacent plates. Similar observations are made in [30], [31] and [32].

In his book "*Buckling Strength of Metal Structures*" published in 1952, Bleich [33] explains that the only case in which proposed buckling factors *k* are accurate to determine the critical stress of a cross-section is the one where both plates buckle simultaneously. In that particular case, both plates have the same critical stress and none is able to provide restraint to the other, which means that all plates behave as simply supported. This limit case is however very rare and therefore, in the majority of cases, restraint is provided by one plate to the other. He therefore proposed formulas for the buckling factors accounting for the restraint provided by adjacent plates. Those equations are presented in Table 1.

Table 1 : Proposed buckling coefficients by Bleich [33]

	Buckling factor *k*	Restraint coefficient
Web	$k=\left(2+\dfrac{2}{10\cdot\zeta+3}\right)^2$	$\zeta=\dfrac{t_w^{\,3}}{t_f^{\,3}}\cdot\dfrac{0.16+0.0056\cdot\left(\dfrac{h}{b/2}\right)^2}{1-9.4\cdot\dfrac{t_w^{\,2}}{t_f^{\,2}}\cdot\dfrac{h^2}{\left(b/2\right)^2}}$

Flanges	$k = \left(0.65 + \frac{2}{3 \cdot \zeta + 4}\right)^2$	$\zeta = 2 \cdot \frac{t_f^{\,3} \cdot h}{t_w^{\,3} \cdot \left(b/2\right)} \cdot \frac{1}{1 - 0.106 \cdot \frac{t_f^{\,2}}{t_w^{\,2}} \cdot \frac{h^2}{\left(b/2\right)^2}}$

When a plate starts to buckle, it is not able to provide restraint to adjacent plates. This means that, in the case of I or H-sections, either the flanges provide restraint to the web or the web provide restraint to the flanges. Therefore, before using these equations, it is necessary to determine which plate provides restraint to the other.

In 2010, a study was conducted by Seif et al. [34] to qualify the impact of plate interaction on buckling. In this study, the authors propose buckling factors *k* for the web and the flanges that take into account the interaction between plates. Table 2 presents the suggested equations to determine the web buckling factor of I shape sections.

Table 2 : Proposed web buckling factors by Seif et al.[34]

Loading	Web buckling factor
Compression	$\frac{1}{k_w} = \frac{1.5}{\left(\left(\frac{h}{t_w}\right) \cdot \left(\frac{2 \cdot t_f}{b}\right)\right)^{2.5}} + 0.18$
Major-axis bending	$\frac{1}{k_w} = \frac{1.5}{\left(\left(\frac{h}{t_w}\right) \cdot \left(\frac{2 \cdot t_f}{b}\right)\right)^{2.5}} + 0.015$
Minor-axis bending	$\frac{1}{k_w} = \frac{1.5}{\left(\left(\frac{h}{t_w}\right) \cdot \left(\frac{2 \cdot t_f}{b}\right)\right)^{2.5}} + 0.008$

Once the web buckling factor is determined, Equation (9) can be used to determine the flange buckling factor.

$$k_f = k_w \cdot \left(\frac{t_w}{h}\right)^2 \cdot \left(\frac{b/2}{t_f}\right)^2 \quad (9)$$

The variable *h* presented in equations from Table 2 and in Equation (9) refers to the distance between the mid-height of the flanges.

1.3.1.7 Post buckling behaviour

Due to the redistribution of the stresses after the critical stress is reached, plates exhibit post buckling resistance contrary to columns. Effectively, when the plate buckles, a tensile membrane action develops and provides additional resistance to the plate [25]. The phenomenon is shown on Figure 16.

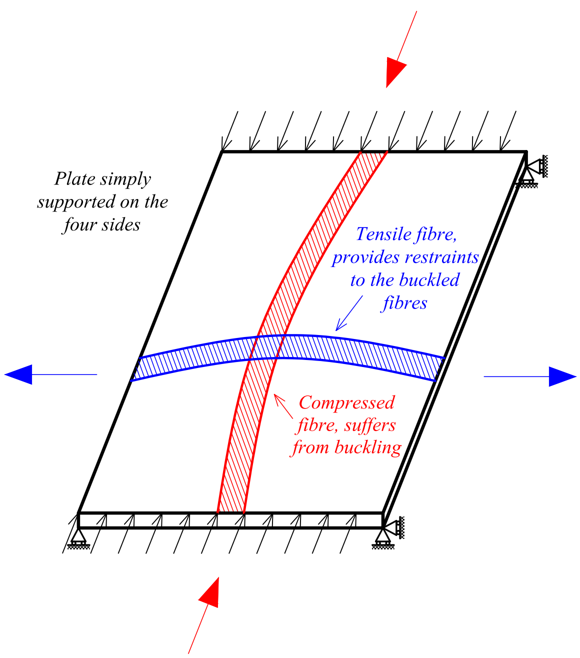

Figure 16 : Stress redistribution after buckling in a plate simply supported on all sides (figure from [3])

This figure shows that the transverse fibers in tension distribute the load of the fibers in compression to the edges. For this post buckling resistance to exist, the plate must be supported on at least one side parallel to the load application. Else, no stress redistribution is possible and the plate acts like a column.

When a column reaches its critical load, failure is reached which is not the case for plates. Figure 17 shows the typical load path for both columns and plates.

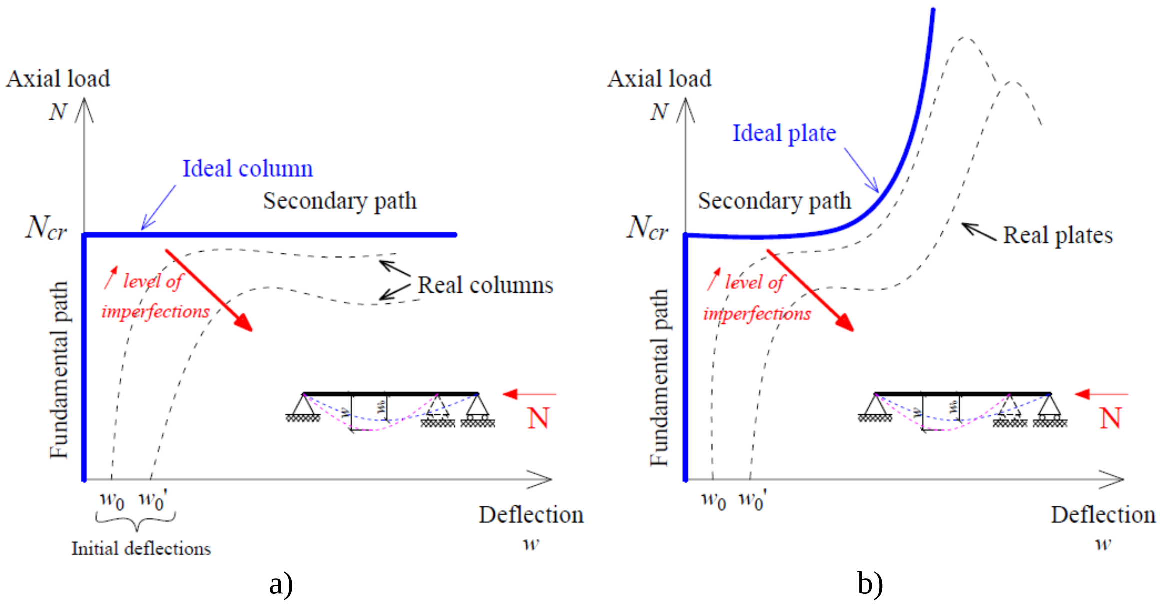

Figure 17 : Typical load path of : a) An axially compressed column ; b) A compressed plate (figure from [3])

Figure 17 shows that the ultimate load of a compressed column governed by instability is reached at a load smaller than the critical load due to the presence of imperfections. If the column is free of any kind of imperfections, then this same column reaches failure when the critical load is attained. The figure also shows that the load path of a compressed plate governed by instability is completely different. Just like for columns, the presence of imperfections reduces the ultimate load. However, the peak load can, in some cases, be reached at a load much higher than the critical load.

Figure 18 describes the theorical load path of a perfect plate which failure is due to both buckling and yielding.

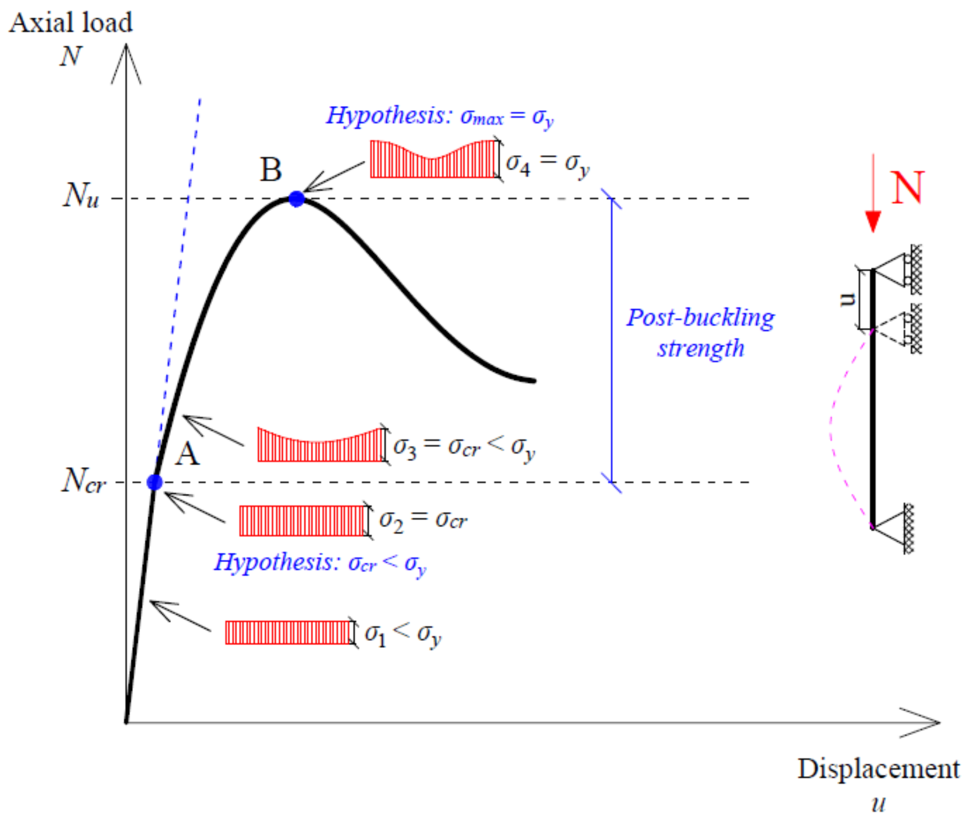

Figure 18 : Theorical load path of a perfect plate in compression (figure from [3])

As explained previously, the compressive stress is uniformly distributed until the critical load is reached. When the applied load is increased over the critical load, stresses increase near the edges and decrease in the center of the plate due to the phenomenon explained by Figure 16. The hypothesis made here is that failure occurs when the fibers on the edge of the plate reach the yield strength of the plate [3].

When codes try to predict the local strength of slender section, they need to consider the true behaviour of real plates where distribution of stresses is no more uniform along the width. The Effective Width Method (E.W.M.) is used in most standards. The concept of the Effective Width Method is presented on Figure 19.

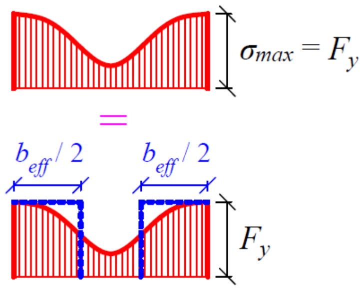

Figure 19 : Concept of the Effective Width Method (figure from [3])

In this method, the non-uniform stress distribution is replaced by a uniform effective stress block of length b_{eff}. In 1932, equations were proposed by Von Karman for the Effective Width Method [35]. The equations were derived by assuming that the critical stress on the effective width is equation to the yield limit. Equations (10) to (13) show how to obtain the effective width based on Von Karman's theory.

$$\sigma_{cr,p} = k \cdot \frac{\pi^2 \cdot E}{12 \cdot \left(1-\nu^2\right)} \cdot \left(\frac{t}{b}\right)^2 \tag{10}$$

$$\sigma_{cr,p,eff} = k \cdot \frac{\pi^2 \cdot E}{12 \cdot \left(1-\nu^2\right)} \cdot \left(\frac{t}{b_{eff}}\right)^2 = F_y \tag{11}$$

$$\frac{F_y}{\sigma_{cr,p}} = \left(\frac{b}{b_{eff}}\right)^2 \tag{12}$$

$$b_{eff} = b \cdot \sqrt{\frac{\sigma_{cr,p}}{F_y}} = b \cdot \overline{\lambda_p} \tag{13}$$

The equations proposed by Von Karman are however not representative of real plates as they consider a perfect plate free of imperfections. A proposal, presented by Equation (14), was made by Winter in 1970 [36] to take into consideration those imperfections [22].

$$b_{eff} = \frac{b}{\overline{\lambda_p}} \cdot \left(1 - \frac{0.22}{\overline{\lambda_p}}\right) \tag{14}$$

Where :

$$\overline{\lambda_p} = \sqrt{\frac{F_y}{\sigma_{cr,p}}} \qquad (15)$$

These last formulas are used in the Canadian code [27] while modified versions of Winter formulas are used in Part 1-5 of the EC3 [37]. The modified formulas for internal and outstand elements are respectively presented in Equations (16) and (17). In Equation (16), ψ is the stress ratio calculated based on the stress distribution.

$$b_{eff} = \frac{b}{\overline{\lambda_p}} \cdot \left(1 - \frac{0.055 \cdot (3+\psi)}{\overline{\lambda_p}}\right) \qquad (16)$$

$$b_{eff} = \frac{b}{\overline{\lambda_p}} \cdot \left(1 - \frac{0.188}{\overline{\lambda_p}}\right) \qquad (17)$$

1.3.1.8 Buckling curves

Buckling curves are used to consider the interaction between resistance and instability. Such buckling curves are the basis of the Overall Interaction concept (O.I.C.) presented previously. An example of a buckling curve is presented on Figure 20.

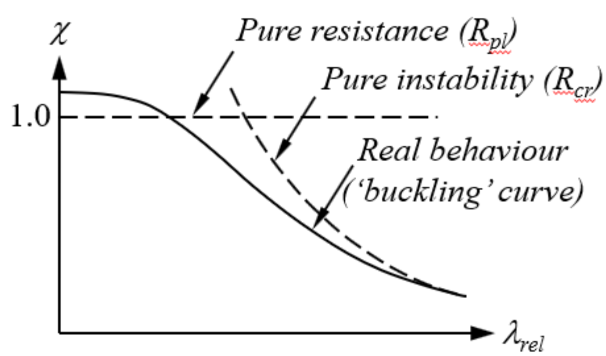

Figure 20 : Example of buckling curve

Buckling curves usually use non-dimensional parameters which allows to compare elements with different section's geometries and material properties. In the case of the O.I.C., the non-dimensional parameters used are the relative slenderness (λ_{rel}) and the ultimate reduction factor (χ).

1.3.1.8.1 European buckling curves

From 1960, the European Convention for Constructional Steelwork (ECCS)'s main objective was to uniformize the method used in standards. In 1970, the ECCS proposed three buckling curves with non-dimensional parameters that consider imperfections. The three curves are defined by the following formula in which $\overline{N}$ is the buckling reduction factor, equivalent to χ in the O.I.C., and $\overline{\lambda}$ is the reduced slenderness, equivalent to λ in the O.I.C. [16]

$$\overline{N} = \frac{1}{\left(0.5+\alpha\cdot\overline{\lambda}^{2}\right)+\sqrt{\left(0.5+\alpha\cdot\overline{\lambda}^{2}\right)^{2}+\beta\cdot\overline{\lambda}^{2}}} \tag{18}$$

The non dimensional parameters are calculated as follow:

$$\overline{N} = \frac{\sigma_K}{F_y} \tag{19}$$

$$\overline{\lambda} = \frac{\lambda}{\lambda_r} = \frac{\lambda}{\pi\cdot\sqrt{E/\sigma_{cr}}} \tag{20}$$

In the last equations, σ_K is the ultimate stress, λ is the slenderness while λ_r is the Euler slenderness. The three curves differ in the value of α and β. Figure 21 shows the three buckling curves [16].

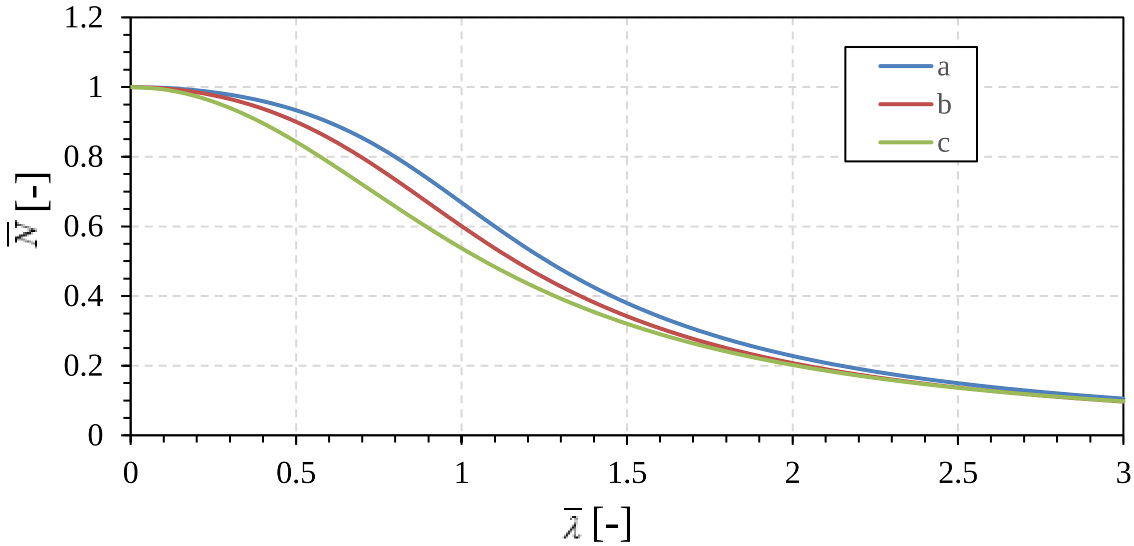

Figure 21 : Three buckling curves initially proposed by ECCS

Those three curves were however criticized. The first principal critic was that there was no plateau for small slenderness. Then, the second principal critic was that the curves were established for the most common steel grade with plate thickness under 40 mm. However, higher steel grades and more important thickness needed to be accounted for to be representative of what was practically used in construction. Five new buckling curves were therefore proposed by ECCS. Many proposals were made before incorporating the final version in Eurocode 3 [16].

The curves currently used in Eurocode 3 depend on both the section's geometry and the material properties. Equation (21) is the general equation used for the buckling curves in Eurocode 3 [26]. In this equation, the reduction factor χ is defined as a function of the non-dimensional slenderness $\overline{\lambda}$.

$$\chi = \frac{1}{\phi + \sqrt{\phi^2 - \overline{\lambda}^2}} \leq 1.0 \tag{21}$$

In this equation, the intermediate calculation parameter ϕ is derived from the following equation.

$$\phi = 0.5 \cdot \left(1 + \alpha \cdot \left(\bar{\lambda} - 0.2\right) + \bar{\lambda}^2\right) \tag{22}$$

As for the non-dimensional slenderness, it is calculated with Equation (23). However, the effective area is used instead of the gross area for class 4 cross-sections.

$$\bar{\lambda} = \sqrt{\frac{A \cdot f_y}{N_{cr}}} \tag{23}$$

The parameter α in Equation (22) is the generalised imperfection factor which is different for each of the five curves. The values of the parameters α are presented in Table 3 [26].

Table 3 : Imperfection factors for the buckling curves from Eurocode 3

Buckling curve	a_0	a	b	c	d
α	0.13	0.21	0.34	0.49	0.76

The five buckling curves are presented on Figure 22.

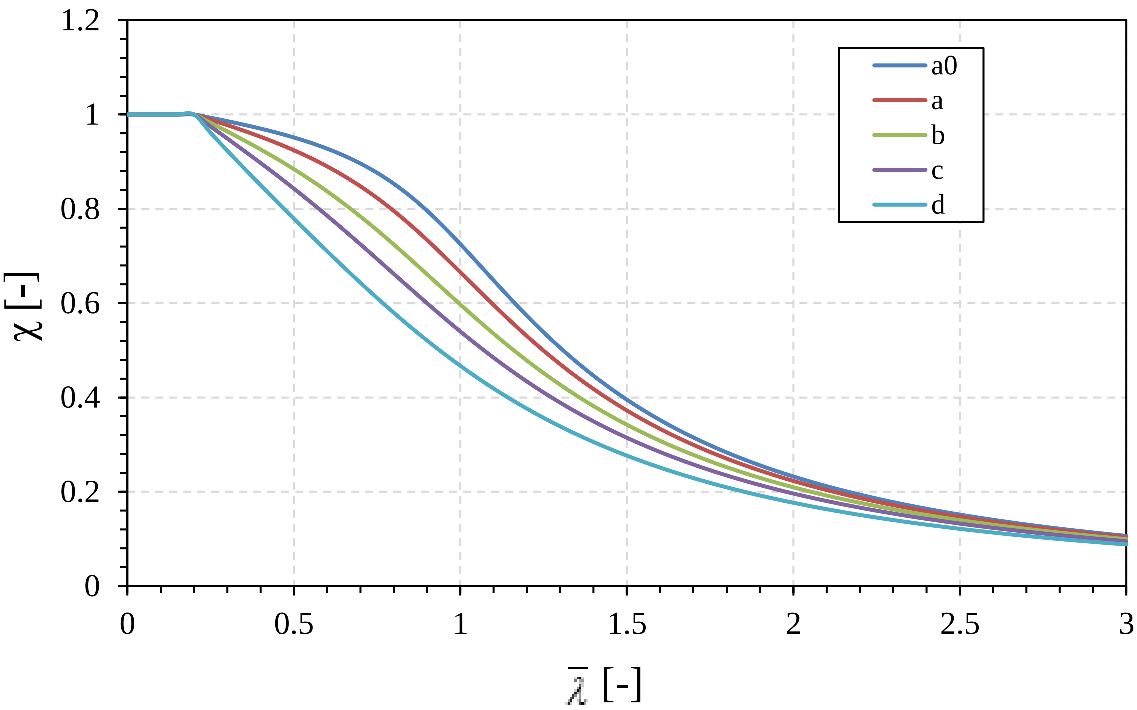

Figure 22 : Buckling curves from Eurocode 3

For all those curves, there is a plateau for slenderness lower than 0.2. Effectively, at such small slenderness, no buckling is considered. The choice of the buckling curves depends on the thickness of the plates, the axis of buckling and the steel grade. Eurocode 3 proposed a table to allow the user to choose the right curve.

1.3.2 Elevated temperatures

It has been explained previously that the stress-strain relationship of steel at high temperatures is no longer linear. Because of this non-linear stress-strain relationship, large strain are needed for the resistance to increase which means that more cross-sections are subjected to buckling at high temperature [4]. Studies have also shown that, as at ambient temperature, even very compact sections can experience buckling after reaching their plastic capacity due to strain hardening effects. This post-plastic local buckling is of interest at high temperatures as it permanently alters the load-bearing capacity of the member during fire exposition and after [38].

The critical stress of a plate free of imperfections can be calculated using the same equation as at ambient temperature but with a Young's modulus adapted to the considered temperature [7]. As explained previously, Young's modulus decreases with the increase in temperature. Therefore, the critical stress of a plate also diminishes with the increase in temperature.

$$\sigma_{cr,\theta} = k \cdot \frac{\pi^2 \cdot E_{a,\theta}}{12 \cdot \left(1-\nu^2\right)} \cdot \left(\frac{t}{b}\right)^2 \tag{24}$$

However, according to Knobloch et al. [7], the factor k is different for slender and stocky plates. For slender plates, which are defined as the plates for which the critical stress is lower than the proportionality limit at a specific temperature, the factor k used at ambient temperature can be used. For stocky plates, plates with critical stresses higher than the proportionality limit, the buckling factors k depend on the plastification rate and on the non-linear stress-strain relationship.

In current codes, when calculating the resistance of slender sections at elevated temperatures, the effective properties are calculated using the effective width method at ambient temperature. However, using the same equations as at ambient temperature does not take into consideration the non-linearity of the stress-strain law. A few proposals have been made to calculate more adequately the effective properties of slender cross-sections.

Quiel and Garlock [38] proposed new equations to calculate effective properties of cross-sections. The proposed reduction factors ρ respectively for internal and external elements are presented below. The factor ρ is the equivalent of the reduction factor χ used in the O.I.C. but applicable to plates.

$$b_{eff,\theta} = \rho_\theta \cdot b \tag{25}$$

$$\rho_\theta = \frac{1.41}{\sqrt{\lambda_{c,T} \cdot \sqrt{k}}} \cdot \sqrt{\frac{k_{p,T}}{k_{y,T}}} \cdot \left(1 - \frac{0.24 \cdot (3+\psi)}{k \cdot \lambda_{c,T}^{(\psi/2-1)}}\right) \leq 1 \tag{26}$$

$$\rho_\theta = \frac{0.81}{\sqrt{\lambda_{c,T} \cdot \sqrt{k}}} \cdot \sqrt{\frac{k_{p,T}}{k_{y,T}}} \cdot \left(\frac{4}{3+\psi}\right) \cdot \left(1 - \frac{0.021 \cdot (5-\psi)}{k \cdot \lambda_{c,T}^{(3\cdot\psi/2-2)}}\right) \leq 1 \tag{27}$$

In those equations, the relative slenderness is calculated according to Equation (28).

$$\lambda_{c,T} = \sqrt{\frac{f_{y,\theta}}{\sigma_{cr,\theta}}} = \sqrt{\frac{k_{y,\theta} \cdot f_y}{k \cdot \frac{\pi^2 \cdot k_{E,\theta} \cdot E}{12 \cdot (1-\nu^2)} \cdot \left(\frac{t}{b}\right)^2}} \tag{28}$$

In those equations, the ratio between the proportionality limit reduction factor and the yield limit reduction factor diminishes the calculated ultimate strength. However, by including this reduction directly in the calculation of the effective properties, the user does not have do use the 0.2 % plastic strain when calculating the ultimate resistance as done in Eurocode 3 [39].

Couto et al. [40] also proposed new equations for the effective width method at high temperatures. Those equations are calibrated based on the equations currently used in Eurocode 3. The proposed formulas for internal and outstand elements are respectively presented in Equations (29) to (31).

$$b_{eff,\theta} = \rho_\theta \cdot b \tag{29}$$

$$\rho_\theta = \frac{\left(\overline{\lambda_p} + \alpha_\theta\right)^{\beta_\theta} - 0.055 \cdot (3+\psi)}{\left(\overline{\lambda_p} + \alpha_\theta\right)^{2 \cdot \beta_\theta}} \leq 1.0 \quad (30)$$

$$\rho_\theta = \frac{\left(\overline{\lambda_p} + \alpha_\theta\right)^{\beta_\theta} - 0.188}{\left(\overline{\lambda_p} + \alpha_\theta\right)^{2 \cdot \beta_\theta}} \leq 1.0 \quad (31)$$

In those equations, factors α_θ and β_θ are temperature-dependant parameters than can be calculated with equations presented in Table 4.

Table 4 : Factors to use in Equations (30) and (31)

	Internal elements	Outstand elements
α_θ	$0.9 - 0.315 \cdot \frac{k_{0.2p,\theta}}{\varepsilon_\theta \cdot k_{y,\theta}}$	$1.1 - 0.63 \cdot \frac{k_{0.2p,\theta}}{\varepsilon_\theta \cdot k_{y,\theta}}$
β_θ	$2.3 - 1.1 \cdot \frac{k_{0.2p,\theta}}{\varepsilon_\theta \cdot k_{y,\theta}}$	$2 - 1.1 \cdot \frac{k_{0.2p,\theta}}{\varepsilon_\theta \cdot k_{y,\theta}}$
ε_θ	$\varepsilon_\theta = 0.85 \cdot \varepsilon = 0.85 \cdot \sqrt{\frac{235}{f_y}}$	

Those proposed equations allow to use the strength at 2% total strain instead of the 0.2% proof strain currently used in Part 1-2 of Eurocode 3, which leads to more optimized cross-sections. In this proposal, an effective section is calculated for both class 3 and class 4 sections. Contrarily to the actual method used in standards, the proposed equations consider the non-linear stress-strain relationship that has a great influence at high temperatures.

In 2006, Fontana and Knobloch [4] proposed a strain-based approach to consider the local buckling of cross-sections at high temperatures. The authors explain that the stress-based approach currently used in codes to determine effective widths at ambient temperatures and at high temperatures is not suitable for high temperatures as the material law is no longer linear. Effectively, at high temperatures, the maximum load-carrying capacity is not reached at the proportional strains as it is at ambient temperature since the proportional strain is not equal to the yield strain. The authors therefore consider that a strain-based approach is more precise to determine those effective widths as the non-linearity of the material law can easily be considered. In this approach, the plates' slenderness is first calculated based on the boundary conditions and on the strain distribution on the plate. With the plate slenderness, the reduction factor can be calculated. The stress distribution within the section can then be obtained and the resistance calculated. The advantage of this method is that the non-linearity of the material law is considered, contrary to common methods, which leads to more accurate results. However, this method is again an improvement to the calculation of effective properties at high temperature. It does not, however, eliminate the need for cross-section classification.

All new proposed methods lead to more accurate results than the actual method used in standard to calculate the effective properties of slender sections. However, the calculation of effective properties remains tedious and does not eliminate the need to resort to cross-section classification.

1.4 Imperfections and their influence

The manufacturing of cross-sections induces geometrical and material imperfections. These imperfections have a non negligible impact on the cross-section resistance. Therefore, when using finite elements models to predict the resistance of cross-sections or members, imperfections must be considered, as the goal of the model is to represent as accurately as possible the real behaviour of those elements.

1.4.1 Geometrical Imperfections

Geometrical imperfections induced by the factoring process include, but are not limited to, eccentricities, out-of-flatness, out-of-straightness, etc. Those imperfections must be incorporated in numerical models as they are present in all steel members and can affect the resistance significantly by trigering premature buckling and yielding. Two types of geometrical imperfections must be taken into consideration: local and global imperfections. However, as this study focuses on the cross-sectional resistance, only local imperfections are discussed in the present section.

Some experiments have been conducted in which researchers have measured the real geometrical imperfections before introducing those in numerical models. However, those experimental experiments are long and complex and it would therefore not be realistic to expect all researchers to conduct this type of measurements before conducting numerical simulations. Those experiments have been conducted to be able to propose simplified methods for the introduction of geometrical imperfections into numerical models. Two simplified methods are generally used to introduce geometrical imperfections into Finite Element Models. Many researchers use the eigenmode's shapes scaled to an appropriate amplitude as initial imperfections. Others prefer to incorporate geometrical imperfections using functions. For example, the geometrical imperfections on the flange of an open sections could be defined by a sinusoidal function. Many studies have proposed guidelines for the introduction of geometrical imperfections. A few are summarized below.

In a study by Yun et al. [41], an experimental campaign was conducted to measure geometrical local imperfections. Numerical simulations were then used to compare the results obtained with the measured imperfections and results obtained with an approximate modelling of local geometrical imperfections. Imperfections were either modeled with the use of sinusoidal functions or with the use of the first eigenmode shape and different maximal amplitudes were considered. Results of the study show that, for I-sections subjected to compression and major-axis bending, the amplitude and shape of local imperfections do not have a significant impact on the results. It was therefore recommended to stay consistent with Eurocode 3 which uses the first eigenmode with an amplitude of h / 200 where h is the clear height of the web.

Schafer and Peköz [42] conducted a study to characterise geometrical imperfections when modeling cold-formed steel. The study recommends a simplified approach which consist in combining at least two different eigenmode shapes. The study also recommends using the following equations to calculate the maximal amplitude (ω_0) based on either the plate's width (w) or the plate's thickness (t).

$$\omega_0 = 0.006 \cdot w \qquad (32)$$

$$\omega_0 = 6 \cdot t \cdot e^{-2 \cdot t} \quad (33)$$

A study was conducted by Gagné et al. [43] in which sinusoidal functions were used to consider the geometrical imperfections on open sections. In this study, many cross-sections shapes were considered from compact to slender. The results of the numerical study show that there was generally no significant differences when using either an amplitude of the sinusoidal function based on the plate's thickness, $0.1 \cdot t$, or based on the plate's width, $a/200$. However, for very slender sections, the use of the plate's width is preferred by the authors.

The use of sinusoidal functions to introduce local imperfections was also studied for steel hollow sections by both Hayeck [44] and Nseir [45] in their PhDs. In both case, multiple amplitudes and periods were tested. Both studies concluded that the use of sinusoidal functions allowed to obtained representative finite element results.

Part 1-5 of Eurocode 3 [37], which is dedicated to plates, also provides some guidelines. The code recommends the use of the first buckling shape obtained from a Linear Buckling Analysis for the shape of the geometrical imperfection. As for the amplitude, it is recommended to use either the minimum value of $a/200$ or $b/200$, where a and b are refered to the dimensions of the plate, or 80 % of the geometric fabrication tolerance. In the case that material imperfections are also to be considered in the numerical model, which is usually the case, Part 1-5 of Eurocode 3 also states that one type of imperfection (either geometrical or material) should be chosen as the primary and that the other one can be reduced by 30 %.

As described above, many guidelines already exist regarding the introduction of imperfections into finite element models. However, there is no consensus on those guidelines. A recent study as be conducted by Gérard et al. [46] to address the influence of different types of imperfections on the local resistance of open sections and to provide guidance in the introduction of geometrical imperfections into numerical models. In this study, geometrical imperfections were introduced by using sinusoidal functions or with the use of the first buckling mode. For the imperfections using sinusoidal functions, different amplitudes and half-wave lengths were tested. For the imperfections using the first buckling mode, different amplitudes were studied.

Although the results of the study show that the use of the first buckling mode shape is convenient and procures adequate results, the study concludes that it is not the most suitable way to introduce geometrical imperfections in finite element models. Effectively, the first eigenmode depends on the loading of the cross-sections and is therefore not constant from one load case to another one and not representative of real distribution when some parts of the cross-sections are almost not affected. Moreover, this method requires additional numerical analysis to obtain the first buckling mode. Therefore, the study recommends the use of sinusoidal functions to introduce geometrical imperfections. Based on the results, the recommended pattern for the study of cross-section resistance is a sinusoidal function with 3 half-waves. The use of an odd number of half-waves allows to have the maximal stress at the center of the member. Then, the use of 3 half-waves allows to have a suitable length in the numerical simulations. Effectively, if only one half-wave was used, the member would be too short, and the end conditions would affect the resistance. On the other hand, using more than 3 half-waves would lead to a length at which global effects can influence the resistance. Figure 23 shows the representation of the sinusoidal functions on a plate.

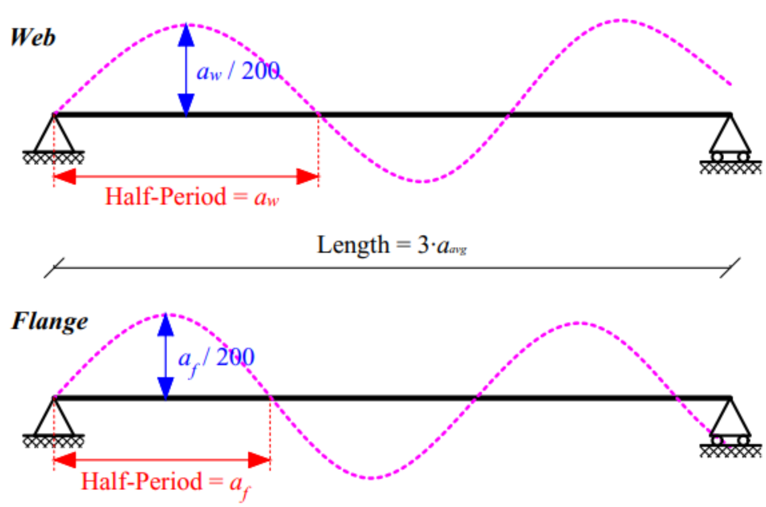

Figure 23 : Sinusoïdal imperfections on web and flanges [46]

The recommended amplitude of the imperfections on the web and the flanges and half-period shown on the figure are expressed in terms of the buckling lengths (a) of the elements which depends on the manufacturing process. For hot-rolled sections, $a_w = h - 2 \cdot t_f - 2 \cdot r$ and $a_f = b - t_w - 2 \cdot r$, while for welded sections, $a_w = h - t_f$ and $a_f = b$ due to the absence of fillets. In both cases, h refers to the full height of the section. Amplitudes of $a_w / 200$ for the web and of $a_f / 200$ for the flanges are used. The half-period length is the average between the buckling lengths of the web and flange: $a_{avg} = 0.5 \cdot (a_w + a_f)$ [46].

1.4.2 Residual stresses

Residual stresses are stresses that are present in the material even if no external loads are applied. They are the result of uneven cooling of the plates that compose a cross-section after the manufacturing process. As hot-rolled and welded sections are manufactured in different ways, they do not present the same type of residual stresses. Both differ in terms of amplitudes and distributions. However, in both cases, the residual stresses are auto-equilibrated on the section. Material imperfections must be incorporated in numerical models as they can induce premature yielding of some fibers in the section and cause stiffness reductions. Residual stresses present in a cross-sections depend on the temperature of the steel.

1.4.2.1 Residual stresses at ambient temperature

The amplitude and the distribution of the residual stresses on a cross-section depends on the geometry of the cross-sections and on the manufacturing process. Many studies have been conducted in which residual stresses were measured on specimens. When performing numerical simulations, residual stresses must be included to ensure reprensentative results. However, measuring residual stresses on specimens and introducing them in the model as measured is not practical and realistic. Over the years, various residual stress patterns have been proposed for both hot-rolled and welded sections.

1.4.2.1.1 Proposed residual stress patterns for hot-rolled cross-sections

A first residual stresses pattern for hot-rolled sections suggested by ECCS [47] is presented on Figure 24.

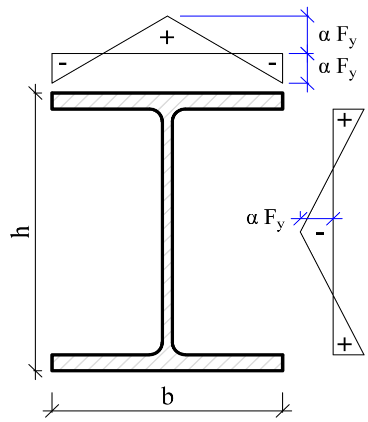

Figure 24 : Residual stresses pattern proposed by ECCS for hot-rolled sections [47] (figure from [3])

In this triangular pattern, the parameter α is dependant on the shape of the sections. For a column shape, $h/b \leq 1.2$, $\alpha = 0.5$, while for a beam shape, $h/b > 1.2$, $\alpha = 0.3$.

Figure 25 presents a second pattern suggested by Galambos and Ketter which is also known as the Lehigh pattern [48]. Contrary to the pattern from ECCS, this proposal suggests the use of a constant tension residual stress along the web of the section.

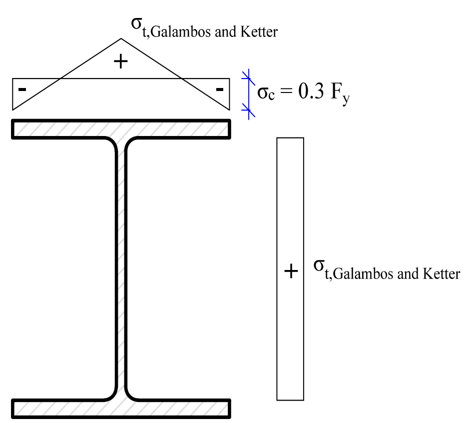

Figure 25 : Residual stresses pattern proposed by Galambos and Ketter for hot-rolled sections [48] (figure from [3])

Equation (34) is used to calculate the maximal tensile stress.

$$\sigma_t = \sigma_c \cdot \frac{b \cdot t_f}{b \cdot t_f + t_w \cdot (d - 2 \cdot t_f)} \qquad (34)$$

A study was conducted by Young in 1975 [49] in which the residual stresses were measured on British structural shapes. This study proposes a residual pattern using a parabolic distribution. The study also concludes that, contrary to both patterns presented previously, the residual stresses pattern does not depend on the yield limit. In this proposal, the maximal stresses are defined as a function of the section's dimensions. Figure 26 presents the proposed pattern.

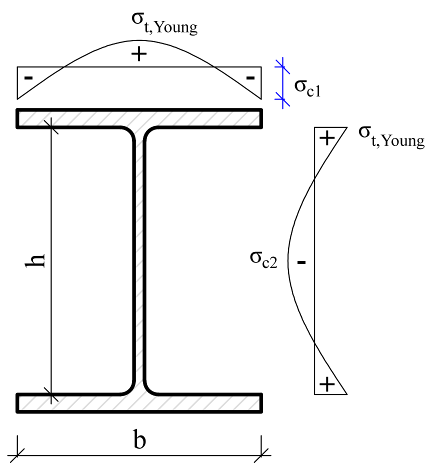

Figure 26 : Residual stresses pattern proposed by Young for hot-rolled sections [49] (figure from [3])

The following equations are used to calculate the maximal stresses presented in Figure 26.

$$\sigma_{c1} = 165 \cdot \left(1 - \frac{h \cdot t_w}{2.4 \cdot b \cdot t_f} \right) \quad (35)$$

$$\sigma_{c2} = 100 \cdot \left(1.5 + \frac{h \cdot t_w}{2.4 \cdot b \cdot t_f} \right) \quad (36)$$

$$\sigma_{t} = 100 \cdot \left(0.7 + \frac{h \cdot t_w}{2 \cdot b \cdot t_f} \right) \quad (37)$$

Another parabolic pattern has been proposed by Boissonnade and Somja [50] and is presented on Figure 27.

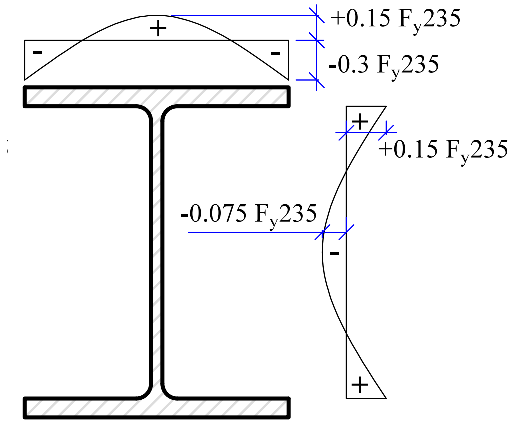

Figure 27 : Residual stresses pattern from Boissonnade and Somja for hot-rolled sections [50] (figure from [2])

In the study, the authors also compare this parabolic pattern with the one proposed by ECCS and presented in Figure 24. Both patterns are also compared using a yield limit of 235 MPa and using actual steel yield limit. The study concludes that both patterns are suitable for the introduction of residual stresses in numerical models. However, the authors recommend the use of 235MPa as the reference yield stress as it has proven to procure results closer to experimental results.

1.4.2.1.2 Proposed residual stresses pattern for welded cross-sections

In welded sections, residual stresses can either be a result of the uneven cooling after welding and/or of the flame cutting of the plates' edges. As welds highly heat the material, resulting residual stresses can reach the yield limit of the cross-section. A first pattern proposed by ECCS [47] is presented on Figure 28.

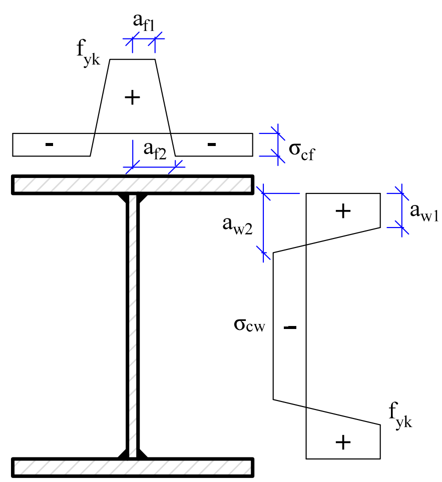

Figure 28 : Residual stresses pattern proposed by ECCS for welded sections [47] (figure from [3])

In this pattern, f_{yk} is the yield limit. It is reached close to the welds. The amplitude of the compressive stress in other areas is obtained with the following equation.

$$\sigma_{cf} = \sigma_{cw} = 0.25 \cdot f_{yk} \tag{38}$$

As for the geometrical dimensions, they can be obtained using the following equations.

$$a_{f1} = 0.075 \cdot b_f \tag{39}$$

$$a_{f2} = 0.125 \cdot b_f \tag{40}$$

$$a_{w1} = 0.075 \cdot b_w \tag{41}$$

$$a_{w2} = 0.125 \cdot b_w \tag{42}$$

An adapted and simplified version of the ECCS proposal was made by Gérard in her PhD and is presented on Figure 29. In this adapted pattern, the trapezoidal shape was replaced by a rectangular shape. The geometry of the pattern is obtained by using the average dimensions of the trapezoidal pattern.

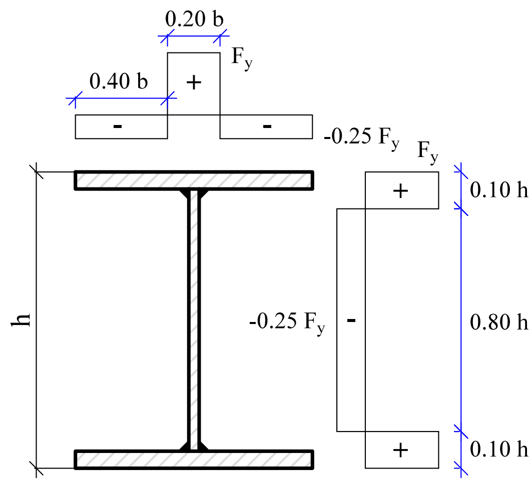

Figure 29 : Adapted Residual stresses pattern proposed by ECCS for welded sections (figure from [3])

Patterns presented on Figure 28 and Figure 29 account for the residual stresses due to welding but do not consider residual stresses resulting of the flame cutting of the flanges. Wang et al. [51] proposed a residual stresses pattern that accounts for the flame-cut flanges and is based on measurements made for their study. It is shown on Figure 30.

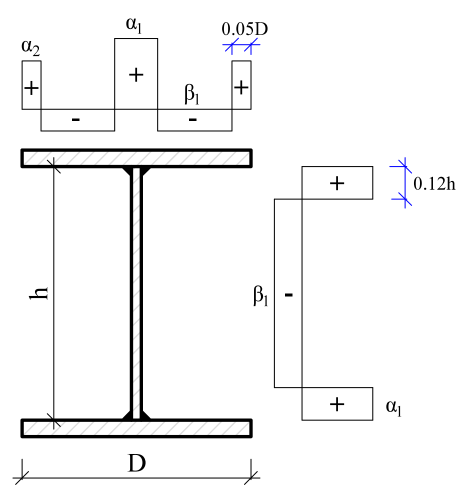

Figure 30 : Residual stresses pattern proposed by Wang et al. for welded sections [51] (figure from [3])

In this pattern, parameters α and β depend on the cross-section's type.

A pattern was also proposed in the PhD of Kim [52] which is referred to as the "Best-fit Prawel" residual stresses. It was obtained based on measurement made by Prawel et al. [53]. It is presented on Figure 31.

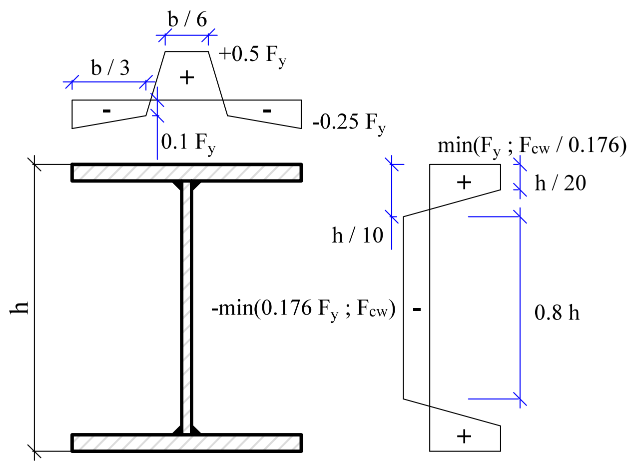

Figure 31 : Best-fit Prawel residual stresses proposed by Kim [52] (figure from [3])

1.4.2.1.3 Comparison of proposed patterns

As described in previous sections, multiple residuals stresses patterns for both hot-rolled and welded cross-sections have been proposed over the years. However, no clear and consensual recommendations on the introduction of those stresses in finite element models are proposed.

Part 1-5 of Eurocode 3 [37] does make recommendations on the introduction of geometrical imperfections into finite element models, but does not give any indication regarding material imperfections. However, it does state that if two types of imperfections are included, one type should be chosen as the primary imperfection and the secondary imperfection amplitude can be reduced by 30 %.

In her PhD thesis, Gérard [3] proposes a comparison between proposed residual patterns. She first provides an analysis on why proposed patterns presents such discrepancies by highlighting the fact that residual stresses pattern used by American and European present major differences. American numerical studies mostly use the Galambos and Ketter pattern [48] presented in Figure 25. European numerical studies on the other hand mostly use the pattern proposed by ECCS [47] and presented on Figure 24. The major differences between both patterns is that Galambos and Ketter proposes a constant tensile stress on the web while the pattern proposed by ECCS has a triangular distribution along the web. The ECCS also provides different patterns for column and beam shapes. Gérard then gathered experimental measurements of residual stresses to compare them with proposed patterns.

She first compared residual stresses patterns proposed for hot-rolled cross-sections. For columns shapes ($h/b < 1.2$), the following patterns were compared to experimental results.

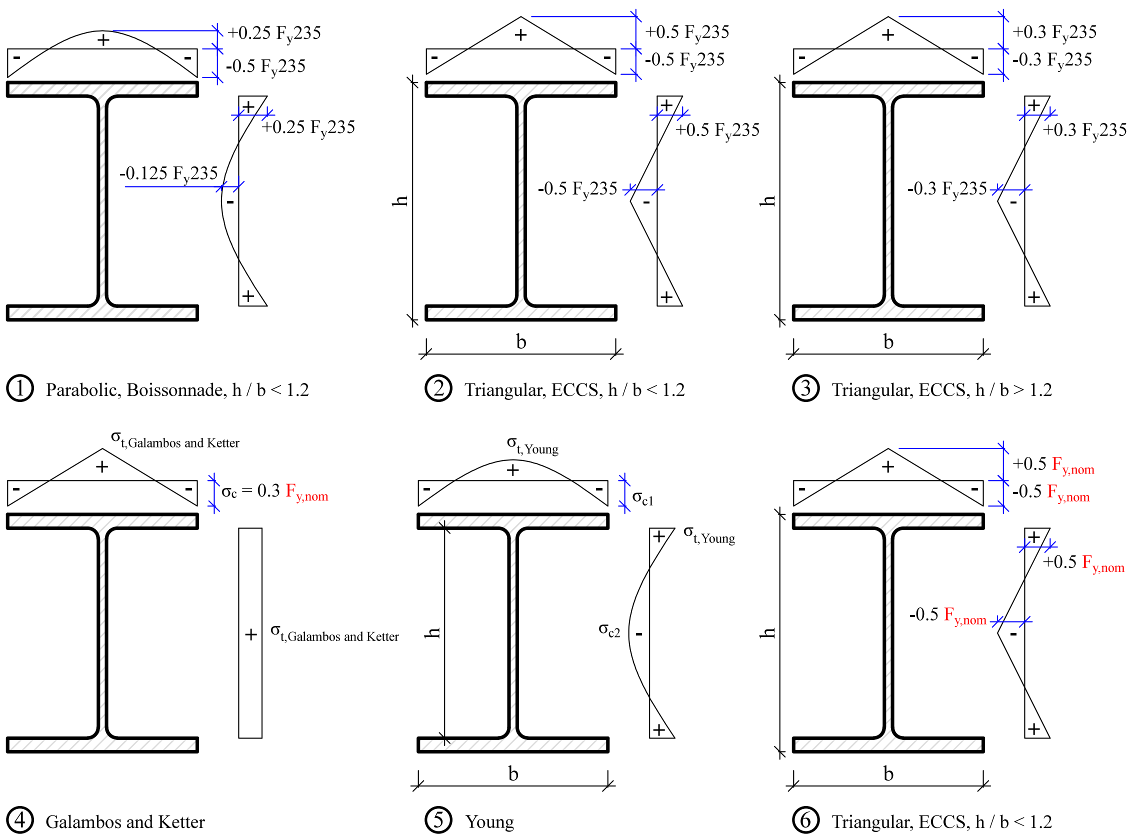

Figure 32 : Residual stresses patterns with respect to column shapes (h/b < 1.2) [3]

As for beam shapes ($h/b \geq 1.2$), Gérard compared the following patterns to experimental results.

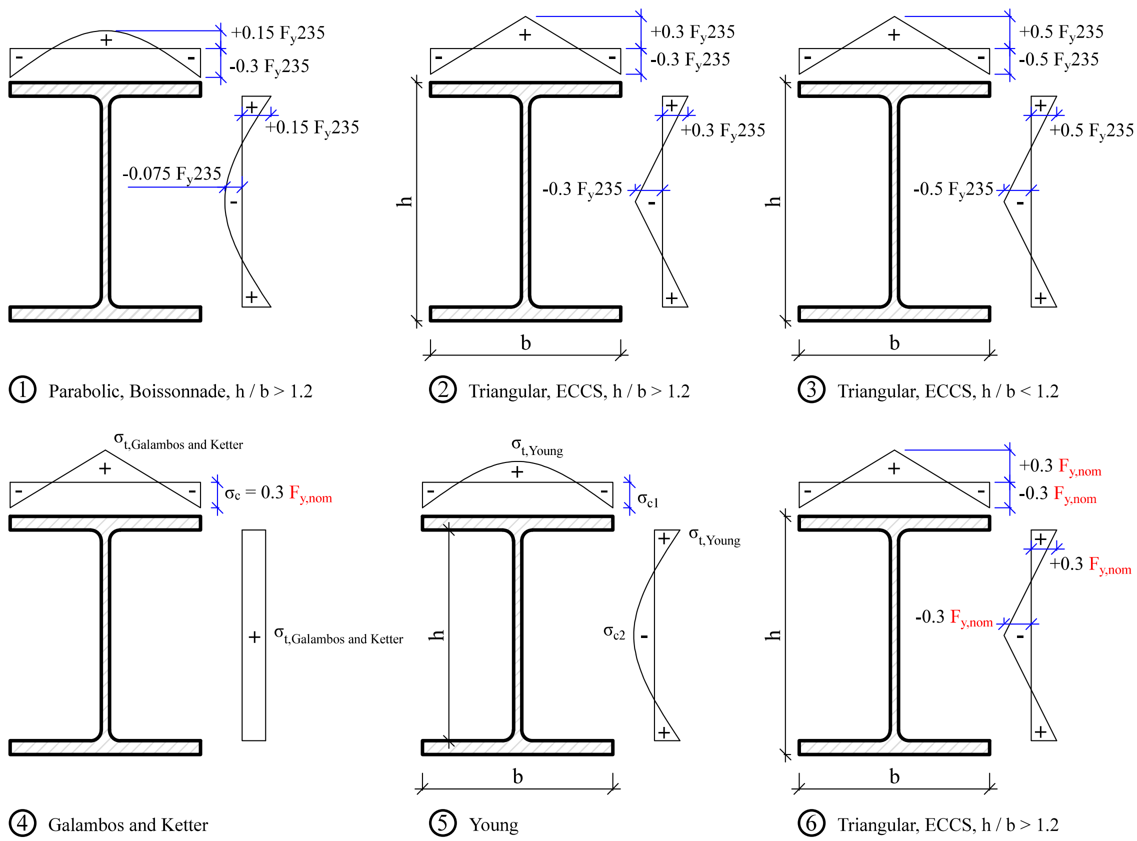

Figure 33 : Residual stresses patterns with respect to beam shapes (h/b > 1.2) [3]

Based on the results of the comparison made in the study, the author concluded that the pattern 1 from Figure 32 and pattern 2 from Figure 33 are respectively the most accurate for column and beam shapes.

Gérard also made a comparison between experimental measurement of residual stresses on welded section and two of the patterns presented previously: the rectangular pattern adapted from ECCS [47] (see Figure 29) and the best-fit Prawel pattern (see Figure 31). It was concluded that the rectangular pattern was overall in agreement with the measured residual stresses while the best-fit Prawel pattern underestimates the stresses.

This comparison allows to see which residual stresses pattern represents most accurately the real distribution of the residual stresses in steel cross-sections. It does not however study how the patterns influence the results obtained in numerical studies. In her PhD, Gérard also compares the influence of proposed patterns on ultimate resistance and make recommendations on the introduction of residual stresses in numerical models [3].

For hot-rolled sections, the triangular pattern proposed by ECCS [47] and parabolic patterns proposed by Boissonnade and Somja [50] were compared using the actual yield limit and a yield limit of 235 MPa. Results of the study show that there is no significative difference in the maximum load reached when using either one of the patterns although the parabolic pattern leads to slightly higher resistances. As for the use of the actual yield limit or of a yield limit of 235 MPa to calculate the maximum residual stress, negligible differences were noticed. The use of 235 MPa was however deemed as the most reasonable option as no experimental measurements justifies the use of a portion of the actual yield limit. Figure 34 presents the recommended parabolic residual stresses pattern by the study.

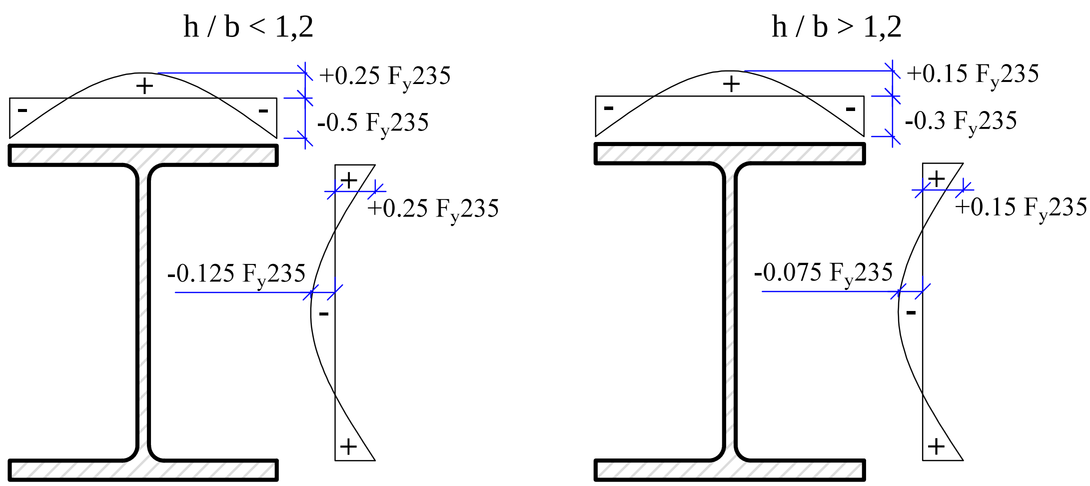

Figure 34 : Recommended residual stresses pattern for hot-rolled sections by Gérard [3]

For welded cross-sections, the rectangular pattern adapted from ECCS [47] and an adapted trapezoidal pattern were compared. Results of the study show that the differences obtained with either pattern are negligible and therefore that both patterns could be used in numerical models. However, the rectangular pattern is much easier to incorporate in a finite element model and is therefore recommended by the author.

1.4.2.2 Residual stresses at elevated temperature

Many studies have been conducted to understand residual stresses at ambient temperature. Yet, little information is available about residual stresses in steel members at elevated temperature. Two experimental studies by Wang et al. [54] and Wang et al. [55] have been conducted respectively on welded high strength sections and thin-walled H-sections to evaluate the residual stresses after fire exposure. In both experimental series, sections were heated at the desired temperature and then cooled down to room temperature. Residual stresses were measured in specimens at ambient temperature and after heat exposure. Both studies' results show that after high temperature exposure and cooling, residual stresses reduce significantly, and that larger reductions are observed as the heating temperature increases. The second study even proposes a residual stresses model based on the exposition temperature (see [55]).

Those studies have shown a significant reduction in measured residual stresses in steel sections after they had been heated and subsequently cooled down. However, the tests performed did not consider loaded sections. Therefore, these tests do not indicate adequately the evolution of residual stresses in a loaded section subjected to high temperatures. As presented in the work of Franssen [56], residual stresses present at ambient temperature should be considered as an initial condition and their evolution depends on both the increase in temperature and on the loading.

The influence of the residual stresses on the lateral-torsional buckling of I-beams was studied by Vila Real et al. [57]. Results of this study shows that the effect of the residual stresses on the resistance decreases with the increase in temperature. Similar conclusions were drawn by Couto et al. [58] in a study on the lateral-torsional buckling of beams with slender cross-sections subjected to fire. Results of the study have shown that residual stresses do have an influence on the resistance. However, the effect of residual stresses in the case of fire is less important than at room temperature. This can be explained by the fact that there seems to be a relaxation of the residual stresses when the beam is heated.

All studies discussed above point to the fact that the detrimental effect of residual stresses on resistance are less important at high temperatures. However, it has also been showed that residual stresses do not completely disappear and do have an effect on the resistance. Residual stresses should therefore not be neglected at high temperatures.

1.5 Current design methods

Standards provide ways to determine the local and global resistance of elements. The intent of this section is to present how to calculate the resistance according to three standards: the European standard, Eurocode 3 (EC3), the Canadian standard, CSA-S16-14 (S16-14), and the American standard, ANSI/AISC 360-16 (AISC). This study focuses on the local resistance of cross-sections. However, the cross-sections used in the numerical simulations do have a certain length (cf. Chapter 2). This length is chosen to avoid the effect of global instabilities. However, this length might be long enough for codes to consider the effect of global instabilities in their equations. Therefore, both the equations for the cross-section's resistance and the global resistance are presented in the next sections.

1.5.1 Concept of cross-section classification

Almost all approaches from standards are based on the concept of cross-section classification. The resistance of compact and semi-compact section is usually obtained by the means of straightforward equations. On the other hand, the resistance of slender sections is often obtained through the use of the Effective Width Method.

The classification of the cross-sections depends on the slenderness of the cross-section and on the ability for sections to experience large rotations. The classification process differs from one standard to the other. Both the European [26] and Canadian [27] standards resort to 4 classes for cross-sections subjected to bending:

- Class 1 are compact cross-sections that can reach their full plastic capacity and to allow a redistribution of the bending moment. No local buckling occurs before the section reaches its full plastic capacity and large deformations can occur;
- Class 2 are compact cross-sections that can also reach their full plastic capacity but there is no guarantee that there will be a redistribution of the bending moment. No local buckling occurs before the section reaches its full plastic capacity, but deformations are limited;
- Class 3 are semi-compact cross-sections that can reach their elastic capacity without any local buckling occurring. However, local buckling occurs before the section reaches its full plastic capacity. Those cross-sections' resistance is between the elastic

and the plastic resistance. The European standard accounts for the reserve of resistance past the elastic resistance while the Canadian standard limits the resistance to the elastic bending moment;

- Class 4 are slender cross-sections that suffer from local buckling before reaching their elastic capacity. Their resistance is limited to their reduced elastic bending moment.

As for the American standard [28], sections subjected to bending are classified as compact, non-compact and slender. In all standards, sections subjected to compression are either compact (class 1, 2 or 3) or non-compact (class 4). The limits from one class to the other are different in each code.

1.5.2 Resistance in fire situations according to European standard [9]

The simplified approach given by part 1-2 of Eurocode 3 to determine the resistance at elevated temperatures consist in using the equations at ambient temperature with a few modifications but by considering the reduced mechanical properties of steel at elevated temperatures. In this simplified approach, the temperature in the cross-section is considered to be uniform. Table 5 presents the reduction factors that must be used to calculate steel properties at a given temperature. Intermediate values that are not given in the table can be obtained by linear interpolation.

Table 5 : Reduction factors for steel at elevated temperature according to Eurocode 3 [9]

Temperature (θ_a) (°C)	Reduction factor for effective yield strength $k_{y,\theta} = f_{y,\theta} / f_y$ (-)	Reduction factor for proportional limit $k_{p,\theta} = f_{p,\theta} / f_y$ (-)	Reduction factor for elasticity modulus $k_{E,\theta} = E_{a,\theta} / E_a$ (-)	Reduction factor for the 0.2% proof strain $k_{0.2p,\theta} = f_{0.2p,\theta} / f_y$ (-)
20	1.000	1.000	1.000	1.000
100	1.000	1.000	1.000	1.000
200	1.000	0.807	0.900	0.890
300	1.000	0.613	0.800	0.780
400	1.000	0.420	0.700	0.650
500	0.780	0.360	0.600	0.530
600	0.470	0.180	0.310	0.300
700	0.230	0.075	0.130	0.130
800	0.110	0.050	0.090	0.070
900	0.060	0.0375	0.0675	0.050
1000	0.040	0.0250	0.0450	0.030
1100	0.020	0.0225	0.0225	0.020
1200	0.000	0.0000	0.0000	0.0000

1.5.2.1 Cross-section classification

The first step is to determine the cross-section classification. In Eurocode 3, the cross-section classification at elevated temperatures is the same as for classification at ambient temperature. The classification of each plate of the cross-sections is made based on the width-to-thickness ratio of the plate (c / t). The width-to-thickness ratio limit between each section class is determine with the use of two different factors: 1) the factor ε which depends on the yield limit and 2) the distribution of stress in the considered plate. At elevated temperatures, a 15% reduction is applied to the value of ε as shown in Equation (43) to take into account the fact that the stability of a plate decreases as the temperature increases.

$$\varepsilon = 0.85\left(\frac{235}{f_y}\right)^{0.5} \tag{43}$$

Equations are then provided by the code for elements with cross-section's class from 1 to 3. Those equations are presented in the following sections. For slender sections (class 4), Eurocode 3 suggest verifying that the reached temperature is not over the critical temperature. However, appendix E of the code specifies that the resistance can be calculated by replacing the area by the effective area and the section's modulus by the effective section's modulus in all equations. Both are calculated according to Part 1-5 of the EC3 with the material properties of steel at 20°C. Moreover, the reduced yield limit is replaced by the proof strength at 0.2% plastic strain. All equations presented are used when the temperature is considered to be uniform in the cross-section. Eurocode 3 proposes other equations when there is a temperature gradient. However, those are not presented here as this study focuses on sections subjected to uniform temperature.

1.5.2.2 Element subjected to compression

According to EC3, a cross-section subjected to compression in a fire situation should satisfy the following equation:

$$\frac{N_{fi,Ed}}{N_{fi,\theta,Rd}} \leq 1.0 \tag{44}$$

In the previous equation, $N_{fi,\theta,Rd}$ is either the cross-section's resistance or the member's resistance. For compact sections (class 1, 2 or 3), the resistance is calculated with Equation (45) considering the whole cross-section area.

$$N_{b,fi,\theta,Rd} = \frac{A \cdot k_{y,\theta} \cdot f_y}{\gamma_{M,fi}} \tag{45}$$

To obtain the member's resistance, the cross-section's resistance is multiplied by a reduction factor as shown in Equation (46). This reduction factor is based on buckling curves as presented in section 1.3.1.8.1 and takes into account flexural buckling.

$$N_{b,fi,\theta,Rd} = \chi_{fi} \cdot \frac{A \cdot k_{y,\theta} \cdot f_y}{\gamma_{M,fi}} \quad (46)$$

The reduction factor is obtained with the following equations:

$$\chi_{fi} = \frac{1}{\phi_\theta + \sqrt{\phi_\theta^2 - \bar{\lambda}_\theta^2}} \leq 1.0 \quad (47)$$

In this equation the parameter ϕ_θ is calculated with the following equation.

$$\phi_\theta = 0.5 \cdot \left(1 + \alpha \cdot \bar{\lambda}_\theta + \bar{\lambda}_\theta^2\right) \quad (48)$$

Counter to the resistance calculations at room temperature, the imperfection parameter α is the same for all cases and is given in Equation (49).

$$\alpha = 0.65 \cdot \sqrt{\frac{235}{f_y}} \quad (49)$$

Finally, the non-dimensional slenderness at high temperature is calculated with equation (50). In this equation, the slenderness at room temperature is modified by the reduction factors used at high temperatures for both the yield limit and Young's modulus.

$$\bar{\lambda}_\theta = \bar{\lambda} \cdot \sqrt{\frac{k_{y,\theta}}{k_{E,\theta}}} = \sqrt{\frac{A \cdot f_y}{N_{cr}}} \cdot \sqrt{\frac{k_{y,\theta}}{k_{E,\theta}}} \quad (50)$$

For class 4 sections, the same equations are used but the area is replaced by the effective area and the 0.2% proof strain is used.

1.5.2.3 Element subjected to bending

According to Eurocode 3, an element subjected to bending in a fire situation should satisfy the following equation:

$$\frac{M_{fi,Ed}}{M_{fi,\theta,Rd}} \leq 1.0 \quad (51)$$

Similar to the resistance for elements subjected to compression, the resistance can be calculated at the cross-section and at the member's level. At the cross-section level, the resistance is calculated using the appropriate section's modulus based on the cross-section's classification. For sections of class 1 or 2, flexural resistance is obtained by considering that the section reaches its full plastic capacity. The following equation is used:

$$M_{fi,\theta,Rd} = M_{pl,fi,\theta,Rd} = \frac{W_{pl} \cdot k_{y,\theta} \cdot f_y}{\gamma_{M,fi}} \tag{52}$$

For class 3 sections, the partial-plastic section modulus, which is obtained from an interpolation between the plastic section modulus and the elastic plastic modulus, is used to calculate the resistance. Equation 53 is used to determine the resisting moment at a precise temperature.

$$M_{fi,\theta,Rd} = M_{ep,fi,\theta,Rd} = \frac{W_{ep} \cdot k_{y,\theta} \cdot f_y}{\gamma_{M,fi}} \tag{53}$$

The partial-plastic section modulus W_{ep} is obtained with the following equations.

$$W_{ep,y} = W_{pl,y} - (W_{pl,y} - W_{el,y}) \cdot \beta_{ep,y} \tag{54}$$

$$W_{ep,z} = W_{pl,z} - (W_{pl,z} - W_{el,z}) \cdot \beta_{ep,z} \tag{55}$$

Equations (56) and (57) are used to determine the value of β factors.

$$\beta_{ep,y} = \max\left(\frac{\frac{c_f}{t_f} - 10\varepsilon}{4\varepsilon}, \frac{\frac{c_w}{t_w} - 83\varepsilon}{38\varepsilon}, 0 \right) \leq 1.0 \tag{56}$$

$$\beta_{ep,z} = \max\left(\frac{\frac{c_f}{t_f} - 10\varepsilon}{6\varepsilon}, 0 \right) \leq 1.0 \tag{57}$$

When the element is subjected to major-axis bending, the resistance to lateral-torsional buckling must be verified. The resistance is obtained by applying the reduction factor $\chi_{LT,fi}$ to the cross-section's resistance. The reduction factor is calculated with the same equations as the reduction factor for compression. However, the slenderness is calculated with Equation (58).

$$\bar{\lambda}_{LT,\theta} = \bar{\lambda}_{LT} \cdot \sqrt{\frac{k_{y,\theta}}{k_{E,\theta}}} = \sqrt{\frac{W \cdot f_y}{M_{cr}}} \cdot \sqrt{\frac{k_{y,\theta}}{k_{E,\theta}}} \tag{58}$$

In this equation, the section's modulus *W* is chosen based on the cross-section's class.

For Class 4 sections, the same equations are used but the section modulus is replaced by the effective section modulus and the 0.2% proof strain is used.

1.5.2.4 Element subjected to combined compression and bending

If the cross-section is subjected to both compression and bending, additional verifications must be made at the cross-section and at the member's level. No formulas are explicitly given in Part 1-2 of Eurocode 3 to verify the interaction at elevated temperature at the cross-section's level. The manual *Fire Design of Steel Structures* [39] gives those equations which are the equations used at ambient temperature adapted to elevated temperatures.

The resistance under fire condition of class 1 and 2 cross-section is obtained from plastic resistance. If an axial force is present on a member subjected to bending about one axis, its effect must be taken into account by satisfying the following criterion:

$$M_{fi,Ed} \leq M_{N,fi,Rd} \tag{59}$$

In this equation, $M_{N,fi,Rd}$ is the plastic moment reduced due to the axial load.

For major-axis bending, the impact of the axial force shall not be taken into consideration if both following criteria are satisfied :

$$N_{fi,Ed} \leq 0.25 \cdot N_{pl,fi,Rd} = 0.25 \cdot \frac{A \cdot k_{y,\theta} \cdot f_y}{\gamma_{M,fi}} \tag{60}$$

$$N_{fi,Ed} = 0.5 \cdot \frac{h_w \cdot t_w \cdot k_{y,\theta} \cdot f_y}{\gamma_{M,fi}} \tag{61}$$

Otherwise, the reduced plastic moment about the major-axis should be calculated using Equation (62).

$$M_{N,y,fi,Rd} = M_{pl,y,fi,Rd} \cdot \frac{(1-n)}{(1-0.5 \cdot a)} \leq M_{pl,y,fi,Rd} \tag{62}$$

$$\text{where : } n = \frac{N_{fi,Ed}}{N_{pl,fi,Rd}} \text{ and} \tag{63}$$

$$a = \frac{(A - 2 \cdot b \cdot t_f)}{A} \tag{64}$$

For minor-axis bending, the impact of the axial force shall not be taken into consideration if the following criterion is satisfied :

$$N_{fi,Ed} = \frac{h_w \cdot t_w \cdot k_{y,\theta} \cdot f_y}{\gamma_{M,fi}} \tag{65}$$

Otherwise, the reduced plastic moment about the minor-axis should be calculated using Equations (66) and (67).

$$M_{N,z,fi,Rd} = M_{pl,z,fi,Rd} \quad \text{if} \quad n \leq a \tag{66}$$

$$M_{N,z,fi,Rd} = M_{pl,z,fi,Rd} \cdot \left[1 - \left(\frac{n-a}{1-a}\right)^2\right] \quad \text{if} \quad n > a \tag{67}$$

If the cross-section is subjected to compression and bi-axial bending, Equation (68) must be satisfied.

$$\left[\frac{M_{y,fi,Ed}}{M_{N,y,fi,Rd}}\right]^{\alpha} + \left[\frac{M_{z,fi,Ed}}{M_{N,z,fi,Rd}}\right]^{\beta} \leq 1.0 \tag{68}$$

$$\text{where : } \alpha = 2 \quad \text{and} \tag{69}$$

$$\beta = 5 \cdot n \geq 1 \tag{70}$$

For cross-section verification of class 3 sections, the same criterion as for class 1 and 2 sections must be satisfied.

$$M_{fi,Ed} \leq M_{N,fi,Rd} \tag{71}$$

The reduced moment due to axial load is calculated using the following equations:

$$M_{N,y,fi,Rd} = M_{pl,y,fi,Rd} \cdot (1-n) \tag{72}$$

$$M_{N,z,fi,Rd} = M_{pl,z,fi,Rd} \cdot (1-n^2) \tag{73}$$

$$\text{where : } n = \frac{N_{fi,Ed}}{N_{pl,fi,Rd}} \tag{74}$$

If the cross-section is subjected to bi-axial bending, Equation (75) must be satisfied.

$$\left[\frac{M_{y,fi,Ed}}{M_{N,y,fi,Rd}}\right]^{\alpha} + \left[\frac{M_{z,fi,Ed}}{M_{N,z,fi,Rd}}\right]^{\beta} \leq 1.0 \tag{75}$$

$$\text{where : } \alpha = 2 \quad \text{and} \tag{76}$$

$$\beta = 5 \cdot n \geq 1 \tag{77}$$

For class 4 sections, the cross-section resistance is verified elastically. In this equation, resistance are obtained with effective properties and with the proof strength at 0.2% plastic strain as explained previously.

$$\frac{N_{fi,Ed}}{N_{fi,\theta,Rd}} + \frac{M_{y,fi,Ed}}{M_{y,fi,\theta,Rd}} + \frac{M_{z,fi,Ed}}{M_{z,fi,\theta,Rd}} \leq 1.0 \qquad (78)$$

At the member's level, the Eurocode 3 gives two interactions formulas that must be verified:

$$\frac{N_{fi,Ed}}{\chi_{\min,fi} \cdot A \cdot k_{y,\theta} \cdot \frac{f_y}{\gamma_{M,fi}}} + \frac{k_y \cdot M_{y,fi,Ed}}{W_y \cdot k_{y,\theta} \cdot \frac{f_y}{\gamma_{M,fi}}} + \frac{k_z \cdot M_{z,fi,Ed}}{W_z \cdot k_{y,\theta} \cdot \frac{f_y}{\gamma_{M,fi}}} \leq 1.0 \qquad (79)$$

$$\frac{N_{fi,Ed}}{\chi_{z,fi} \cdot A \cdot k_{y,\theta} \cdot \frac{f_y}{\gamma_{M,fi}}} + \frac{k_{LT} \cdot M_{y,fi,Ed}}{\chi_{LT,fi} \cdot W_y \cdot k_{y,\theta} \cdot \frac{f_y}{\gamma_{M,fi}}} + \frac{k_z \cdot M_{z,fi,Ed}}{W_z \cdot k_{y,\theta} \cdot \frac{f_y}{\gamma_{M,fi}}} \leq 1.0 \qquad (80)$$

In those equations, W_y must be chosen based on the cross-section classification. Parameters k_y, k_z and k_{LT} are interaction factors.

1.5.3 Resistance in fire situations according to Canadian standards [27]

The simplified approach suggested by CSA S16-14 to predict the cross-section resistance is to consider a uniform temperature and to use equations provided at ambient temperature with reduced mechanical properties. The reduction factors are the ones proposed in Eurocode 3 and are presented in Table 5. The effective yield strength, used to calculate the resistance at a specific temperature, should be determined as follow:

$$F_y(T) = k_y \cdot F_y \qquad (81)$$

New equations are however provided for flexural buckling and for lateral torsional buckling.

1.5.3.1 Cross-section classification

In CSA S16-14, no specifications are given for the cross-section classification at high temperatures. Therefore, the classification is done in the same way as at ambient temperature. The classification is made based on the slenderness of the plates (b_{el} / t). The limit between classes is based on the loading and on the yield limit. No indications are given in the standards for the cross-section classification. At elevated temperatures, it was therefore decided to make the classification by using the yield limit at ambient temperature instead of the reduced mechanical properties. Effectively, using the reduced mechanical properties to classify cross-sections would result in higher limits between classes. Cross-sections would therefore be considered as less slender at elevated temperature. However, the slenderness is known to increase with elevated temperature. Using properties at ambient temperature is therefore more appropriate although it does not consider the increase in slenderness caused by the increased temperature.

1.5.3.2 Elements subjected to compression

According to CSA S16-14, the cross-section resistance is determined by using the following equations. In these equations, ϕ is a safety factor and is equal to 0.9. For non-slender section (class 1, 2 or 3), the resistance is calculated with Equation (82) considering the whole cross-section area.

$$C_r(T) = \phi \cdot A \cdot F_y(T) \tag{82}$$

For slender sections (class 4), only the effective cross-section area is considered. It is determined using the reduced element widths determined with the maximum width-to-thickness ratio. This method used for the calculation of the effective area is specific to the Canadian standards. Equation (83) shall be used to calculate the resistance.

$$C_r(T) = \phi \cdot A_{eff} \cdot F_y(T) \tag{83}$$

As for the resistance to flexural buckling, Annex K recommends using the following equations. In Equation (84), *n* depends on the fabrication process. In the case of hot-rolled and welded sections, n is equal to 1.34. In the same equation, the constant d = 0.6 and is used to reduce the variable *n* therefore lowering the buckling curve and reducing the resistance. As for the factor *K* in Equation (85) is the effective length factor that depends on the boundary conditions. It is equal to 1.0 in the case of a simply supported column.

$$C_r(T) = \frac{A \cdot F_y(T)}{\left(1 + \lambda(T)^{2 \cdot d \cdot n}\right)^{\frac{1}{d \cdot n}}} \tag{84}$$

$$\lambda(T) = \frac{K \cdot L}{r} \cdot \sqrt{\frac{F_y(T)}{\pi^2 \cdot E(T)}} \tag{85}$$

In this new equation, no indication is given related to the use of an effective area for class 4 sections. In the article from which this equation was obtained [59], the authors explain that this can lead to unconservative results for class 4 sections but only for very small lengths that are not commonly used in constructions. The equation is therefore used for all section classes.

1.5.3.3 Members subjected to bending

According to CSA S16-14, the cross-section resistance is obtained by using the appropriate section's modulus based on the classification as shown in the following equations. In all equations, ϕ is a safety factor and is equal to 0.9. The resistance of a cross-section of class 1 or 2 subjected to bending in a fire situation is obtained by considering that the section reaches its full plastic capacity. The plastic section modulus Z is used to calculate the resistance in the following equations.

$$M_r(T) = \phi \cdot Z \cdot F_y(T) \tag{86}$$

It is considered that for class 3 sections, the elastic capacity is reached. Equation (87) is used to determine the elastic resisting moment at a precise temperature. The elastic resistance is obtained with the elastic section modulus S.

$$M_r(T) = \phi \cdot S \cdot F_y(T) \tag{87}$$

For class 4 sections, the effective section's modulus is used to calculate the resistance.

$$M_r(T) = \phi \cdot S_{eff} \cdot F_y(T) \tag{88}$$

The effective section's modulus depends on the individual classification of the web and of the flanges. If both the web and the flanges exceed the limit of class 3 sections, the effective properties of the section are determined based on the specification of CSA S136. If only the web exceeds the limit of class 3 sections, the following equation can be used to reduce the resistant moment in which $M_r(T)$ is obtained with Equation (89).

$$M_r(T)' = M_r(T) \cdot \left[1 - 0.0005 \cdot \frac{A_w}{A_f} \cdot \left(\frac{h}{w} - \frac{1900 \cdot \left(1 - 0.65 \dfrac{C_f}{\phi \cdot C_y(T)} \right)}{\sqrt{\dfrac{M_f}{\phi \cdot S}}} \right) \right] \leq \phi \cdot M_y(T) \quad (89)$$

Finally, for cross-sections with only flanges exceeding the class 3 limit, the length of the flanges is determined by the maximum width-thickness-ratio.

As for the resistance to lateral torsional buckling, Annex K proposes the following adapted equations in which $C_K = 0.12$ and $M_p(T)$ is the plastic moment calculated with $F_y(T)$.

$$M_r(T) = C_K \cdot M_p(T) + (1 - C_K) \cdot M_p(T) \cdot \left(1 - \left(\frac{C_K \cdot M_p(T)}{M_u(T)} \right)^{0.5} \right)^{C_z(T)} \quad (90)$$

$$M_u(T) = \frac{\omega_2 \cdot \pi}{L} \cdot \sqrt{E(T) \cdot I_y \cdot G(T) \cdot J + I_y \cdot C_w \left(\frac{\pi \cdot E(T)}{L} \right)^2} \quad (91)$$

$$C_z(T) = \frac{T + 800}{500} \leq 2.4 \quad (92)$$

As for the proposed equation for the flexural buckling, no indications are provided about section's classification. The equation is therefore used for all cross-sections.

1.5.3.4 Cross-section subjected to combined compression and bending

If the cross-section is subjected to both compression and bending, an additional verification must be made. For class 1 and 2 sections, Equation (93) must be satisfied.

$$\frac{C_f}{C_r(T)}+\frac{0.85\cdot U_{1x}\cdot M_{fx}}{M_{rx}(T)}+\frac{\beta\cdot U_{1y}\cdot M_{fy}}{M_{ry}(T)}\leq 1.0 \tag{93}$$

For class 3 and 4 sections, Equation (94) must be satisfied.

$$\frac{C_f}{C_r(T)}+\frac{U_{1x}\cdot M_{fx}}{M_{rx}(T)}+\frac{U_{1y}\cdot M_{fy}}{M_{ry}(T)}\leq 1.0 \tag{94}$$

For all sections, Equation (95) must also be satisfied.

$$\frac{M_{fx}}{M_{rx}(T)}+\frac{M_{fy}}{M_{ry}(T)}\leq 1.0 \tag{95}$$

In Equations (93) and (94), $U_{1,x}, U_{1,y}$ and β depend on the verification that is being made. Three verifications must be made with these equations: cross-sectional strength, overall member strength and lateral-torsional buckling strength.

1.5.4 Resistance in fire situations according to American standards [28]

Appendix 4 of the American standard gives specifications to determine the resistance of steel elements at elevated temperature. As for other standards, reduced mechanical properties must be used to consider the loss in resistance at elevated temperature. The effective yield strength at a specific temperature should be determined as follows:

$$F_y(T)=k_y\cdot F_y \tag{96}$$

The modulus of elasticity should be determined using the following equation:

$$E(T)=k_E\cdot E \tag{97}$$

Table 6 presents the reduction factors recommended.

Table 6 : Reduction factors for steel at elevated temperature according to the American standard

Temperature (θ_a) (°C)	Reduction factor for effective yield strength $k_y = F_y(T)/F_y$ (-)	Reduction factor for proportional limit $k_p = F_p(T)/F_y$ (-)	Reduction factor for elasticity modulus $k_y = E(T)/E$ (-)
20	1.000	1.000	1.000
93	1.000	1.000	1.000
200	1.000	0.80	0.900
320	1.000	0.58	0.78
400	1.000	0.42	0.70
430	0.94	0.40	0.67
540	0.66	0.29	0.49
650	0.35	0.13	0.22
760	0.16	0.06	0.11
870	0.07	0.04	0.07
980	0.04	0.03	0.05
100	0.02	0.01	0.02
1200	0.00	0.00	0.00

1.5.4.1 Cross-section classification

The cross-section classification depends on the width-to-thickness ratio (b / t). Limits between different classes depend on the loading, the yield limit, and the elasticity modulus. To determine the classification of cross-sections, mechanical properties at the considered temperature are used as they provide more conservative results.

1.5.4.2 Cross-section subjected to compression

According to AISC, the resistance to compression at high temperatures must be calculated using the equations from room temperature, but with the modified mechanical properties. However, a new equation is provided for flexural buckling :

$$P_c(T) = \phi_c \cdot P_n(T) \tag{98}$$

In this equation, ϕ_c = 0.90 and the nominal compressive strength (P_n) is determined based on the classification of the flange and the web.

For cross-sections without slender elements, the nominal compressive strength is determined using the whole section and the following equation:

$$P_n(T) = F_{cr}(T) \cdot A_g \tag{99}$$

For hot-rolled sections, the critical stress for flexural buckling at high temperatures is calculated with Equations (100) and (101).

$$F_{cr}(T) = \left(0.42^{\sqrt{\frac{F_y(T)}{F_e(T)}}} \right) \cdot F_y(T) \tag{100}$$

$$F_e(T) = \frac{\pi^2 \cdot E(T)}{\left(\frac{L}{r} \right)^2} \tag{101}$$

For built-up members, the critical stress is the minimum between the critical stress for flexural buckling calculated with Equations (100) and (101) and the critical stress for torsional and flexural buckling calculated with Equations (100) and (102).

$$F_e(T) = \left(\frac{\pi^2 \cdot E(T) \cdot C_w}{L^2} + G(T) \cdot J \right) \cdot \frac{1}{I_x + I_y} \tag{102}$$

For cross-section with slender elements, the resistance is calculated with Equation (103) which replaces the gross area of the cross-section by the effective area. The critical stress is calculated in the same way as for compact sections.

$$P_n(T) = F_{cr}(T) \cdot A_e \tag{103}$$

The effective area is determined using the formulas provided in the standard and the properties at high temperatures.

1.5.4.3 Cross-section subjected to bending

According to the American standards, the bending resistance is determined with the following equation:

$$M_c(T) = \phi_b \cdot M_n(T) \tag{104}$$

In this equation, ϕ_b = 0.90 and the nominal flexural strength (M_n) is determined based on the classification of the flange and the web. The bending resistance at high temperature must be calculated using the equations from room temperature but with the modified mechanical properties. However, different equations are provided for lateral-torsional buckling.

1.5.4.3.1 Sections with compact web bent about their major axis

1.5.4.3.1.1 *Sections with compact flanges*

If the cross-section has flanges classified as compact, the nominal flexural strength is either governed by yielding of the section or by lateral-torsional buckling. For the resistance to yielding, the value of M_n is obtained with Equation (105).

$$M_n(T) = M_p(T) = F_y(T) \cdot Z_x \tag{105}$$

The calculation of the resistance to lateral-torsional buckling depends on if the unsupported length of the member is under or over the limiting unbraced length which is calculated with the following equations:

$$L_r(T) = 1.95 \cdot r_{ts} \cdot \frac{E(T)}{F_L(T)} \cdot \sqrt{\frac{J}{S_x \cdot h_0} + \sqrt{\left(\frac{J}{S_x \cdot h_0}\right)^2 + 6.76 \cdot \left(\frac{F_L(T)}{E(T)}\right)^2}} \tag{106}$$

$$F_L(T) = F_y \cdot \left(k_p - 0.3 \cdot k_y\right) \tag{107}$$

If the unsupported length of the member is under or equal to the limiting unbraced length, the value of M_n for the lateral-torsional buckling is calculated with Equations (108) and (109).

$$M_n(T) = C_b \cdot \left(M_r(T) + \left(M_p(T) - M_r(T) \right) \cdot \left(1 - \frac{L_b}{L_r(T)} \right)^{C_z} \right) \leq M_p(T) \qquad (108)$$

$$M_r(T) = F_L(T) \cdot S_x \qquad (109)$$

Otherwise, the value of M_n is calculated with Equations (110) and (111).

$$M_n(T) = F_{cr}(T) \cdot S_x \leq M_p(T) \qquad (110)$$

$$F_{cr}(T) = \frac{C_b \cdot \pi^2 \cdot E(T)}{\left(\frac{L_b}{r_{ts}} \right)^2} \cdot \sqrt{1 + 0.078 \cdot \frac{J}{S_x \cdot h_0} \cdot \left(\frac{L_b}{r_{ts}} \right)^2} \qquad (111)$$

1.5.4.3.1.2 *Sections with noncompact flanges*

For sections with non-compact flanges, the resistance is either governed by the lateral-torsional buckling or by the compression flange local buckling. The resistance to lateral-torsional buckling is calculated with Equations (106) to (111). The resistance to the compression flange buckling is obtained with Equation (112).

$$M_n(T) = M_p(T) - (M_p(T) - 0.7 \cdot F_y(T) \cdot S_x) \cdot \left(\frac{\lambda - \lambda_{pf}}{\lambda_{rf} - \lambda_{pf}} \right) \qquad (112)$$

1.5.4.3.1.3 *Sections with slender flanges*

As for the sections with the noncompact flanges, the resistance of sections with slender flanges is either governed by the lateral-torsional buckling or by the compression flange local buckling. The resistance to lateral-torsional buckling is calculated with Equations (106) to (111). The resistance to the compression flange buckling is obtained with Equation (113).

$$M_n(T) = \frac{0.9 \cdot E(T) \cdot k_c \cdot S_x}{\lambda^2} \tag{113}$$

1.5.4.3.2 Sections with noncompact web bent about their major axis

1.5.4.3.2.1 *Sections with compact flanges*

For section with compact flanges, the resistance is controlled either by compression flange yielding or by lateral-torsional buckling. The resistance to compression flange yielding is obtained with Equation (114).

$$M_n(T) = R_{pc} \cdot M_{yc}(T) = R_{pc} \cdot F_y(T) \cdot S_{xc} \tag{114}$$

The resistance to lateral-torsional buckling must be calculated if the unsupported length of the member is over the limiting laterally unbraced length for the limit state of yielding which is calculated with the following equation:

$$L_p(T) = 1.1 \cdot r_t \cdot \sqrt{\frac{E(T)}{F_y(T)}} \tag{115}$$

Otherwise, the calculation of the resistance to lateral-torsional buckling depends on if the unsupported length of the member is under or over the limiting unbraced length which is calculated with Equation (106) presented previously but with $F_L(T) = 0.7 \cdot F_y(T)$. If the length of the member is under the limiting unbraced length, Equation (116) must be used to determine the resistance to lateral-torsional buckling.

$$M_n(T) = C_b \left(R_{pc} \cdot M_{yc}(T) - (R_{pc} \cdot M_{yc}(T) - F_L(T) \cdot S_{xc}) \cdot \left(\frac{\lambda - \lambda_{pf}}{\lambda_{rf} - \lambda_{pf}} \right) \right) \leq R_{pc} \cdot M_{yc}(T) \tag{116}$$

Else, the resistance to lateral-torsional buckling is calculated with Equation (117).

$$M_n(T) = F_{cr} \cdot S_{xc} \le R_{pc} \cdot M_{yc}(T) \tag{117}$$

In this equation, the critical stress is calculated with Equation (118).

$$F_{cr}(T) = \frac{C_b \cdot \pi^2 \cdot E(T)}{\left(\frac{L_b}{r_t}\right)^2} \cdot \sqrt{1 + 0.078 \cdot \frac{J}{S_x \cdot h_0} \cdot \left(\frac{L_b}{r_t}\right)^2} \tag{118.}$$

1.5.4.3.2.2 *Sections with noncompact and slender flanges*

For sections with noncompact and slender flanges, the resistance is controlled either by the compression flange yielding, by lateral-torsional buckling or by compression flange local buckling. The resistance to the first two failure modes is calculated with the equations presented in the preceding section.

The resistance to the compression flange local buckling of sections with noncompact or slender is determined using respectively Equations (119) and (120).

$$M_n(T) = R_{pc} \cdot M_{yc}(T) - (R_{pc} \cdot M_{yc}(T) - F_L(T) \cdot S_{xc}) \cdot \left(\frac{\lambda - \lambda_{pf}}{\lambda_{rf} - \lambda_{pf}}\right) \le R_{pc} \cdot M_{yc}(T) \tag{119}$$

$$M_n(T) = \frac{0.9 \cdot E(T) \cdot k_c \cdot S_{xc}}{\lambda^2} \le R_{pc} \cdot M_{yc}(T) \tag{120}$$

1.5.4.3.3 Sections with slender web bent about their major axis

1.5.4.3.3.1 *Sections with compact flanges*

For sections with compact flanges, the resistance is controlled either by compression flange yielding or by lateral-torsional buckling. The resistance to compression flange yielding is obtained with Equation (121).

$$M_n(T) = R_{pg} \cdot F_y(T) \cdot S_{xc} \tag{121}$$

The resistance to lateral-torsional buckling must be calculated if the unsupported length of the member is over the limiting laterally unbraced length for the limit state of yielding which is calculated with Equation (115) presented previously. If lateral-torsional buckling must be considered, the resistance is obtained with the following equation:

$$M_n(T) = R_{pg} \cdot F_{cr}(T) \cdot S_{xc} \tag{122}$$

The critical stress depends on the length of the section compared to the limiting unbraced length for the limit state of inelastic lateral-torsional buckling which is calculated with Equation (123).

$$L_r(T) = \pi \cdot r_t \cdot \sqrt{\frac{E(T)}{0.7 \cdot F_y(T)}} \tag{123}$$

If the unsupported length of the member is under or equal to the limiting unbraced length, the value of M_n for the lateral-torsional buckling is calculated with Equation (124).

$$F_{cr}(T) = C_b \cdot \left(F_y(T) - \left(0.3 \cdot F_y(T)\right) \cdot \left(\frac{L_b - L_p(T)}{L_r(T) - L_p(T)} \right) \right) \leq F_y(T) \tag{124}$$

Else, equation 125 must be used.

$$F_{cr}(T) = \frac{C_b \cdot \pi^2 \cdot E(T)}{\left(\frac{L_b}{r_t} \right)^2} \leq F_y(T) \tag{125}$$

1.5.4.3.3.2 *Sections with noncompact and slender flanges*

For section with noncompact and slender flanges, the resistance is controlled either by the compression flange yielding, by lateral-torsional buckling or by compression flange local buckling. The resistance to the first two failure modes is calculated in the preceding section.

The resistance to compression flange local buckling is determined using respectively Equation (126).

$$M_n(T) = R_{pg} \cdot F_{cr}(T) \cdot S_{xc} \tag{126}$$

The critical stress for sections with noncompact and slender flanges is respectively determined with the following equations:

$$F_{cr}(T) = F_y(T) - \left(0.3 \cdot F_y(T)\right) \cdot \left(\frac{\lambda - \lambda_{pf}}{\lambda_{rf} - \lambda_{pf}} \right) \tag{127}$$

$$F_{cr}(T) = \frac{0.9 \cdot E(T) \cdot k_c}{\left(\frac{b_f}{2 \cdot t_f} \right)^2} \tag{128}$$

1.5.4.3.4 Sections bent about their minor axis

1.5.4.3.4.1 *Sections with compact flanges*

If the cross-section has flanges classified as compact, the nominal flexural strength is the resistance to yielding determined using the following equation:

$$M_n = M_p = F_y(T) \cdot Z_y \leq 1.6 \cdot F_y(T) \cdot S_y \tag{129}$$

1.5.4.3.4.2 *Sections with noncompact and slender flanges*

For sections with noncompact and slender flanges, the resistance to minor-axis bending is either governed by the resistance to yielding obtained with Equation (129) or by the resistance to flange local buckling.

The nominal flexural strength is determined with the following equation if the section has noncompact flanges:

$$M_n(T) = M_p(T) - (M_p(T) - 0.7 \cdot F_y(T) \cdot S_y) \cdot \left(\frac{\lambda - \lambda_{pf}}{\lambda_{rf} - \lambda_{pf}} \right) \tag{130}$$

If the flanges are classified as slender, the following equation must be used:

$$M_n(T) = F_{cr}(T) \cdot S_y \tag{131}$$

where
$$F_{cr}(T) = \frac{0.69 \cdot E(T)}{\lambda^2} \tag{132}$$

1.5.4.4 Cross-section subjected to combined compression and bending

If the cross-section is subjected to both compression and bending, an additional verification must be made.

If $\frac{P_r}{P_c(T)} \geq 0.2$,
$$\frac{P_r}{P_c(T)} + \frac{8}{9} \cdot \left(\frac{M_{rx}}{M_{cx}(T)} + \frac{M_{ry}}{M_{cy}(T)} \right) \leq 1.0 \tag{133}$$

If $\frac{P_r}{P_c(T)} < 0.2$,
$$\frac{P_r}{2 \cdot P_c(T)} + \left(\frac{M_{rx}}{M_{cx}(T)} + \frac{M_{ry}}{M_{cy}(T)} \right) \leq 1.0 \tag{134}$$

1.5.5 Comments on methods proposed by standards

For cross-sections of classes 1 and 2, all three codes use the stress at 2% plastic strain with the plastic modulus to calculate the resistance. The 2% plastic stress is also used to calculate the resistance of class 3 sections with the elastic modulus. According to Knobloch and Fontana [4], the method of calculation is unconservative as the strains at this level lead to local buckling even for compact sections.

As for class 4 sections, the calculation method depends on the code. The method proposed by Eurocode 3 do consider the increase in slenderness at high temperatures by using a reduction factor of 0.85 when classifying the cross-section. This is however a simplification of the real ratio between reduction factors used for the elasticity modulus and the yield limit [39]. Moreover, this reduction factor is not considered when using the Effective Width Method to calculate the effective properties of class 4 cross-sections. According to a study made by Knobloch and Fontana [4], the simplification made in the code results in a discontinuity at the class 4 limit which could be reduced by using the reduction factor of 0.85 to calculate the effective properties. The method also proposes to use 0.2% proof stress when calculating the resistance of class 4 sections. However, this method leads to conservative results and does not allow for an economical design.

The Canadian standards do not consider the temperature when either classifying the cross-sections or calculating the effective properties. As a result, the increase in slenderness caused by the increase in temperature is not accounted for which means that the resistance of sections considered to be of class 3 at ambient temperature can be overestimated at high temperatures as some of them may buckle before reaching their elastic capacity. Moreover, when calculating the resistance, the 2% total stess is used which may lead to unconservative results.

Finally, in the American standards, the properties at high temperatures are used for both the classification and the calculation of the effective properties. This allows to consider the increase in slenderness caused by the increase in temperature.

1.6 New proposals at high temperatures

In 2018, an equivalent stress method was proposed by Maraveas et al. [60]. This method proposes to modify the stress-strain relationship for compression to consider local buckling. To do so, the following expression is proposed to calculate the buckling reduction factor:

$$k_\theta = \frac{1}{\alpha \cdot {\lambda_{p,\theta}}^2 + \beta \cdot \lambda_{p,\theta} + \gamma} \tag{135}$$

In this equation the non-dimensional plate slenderness is calculated as in Part 1-5 of Eurocode 3 [37] :

$$\lambda_{p,\theta} = \frac{b/t}{28.4 \cdot \varepsilon \cdot \sqrt{k_\sigma}} \tag{136}$$

The parameter ε is calculated with the following equation where $k_{E,\theta}$ et $k_{y,\theta}$ are the reduction factors for Young's modulus and the yield strength used in Eurocode 3 [39].

$$\varepsilon = \sqrt{\frac{k_{E,\theta}}{k_{y,\theta}}} \cdot \sqrt{\frac{235}{f_y}} \tag{137}$$

The other parameters from Equation (135) are temperature-dependant and can be found in Table 7.

Table 7 : Proposed parameters for the equivalent stress method [60]

Type of plate	Temperature (°C)	α	β	γ
Flange	20	-0.19800	1.375	-0.0368
	200	-0.10000	1.000	0.6350
	> 300	-0.05500	1.130	0.6200
Web	20	-0.00066	0.446	0.9000
	200	0.04860	0.723	0.7400
	> 300	-0.03100	1.347	0.5300

Figure 35 shows the modified stress strain relationship.

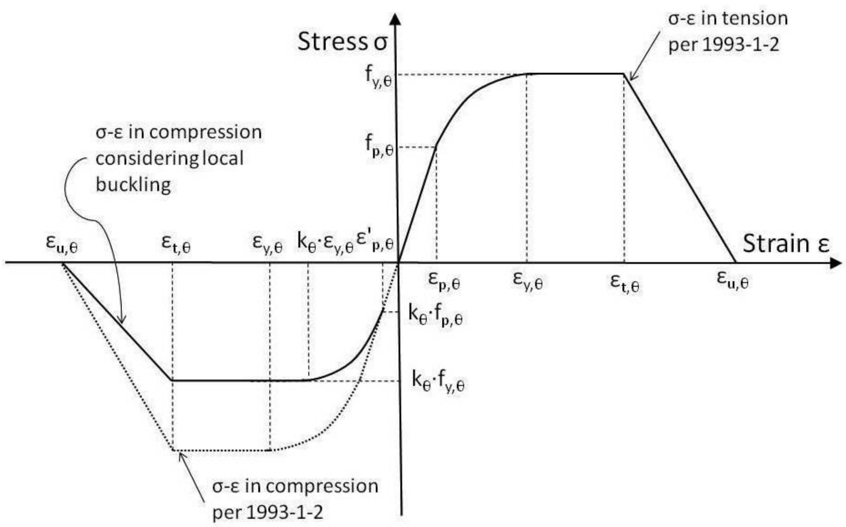

Figure 35 : Proposed modified stress-strain relationship [60]

This method allows to use more representative stresses based on the loading. However, it does not improve the overall design method.

Chapter 2 : Finite element modeling and validation

The intent of this chapter is to present a description of the finite element model used to conduct the study.

2.1 Finite element model's characteristics and features

The finite element software ABAQUS is used to perform numerical simulations. In the present study, Geometrically and Materially Non-linear Analysis (G.M.N.I.A.) and Linear Buckling Analysis (L.B.A.) are performed. G.M.N.I.A. analysis are performed using Riks' method which allows to go easily beyond the peak load and the subspace iteration method is used to perform the L.B.A. analysis.

S4R shell elements are used in the model. Those elements are 4 nodes, quadrilateral elements with reduced integration. These elements were chosen as they are widely used in numerical simulations and give good results. The shell elements are placed at mid-thickness of the real plate and given the appropriate thickness. The shell elements allow an adequate consideration of plate buckling as they can be loaded in their plane.

For hot-rolled sections, a specific modeling was done for the web-to-flange area. This area suffers from 2 problems when modeled with shell elements:

1) There is an overlap of the elements at the intersection of the web and the flange caused by the modelling with shell elements;
2) The radius area is not taken into consideration.

Both problems are illustrated on Figure 36. To fix those problems, beam elements are added at the centre of gravity of the two radius areas. The beams have a square shape which area is set to represent the radius area minus the overlapped area. A box shape is used to capture the additional torsional inertia provided to the cross-section by the radius. With the use of beam elements, the cross-sections geometrical properties are equal to the actual profiles' properties [50]. Moreover, the radius of a hot-rolled cross-section procures additional rigidity to the flange-to-web area which is not considered in the shell modelling. To account for that additional rigidity, relatively rigid spring elements are added between the web and the flanges. Those springs help the area to remain relatively unaffected by local buckling as it would be in reality. Added beam and spring elements are shown on Figure 36.

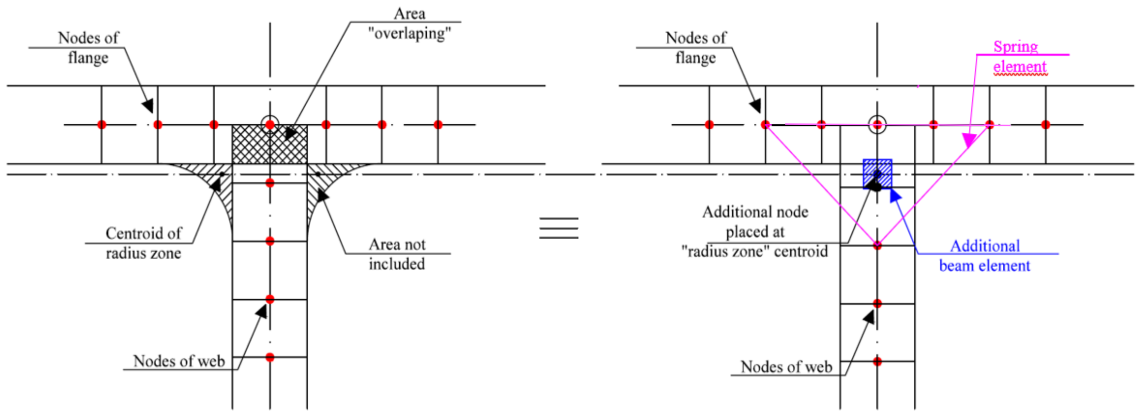

Figure 36 : Web-to-flange intersection modelling for hot-rolled sections

For welded sections, both beam elements and spring elements are excluded from the model. Effectively, in those sections, the welds are not considered in the cross-section area and do not provide a significant restraint to local buckling. The small overlap between shell elements from the web and shell elements from the flange is not considered to have a significant impact on the results.

2.2 Mesh density study

To ensure the accuracy of the results, a mesh density study was conducted. The goal of the study was to select a mesh that provides accurate results with minimum computation time. With a finer mesh, the accuracy is better, but computation time is high. On the other hand, a coarser mesh provides rapid computation time, but the results loose accuracy. Analyses were conducted with five types of meshes, from coarse to fine, to determine the most appropriate one to use in the numerical study. The five types of mesh differ in the number of elements used in the web and in the flanges. Figure 37 shows the different mesh configurations tested for both I and H sections. On this figure, it is possible to see that the mesh is not uniform especially for the coarser meshes. This is due to the fact that nodes are "manually" placed to introduce accurately the residual stresses and geometrical imperfections.

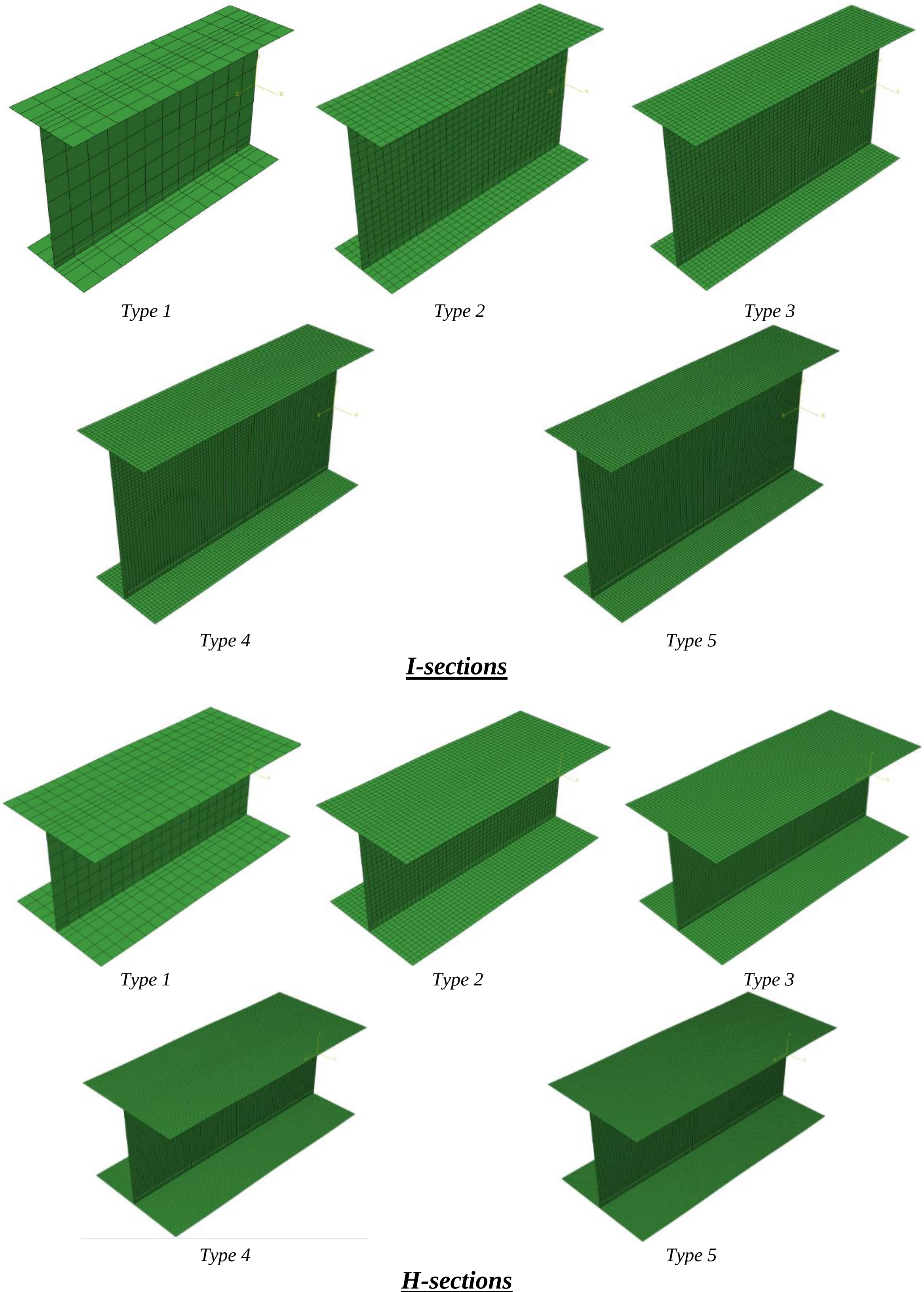

Figure 37 : Mesh configurations

The following parameters were considered to ensure a complete and accurate mesh study:

- Two types of analysis were performed: L.B.A. and G.M.N.I.A. analysis;
- Two load cases were considered: compression and major-axis bending;
- Twelve different sections were modeled (six IPE sections and six HEA sections). Those sections include regular sections and modified sections obtained by reducing all thickness of existing sections by 30%. Reduced sections are denoted with "-";
- Two temperatures were considered: 450°C and 700°C;
- Two values of Fy were considered: 355 MPa and 690 MPa.

A total of 480 G.M.N.I.A. and 480 L.B.A. numerical simulations were carried out. In all simulations, the initial load applied to the cross-section is the load carrying capacity predicted by EC3 divided by 3,5 which allows an easy convergence with the used convergence parameters. Initial imperfections and residual stresses were applied according to the recommendations presented in sections 2.5 and 2.6. As for the length of the cross-section, it was limited to three times the half-period length of the sinusoidal functions used for the material imperfections to avoid global instabilities.

Figure 59 to Figure 41 present L.B.A. and G.M.N.I.A. results. The results obtained are in terms of the critical buckling load multiplier, R_{cr}, for L.B.A. simulations and in terms of the ultimate load multiplier, $R_{ult,}$ for G.M.N.I.A. simulations. In all cases, the results obtained with the finest mesh (Type 5) is used as reference. Effectively, as type 5 mesh is very fine, it is considered that the results obtained with this type of mesh are close enough to the real value. The vertical axis of graphs is the load multiplier of the studied case divided by the load multiplier obtained with the type 5 mesh. A value of 1 means that the result is "exact".

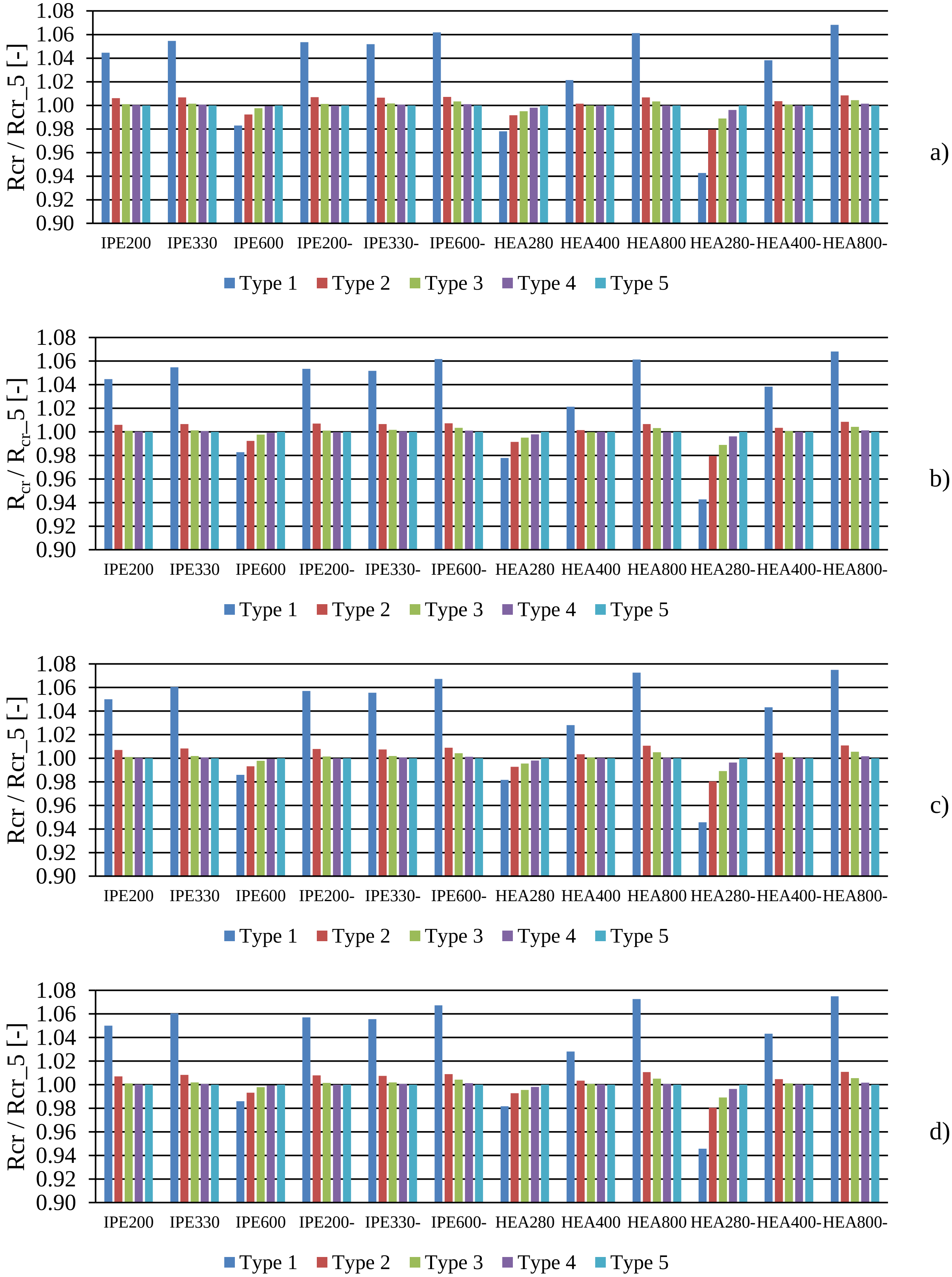

Figure 38 : Mesh study, L.B.A. results for compression: a) F_y=355 MPa and T=450°C; b) F_y=690 MPa and T=450°C; c) F_y=355 MPa and T=700°C; d) F_y=690 MPa and T=700°C

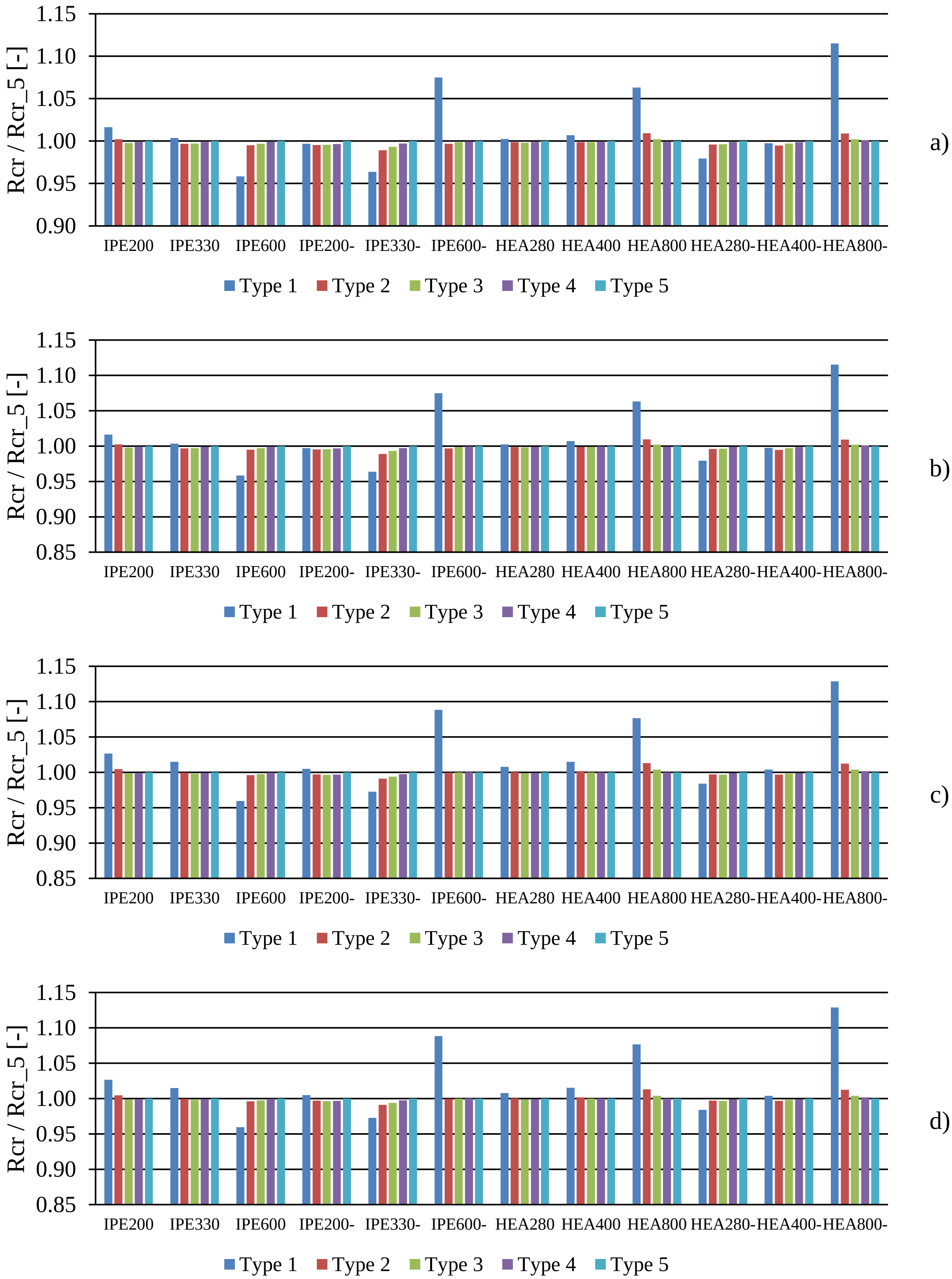

Figure 39 : Mesh study, L.B.A. results for major-axis bending: a) F_y=355 MPa and T=450°C; b) F_y=690 MPa and T=450°C; c) F_y=355 MPa and T=700°C; d) F_y=690 MPa and T=700°C

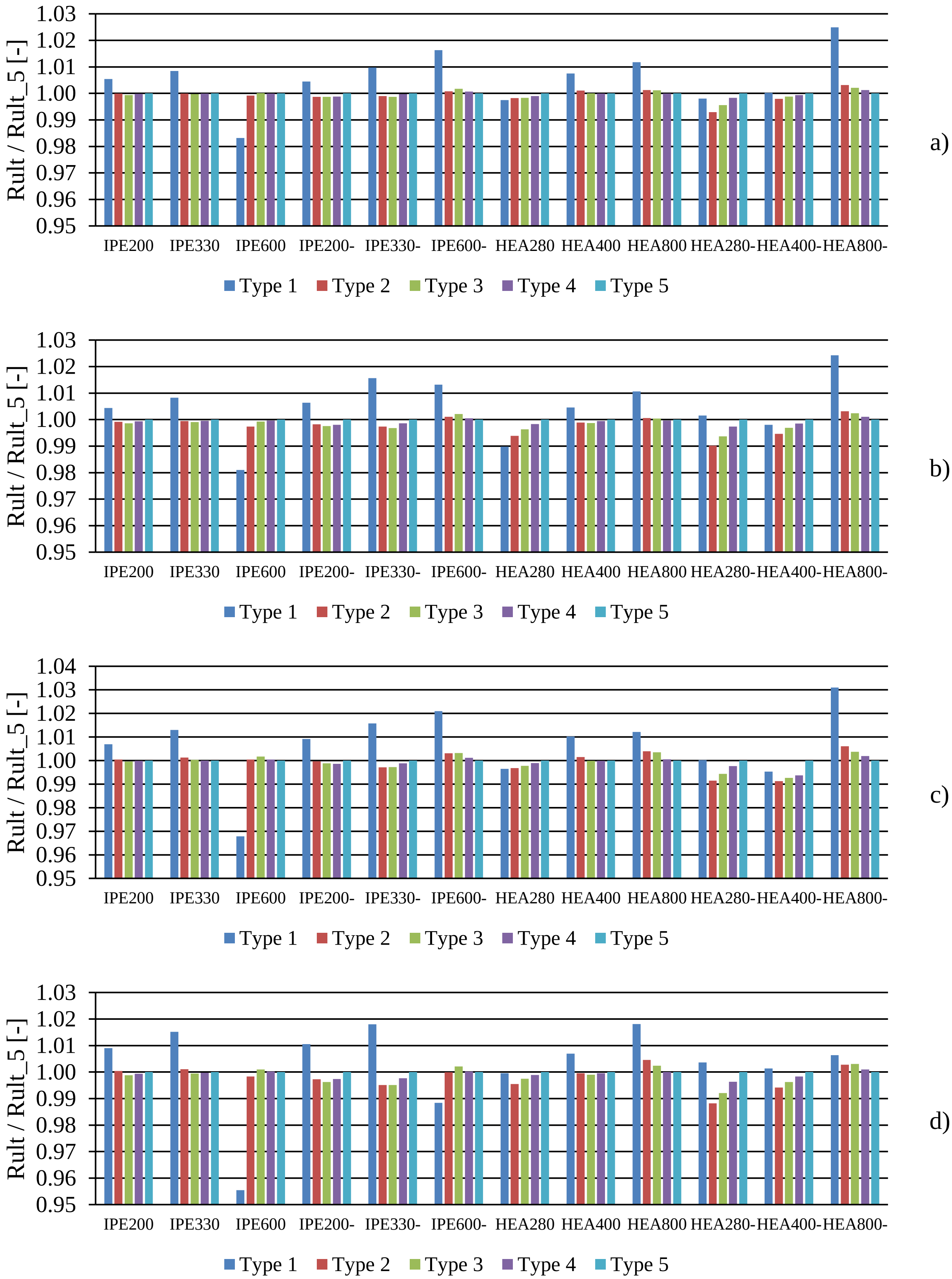

Figure 40 : Mesh study, G.M.N.I.A. results for compression: a) F_y=355 MPa and T=450°C; b) F_y=690 MPa and T=450°C; c) F_y=355 MPa and T=700°C; d) F_y=690 MPa and T=700°C

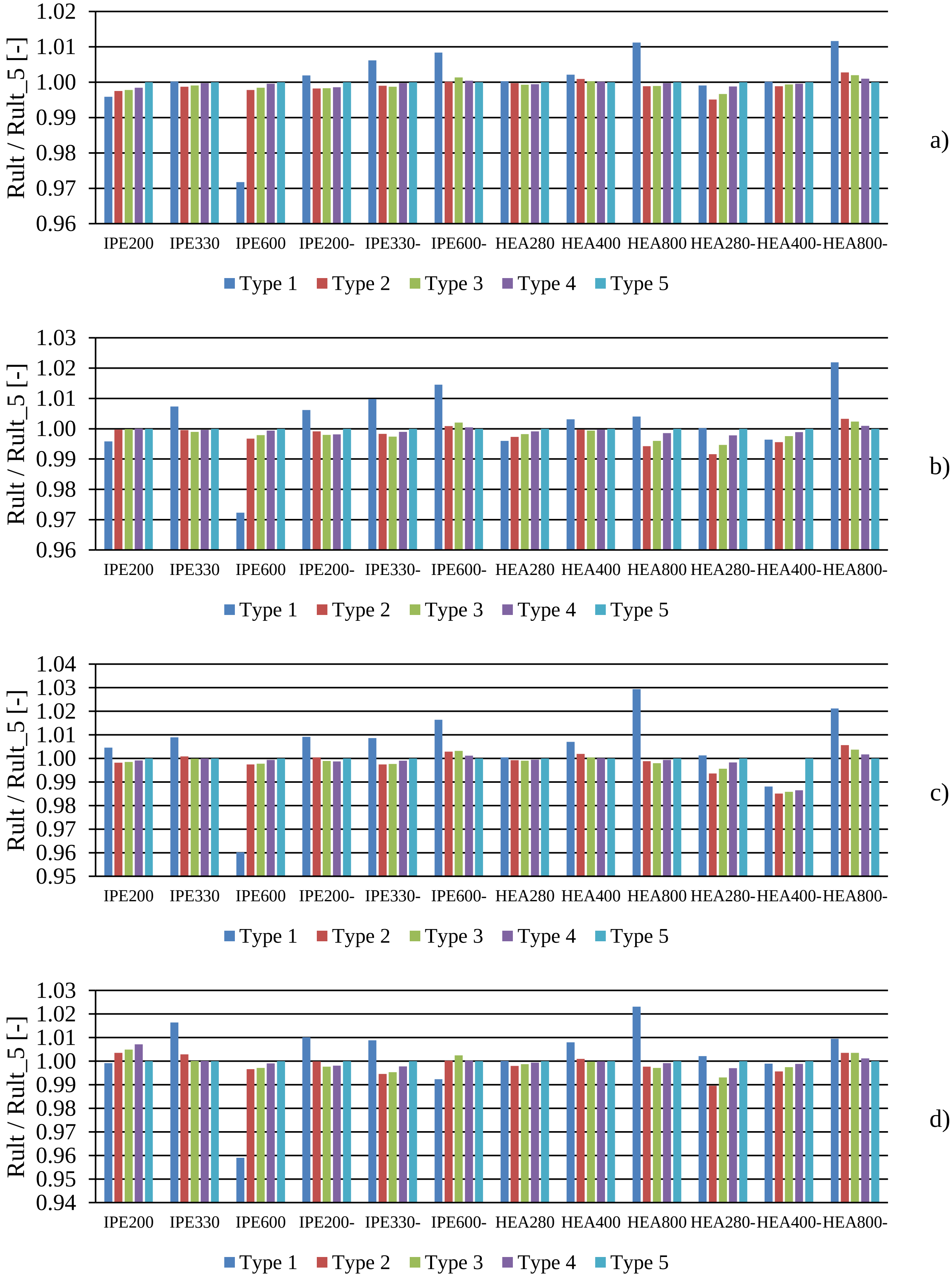

Figure 41 : Mesh study, G.M.N.I.A. results for major-axis bending: a) F_y=355 MPa and T=450°C; b) F_y=690 MPa and T=450°C; c) F_y=355 MPa and T=700°C; d) F_y=690 MPa and T=700°C

All graphs show that the results obtained with the Type 1 mesh present significant discrepancies with the reference results in most cases. As for the other types of mesh, the results obtained do not present pronounced differences. Table 8 presents the maximum deviations obtained with both types of analyses and for both types of loads.

Table 8 : Maximal deviation from exact result

		Type 1	Type 2	Type 3	Type 4
L.B.A.	N	7.49%	2.05%	1.12%	0.38%
	M	12.89%	1.32%	0.67%	0.34%
G.M.N.I.A.	N	4.46%	1.18%	0.80%	0.63%
	M	4.10%	1.49%	1.41%	1.35%

The table shows that the maximal deviation for Type 3 and over is 1.41%. This is considered accurate as it is below the confidence threshold of the numerical simulation which is between 3 and 5%. Any of these 3 meshes could therefore be used in numerical simulations. The other important factor to consider is the computation time needed to get the results of a simulation. The average computation times for G.M.N.I.A. analyses for each type of mesh and for both types of loads are presented on Figure 42.

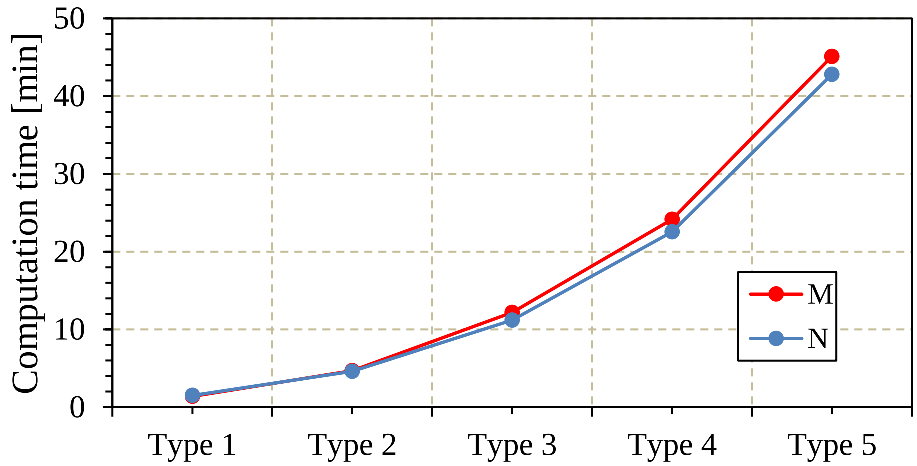

Figure 42 : Average computation time for each type of mesh

The figure above shows that the computation time significantly increases when the mesh becomes finer. The computation time is multiplied by a factor of about 2 between mesh types.

Based on the results, the Type 3 mesh was deemed the most appropriate. It has proven to procure accurate results while minimizing the computation time.

2.3 Material behaviour

As explained previously, the temperature has a significative impact on steel's properties. In the finite element model, the material law recommended by EC3 is used. At low temperatures, 20°C to 100°C, the material law is elastic-perfectly plastic. At higher temperatures, the material law becomes elastic-elliptic-perfectly plastic. In all cases, no strain hardening is considered which is conservative [39]. Figure 43 presents the stress-strain relationship for carbon steel at various temperatures.

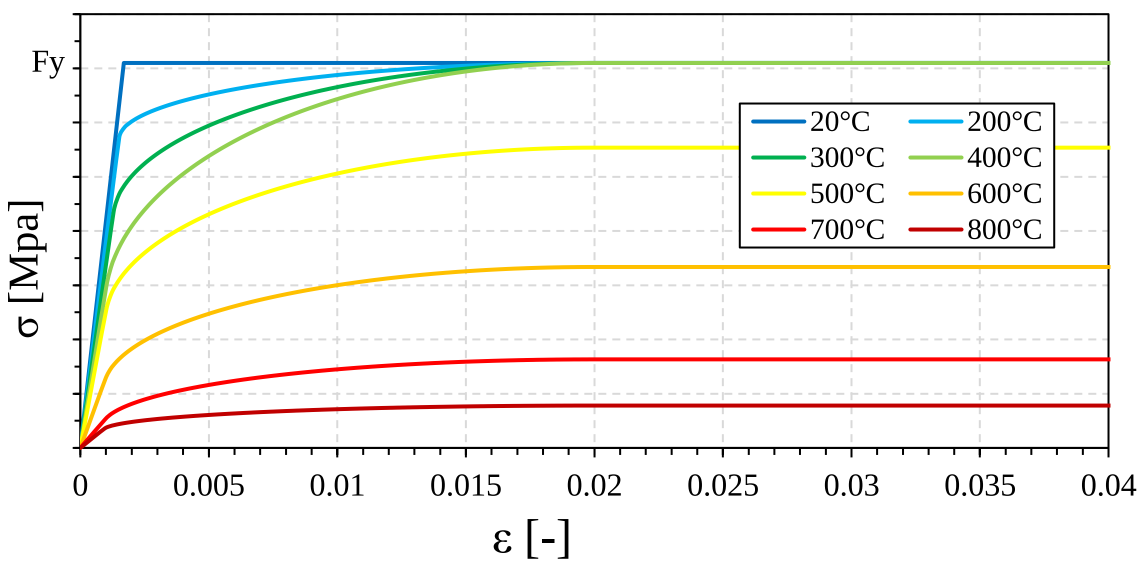

Figure 43 : Stress-strain relationship for carbon steel at elevated temperatures [39]

The stress-strain relationships shown on Figure 43 are obtained with the constitutive law recommended by Part 1.2 of Eurocode 3 and presented previously which is divided in four zones: a linear segment until the proportional limit is reached ($f_{p,\theta}$), an elliptic transition ending at the effective yield stress ($f_{y,\theta}$), a plateau and a linear descending branch at large strains [39]. The four zones are visible on Figure 44. In the present study, the last part of the constitutive law, the descending branch, is not considered. Table 9, obtained from Part 1.2 of Eurocode 3 [35], gives the equations needed to plot the constitutive law.

Table 9 : Steel constitutive law at elevated temperatures [39]

Strain range	Stress σ	Tangent modulus
$\varepsilon \le \varepsilon_{p,\theta}$	$\varepsilon \cdot E_{a,\theta}$	$E_{a,\theta}$
$\varepsilon_{p,\theta} < \varepsilon < \varepsilon_{y,\theta}$	$f_{p,\theta} - c + (b/a)\cdot\left[a^2 - (\varepsilon_{y,\theta} - \varepsilon)^2\right]^{0.5}$	$\dfrac{b\cdot(\varepsilon_{y,\theta} - \varepsilon)}{a\cdot\left[a^2 - (\varepsilon_{y,\theta} - \varepsilon)^2\right]^{0.5}}$
$\varepsilon_{y,\theta} \le \varepsilon \le \varepsilon_{t,\theta}$	$f_{y,\theta}$	0
$\varepsilon_{t,\theta} < \varepsilon < \varepsilon_{u,\theta}$	$f_{y,\theta}\cdot\left[1 - \dfrac{\varepsilon - \varepsilon_{t,\theta}}{\varepsilon_{u,\theta} - \varepsilon_{t,\theta}}\right]$	-
$\varepsilon = \varepsilon_{u,\theta}$	0.00	-
Parameters	$\varepsilon_{p,\theta} = \dfrac{f_{p,\theta}}{E_{a,\theta}}$ $\quad \varepsilon_{y,\theta} = 0.02$	$\varepsilon_{t,\theta} = 0.15$ $\quad \varepsilon_{u,\theta} = 0.20$
Functions	$a^2 = (\varepsilon_{y,\theta} - \varepsilon_{p,\theta})\cdot\left(\varepsilon_{y,\theta} - \varepsilon_{p,\theta} + \dfrac{c}{E_{a,\theta}}\right)$ $b^2 = c\cdot(\varepsilon_{y,\theta} - \varepsilon_{p,\theta})\cdot E_{a,\theta} + c^2$ $c = \dfrac{(f_{y,\theta} - f_{p,\theta})^2}{(\varepsilon_{y,\theta} - \varepsilon_{p,\theta})\cdot E_{a,\theta} - 2\cdot(f_{y,\theta} - f_{p,\theta})}$	

Where :

$f_{y,\theta}$	Effective yield strength
$f_{p,\theta}$	Proportional limit
$E_{a,\theta}$	Elasticity modulus
$\varepsilon_{p,\theta}$	Strain at the proportional limit
$\varepsilon_{y,\theta}$	Yield strain
$\varepsilon_{t,\theta}$	Limiting strain for yield strength
$\varepsilon_{u,\theta}$	Ultimate strain

Figure 44 is a representation of the constitutive law described in the previous table.

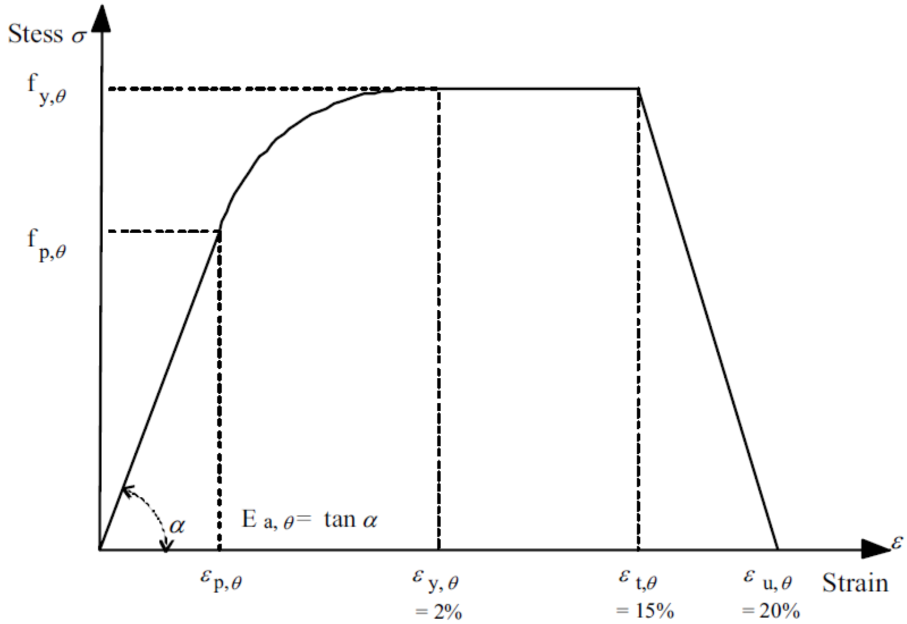

Figure 44 : Stress strain relationship of steel at elevated temperatures [39]

The different parameters that are temperature-dependant ($f_{y,\theta}$, $f_{p,\theta}$, $E_{a,\theta}$) are obtained by multiplying the value at room temperature by reduction factors that vary with the temperature [39]. Reduction factors recommended by EN 1993-1-2 are presented in Table 10.

Table 10 : Reduction factors for steel at elevated temperature [39]

Temperature (θ_a) (°C)	$k_{y,\theta} = f_{y,\theta} / f_y$ (-)	$k_{p,\theta} = f_{p,\theta} / f_y$ (-)	$k_{E,\theta} = E_{a,\theta} / E_a$ (-)
20	1.000	1.000	1.000
100	1.000	1.000	1.000
200	1.000	0.807	0.900
300	1.000	0.613	0.800
400	1.000	0.420	0.700
500	0.780	0.360	0.600
600	0.470	0.180	0.310
700	0.230	0.075	0.130
800	0.110	0.050	0.090
900	0.060	0.0375	0.0675
1000	0.040	0.0250	0.0450
1100	0.020	0.0225	0.0225
1200	0.000	0.0000	0.0000

Both f_y and E_a are taken at ambient temperature. Interpolation is used for intermediate values.

2.4 Support conditions and loading

Ideal fork conditions are applied in the finite element model allowing axial displacement, strong and weak axis rotation and warping. Axial displacement is blocked at the middle of the cross section allowing both ends to move. Figure 45 shows the applied boundary conditions.

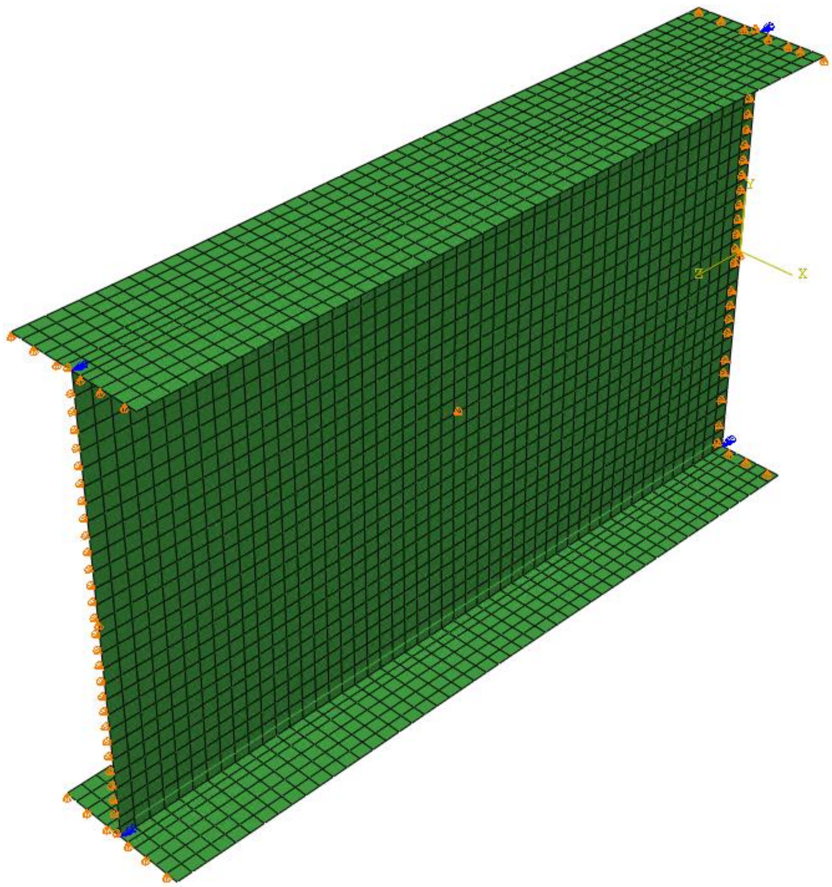

Figure 45 : Boundary conditions applied in the finite element model

Kinematic linear constraints are used at the end sections so that the displacement of each node is governed by the 4 corner nodes (not shown on figure). Linear constraints ensure that Bernoulli's principle, "all plane sections remain plane", is respected and allow the loads to be applied as axial load directly at the 4 corner nodes. Figure 46 shows how loads are applied. If multiple loads are applied, concentrated loads at nodes are added to create the full loading.

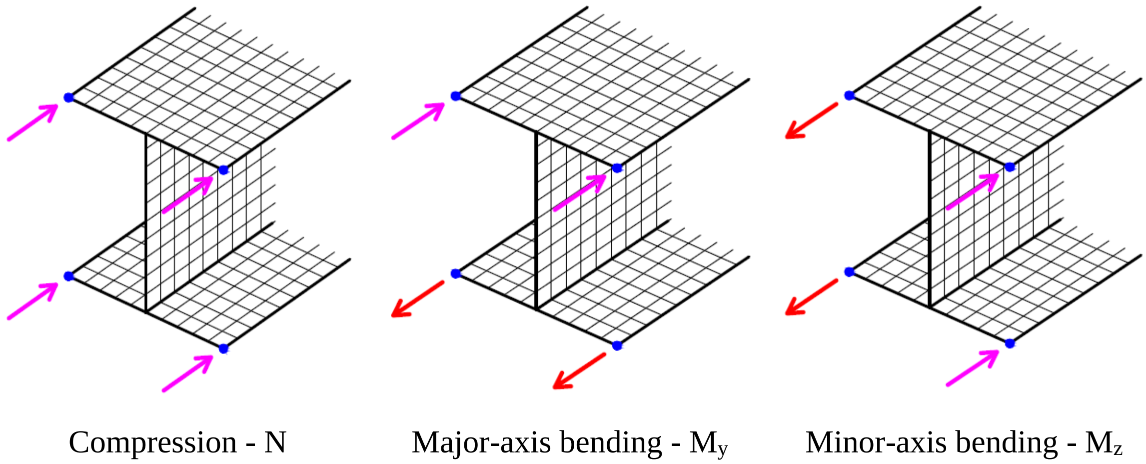

Figure 46 : Loading applied in the finite element model [3]

For combined load cases where all three forces are applied to the cross-section ($N + M_y + M_z$), previous studies have shown that, under fork support conditions, the cross-section is not able to reach its full plastic capacity [61]. When all three loads are applied on the cross-section, the plastic distribution of stresses can be represented as shown on Figure 47.

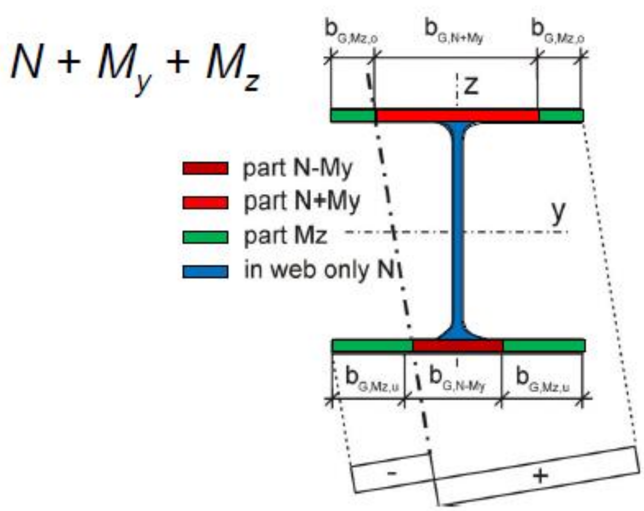

Figure 47 : Plastic distribution of stresses under N + My + Mz [62]

The figure shows that the stresses due to the minor axis bending moment in the lower and upper flange are not equal. Figure 48 shows that the warping moment is needed to obtain the plastic distribution shown on Figure 47.

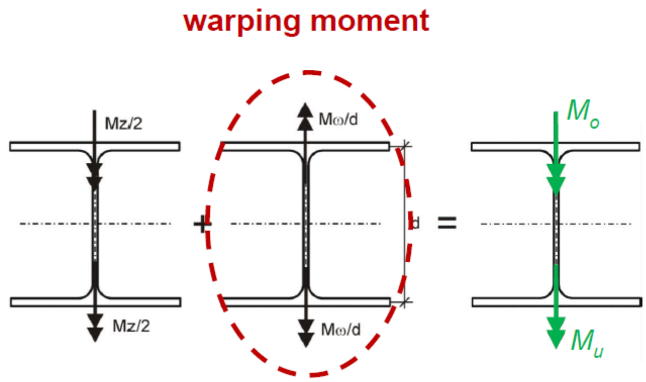

Figure 48 : Interaction between the minor axis bending moment and warping moment [62]

As the warping moment is needed to reach the full plastic distribution and therefore the full plastic capacity, some warping restraint must be provided to allow the warping moment to develop.

Studies were conducted on the effect of warping restraint in both [3] and [61]. In those studies, end plates were used to create warping restraint at both ends of cross-sections. Both studies showed that when no warping restraint is provided on very short members (cross-sections), it is not possible to reach the full plastic capacity by comparing the obtained numerical results with results from Materially Non-linear Analysis (M.N.A.). The studies also showed that the use of warping restraint is not needed for the study of members, Effectively, when performing simulation on members, the loading on the length of the member is not uniform. Less loaded parts of the member are therefore able to create additional warping restraints allowing the section to reach the full plastic capacity. However, when performing simulations at the cross-section level, loading is uniform throughout the section and no warping restraints is provided. Therefore, the section can not reach its full plastic capacity.

To allow the cross-sections subjected to both axial force and biaxial moment to reach the full plastic capacity, warping restraint is added to the finite element model using a rigid body condition which acts in the same way as the endplates discussed previously. All nodes at one end of the cross-section are set as a rigid body, and the node at mid-height of the web is set as the reference node. By doing so, all nodes at the end of the section undergo the same displacement, which prevents the flanges from moving in opposite directions and ensure that, following Bernoulli's principle, "plane sections remain plane". When using the rigid body, all boundary conditions and loads are applied directly at the reference node.

Numerical simulations were conducted with both models to evaluate the impact of warping restraint on the results. Figure 49 shows results obtained with and without warping restraints for cross-sections subjected to both axial force and biaxial moment. Results are shown for two different levels of compression defined by the variable *n*, which is obtained by dividing the applied compression load by the plastic resistance in compression of the cross-section.

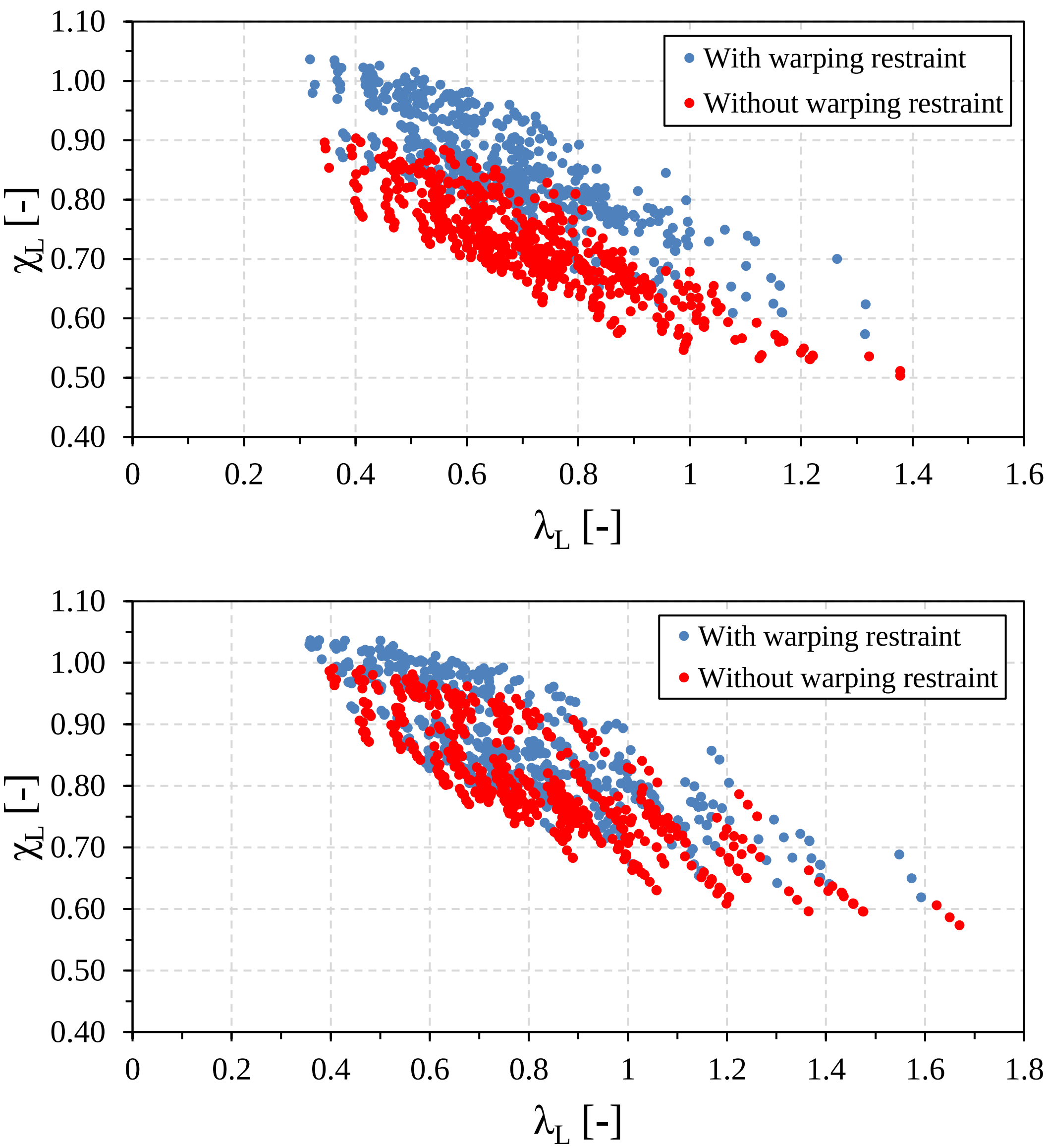

a)

b)

Figure 49 : Influence of warping restraint on results for : a) n = 0.4; b) n = 0.8

As expected, the figure shows that the results obtained without warping restraint are significantly lower than the ones obtained with warping restraint which confirms that when no warping restraint is provided, the cross-section is not able to reach its ultimate capacity. Figure 49 exhibits that even sections with low slenderness are not able to reach the full plastic capacity.

It was noticed that both the ultimate resistance multiplier (R_u) and the critical resistance multiplier (R_{cr}) are larger when warping restraint is applied in the model. Table 11 presents the maximum, average and minimum deviation in the results obtained with and without warping restraint.

Table 11 : Influence of warping restraint on results

	n = 0.4		n = 0.8	
	R_u (-)	R_{cr} (-)	R_u (-)	R_{cr} (-)
Maximum deviation (%)	31	23	14	29
Minimal deviation (%)	10	9	4	9
Average deviation (%)	18	14	7	14

Results confirm that the ultimate load obtained is significantly lower when no warping restraint is provided which agrees with results obtained in both [3] and [61]. Results show that this is particularly true for cross-sections subjected to lower axial force. Warping restraint is therefore needed so that the ultimate load of the section is not underestimated. As for the critical load, results are on average 14 % lower when no warping restraint is provided. This can be explained by the fact that the additional restraint increases the stability. The critical load obtained without warping restraint is more representative of the real buckling load as it is calculated with fork boundary conditions. However, in order to stay consistent throughout the numerical study, all simulations, L.B.A. and G.M.N.I.A., for load cases with axial force and biaxial bending are done with warping restraint.

2.5 Geometrical imperfections

Based on the recommendations made by Gérard et al. [46], sinusoidal functions with 3 half-waves are used to introduce local geometrical imperfections in the finite element model. Figure 50 shows the representation of the sinusoidal imperfections.

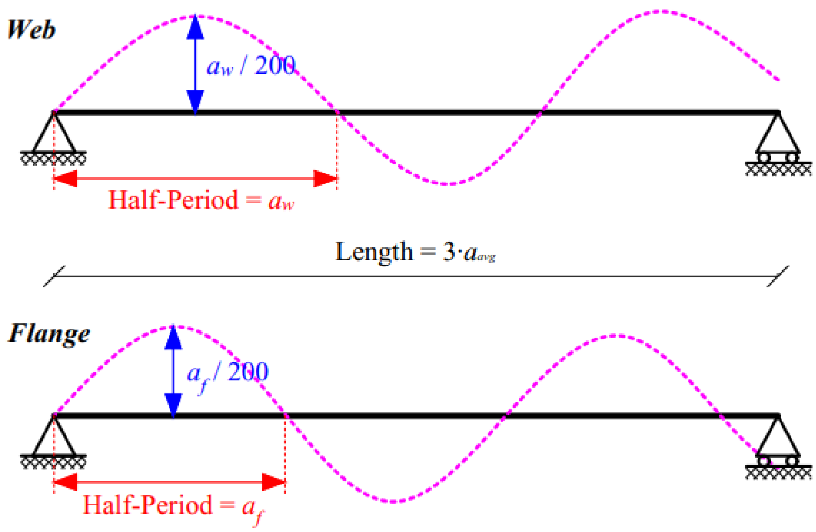

Figure 50 : Sinusoïdal imperfections on web and flanges [46]

The amplitude of the imperfections on the web and the flanges and the half-period shown on the figure are expressed in terms of the buckling lengths (*a*) of the elements which depends on the manufacturing process. For hot-rolled sections, $a_w = h - 2 \cdot t_f - 2 \cdot r$ and $a_f = b - t_w - 2 \cdot r$, while for welded sections, $a_w = h - t_f$ and $a_f = b$ due to the absence of fillets. In both cases, h refers to the full height of the section. Amplitudes of $a_w / 200$ for the web and of $a_f / 200$ for the flanges are used. The half-period length is the average between the buckling lengths of the web and flange: $a_{avg} = 0.5 \cdot (a_w + a_f)$ [46].

2.6 Residual stresses

As discussed in section 1.4.2.2, the evolution of residual stresses for sections submitted to high temperatures under load is not well known. However, many studies have shown a significant reduction in residual stresses when sections are subjected to high temperature. Therefore, this reduction was considered when introducing residual stresses in the finite element model for both welded and hot-rolled cross-sections by reducing the maximal amplitude of the residual stresses.

2.6.1 Welded sections

For welded sections, the same residual stress pattern is used for cross-sections at ambient and elevated temperatures. The pattern used is the one recommended by Lucile Gérard in her PhD thesis [3] and is presented on Figure 51.

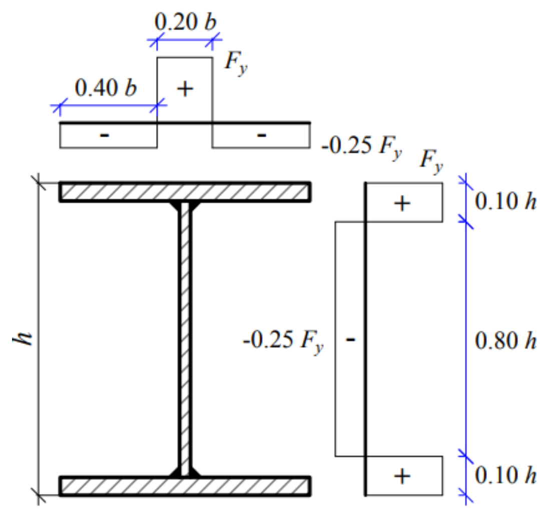

Figure 51 : Residual stress pattern for welded sections [3]

When residual stresses are added to the finite element model, the first step of the numerical analysis is a stress redistribution even before external loading is applied. If there are no geometrical imperfections introduced in the model and if the pattern used for the residual stresses is perfectly auto equilibrated, very limited stress redistribution occurs. After introducing the residual stresses in a finite element model at ambient temperature without any geometrical imperfections, no stress redistribution was noted which confirms that the pattern used is auto equilibrated.

As mentioned previously, the same residual stress pattern is used for cross-sections subjected to elevated temperatures. However, as the yield strength diminishes with the increase in temperature, the yield strength corresponding to temperature studied is used. With this approach, it was anticipated that there would not be any stress redistribution after the application of the residual stresses in the finite element model when no geometrical imperfections are introduced as discussed previously. A test was conducted with a section at a temperature of 200°C. At this temperature, there is no reduction in yield limit. Therefore, the residual stresses applied are exactly the same as for a cross section at 20°C. Figure 52 presents the distribution of stresses in the section before and after redistribution.

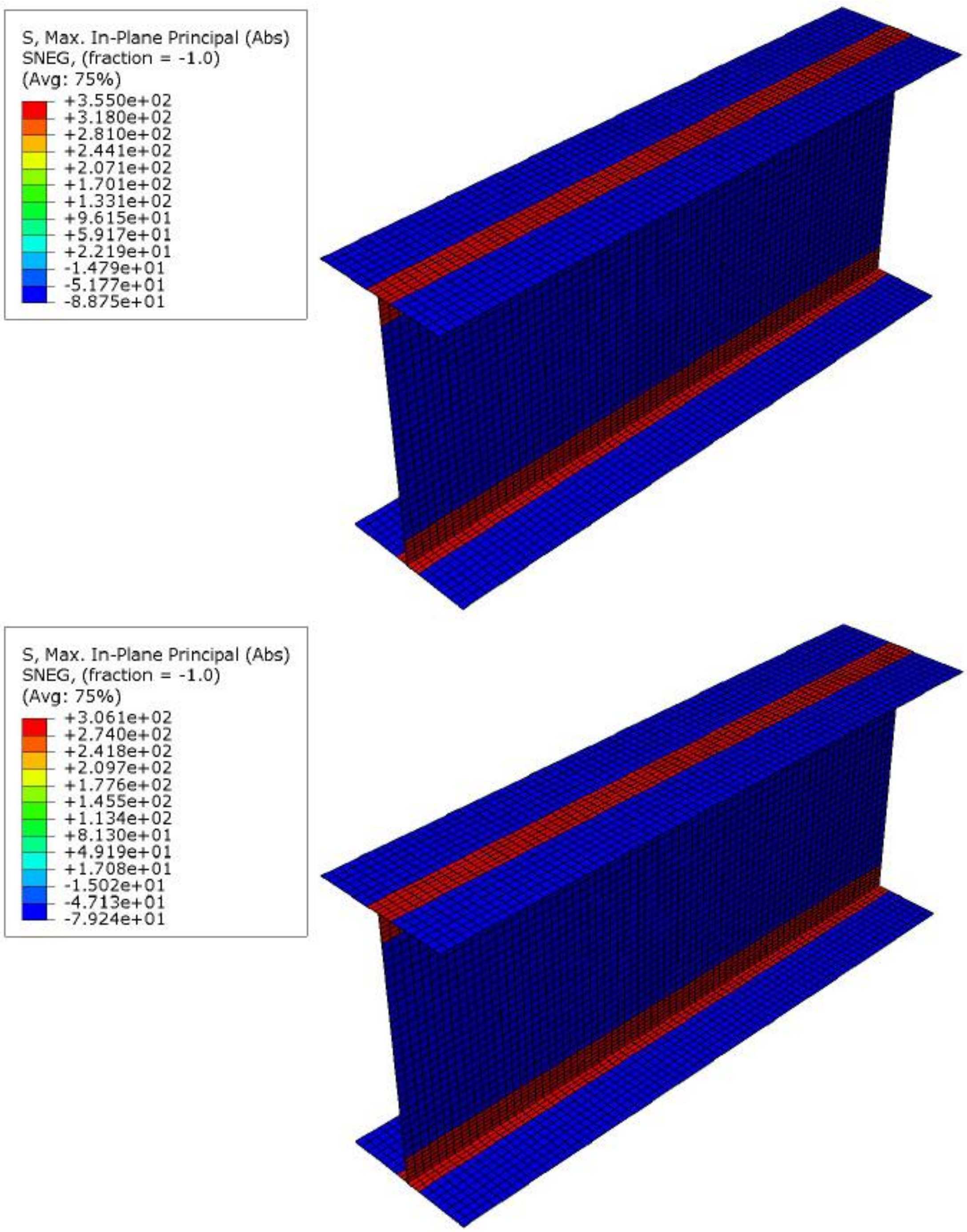

a)

b)

Figure 52 : Maximal stress distribution in cross-section (MPa) : a) Before stress redistribution ; b) After stress redistribution

The legend on the figure shows a significative stress redistribution (up to 14% difference). The stress redistribution can be explained by the fact that even thought there is no reduction in Fy at 200°C, the material law is no longer elastic-perfectly plastic and the elasticity limit is no longer equal to the yield limit. Table 12 presents the yield limit and the elasticity limit at 20°C and 200°C.

Table 12 : Material properties at 20°C and 200°C

Temperature (°C)	F_y (MPa)	F_p (MPa)
20	355	355
200	355	286

Values in Table 12 show that there is a significative difference between the yield limit and the proportionality limit even at low temperature. The non-linearity of the material law at elevated temperatures induces a stress redistribution which is not present at ambient temperature. It was therefore considered to use the proportionality limit as the maximal residual stress applied in the finite element model instead of the yield limit. When applying the residual stresses with this maximal stress, no stress redistribution was noted in the cross-section. As the residual stress pattern used is auto equilibrated this result was expected and desired.

A sub-study was conducted to quantify the impact of the two proposed methods used to introduce the residual stresses on the results. The following parameters were considered to ensure a complete and accurate study:

- GMINIA analysis were performed;
- No geometrical imperfections were introduced so that the effect of the introduction of residual stresses could be studied;
- Two load cases were considered: compression and major-axis bending;
- Two maximal residual stresses were considered: F_y and F_p;
- Twelve different cross-sections were modeled (six I-shape sections and six H-shape sections). Those sections include regular sections and modified sections obtained by reducing all thickness to obtain more slender sections;
- Three temperatures were considered: 300°C, 450°C and 700°C.

A total of 144 numerical simulations were carried out. In all simulations, the initial load applied to the cross-section was the load carrying capacity predicted by EC3 divided by 3,5 which allows an easy convergence. The length of the "cross-section" was limited to three times the half-period length of the sinusoidal functions used when geometrical imperfections are included to avoid global instabilities.

Figure 53 and Figure 54 present the simulation results in O.I.C. format.

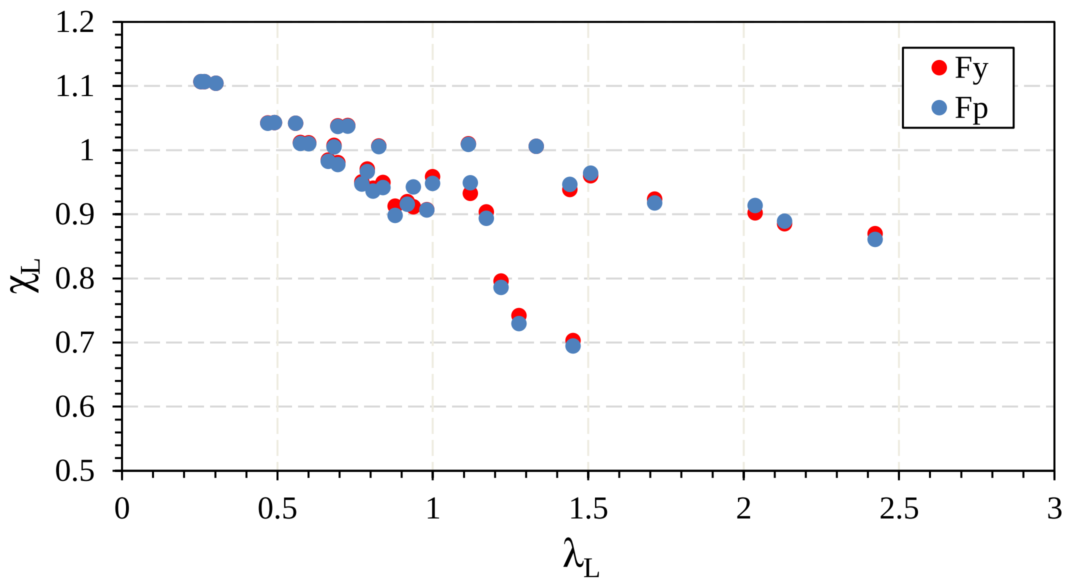

Figure 53 : Resistance of cross-sections under pure compression with maximal residual stress F_y and F_p

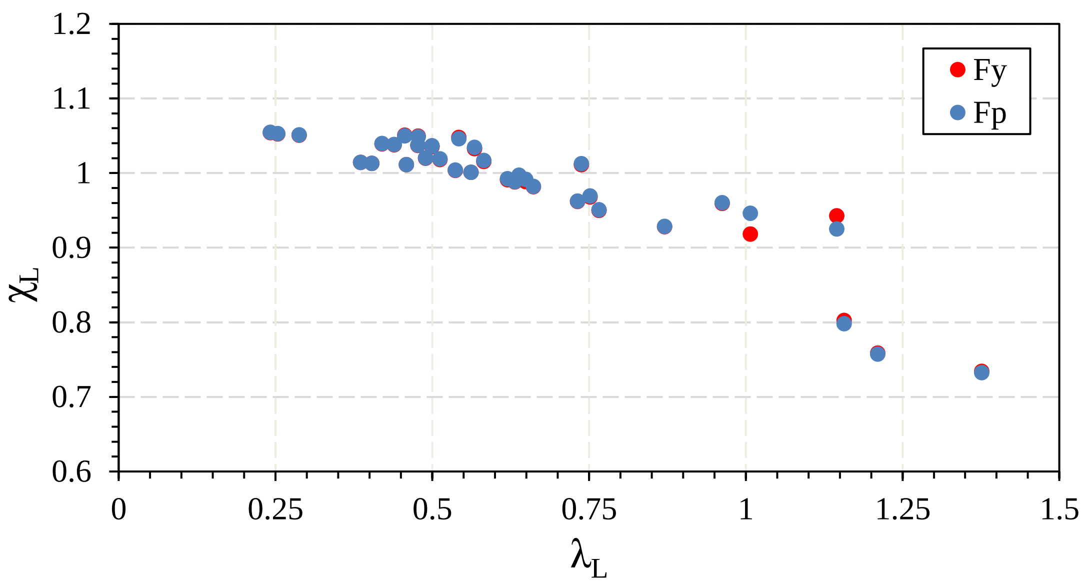

Figure 54 : Resistance of cross-sections under major-axis bending with maximal residual stress F_y and F_p

Table 13 presents the average and maximum deviation between results for both load cases.

Table 13 : Average and maximum deviation between results obtained with F_y and F_p for welded sections

	Average deviation (%)	Maximum deviation (%)
Compression	0.61	3.39
Major-axis bending	0.23	3.04

Results show that there is almost no impact on the maximal load capacity of the cross-sections when using either the yield strength or the proportionality limit as the maximal residual stress. It was therefore chosen to use the proportionality limit as the maximal residual stress since it ensures no load redistribution during the initial step of the simulation.

2.6.2 Hot-rolled sections

For hot-rolled sections, the same residual stress pattern is used for cross-sections at ambient and elevated temperatures. The pattern used is the one recommended by Lucile Gérard in her PhD thesis [3] and is presented on Figure 55. The maximum value for F_y is set at 235 MPa as discussed in section 1.4.2.

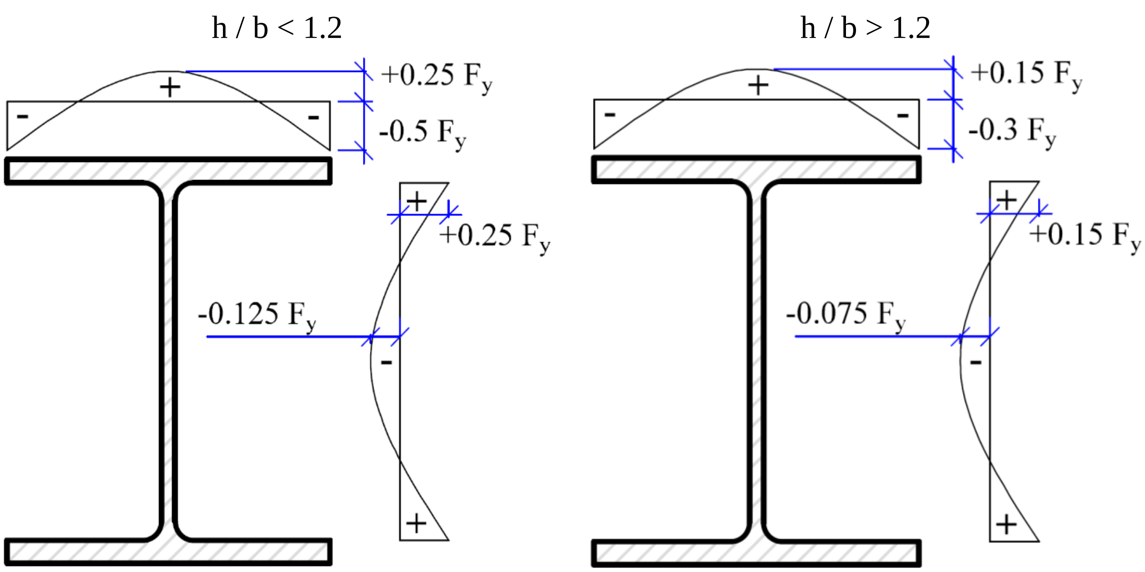

Figure 55 : Residual stress pattern for hot-rolled sections [3]

The introduction of the residual stress pattern in the finite element model is complex due to its parabolic form. To facilitate the incorporation of the residual stresses in the model, the residual stresses are calculated in the middle of each shell element and the value obtained is applied to the entire element. This method allows to estimate the residual stresses by a discontinuous pattern which is shown on Figure 56.

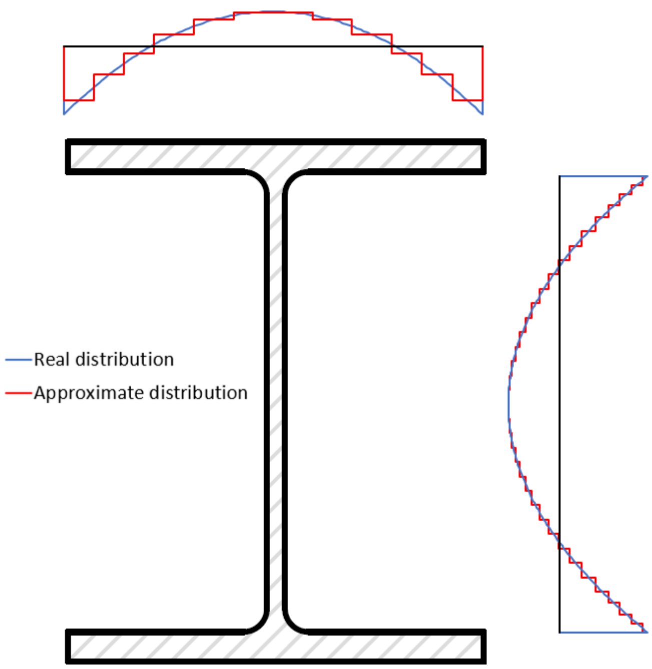

Figure 56 : Stair pattern used to introduce residual stresses in the finite element model

When residual stresses are added to the finite element model, the first step of the analysis is a stress redistribution. If there are no geometrical imperfections introduced in the model and if the pattern used for the residual stresses is perfectly auto-equilibrated, no stress redistribution occurs. After introducing the residual stresses with the stair pattern in a finite element model without any geometrical imperfections, a small stress redistribution was noted. This redistribution occurred since the stair pattern is not perfectly auto-equilibrated. Stresses in the cross-sections were compared before and after the redistribution to ensure the validity of the chosen pattern. Figure 57 shows the stresses before and after the redistribution for a cross-section at ambient temperature.

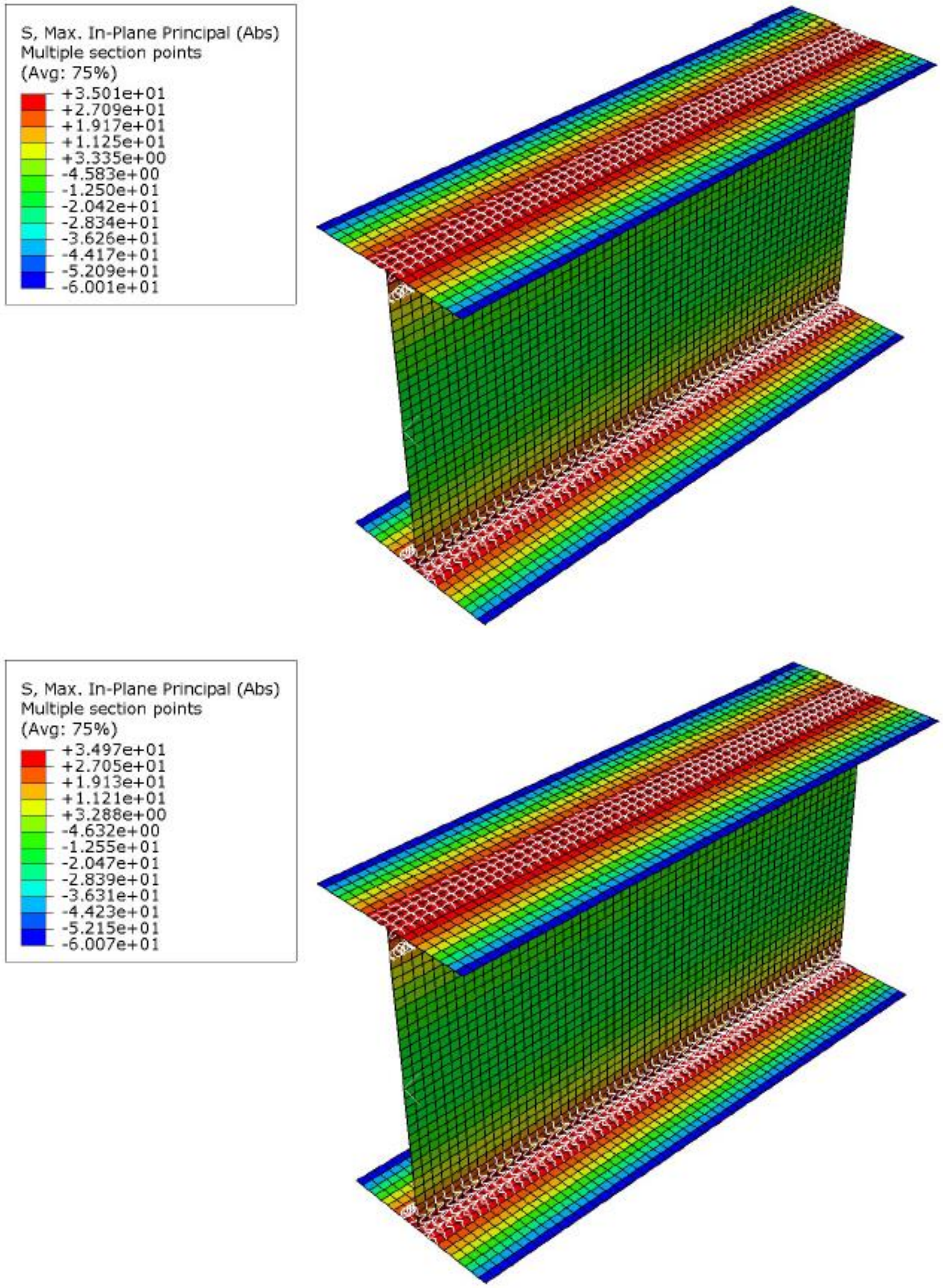

Figure 57 : Maximal stress distribution in cross-section (MPa) : a) Before stress redistribution ; b) After stress redistribution

As shown in the figure, the stress redistribution is very small and can be neglected, which confirms that the chosen way to introduce residual stresses is appropriate.

As mentioned previously, the same pattern is used for cross-sections at elevated temperatures. However, as the yield strength diminishes with the increase in temperature, the yield strength corresponding to the temperature studied is used like for welded cross-sections. Such as for sections at ambient temperature, a maximum value of 235 MPa is considered. Residual stresses considered for hot-rolled sections are significatively lower than the ones considered for welded sections. Effectively, as shown on the pattern on figure 5, the maximal residual stress that can be applied is 0.5 F_y. Table 14 shows the yield and proportionality limits at various temperature, the value used as F_y for the residual stresses (F_{y_used}) and the value of 0.5 F_{y_used}.

Table 14 : Yield and proportionnality limits and used value for the residual stresses at various temperatures

Temperature (°C)	F_y (MPa)	F_p (MPa)	F_{y_used} (MPa)	0.5 F_{y_used} (MPa)
20	355	355	235	117,5
300	355	218	235	117,5
450	316	138	235	117,5
550	222	96	222	111
700	82	27	82	41

As shown in the table, the maximal applied residual stress is almost never over the proportionality limit. Therefore, the redistribution of stresses would only happen at very high temperatures and even at those temperatures, the redistribution would not be as important as for welded sections since the difference between the maximal applied stress and the proportionality limit is small.

However, to be consistent with the way residual stresses are applied for welded sections, it was considered to use the proportionality limit as the maximal residual stress applied in the finite element model instead of the yield strength like for welded section.

A sub-study was conducted to quantify the impact of the two proposed methods used to introduce the residual stresses. The following parameters were considered to ensure a complete and accurate study:

- GMINIA analysis were performed;

- No geometrical imperfections were introduced so that the effect of the introduction of residual stresses could be studied;
- Two loads cases were considered: compression and major-axis bending;
- Two maximal residual stresses were considered: F_y and F_p with a maximum value of 235 MPa;
- Twelve different cross-sections were modeled (seven I-shape sections and six H-shape sections). Those sections include regular sections and modified sections obtained by reducing all thickness to obtain more slender sections;
- Three temperature were considered: 300°C, 450°C and 700°C.

A total of 144 numerical simulations were carried out. In all simulations, the initial load applied to the cross-section was the load carrying capacity predicted by EC3 divided by 3,5 which allows an easy convergence. The length of the cross-section was limited to three times the half-period length of the sinusoidal functions used when material imperfections are included to avoid global instabilities.

Figure 58 and Figure 59 presents the simulation results in O.I.C. format.

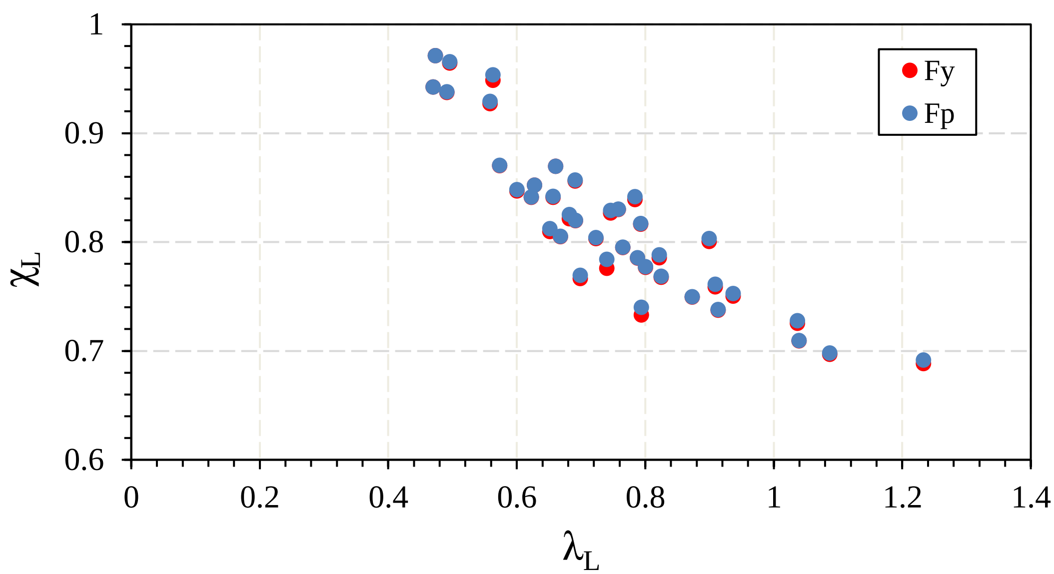

Figure 58 : Resistance of cross-sections under pure compression with maximal residual stress F_y and F_p

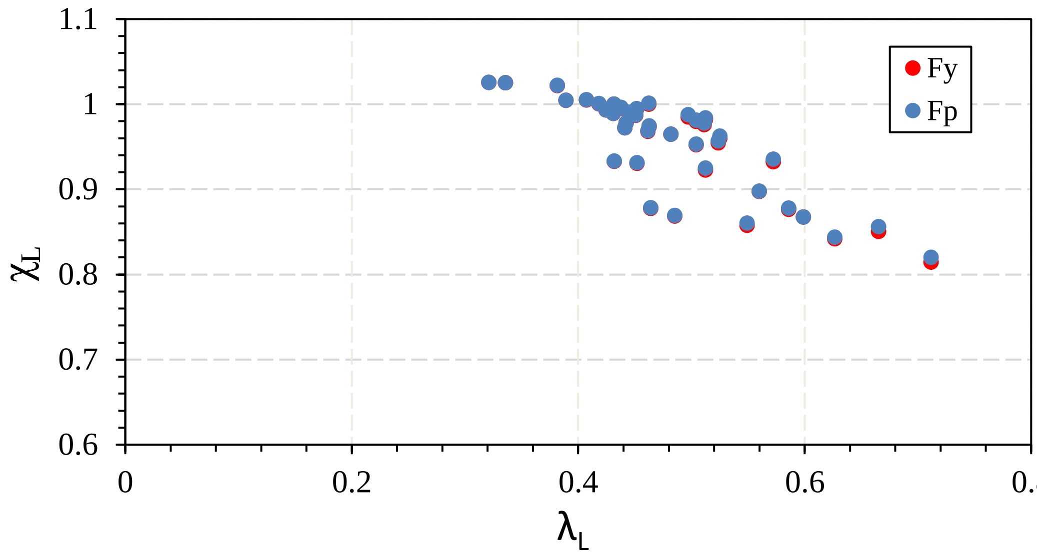

Figure 59 : Resistance of cross-sections under major-axis bending with maximal residual stress F_y and F_p

Table 15 presents the average and maximum deviation between results for both load cases.

Table 15 : Average and maximum deviation between results obtained with F_y and F_p for hot-rolled sections

	Average deviation (%)	Maximum deviation (%)
Compression	0.20	1.05
Major-axis bending	0.12	0.69

Results show that there is almost no impact on the maximal load capacity of the cross-sections when using either the yield strength or the proportionality limit as the maximal residual stress. It was chosen to use the proportionality limit as the maximal residual stress since it ensures no load redistribution during the initial step of the simulation.

2.7 Model validation

To ensure the validity of the finite element model, it was tested against experimental results and assumptions made for boundary conditions and residual stresses were verified. The experimental results used for the comparison were obtained from the PhD thesis of Pauli

[63]. In her study, many HEA100 short columns were tested with different loading and at different temperatures. In all case, a compression load is applied at the top of the specimen. For the combined load cases, the compression load is applied with an eccentricity to create a bending moment. The use of stub columns allowed to obtain the cross-section resistance. Table 16 presents the 20 studied specimens and the ultimate load reached.

Table 16 : Studied specimens by Pauli [63]

Specimen	Temperature	Boundary conditions		Load excentricity		Ultimate Load		
		y	z	e_y	e_z	N	M_y	M_z
[-]	[°C]	[-]	[-]	[mm]	[mm]	[kN]	[kNm]	[kNm]
S02	550	pin	tie	0	10	389	3.89	0
S03	550	pin	tie	0	50	225	11.25	0
S04	20	tie	tie	0	0	1124	0	0
S05	20	pin	tie	0	10	845	8.45	0
S06	550	tie	pin	10	0	376	0	3.76
S07	550	tie	tie	0	0	434	0	0
S08	400	pin	tie	0	10	764	7.64	0
S09	400	tie	pin	10	0	739	0	7.39
S10	20	pin	tie	0	50	510	25.5	0
S12	20	tie	pin	10	0	724	0	7.24
S13	550	tie	tie	0	0	511	0	0
S14	400	tie	pin	50	0	288	0	14.4
S15	550	pin	tie	0	50	236	11.8	0
S16	20	tie	pin	50	0	309	0	15.45
S17	400	pin	tie	0	50	467	23.35	0
S18	550	tie	pin	50	0	140	0	7
S19	400	tie	tie	0	0	996	0	0
S20	20	tie	tie	0	0	1028	0	0
S21	700	tie	tie	0	0	135	0	0
S22	700	tie	tie	0	0	162	0	0

2.7.1 Validation against numerical model using experimental data

Firstly, a validation was made to ensure that the numerical model is able to reproduce the experimental tests that were performed. In this validation, the specimens were modeled as closely as possible to the ones used during the experiments. First, the measured widths and thicknesses from the experimental study of Pauli were used [63]. The average dimensions of each part of the cross-sections were calculated and introduced in the model. Table 17 presents the dimensions used.

Table 17 : Average dimensions used in the numerical model

Specimen	Geometrical dimensions							
	h	b_1	b_2	t_w	t_{f1}	t_{f2}	r	L
[-]	[mm]	[mm]	[mm]	[mm]	[mm]	[mm]	[mm]	[mm]
S02	98.75	101.3	101.65	5.59375	8.0825	8.0625	12	297.5
S03	98.9	101.4	101.3	5.4975	8.0525	8.0875	12	298.0
S04	98.85	101.55	101.25	5.5025	8.0892	8.0767	12	298.3
S05	98.95	101.7	101.4	5.5125	8.085	8.07	12	298.3
S06	98.725	101.25	101.65	5.5225	8.0983	8.0475	12	297.5
S07	98.8	101.25	101.65	5.51375	8.0725	8.0825	12	298.0
S08	98.85	101.35	101.7	5.52	8.0658	8.0467	12	297.5
S09	98.825	101.4	101.7	5.48875	8.09	8.058	12	297.3
S10	98.75	101.75	101.15	5.4825	8.0517	8.0617	12	301.3
S12	98.925	101.2	101.7	5.4825	8.06417	8.0817	12	297.3
S13	98.825	101.7	101.35	5.47625	8.04	8.0508	12	299.0
S14	98.775	101.15	101.65	5.49625	8.0475	8.0233	12	301.8
S15	98.725	101.15	101.65	5.5075	8.0767	8.0775	12	301.0
S16	98.85	101.55	101.35	5.50375	8.0708	8.0542	12	301.0
S17	98.8	101.45	101.25	5.48875	8.0517	8.0483	12	301.8
S18	98.75	101.65	101.3	5.51375	8.0467	8.07	12	301.3
S19	98.85	101.65	101.2	5.5175	8.0825	8.0517	12	298.5
S20	98.9	101.65	101.5	5.53	8.075	8.084	12	298.3
S21	98.85	101.45	101.1	5.4825	8.13	8.0908	12	298.0
S22	98.85	101.25	101.6	5.5125	8.0608	8.075	12	298.5

Then, the material laws determined experimentally by tensile material coupon tests were used. They were modelled using the measured data during the experimental test. Figure 60 shows the experimental material laws. Material laws for the HEA100 sections are used in the model.

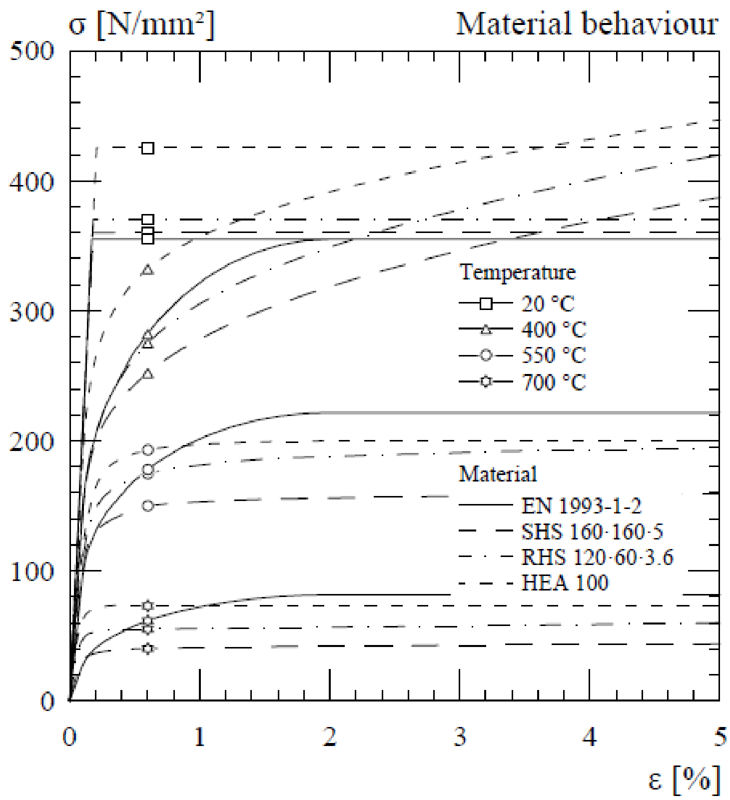

Figure 60 : Experimental material laws [63]

Then, the specimens were modelled as close as possible to real the test setup. Figure 61 presents the test setup used in the experimental study [63].

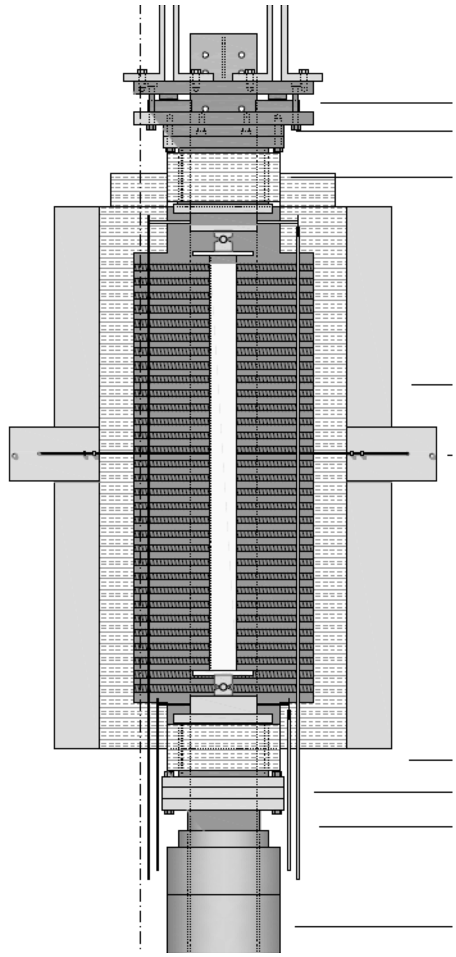

Figure 61 : Test setup from the Ph.D. of Pauli [63]

As it can be seen on Figure 61,Figure 61 : Test setup from the Ph.D. of Pauli [63] endplates were used in the experimental tests. They were therefore introduced in the finite element model. Also, Figure 61 shows that the supports are not placed directly after the end plate. The end supports were therefore placed away from the end plates. As the exact distance between the end plates and the support was not given in the PhD report, it was estimated based on the dimensions that were provided. The boundary conditions were defined as the ones used experimentally: rotation is blocked around an axis when the specimen is not subjected to bending around that same axis. Numerical simulations were performed with residual stresses and geometrical imperfections. No information was provided about the real residual stresses. Residual stresses where therefore introduce in the model according to section 2.6. As for the geometrical imperfections, they were measured during the experiment. It would, however, have been hard to model precisely the real geometrical imperfections and they were, consequently, modelled according to section 2.5. Finally, the initial load applied in the numerical model was the maximal load obtained experimentally divided by 3.5.

Table 18 shows the comparison between the maximal compression load obtained experimentally and numerically. In this table, a negative difference indicates that the numerical value is lower than the experimental value while a positive difference indicates that the numerical results is higher.

Table 18 : Comparison of experimental and numerical results

Specimen	Strain rate [%/min]	Experimental peak compression load [kN]	Numerical peak compression load [kN]	Difference [%]
S02	0.10	389	369	-5.17
S03	0.10	225	218	-3.10
S04	0.10	1124	995	-11.45
S05	0.10	845	792	-6.32
S06	0.10	376	344	-8.61
S07	0.02	434	479	10.34
S08	0.10	764	734	-3.86
S09	0.10	739	632	-14.49
S10	0.10	510	457	-10.35
S12	0.10	724	741	2.33
S13	0.10	511	477	-6.68
S14	0.10	288	268	-6.91
S15	0.10	236	218	-7.66
S16	0.10	309	322	4.14
S17	0.10	467	444	-4.84
S18	0.10	140	148	5.41
S19	0.10	996	1000	0.44
S20	0.10	1028	999	-2.86
S21	0.02	135	172	27.55
S22	0.10	162	172	6.10
			Average (abs)	7.43
			Min	0.44
			Max	27.55
			Standard deviation	5.84

Results show that the maximal loads obtained with the numerical model are quite close to the maximal loads obtained experimentally with an average difference of 7.43 %. It can also be noticed that the two most unconservative results, for specimens S07 and S21, are obtained for specimens that were experimentally loaded using a smaller strain rate (0.02 %/min instead of 0.10%/min). Those “bad results” can be explained by the fact that material laws used in the simulations were obtained with tensile tests performed using a strain rate 0.10%/min. As described in Chapter 1, the strain rate has an important effect on the results. Numerical results for which the material law was obtained at a strain rate of 0.10%/min can therefore not be compared to experimental results obtained at another strain rate. If those results are discarded, the average difference between experimental and numerical results is reduced to 6.15 % with a maximum difference of 14.5%, which is much more acceptable. The very good results obtained with the numerical simulations also confirms that the use of residual stresses in the simulations is justified.

In addition to the comparison of the peak loads, the force-displacement curves obtained experimentally and numerically were compared. Two examples of such curves are presented on Figure 62Figure 64. All other curve comparisons are presented in Appendix 1. To obtain those graphs, the load-displacement curves were extracted from the PhD of Pauli [63] and the numerical curves were then scaled and placed over the graphs to allow comparison.

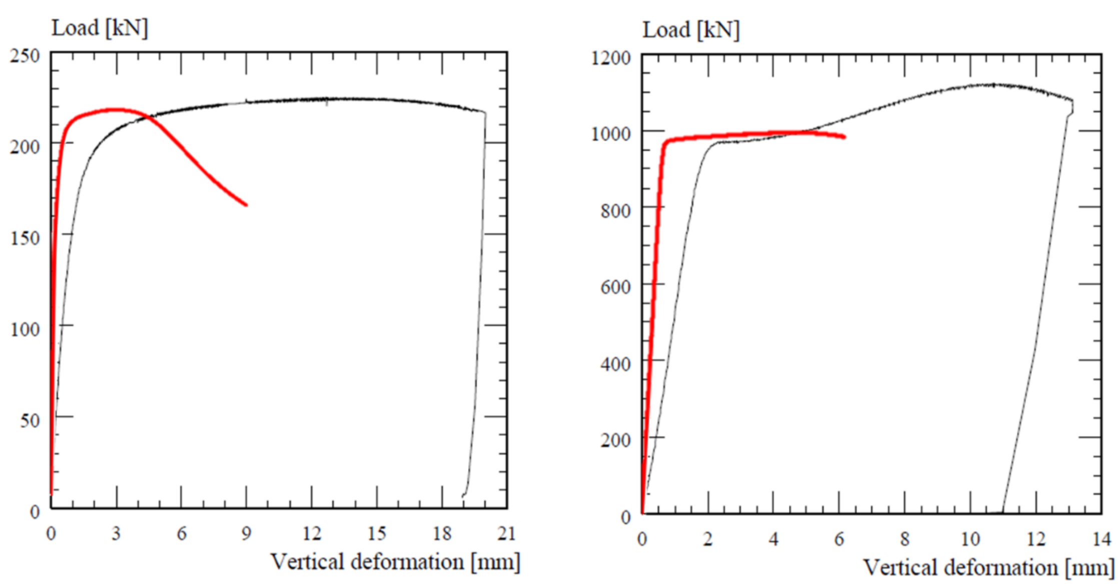

S03 – 550 °C – N+My S04 – 20 °C – N

Figure 62 : Comparison of experimental [63] and numerical load-displacement curves

For all specimens, except specimen S13, the initial slope from the numerical model is higher than the slope obtained experimentally. This can be explained by the fact that the modeled specimen is more rigid than the specimen in the experimental setup. Effectively, the setup is not entirely modeled in the finite element simulations which leads a smaller number of sources of deformability. This also results in smaller displacements at peak load in the numerical simulations. As only the peak loads are of interest in the present study, this aspect is considered acceptable.

The graphs also allow to understand why most results at 20°C are underestimated. Effectively, as it can be seen on the graph of specimen S04, strain hardening allows to reach higher peak loads. The red curve on Figure 62 shows that the peak load reached by the numerical simulation is the load attained on the plateau before strain hardening effects. As the material law used for 20°C in the numerical model, which is presented on Figure 60, is elastic perfectly plastic, no strain hardening effects are accounted for in the numerical simulation. The good correlation between the red curve and the first plateau of the experimental curves confirms the good performance of the model. To capture the effect of strain hardening with the numerical model, the material law would need to consider this effect. However, no information about the material law at larger deformations was given in the study of Pauli and it was therefore not possible to use the material law with stain hardening in the numerical model.

The deformations of the specimens obtain in the experimental and the numerical studies were also compared. Figure 63 shows the comparison for specimen S09.

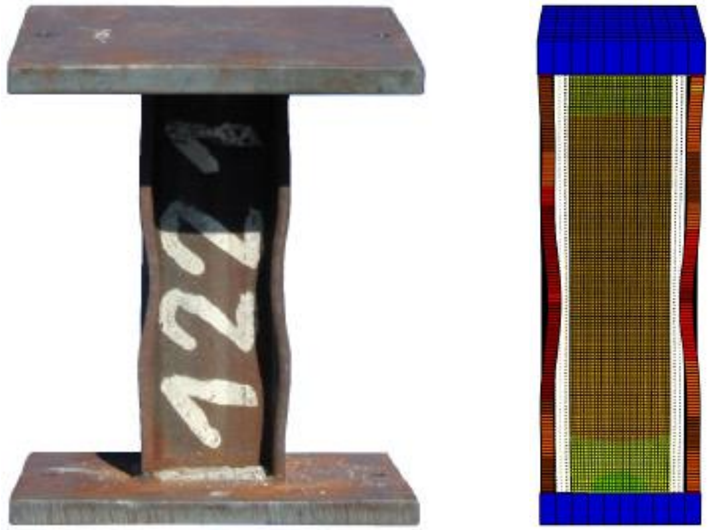

S09 – 400 °C – N+Mz

Figure 63 : Comparaison of experimental [63] and numerical deformations

The figure shows that the deformations obtained experimentally and numerically are very similar which confirms that the numerical model can reproduce the actual behaviour of steel sections. All compared deformation present strong similarities and are presented in Appendix 1.

In conclusion, the first validation allowed to confirm that the numerical model was able to reproduce experimental results. Effectively, the average difference of 7.43% with a standard deviation of 5.84% between numerical and experimental peak loads was judged acceptable. Moreover, the comparison of the numerical and experimental deformations allowed to confirm that the numerical model can reproduce the behaviour of the cross-sections.

2.7.2 Validation against the actual numerical model used in the study

Then, a validation study was conducted to see the performance of the actual model used for the numerical study. In this model, no end plates are used and the material laws considered are the ones from Eurocode 3. Multiple comparisons were made. First, the model was used exactly as described in sections 2.1 to 2.2, i.e. with residual stresses and fork boundary conditions. Then, numerical simulations were carried out without residual stresses and with the boundary conditions used during the experimental test. Results are shown on Figure 64. In this figure, the ultimate load obtained with the finite element model is divided by the ultimate load obtained experimentally. A result over 1.0 indicates that the prediction given by the numerical model is higher than the results obtain with the experimental test.

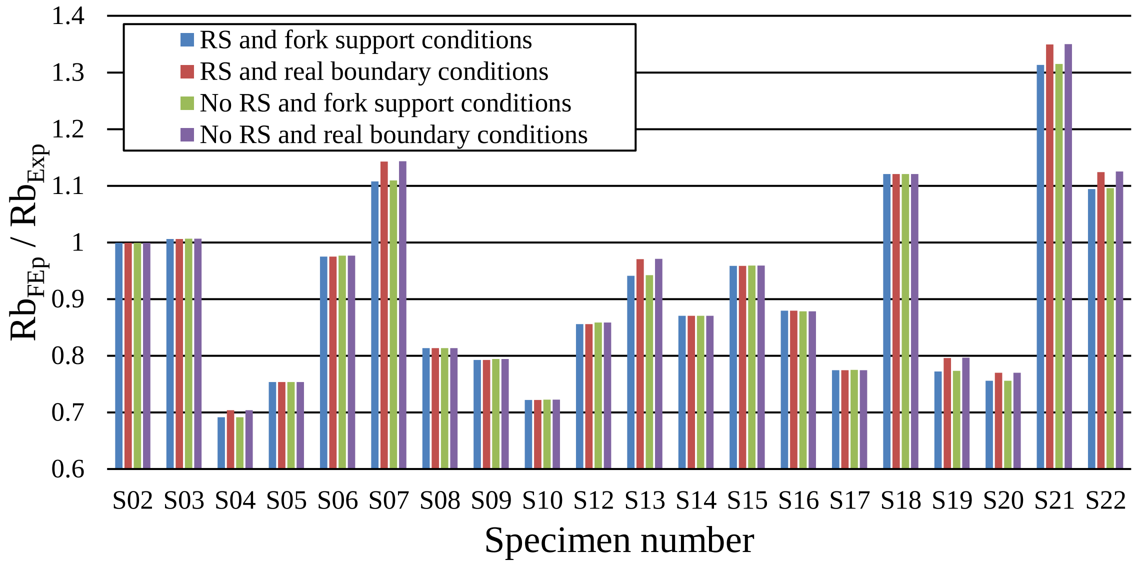

Figure 64 : Comparison between experimental results and numerical results obtained with numerical model used for the actual study

The results first show that the use of residual stresses or not in the numerical simulations has almost no impact on the ultimate load reached. Effectively, the maximal difference between results obtained with and without residual stresses is 0.15 %, which is negligible. It is however important to keep in mind that only hot-rolled sections are considered in the present validation. As residual stresses are higher in welded cross-sections, the difference should be higher in those type of cross-sections. The difference should stay however small.

As for the boundary conditions, results show that the use of fork boundary conditions or of the real boundary conditions used in the experiment has little effect on the ultimate load reached. The maximum difference observed is 3.1%. The maximal difference is observed for cases where the load applied is pure compression and where rotations are blocked around both axes in the experimental tests. The difference can therefore be explained by the fact that by providing more restraint, the cross-sections is less subjected to local buckling. A more significant difference is observed when the section is subjected to pure compression as it is the loading case that has the most influence on local buckling.

To compare the performance of the model with the experimental results, only the results obtained with residual stresses and fork support conditions (blue lines on Figure 64) are considered as they represent the model used for the numerical study and as it has been demonstrated that the difference with results obtained without residual stresses and with the real boundary conditions are very small. Table 19 presents the maximum, minimum and average difference between experimental results and finite element results.

Table 19 : Differences between experimental results and finite element results

Average difference	Minimal difference	Maximal difference	Standard deviation
15.4 %	0.1 %	31.3 %	10.0%

Results show that there is a large variability in the performance of the model. The cases for which the differences between experimental and numerical results are the higher are the ones at ambient temperature (S04, S05, S10, S12, S16 and S20). In all cases, the resistance reached with the numerical model is lower than the one obtained experimentally. This can be explained by the fact that in the numerical model, an elastic-perfectly plastic material law without strain hardening is used, which neglects the gain of resistance from strain hardening of the steel. Moreover, the material law used in the numerical model considers a yield limit at 355 MPa. By looking at the experimental material law on Figure 60, it can be noticed that the yield limit is much higher which explains the difference between the results.

For other temperatures, there is again a large variability in the differences between experimental and numerical results. This can be again explained by the material law used in the model. Figure 60 shows the material laws proposed by Eurocode 3 and the material laws determined experimentally. It is possible to see that the material law proposed by Eurocode 3 do not have the exact same shape as the material law for experimental study and do not reach the same maximal stress. The difference between laws can therefore explain the difference in the results.

Although the results show a variability between experimental and numerical results, the model is still considered accurate. Effectively, conducting experimental study on steel sections subjected to fire is very hard and results are not always precise. Results depend, for example, on the heat distribution in the section and on the strain rate. Strain rate can particularly have an impact on the results. For example, specimen S21 and S22 were both loaded with pure compression at 700°C. The first one was loaded with a strain rate of 0.02%/min while the second one was loaded with a strain rate of 0.10%/min. The ultimate resistance of the first one was 135 kN while the ultimate resistance of the second one was 162 kN, which is a 20 % difference. As experimental results can also have a large variability, it is considered adequate to use the numerical model for the present study.

Chapter 3 : Numerical parametric studies

The intent of this chapter is to present parameters considered in the numerical parametric studies. By considering all those parameters a total of 12 960 simulations were conducted.

3.1 Types of analysis

In the numerical parametric studies, 2 types of analysis are performed: L.B.A. and G.M.N.I.A..

Linear Buckling Analysis (L.B.A.) are performed to obtain the critical multiplier (R_{cr}). The critical multiplier is the value of the first eigenvalue which correspond to the first buckling mode. As only the local behaviour is studied, the length of the members is chosen to ensure that no global buckling occurs as explained before. Figure 65 presents an example of a local buckling mode for a cross-section subjected to pure compression.

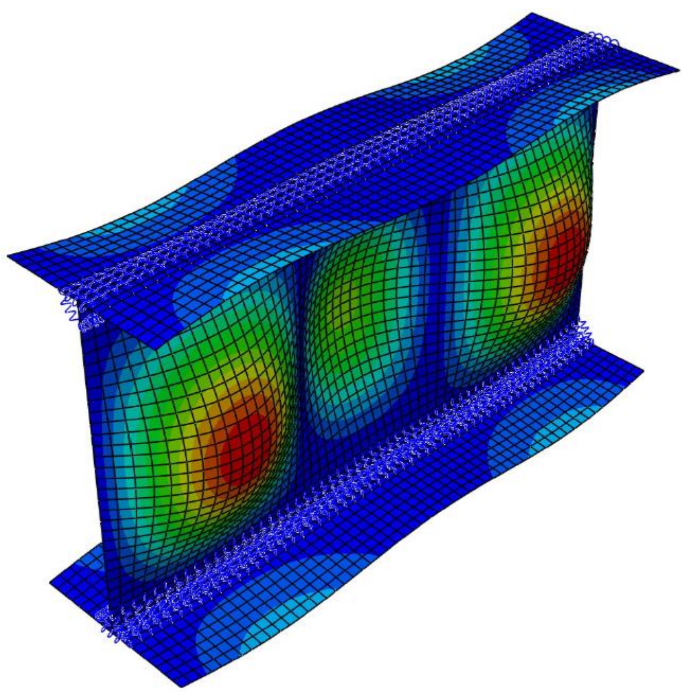

Figure 65 : First local buckling mode of a cross-section subjected to pure compression

Geometrically and Materially Non-linear with Imperfections Analysis (G.M.N.I.A.) are performed to obtain the ultimate capacity of the cross-sections. The ultimate capacity is the peak load obtained during the analysis. For the peak load to be considered accurate, the criterion presented on Figure 66 must be verified for the last positive increment (ΔR_1) and for the first negative increment (ΔR_2). On the figure, R_b is the maximum load multiplier. A tolerance of 0.2% is adopted for the present parametric study.

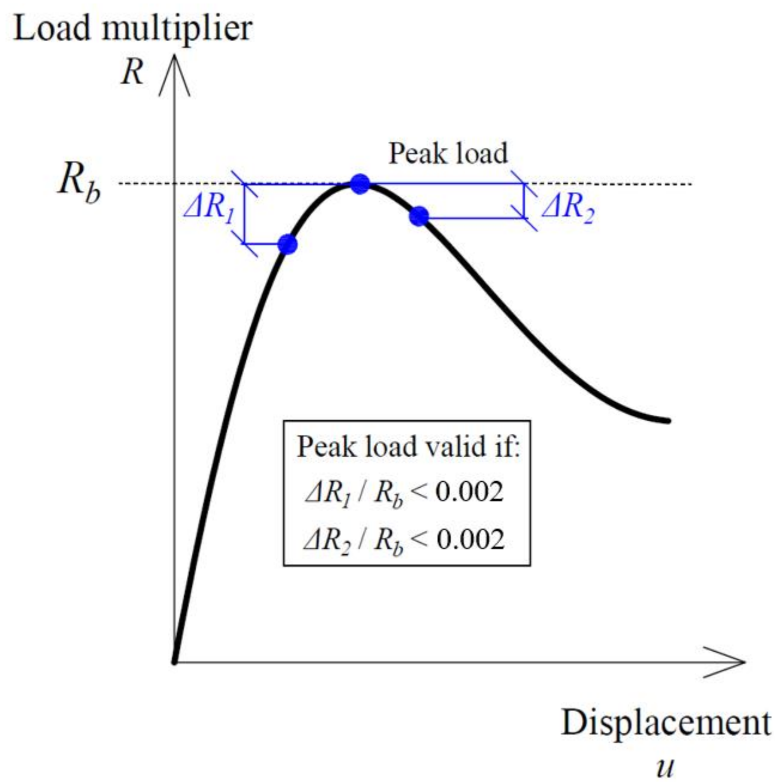

Figure 66 : Criterion for peak load [3]

3.2 Choice of cross-sections

Multiple hot-rolled and welded cross-sections were chosen to cover a wide range of slenderness. The chosen sections are presented below. The length of each sections is chosen short enough to avoid global instabilities during simulations. The length is set to three times the half-period length used to incorporate geometrical imperfections which is the average between the web height and the flange width.

3.2.1 Hot-rolled sections

A total of 13 hot-rolled sections are considered in the parametric study. The geometrical properties of the chosen sections are presented in Table 20. The selection of sections contains both beam shapes (IPE) and column shapes (HEA).

Table 20 : Choice of hot-rolled cross-sections for the parametric study

Designation	Flange width (b)	Height (h)	Flange thickness (t_f)	Web thicknesss (t_w)	Radius (r)
(-)	(mm)	(mm)	(mm)	(mm)	(mm)
IPE120	64	120	6.3	4.4	7
IPE220	110	220	9.2	5.9	12
IPE270	135	270	10.2	6.6	15
IPE360	170	360	12.7	8.0	18
IPE400	180	400	13.5	8.6	21
IPE600	220	600	19.0	12.0	24
HEA120	120	114	8.0	5.0	12
HEA240	240	230	12.0	7.5	21
HEA300	300	290	14.0	8.5	27
HEA400	300	390	19.0	11.0	27
HEA500	300	490	23.0	12.0	27
HEA600	300	590	24.0	13.0	27
HEA1000	300	990	31.0	16.5	30

3.2.2 Welded Sections

A total of 14 welded sections are considered for the parametric study. The geometrical properties of the chosen sections are presented in Table 21. The selection of sections contains both beam and column shapes.

Table 21 : Choice of welded cross-sections for the parametric study

Designation	Flange width (b)	Height (h)	Flange thickness (t_f)	Web thicknesss (t_w)	Flange radius (r)
(-)	(mm)	(mm)	(mm)	(mm)	(mm)
IPE220	110	220	9.2	5.9	0
IPE360	170	360	12.7	8	0
IPE600	220	600	19	12	0
WWF700x245	400	700	30	11	0
WWF900x347	500	900	35	11	0
WWF1200x302	400	1200	25	16	0
WWF1200x302-	400	1200	17.5	11.2	0
WWF500x651	500	500	60	60	0
WWF550x503	550	550	50	20	0
WWF650x499	650	650	40	20	0
WWF600x369	600	600	30	20	0
WWF450x177	450	450	20	11	0
WWF500x197	500	500	20	11	0
WWF500x197-	500	500	14	7.7	0

Some IPE shapes, which are normally hot-rolled sections, have been included in the welded sections' selection. These have the same plate dimensions has typical IPE sections, however, as they are considered as welded sections, no radius are considered. This choice will allow the comparison of the same sections under the effect of different residual stresses specific to the manufacturing processes. It will also allow to study the influence of the radius. Sections denoted by "-" are sections for which the thicknesses of the web and flange has been reduced to obtain more slender sections.

3.3 Load cases

Both simple and combined load cases are considered in the parametric study. First, simulations are carried out for sections under pure compression (N), pure major axis bending (M_y) and pure minor axis bending (M_z). For those simulations, the initial load applied to the cross-section is the ultimate capacity predicted by Eurocode 3 divided by 3,5 which allows an easy convergence.

Then, simulations are conducted with multiple load case combinations. Load combinations are defined by 2 parameters: *n*, which is the quantity of axial force applied and θ, which represents the degree of biaxial bending. The parameter *n* is defined as the ratio between the applied load and the plastic capacity of the section. The parameter θ links the quantity of both types of bending, m_y and m_z by the following relationship:

$$\tan(\theta) = m_z / m_y \qquad (138)$$

where m_y and m_z are defined as the ratio between the applied load and the plastic capacity. Figure 67 represents different proportions between biaxial bending and axial compression. The figure also shows basic interaction formulas.

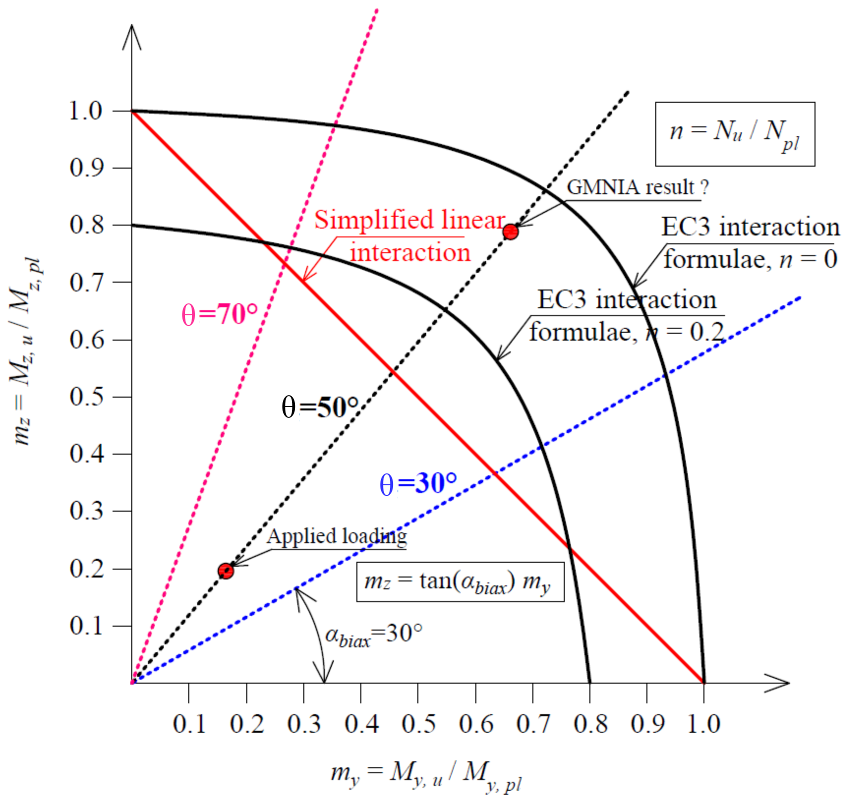

Figure 67 : Interaction between biaxial bending and axial compression [3]

Doted lines represent different proportions of biaxial bending. If θ = 0°, there is only major axis bending. On the contrary, if θ = 90°, there is only minor axis bending. Any value in between indicates that both kind of bending are presents. Then, for any value of θ chosen, the doted lines represent the various values of *n*, quantity of axial force, that can be considered. If *n* = 0 then the section is only under bending loads. On the contrary, if *n* = 1, the sections is only subjected to compression.

The simplified linear interaction represented on the figure is described by the following equations.

$$n + m_y + m_z \leq 1 \tag{139}$$

$$\frac{N_u}{N_{pl}} + \frac{M_{y,u}}{M_{y,pl}} + \frac{M_{z,u}}{M_{z,pl}} \leq 1 \tag{140}$$

After choosing a value of n, the quantity of axial load, the value of m_y and m_z can be calculated with the chosen θ and Equations (138) and (139) presented previously. Using the plastic capacities of the section, the ultimate loads can then be calculated. Those ultimate loads are used to determine the initial load applied in the simulations. Initial loads are obtained by dividing the ultimate loads by 3,5 which allows an easy converge. Those initial loads are used to calculate the needed multipliers which are obtained by increasing proportionally all loads.

The different values of n and θ chosen for the study are presented in Table 22. For all chosen values, all possible combinations are tested. The choices made allow to sweep the entire graph.

Table 22 : Levels of axial force and of biaxial bending applied

n	0; 0.40; 0.80
θ	0; 30; 50; 70; 90

Interaction formulas from EC3, which represent the approached plastic capacity of a section under combined loading, are also represented on the figure. Those curves show that the simplified interaction formula used to determine the initial applied load is conservative when there is biaxial bending. Therefore, the expected G.M.N.I.A. result is higher than the simplified interaction curve as shown on the figure.

As for the application of the combined loads, many sequences can be considered. Loads can be applied at different times and increase in various way. Studies have been conducted to quantify the impact of the sequence on the peak load [45]. The results of these studies indicate that no sequence is perfect. However, it was recommended to apply all forces at the same time and to then increase all loads proportionally. This method procures a greater adequacy with numerical tools used during the O.I.C. process and provide results that are on the safe side.

3.4 Temperatures

In the present study, the temperature of the steel is considered uniform throughout the cross-sections. Five different temperature are studied: 20°C, 350°C, 450°C, 550°C and 700°C. Figure 68 present the impact of temperature on the material law.

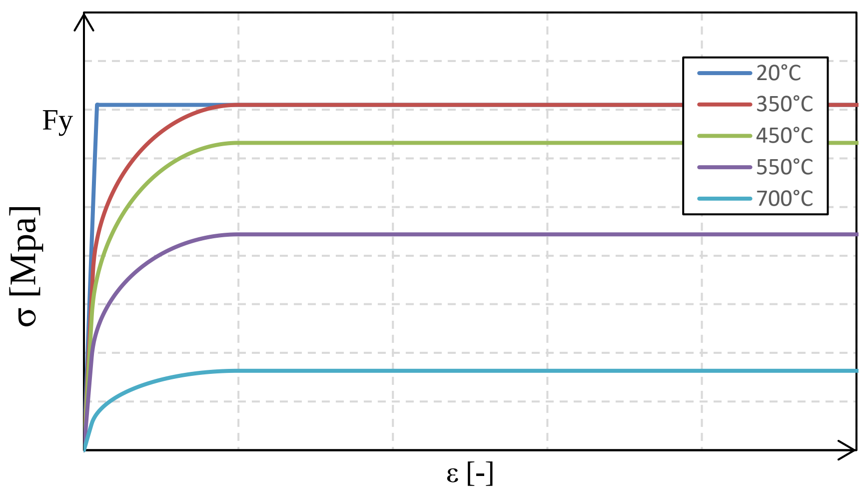

Figure 68 : Material law for different temperatures

As explained before, as the temperature increases, both the yield limits and the elasticity modulus decrease. Therefore, the increase in temperature diminishes the ultimate capacity of the cross section first by limiting the stresses that can be reached in the cross section and second by increasing the slenderness of the cross section which is then more prone to local buckling.

Studying various temperature allows to compare the behaviour of the cross section at ambient and elevated temperature. It also allows to quantify the effect of various increases in temperature on the cross-section’s behaviour and resistance.

The high temperatures between 350°C and 700°C were chosen as they represent the temperatures at which a real building is expected to stand in a real fire situation. Effectively, in a real fire, the temperature increases rapidly and temperature below 350°C are therefore not expected for long period of time. On the other, temperatures over 700°C are reached after a certain period of time after which buildings are not expected to stand.

3.5 Yield stress

Three different values of F_y are used to conduct the simulations: 355 MPa, 460 MPa et 690 MPa. The different values allow to reach different level of stresses in the cross-sections. It also allows to study the behaviour of the cross-sections at different level of slenderness as sections become more slender as the yield limit increases. Therefore, they become more prone to local buckling instabilities which affect the ultimate resistance of the section.

Chapter 4 : Identification of parameters governing the resistance

4.1 Introduction

As explained in the previous chapter, many parameters such as different geometries, load cases, temperatures and yield limits were chosen to perform a large number of numerical simulations. The results of those simulations are used to determine the parameter that influences the resistance and that will be needed to make O.I.C. proposals. The O.I.C. format allows to take into consideration the yield limit by the means of the plastic multiplier (R_{pl}) and to consider the buckling behaviour through the critical multiplier (R_{cr}). The influence of the temperature is also considered in both these multipliers as the yield limit and Young's modulus are both reduced by temperature. However, geometrical and material imperfections are not considered by either of these factors.

Figure 69 shows the results obtained for welded sections subjected to compression.

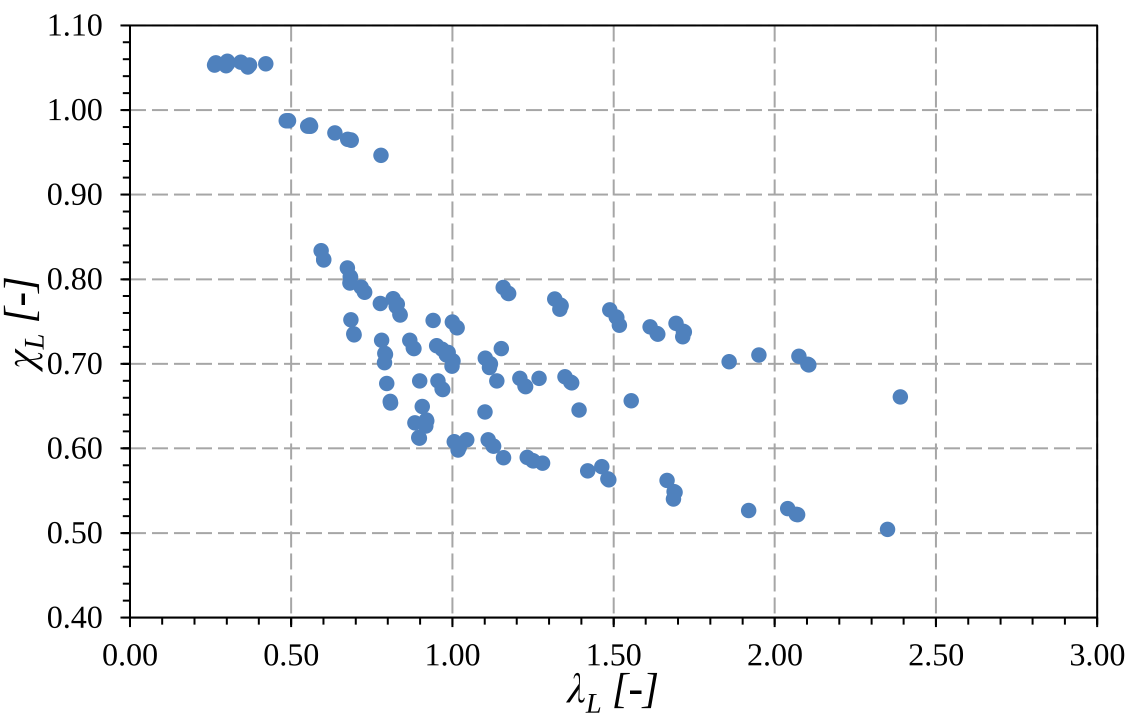

Figure 69 : Results for welded sections subjected to compression

This figure shows that the results are widely spread even though many parameters are already accounted for. It would be possible to use only one buckling curve placed underneath all the points to predict the resistance. It would however lead, in some cases, to very conservative results. To avoid this issue, points need to be group and associated to a series of buckling curves. The goal of this section is therefore to determine which parameters influence the resistance and can be used to efficiently group the points.

4.2 Influence of temperature

This study focuses on the resistance of steel at high temperature. Therefore, the influence of temperature on the results is first studied. On Figure 70 and on Figure 71, results are plotted in O.I.C. format with different series for the various temperature considered in the simulations. Only results obtained for sections under pure compression are presented on the graphs so that figures are not overloaded with data. The same tendencies were however noticed for the other load cases.

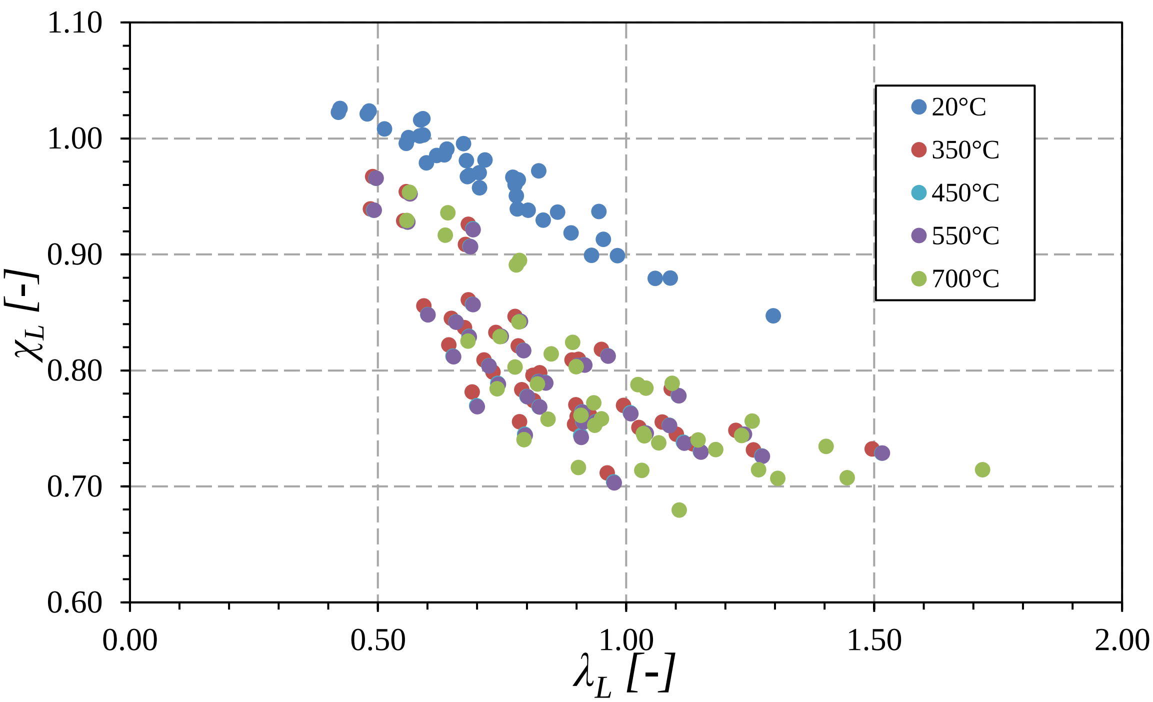

Figure 70 : Influence of the temperature on the results for hot-rolled sections subjected to compression

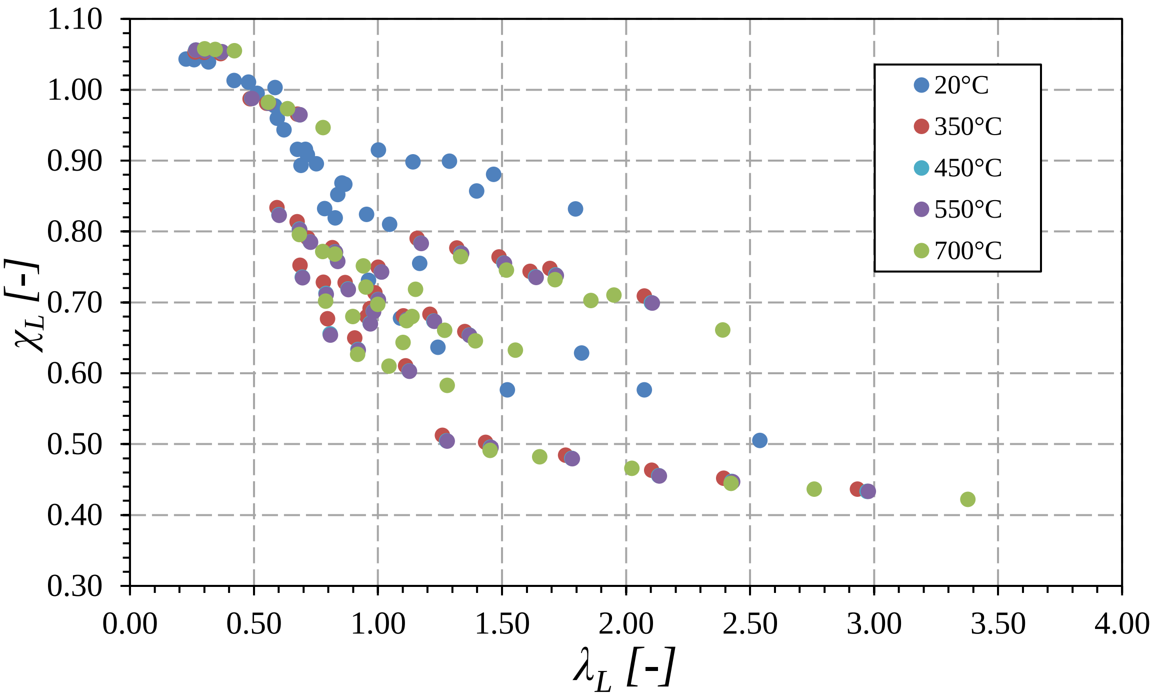

Figure 71 : Influence of the temperature on the results for welded sections subjected to compression

On both graphs, it is possible to see that the tendencies are very different at room temperature and at high temperatures even thought the lost in resistance and the lost in rigidity is considered by the non-dimensional parameters. This can be explained by the fact that the material law at high temperatures is not linear, therefore inducing a different behaviour. Accordingly, different proposals must be made for cold and high temperatures. However, for all high temperatures, even though the increase in temperature does have an impact on the local slenderness (λ_L), it does not affect the tendencies. Effectively, the results obtained at the different high temperatures seam to follow the same buckling curves. As the present study focuses on the response at high temperatures, results obtained at room temperature will not be considered when searching for the leading parameter and when formulating the design proposals.

4.3 Influence of F_y

As mentioned previously, the influence of F_y is already considered through the plastic multiplier (R_{pl}). However, further investigation was made to ensure no further consideration was needed. Figure 72 and Figure 73 show the influence of the yield limit on the results. As for the influence of the temperature, only results for sections under compression are shown in those figures so that the tendencies are easier to identify.

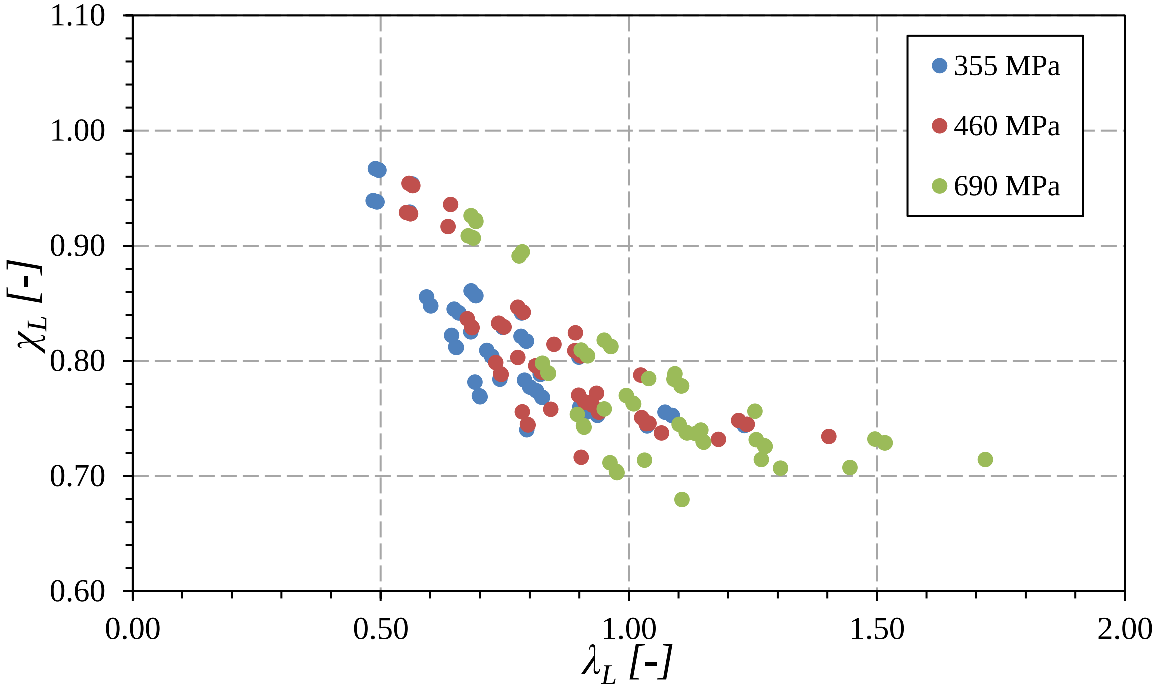

Figure 72 : Influence of F_y on the results for hot-rolled sections subjected to compression

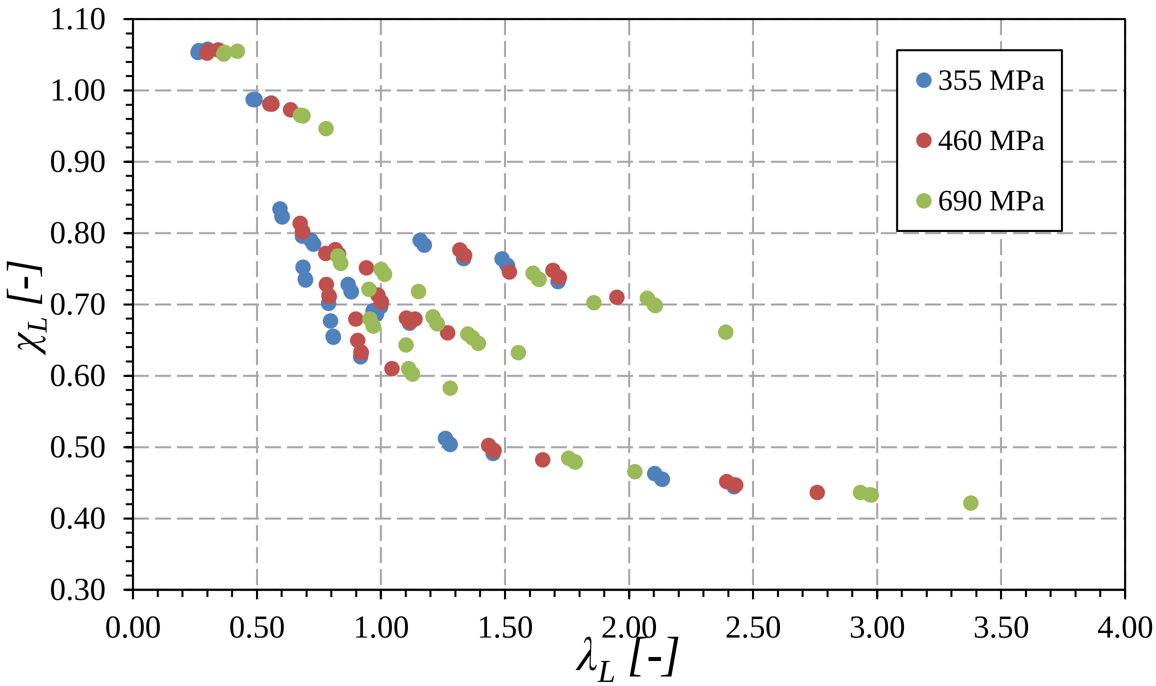

Figure 73 : Influence of F_y on the results for welded sections subjected to compression

Both graphs show that the increase in yield limit increases the local slenderness (λ_L). However, as for the different temperatures, no significant tendencies can be observed which indicates that the yield limit is considered adequately by the plastic multiplier (R_{pl}) and that it does not need to be accounted for again.

4.4 Geometrical parameters

Both the temperature and the yield limit have been studied in the previous sections. Based on the results, those two parameters have proven to be already considered adequately by the O.I.C. approach. Therefore, geometrical parameters will be studied in this section to find the one that influences the most the resistance of the cross-sections. All the studied parameters are formulated based on the sections' dimensions defined on Figure 74.

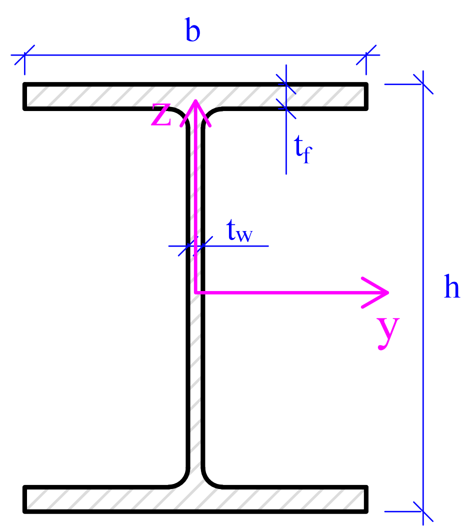

Figure 74 : Definition of the sections' dimensions

As the behaviour of hot-rolled and welded sections is different, parameters are studied separately for both fabrication processes. In order to have a simple design proposal, one of the main objectives while searching for leading parameters was to find one that is suitable for all load cases. The following sections summarize the results of the investigations for both hot-rolled and welded sections.

4.4.1 Welded sections

Table 24 presents the results of the investigations made regarding the leading parameter for welded cross-sections. In this table, all parameters studied are presented as well as all different load cases considered. The value of *n* indicates the importance of the compressive force. A value of 1 indicates pure compression. The value of θ indicates the degree of biaxiality. A value of 0 indicates pure majors-axis bending while a value of 90 indicates pure minor-axis bending. The check marks (✓) indicate that the studied parameter seams suitable for the considered while the cross marks (✕) indicate that it is not. For each parameter and each load case, a graph must be plotted in the O.I.C. format to determine if the parameter is suitable or not. Figure 75 shows an example of a graph plotted for welded sections subjected to compression.

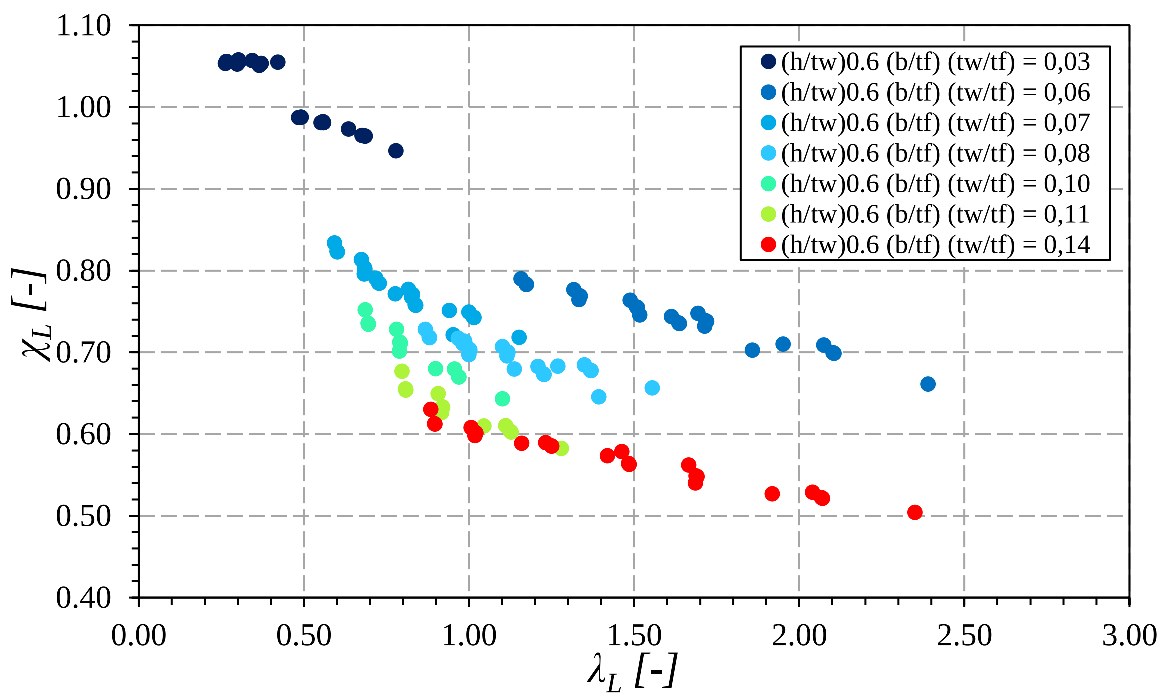

Figure 75 : Example of a good leading parameter for welded sections subjected to compression

In this graph, the points are separated in different series based on the value of the studied parameter. A gradation of colours is used to efficiently see the tendencies: the dark blue points are used for the lowest value of the studied parameter while the red points are used for the highest value of the studied parameter. A parameter is considered suitable when it is possible to observe a trend on the graph. For example, on Figure 75, the blue points are at the top of the graph and the red points are at the bottom of the graph with points in between organised logically. It is important to note that the observed trend does not need to be as good as the one showed on Figure 75 for a parameter do be judged acceptable.

Figure 76 shows an example of a leading parameter which is not suitable for the studied load case. Effectively, on this graph, it is possible to see that no clear trend can be identify as the colour are not organised. It would therefore not be possible to use this parameter to define a series of buckling curves.

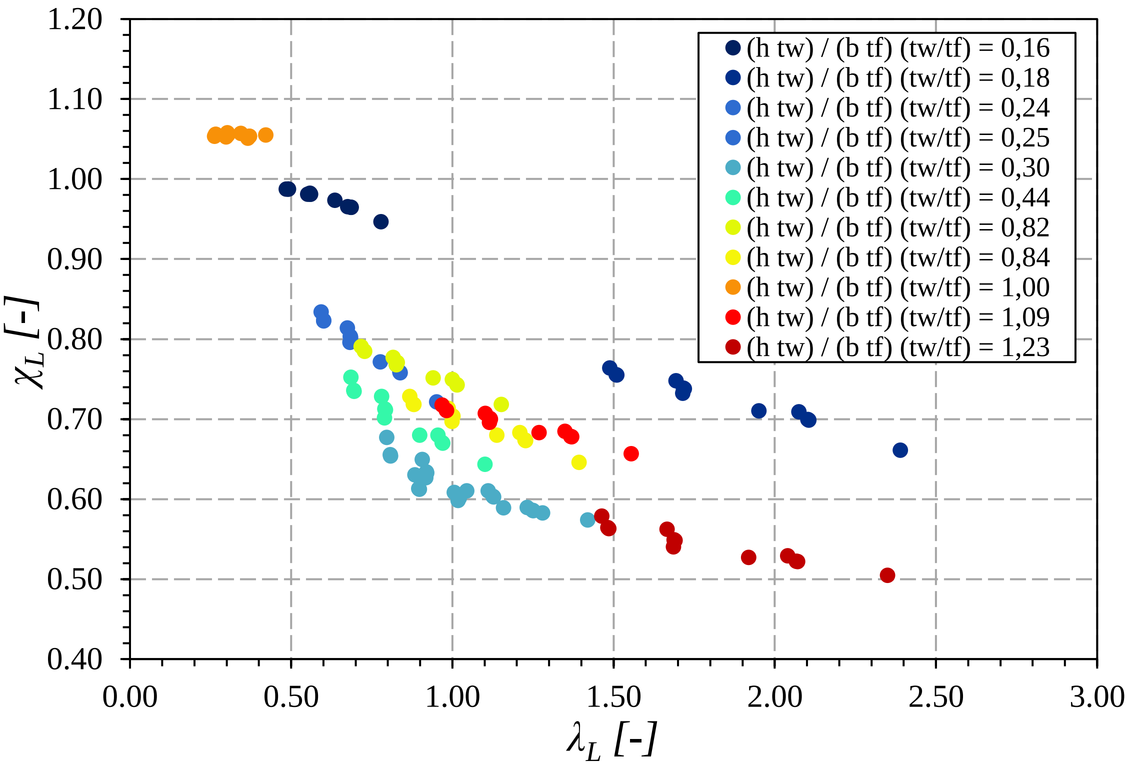

Figure 76 : Example of a bad leading parameter for welded sections subjected to compression

Table 23 : Leading parameters tested for welded sections

Load combination	N	M_y	M_z	$M_y + M_z$			$N + M_y + M_z$									
n	1	0	0	0			≤ 0.6					> 0.6				
θ	-	0	90	30	50	70	0	30	50	70	90	0	30	50	70	90
$\frac{k_{\sigma,w}}{k_{\sigma,f}} \cdot \left(\frac{b_f}{t_f}\right)^2 \cdot \left(\frac{t_w}{h_w}\right)^2$	✗	✗	✗	✗	✗	✓	✗	✗	✗	✗	✗	✗	✗	✗	✗	✗
$\frac{h}{b}$	✗	✗	✗	✗	✓	✗	✗	✗	✓	✗	✗	✗	✗	✗	✗	✗
$\left(\frac{h \cdot t_w}{b \cdot t_f}\right) \cdot \left(\frac{t_w}{t_f}\right)$	✗	✗	✗	✗	✗	✗	✗	✗	✗	✗	✗	✗	✗	✗	✗	✗
$\left(\frac{h}{t_w}\right) \cdot \left(\frac{b}{t_f}\right) \cdot \left(\frac{t_w}{t_f}\right)$	✓	✓	✗	✓	✓	✓	✓	✓	✓	✓	✓	✓	✓	✓	✓	✓
$\left(\frac{h}{t_w}\right)^3 \cdot \left(\frac{b}{t_f}\right) \cdot \left(\frac{t_w}{t_f}\right)^2$	✓	✓	✗	✓	✗	✗	✓	✓	✓	✗	✗	✗	✗	✗	✗	✗
$\left(\frac{h}{t_w}\right)^2 \cdot \left(\frac{b}{t_f}\right) \cdot \left(\frac{t_w}{t_f}\right)$	✓	✓	✗	✓	✓	✗	✓	✓	✓	✗	✗	✗	✗	✗	✗	✗
$\left(\frac{t_w}{h}\right)^2 \cdot \left(\frac{b}{t_f}\right)^3 \cdot \left(\frac{t_w}{t_f}\right)$	✗	✗	✗	✗	✓	✗	✗	✗	✗	✗	✗	✗	✗	✗	✗	✗
$\left(\frac{t_w}{h}\right)^2 \cdot \left(\frac{b}{t_f}\right)^2 \cdot \left(\frac{t_w}{t_f}\right)$	✗	✗	✗	✗	✓	✓	✗	✗	✓	✗	✗	✗	✗	✗	✗	✗
$\left(\frac{b}{h}\right) \cdot \left(\frac{t_w}{t_f}\right)$	✗	✗	✓	✗	✗	✓	✗	✗	✗	✗	✗	✗	✗	✗	✗	✗

Based on the results, the parameter η is the most suitable even thought it is not perfect for all load cases.

$$\eta = \left(\frac{h}{t_w}\right) \cdot \left(\frac{b}{t_f}\right) \cdot \left(\frac{t_w}{t_f}\right) \qquad (141)$$

This parameter combines the effect of (a) the slenderness of the web through h/t_w, (b) the slenderness of the flanges through b/t_f and (c) the ratio of the plates thickness t_w/t_f which indicates the rotational restraint provided by one plate to the other . To get the best parameter as possible, various exponents were tested on h/t_w [3]. After many tests, the parameter μ was chosen as the final leading parameter for welded sections.

$$\mu = \left(\frac{h}{t_w}\right)^{0.6} \cdot \left(\frac{b}{t_f}\right) \cdot \left(\frac{t_w}{t_f}\right) \qquad (142)$$

This parameter will be used in the design proposal for welded sections presented in the next chapter.

4.4.2 Hot-rolled sections

Table 24 presents the results of the investigations made regarding the leading parameter for hot-rolled cross-sections. In this table, all parameters studied are presented as well as all different load cases considered. The check marks (✓) indicate that the studied parameter seams suitable for the considered while the cross marks (✕) indicate that it is not. The value of n indicates the importance of the compressive force. A value of 1 indicates pure compression. The value of θ indicates the degree of biaxiality. A value of 0 indicates pure majors-axis bending while a value of 90 indicates pure minor-axis bending.

Table 24 : Leading parameters tested for hot-rolled sections

Load combination	N	M_y	M_z	$M_y + M_z$			$N + M_y + M_z$									
n	1	0	0	0			≤ 0.6					> 0.6				
θ	-	0	90	30	50	70	0	30	50	70	90	0	30	50	70	90
$\frac{k_{\sigma,w}}{k_{\sigma,f}} \cdot \left(\frac{b_f}{t_f}\right)^2 \cdot \left(\frac{t_w}{h_w}\right)^2$	✗	✗	✗	✓	✓	✓	✗	✗	✗	✓	✗	✗	✗	✗	✗	✗
$\frac{h}{b}$	✗	✗	✓	✓	✓	✓	✗	✗	✓	✓	✓	✗	✗	✗	✗	✗
$\left(\frac{h \cdot t_w}{b \cdot t_f}\right) \cdot \left(\frac{t_w}{t_f}\right)$	✗	✗	✓	✗	✗	✗	✗	✗	✗	✗	✗	✗	✗	✗	✗	✗
$\left(\frac{h}{t_w}\right) \cdot \left(\frac{b}{t_f}\right) \cdot \left(\frac{t_w}{t_f}\right)$	✓	✓	✗	✗	✗	✗	✓	✓	✗	✗	✗	✓	✓	✓	✗	✗
$\left(\frac{h}{t_w}\right)^3 \cdot \left(\frac{b}{t_f}\right) \cdot \left(\frac{t_w}{t_f}\right)^2$	✓	✗	✗	✓	✓	✓	✓	✓	✓	✓	✓	✓	✓	✓	✓	✗
$\left(\frac{h}{t_w}\right)^2 \cdot \left(\frac{b}{t_f}\right) \cdot \left(\frac{t_w}{t_f}\right)$	✓	✗	✗	✓	✓	✓	✓	✓	✓	✓	✓	✓	✓	✓	✓	✓
$\left(\frac{t_w}{h}\right)^2 \cdot \left(\frac{b}{t_f}\right)^3 \cdot \left(\frac{t_w}{t_f}\right)$	✗	✗	✓	✓	✗	✓	✗	✗	✗	✗	✗	✗	✗	✗	✗	✗
$\left(\frac{t_w}{h}\right)^2 \cdot \left(\frac{b}{t_f}\right)^2 \cdot \left(\frac{t_w}{t_f}\right)$	✗	✗	✓	✓	✓	✓	✗	✗	✗	✗	✗	✗	✗	✗	✗	✗

As shown in the table, no parameter is perfectly suitable for all load cases. The parameter γ was however chosen for the design proposal of hot-rolled sections as it is the one which is the most suitable. Moreover, this parameter has proven to be suitable for hot-rolled sections at room temperature.

$$\gamma = \left(\frac{h}{t_w}\right)^2 \cdot \left(\frac{b}{t_f}\right) \cdot \left(\frac{t_w}{t_f}\right) \qquad (143)$$

This parameter is very similar to the one chosen for welded sections as it also combines the effect of (a) the slenderness of the web through h/t_w, (b) the slenderness of the flanges through b/t_f and (c) the ratio of the plates thickness t_w/t_f which indicates the rotational restraint provided by one plate to the other. The only difference between the two parameters is the exponent on h/t_w. Even if both parameters are similar, it was not possible to find a parameter suitable for both section types. Effectively, the differences in residual stresses, in generally used cross-section shapes and in plate thicknesses between both section types lead to different behaviour.

Chapter 5 : Proposed design curves

5.1 Background of the proposed approach

As explained in the introduction, the Overall Interaction Concept (O.I.C.) is based on the concept of buckling curves. This concept allows to consider both the influence of the resistance and the stability. As shown previously in Figure 2, the buckling curves are expressed in the form $\chi = f°(\lambda)$, where χ is a reduction factor while λ is the slenderness. The equations used to calculate both parameters in the case of local resistance are respectively presented in Equation (2) and Equation (1). As those parameters are non-dimensional, they can be used to compare sections with various geometries and material properties.

The formulation used for the O.I.C. proposals is based on the Ayrton-Perry approach which is presented in the following equations:

$$\chi = \frac{1}{\phi + \sqrt{\phi^2 - \overline{\lambda}^2}} \qquad (144)$$

$$\phi = 1 + \overline{\lambda}^2 + \alpha \cdot \left(\overline{\lambda} - 0.2\right) \qquad (145)$$

In this formulation, α is used to consider the influence of imperfections.

The modified version of the Ayrton-Perry formulas used in the O.I.C. approach at the cross-section level is as follows:

$$\chi_L = \frac{1}{\phi + \sqrt{\phi^2 - {\lambda_L}^{\delta}}} \qquad (146)$$

$$\phi = 0.5 \cdot \left(1 + \alpha_L \cdot \left(\lambda_L - \lambda_0\right) + {\lambda_L}^{\delta}\right) \qquad (147)$$

In this formulation, α_L accounts for imperfections and δ considers post-buckling effects. Both parameters depend on the leading parameter identified.

For very small slenderness, χ_L obtained numerically can be over 1.0 due to strain hardening. However, in the proposal, the value of χ_L is limited to 1.0. The parameter λ_0 in Equations (146) and (147) corresponds to the end of the plateau.

One of the main goals while formulating the O.I.C. proposals is to keep the continuity between the various load cases. To do so, the same leading parameter must be identified for all load cases. In this respect, a 3-dimensional loading space is defined to encompass all possible load combinations. In this loading space, the amount of compression and the amount of bi-axial bending in the load combination are defined by two angles, ϕ and θ. Those angles are shown on Figure 77.

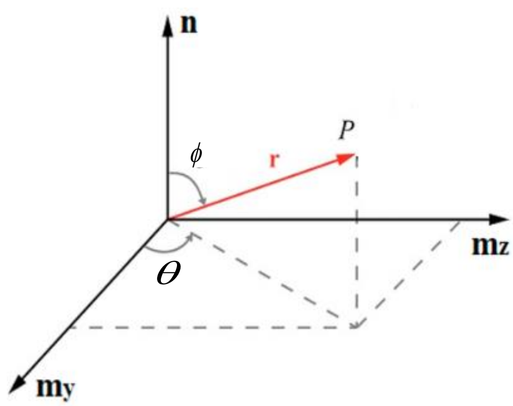

Figure 77 : Angles used to define the loading

Both angles can take any value between 0° and 90°. If ϕ = 0°, the loading is pure compression and if ϕ = 90°, the loading is pure bending, either about one or both axes. As for the bi-axial bending angle, if θ = 0°, there is only major-axis bending while if θ = 90°, there is only minor-axis bending. Any value in between those extreme values for either of these angles indicates a combined load case. For any load combination, both angles can be calculated based on the relationship between n, m_y and m_z also identified on Figure 77. Those three variables are calculated with the following equations.

$$n = \frac{N_u}{N_{pl}} \tag{148}$$

$$m_y = \frac{M_{y,u}}{M_{y,pl}} \tag{149}$$

$$m_z = \frac{M_{z,u}}{M_{z,pl}} \tag{150}$$

In theses previous equations, the ultimate loads are used. However, when starting the O.I.C. process, the ultimate load are not known yet. As the O.I.C. uses the principle of load multiplier to get the ultimate resistance and as this multiplier is the same for all types of load, the initial loads can be used to calculate the variables n, m_y and m_z that are used to calculate the two angles. Effectively, ultimately the initial loads will all be multiplied by the same multiplier to obtain the ultimate resistance. Therefore, the increase in loading is proportional and the use of the initial loads in the calculation does not affect the relationship between all three variables. The formulas used to calculate angles are as follows:

$$m_z = m_y \cdot \tan(\theta) \tag{151}$$

$$m_y = n \cdot \tan(\phi) \cdot \cos(\theta) \tag{152}$$

$$m_z = n \cdot \tan(\phi) \cdot \sin(\theta) \tag{153}$$

All possible combinations of these two angles create the 3-dimensional loading space used in the O.I.C. design proposal. The loading space is shown on Figure 78.

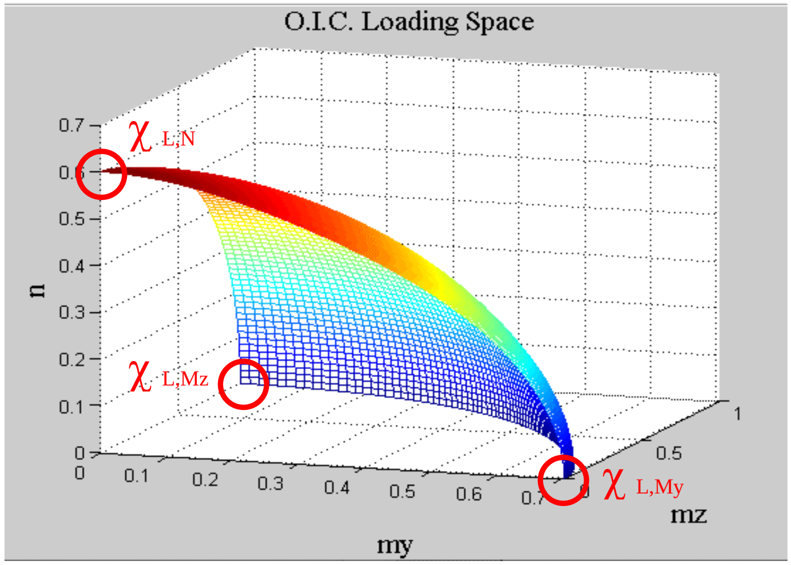

Figure 78 : 3-dimensional loading space

In this loading space, three extreme cases can be identified and are circled on Figure 78. Those cases are the simple load cases. Therefore, the first step while formulating an O.I.C. proposal is to determine the buckling curves for all three simple load cases. Theses buckling curves allow to obtain the local reduction factors for all three simple load case and are defined as follow.

$$\chi_{L,N} = f\left(\lambda_{L,N}\right) \quad (154)$$

$$\chi_{L,My} = f\left(\lambda_{L,My}\right) \quad (155)$$

$$\chi_{L,Mz} = f\left(\lambda_{L,Mz}\right) \quad (156)$$

The buckling curves are defined using the modified Ayrton-Perry formulae presented previously in Equations (146) and (147) and using the chosen leading parameter. Once all three reduction factors have been determined, they can be combined with the following equation to obtain the reduction factor for the combined load case studied.

$$\chi_L = \left[\left(\chi_{L,N}\cdot\cos(\phi)^a\right)^n + \left(\chi_{L,My}\cdot\sin(\phi)^b\cdot\cos(\theta)^c\right)^n + \left(\chi_{L,Mz}\cdot\sin(\phi)^d\cdot\sin(\theta)^e\right)^n\right]^{(1/n)} \quad (157)$$

In this equation, the different exponents are determined during the formulation process during which all the results from the numerical study are considered. The equation is built so that, when calculating the ultimate reduction factor, only the reduction factors associated to the loading are considered. For example, if the load case $N + M_y$ is considered, only $\chi_{L,N}$ and $\chi_{L,My}$ will be considered in the calculation of χ_L.

To summarize, here are the steps that must be followed when using the O.I.C. proposal for combined load cases. For simple load cases, only steps 1), 4) and 5) apply.

1) Determine the loading on the section;
2) Calculate n, m_y and mz using Equations (148), (149) and (150);
3) Calculate angles ϕ and θ using Equations (151), (152) and (153);
4) Determine all required load multipliers;
5) Calculate reduction factors for simple load cases;
6) Calculate the reduction factor for the combined load case studied.

To calculate the values of n, my and mz and to calculate the plastic multipliers, the value of Fy reduced according to the temperature is needed. The reducing factors $k_{y,\theta}$ from Eurocode 3 are used to determine the values of $Fy_{,\theta}$.

As hot-rolled sections and welded sections present different characteristics and do not follow the same tendencies, a different leading parameter was identified for those different manufacturing processes in the previous chapter. Therefore, two proposals are presented in the following sections: one for hot-rolled sections and one for welded sections.

5.2 Proposal for welded sections

After the investigation made to find the most appropriate leading parameter and presented in Chapter 4, the parameter chosen for welded sections is μ which is defined with the following equation:

$$\mu = \frac{\left(\frac{h}{t_w}\right)^{0.6} \cdot \left(\frac{b}{t_f}\right) \cdot \left(\frac{t_w}{t_f}\right)}{1000} \qquad (158)$$

This parameter indicates that the behaviour of hot-rolled sections is influence by the slenderness ratio of the web, the slenderness ratio of the flanges and the ratio between the thickness of the web and the thickness of the flanges.

5.2.1 Proposed equations

As explained previously, buckling curves are first presented independently for each simple load case. An interaction formula is then used for the combined load cases. Then, the performance of the model is studied in section 5.2.2.

5.2.1.1 Equations for compression

Table 25 presents the proposed O.I.C. design for compression.

Table 25 : Design proposal for compression

<table>
<tr><td>For $\lambda_{L,N} \leq \lambda_0$</td><td colspan="3">For $\lambda_{L,N} > \lambda_0$</td></tr>
<tr><td rowspan="4">$\chi_{L,N} = 1.0$</td><td colspan="3">$\phi = 0.5 \cdot \left(1 + \alpha_L \cdot \left(\lambda_{L,N} - \lambda_0\right) + \lambda_{L,N}{}^{\delta}\right)$</td></tr>
<tr><td colspan="3">$\chi_{L,N} = \frac{1}{\phi + \sqrt{\phi^2 - \lambda_{L,N}{}^{\delta}}}$</td></tr>
<tr><td>λ_0</td><td>α_L</td><td>δ</td></tr>
<tr><td>0.2</td><td>$-0.079 + 2.92 \cdot \mu$</td><td>$0.29 - 2.71 \cdot \mu \geq 0$</td></tr>
</table>

Figure 79 presents the results from numerical simulations and design curves obtained for different values of the leading parameter μ. On this figure, curves for specific values of the leading parameter are associated to points that lie in an interval of leading parameter values. The figure is used to give a first idea of the good performance of the model. However, to accurately assess the performance of the model, each numerical result must be compared to the prediction made by the proposal for its specific value of the leading parameter. This comparison is made in section 5.2.2.

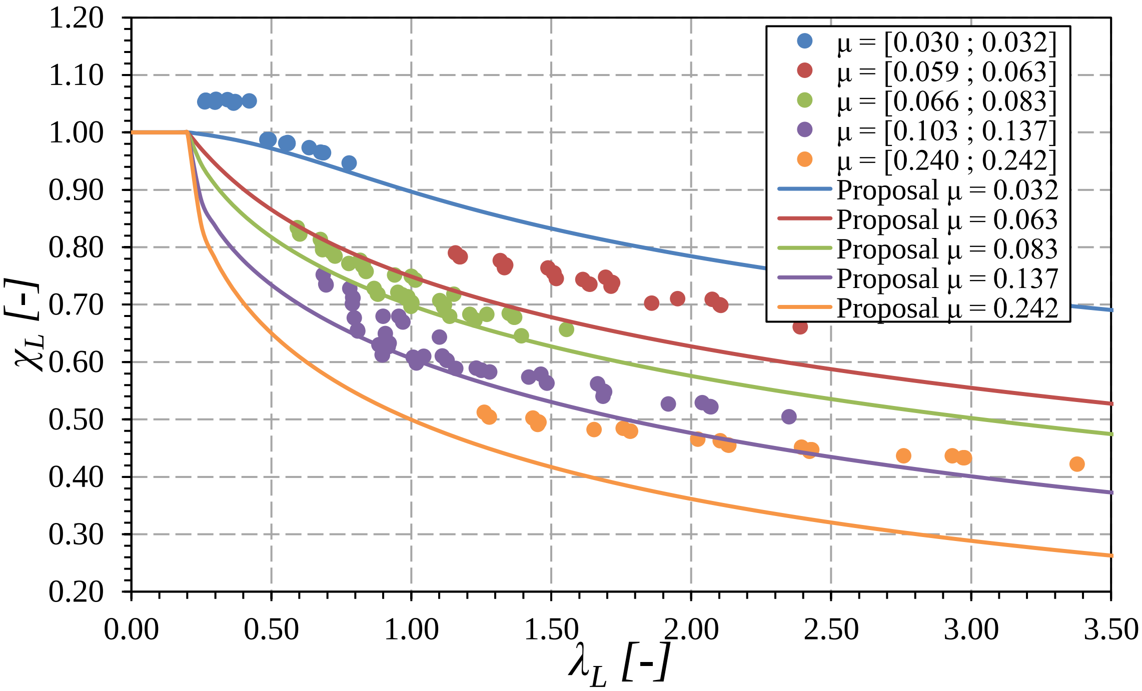

Figure 79 : Design proposal for welded sections under compression

5.2.1.2 Equation for major-axis bending

Table 26 presents the proposed O.I.C. design for major-axis bending.

Table 26 : Design proposal for major-axis bending

<table>
<tr><td>For $\lambda_{L,My} \leq \lambda_0$</td><td colspan="3">For $\lambda_{L,My} > \lambda_0$</td></tr>
<tr><td rowspan="4">$\chi_{L,My} = 1.0$</td><td colspan="3">$\phi = 0.5 \cdot \left(1 + \alpha_L \cdot \left(\lambda_{L,My} - \lambda_0\right) + \lambda_{L,My}{}^{\delta}\right)$</td></tr>
<tr><td colspan="3">$\chi_{L,My} = \dfrac{1}{\phi + \sqrt{\phi^2 - \lambda_{L,My}{}^{\delta}}}$</td></tr>
<tr><td>λ_0</td><td>α_L</td><td>δ</td></tr>
<tr><td>0.3</td><td>$-0.019 + 1.84 \cdot \mu$</td><td>$0.86 - 8.23 \cdot \mu \geq 0$</td></tr>
</table>

Figure 80 presents the results from numerical simulations and design curves obtained for different values of the leading parameter μ.

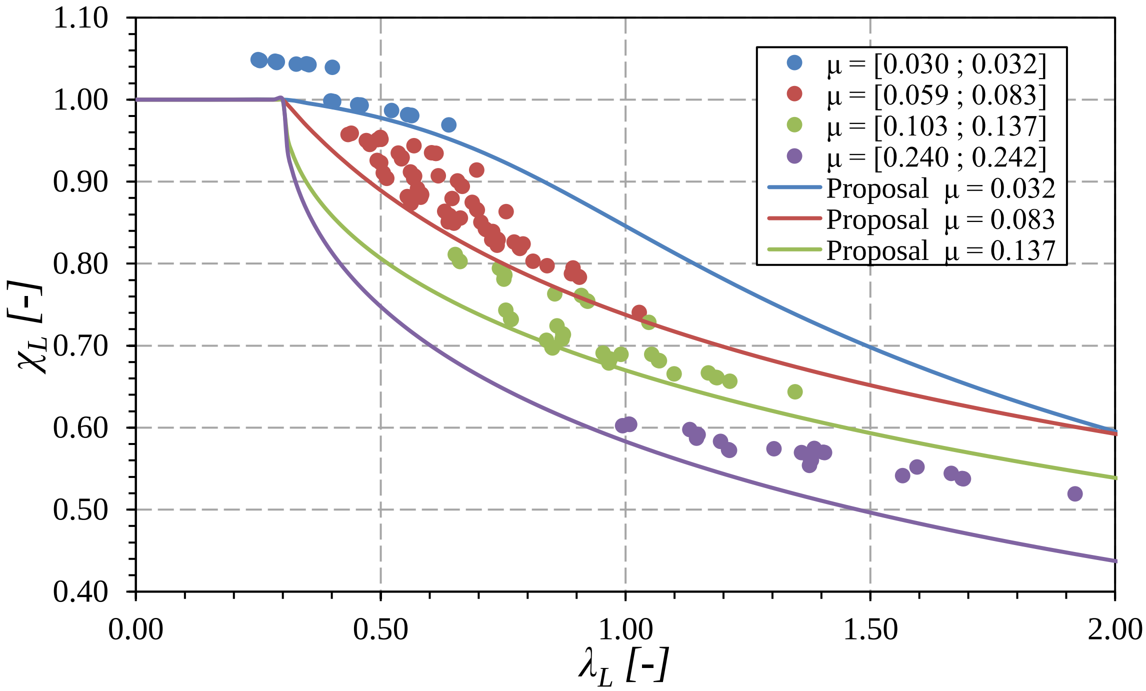

Figure 80 : Design proposal for welded sections under major-axis bending

Equation for minor-axis bending

Table 27 presents the proposed O.I.C. design for minor-axis bending.

Table 27 : Design proposal for minor-axis bending

<table>
<tr><td>For $\lambda_{L,Mz} \leq \lambda_0$</td><td colspan="3">For $\lambda_{L,Mz} > \lambda_0$</td></tr>
<tr><td rowspan="4">$\chi_{L,Mz} = 1.0$</td><td colspan="3">$\phi = 0.5 \cdot \left(1 + \alpha_L \cdot \left(\lambda_{L,Mz} - \lambda_0\right) + \lambda_{L,Mz}{}^{\delta}\right)$</td></tr>
<tr><td colspan="3">$\chi_{L,Mz} = \dfrac{1}{\phi + \sqrt{\phi^2 - \lambda_{L,Mz}{}^{\delta}}}$</td></tr>
<tr><td>λ_0</td><td>α_L</td><td>δ</td></tr>
<tr><td>0.3</td><td>$-0.024 + 1.42 \cdot \mu$</td><td>$0.86 - 6.27 \cdot \mu \geq 0$</td></tr>
</table>

Figure 87 presents the results from numerical simulations and design curves obtained for different values of the leading parameter μ.

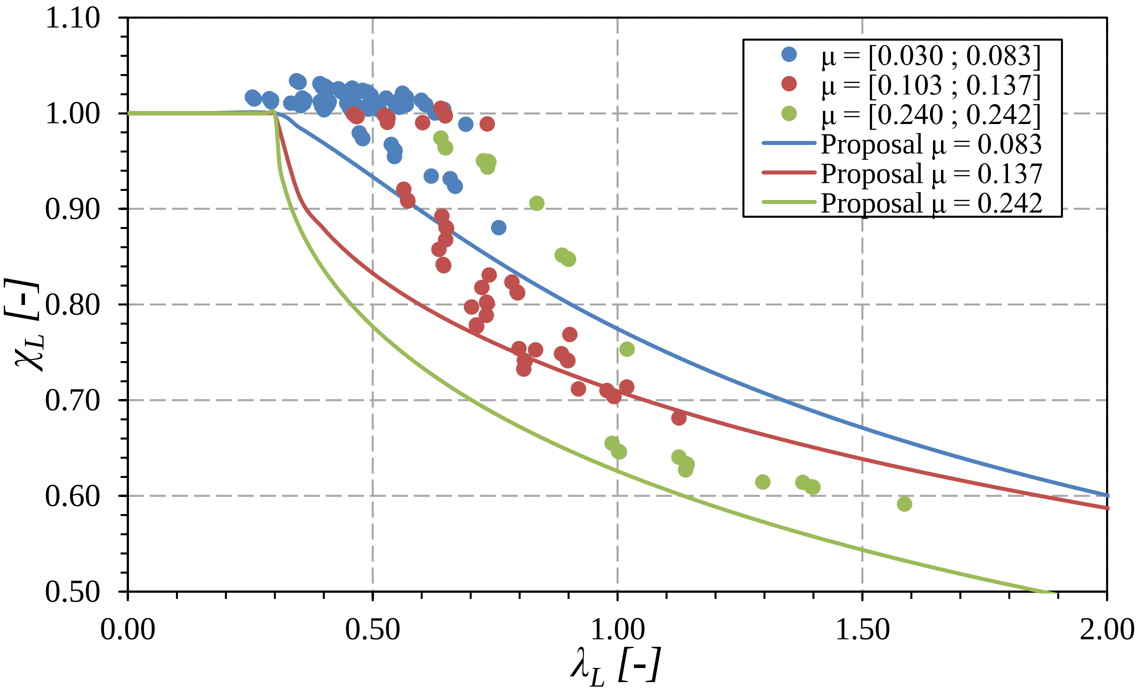

Figure 81 : Design proposal for welded sections under minor-axis bending

5.2.1.3 Equation for combined load cases

As explained previously, for combined load cases, the reduction factor is obtained by combining the reduction factors obtained for simple load cases. For hot-rolled section, the local reduction factor is obtained with Equation (161).

$$\chi_L = \left[\left(\chi_{L,N} \cdot \cos(\phi)^{0.17} \right)^3 + \left(\chi_{L,My} \cdot \sin(\phi)^{2.6} \cdot \cos(\theta)^{0.4} \right)^3 + \left(\chi_{L,Mz} \cdot \sin(\phi)^{8} \cdot \sin(\theta)^{5.5} \right)^3 \right]^{(1/3)} \quad (159)$$

5.2.2 Performance of the proposal

To assess the performance of the proposed model, graphs are plotted. In those graphs, values are represented as the ratio between $\chi_{L\_O.I.C.}$ and χ_{L_FE}. A value of 1.0 means that the model can predict exactly the resistance. A value over 1.0 means that the prediction by the model is unconservative while a value lower than 1.0 means that the prediction by the model is conservative. The first graph presented on Figure 82 is a histogram of all results obtained for the proposal. As mentioned in section 3.2.2, some reduced sections with reduced flange and web thicknesses have been considered for the welded sections. Therefore, two series are shown on the graph: one with all results and one without the reduced sections.

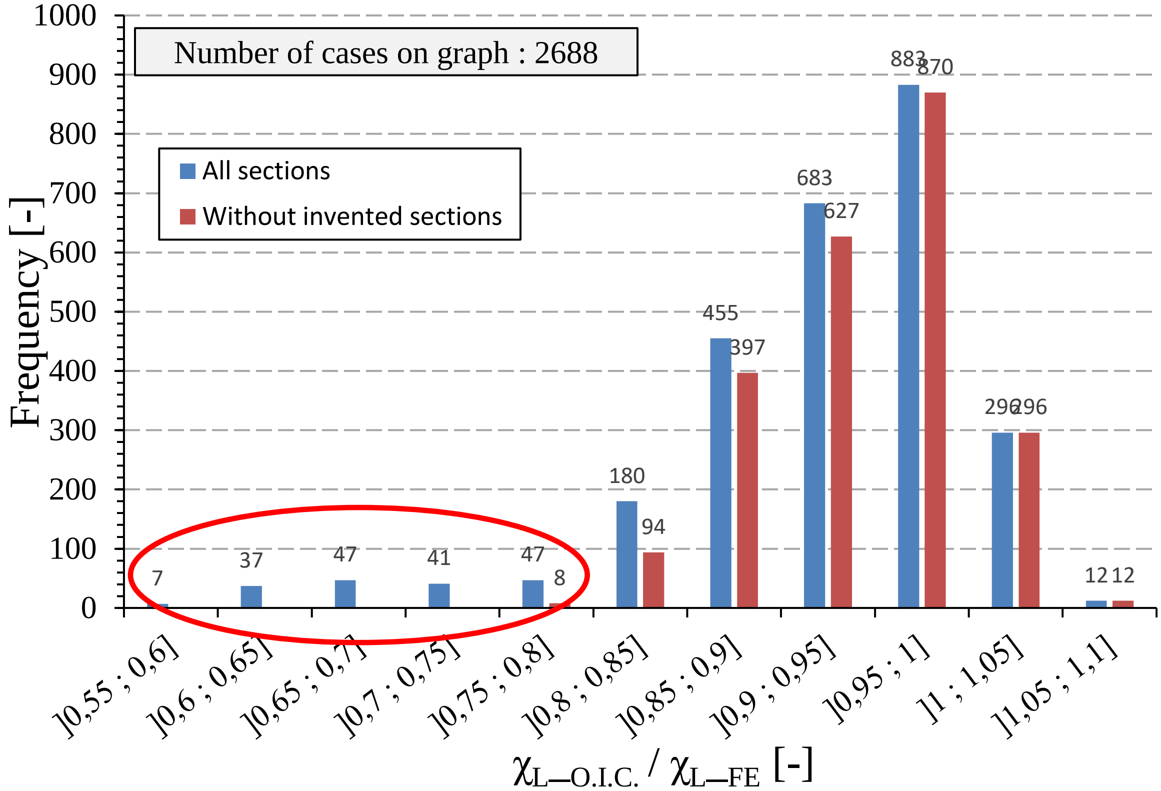

Figure 82 : Accuracy of O.I.C. proposal for welded sections

The graph shows that the overall performance of the model is good as most results are between 0.85 and 1.05 with the biggest portion between of the results between 0.9 and 1.0. Moreover, most of the unconservative results are below 1.05 which is considered acceptable since no safety factor is currently considered. The proposal seams however to lead to some results which are too conservative. Those results are circled in red on the graph. By comparing the two series, it is possible to conclude that those very conservative results are obtained for the reduced sections. The purpose of considering those sections was to see if the proposal could extend outside of the range of cross-sections typically used in construction. Results show that for very slender sections that are not typically used, the proposal might not have such a good performance. However, the proposal is very performant for typical sections. Accordingly, the rest of the evaluation of the performance of the model will be performed without those reduced sections.

Figure 83 presents the performance of the O.I.C. proposal for the different load combinations.

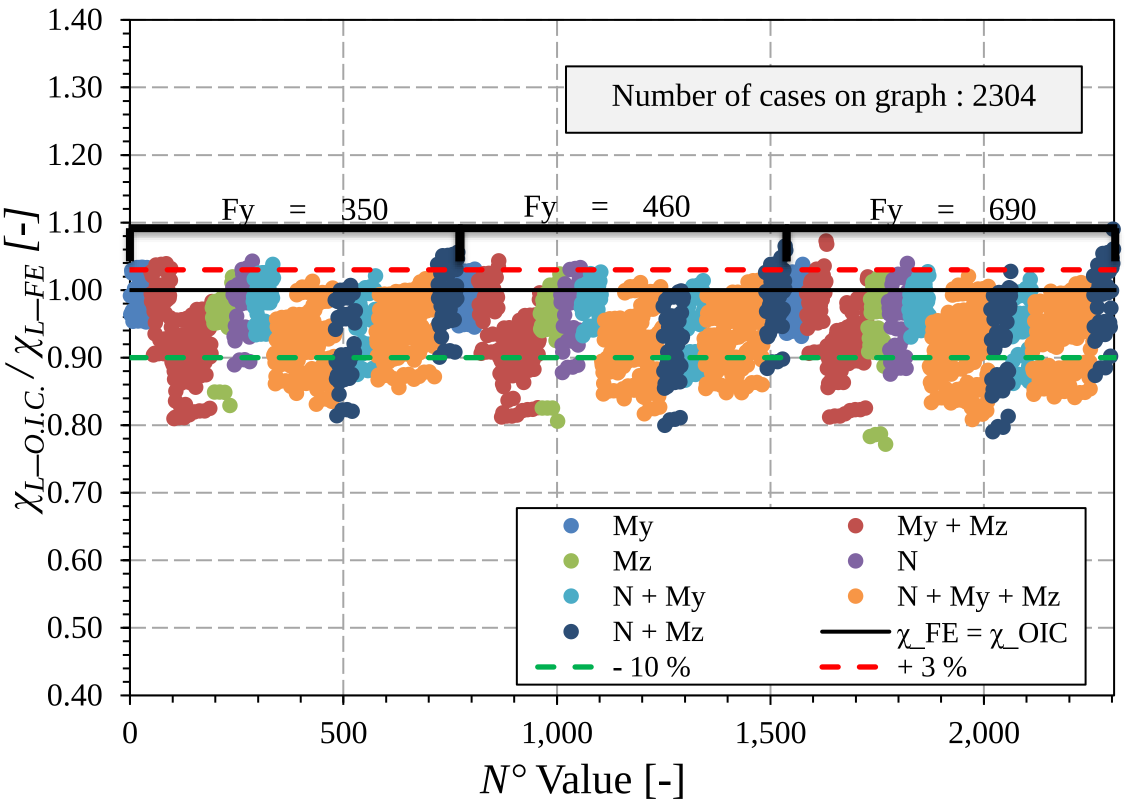

Figure 83 : Performance of proposal for welded sections based on the load combination

On the graph, two lines are displayed to show the targeted upper (1.03) and lower (0.90) limits. The red line indicates that a unconservative results of maximum 3 % are desirable while the green line indicates that conservative results of maximum 10 % are desirable. The black line indicates a perfect prevision.

This graph confirms that the overall performance of the model is good as the majority of the results lie between the fixed limits. Moreover, the results that do not fall within the fixed interval mostly are on the conservative side. The results on the unconservative side are in the worst cases 9% too high with very few results over 3% which is considered acceptable. Effectively, the proposal will ultimately be associated to a safety factor which will compensate for the results that are slightly over 1.0. Table 28 presents the statistics of the results based on the different load combinations.

Table 28 : Statistical study of O.I.C. proposal for welded sections for all load cases

Load combination	N	M_y	M_z	$N+M_y$	$N+M_z$	M_y+M_z	$N+M_y+M_z$	All
Mean	0.97	0.99	0.95	0.97	0.95	0.93	0.93	0.94
Max.	1.04	1.04	1.02	1.04	1.09	1.07	1.02	1.09
Min.	0.88	0.93	0.77	0.86	0.79	0.81	0.81	0.77
C.O.V.	0.043	0.030	0.052	0.039	0.065	0.059	0.051	0.053
Values < 0.8	0	0	4	0	4	0	0	8
Values < 0.9	13	0	13	22	64	117	270	499
Values > 1.0	37	50	15	58	64	49	35	308
Values > 1.03	7	11	0	1	28	14	0	61
Values > 1.1	0	0	0	0	0	0	0	0
Values > 1.25	0	0	0	0	0	0	0	0
Total number of cases	144	144	144	288	288	432	864	2304

First, the table shows that the accuracy of the proposal is great for simple load cases. Effectively, the means of those load cases vary between 0.95 and 0.99 which is very good as it is only slightly lower then 1.0. Moreover, the C.O.V. for those load cases is small (max 5.2%), which indicates that all obtained results are very close to the mean. It is possible to see that a considerable number of results are however over 1.0 for the compression and the major-axis load cases. Nevertheless, very few of theses results are over 1.03 with a maximum value of 1.04, which is considered to be more than acceptable. Effectively, as mentioned previously, for the proposal to be used in real design situations, it will have to be associated to a safety factor. With that safety factor, the unconservative results that are less than 1.04 will become very close to 1.0. On the other side, the most conservative results are obtained for M_z with a minimal value 23% too conservative. However, the table shows that only 13 results are under the target of 0.9 which is therefore acceptable.

As for the combined load cases, the load case $N + M_y$ is the one with the best performance with its mean of 0.97, its small coefficient of variation of 3.9% and its maximal value of 1.04. It is also the one with the less number of results below 0.9. The performance of this load case is similar to the performance of the simple load cases. The load combinations with the worst performances are $M_y + M_z$ and $N + M_z$. Effectively, these are the load cases that have the most unconservative values and the biggest coefficients of variation (6.5% and 5.9%). Both also have a significative number of conservative results (<0.9) but very few of those are below 0.8 which is therefore considered acceptable. As for the load case $N + M_y + M_z$, it is the one with the most conservative results. Effectively, it has a mean of 0.93 with almost no values over 1.0 (4%) and a maximal value of 1.02. With the use of a safety factor, those results would be even more conservative. However, as the C.O.V. is small (5.1%) most results are between 0.88 and 1.0 which is very good.

Even if the performance is not the same for all load cases, the table shows that the global performance of the model is good as the mean of the all the values is 0.94 with a coefficient of variation of 5.3 % and only a few results over the upper limit of 3% (2.6% of results). Moreover, the results on the unconservative side are under 1.09 which is considered acceptable as a safety factor will be needed for the proposal to be used.

Figure 83, presented previously, also shows the results obtained with the different values of F_y. As can be seen in the figure, the value of F_y does not significantly impact the performance of the model. Table 29 presents the statistics of the results based on the value of F_y.

Table 29 : Statistical study of O.I.C. proposal for welded sections for different value of F_y

F_y (MPa)	355	460	690
Mean	0.95	0.94	0.94
Min	0.81	0.80	0.77
Max	1.06	1.07	1.09
C.O.V.	0.054	0.055	0.058
Values > 1.0	145	99	125
Values > 1.03	29	11	21
Values > 1.1	0	0	0
Values > 1.25	0	0	0
Total number of cases	768	768	768

The table shows that results obtained with F_y = 355 MPa are slightly more precise as the mean is closer to 1.0 and the C.O.V. is slightly lower. It is also the value of F_y for which the maximal value is the lowest. On the other side, the variability in the results increases as the value of F_y increases. However, results are very similar, and it can be concluded that the proposal is adequate for all values of F_y.

Figure 84 presents the influence of the temperature on the precision of the proposed model.

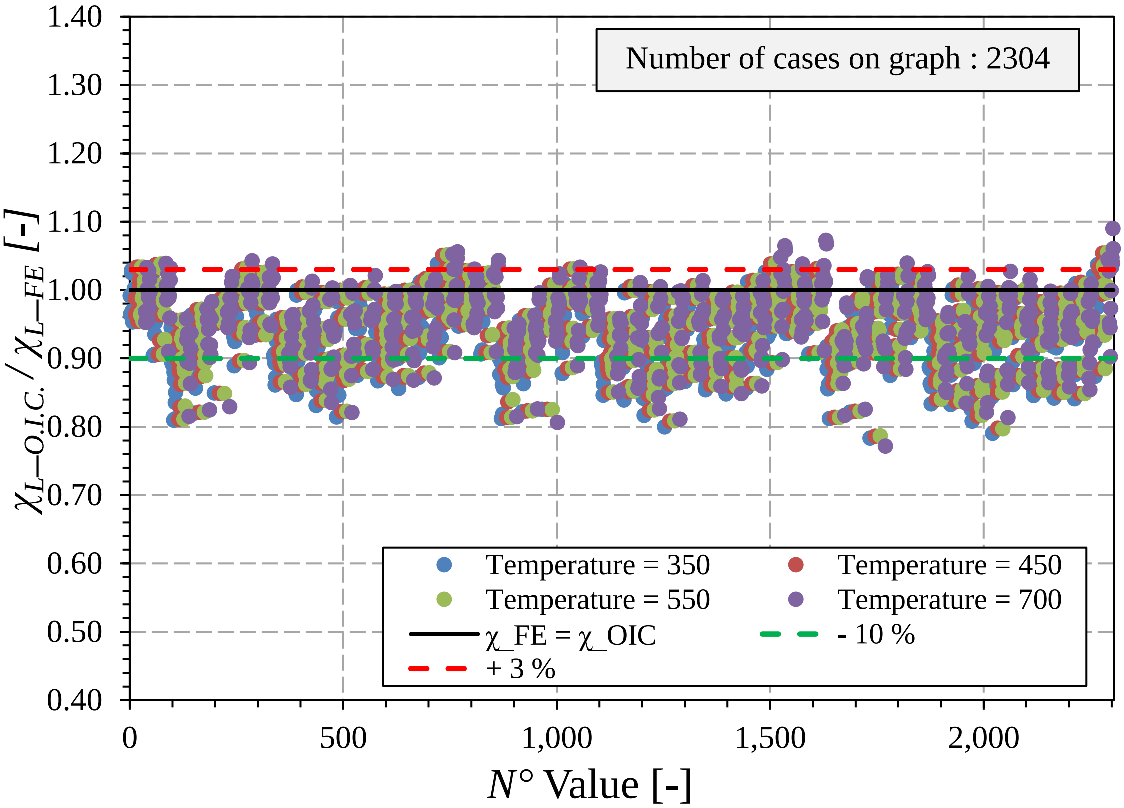

Figure 84 : Performance of proposal for welded sections based on the temperature

Based on the results, it can be concluded that the temperature does not affect the precision of the model. Effectively, no general tendencies related to the temperature can be noticed.

5.3 Proposal for hot-rolled sections

After the investigation made to find the most appropriate leading parameter and presented in Chapter 4, the parameter chosen is γ which is defined with the following equation.

$$\gamma = \frac{\left(\frac{h}{t_w}\right)^2 \cdot \left(\frac{b}{t_f}\right) \cdot \left(\frac{t_w}{t_f}\right)}{100000} \qquad (160)$$

This parameter shows that the behaviour of hot-rolled sections is influenced by the slenderness ratio of the web, the slenderness ratio of the flanges and the ratio between the thickness of the web and the thickness of the flanges.

5.3.1 Proposed equations

As explained previously, buckling curves are first presented independently for each simple load case. A interaction formula is then used for the combined load cases. The purpose of the following sections is only to present the equations used in the proposal. The performance of the proposal is studied in section 5.3.2.

5.3.1.1 Equations for pure compression

Table 30 presents the proposed O.I.C. design approach for pure compression.

Table 30 : Design proposal for pure compression

For $\lambda_{L,N} \leq \lambda_0$	For $\lambda_{L,N} > \lambda_0$		
$\chi_{L,N} = 1.0$	$\phi = 0.5 \cdot \left(1 + \alpha_L \cdot \left(\lambda_{L,N} - \lambda_0\right) + \lambda_{L,N}{}^{\delta}\right)$		
	$\chi_{L,N} = \dfrac{1}{\phi + \sqrt{\phi^2 - \lambda_{L,N}{}^{\delta}}}$		
	λ_0	α_L	δ
	0.2	$-0.003 + 0.89 \cdot \gamma$	$0.41 - 2.18 \cdot \gamma$

Figure 85 presents the results from numerical simulations and design curves obtained for different values of the leading parameter γ.

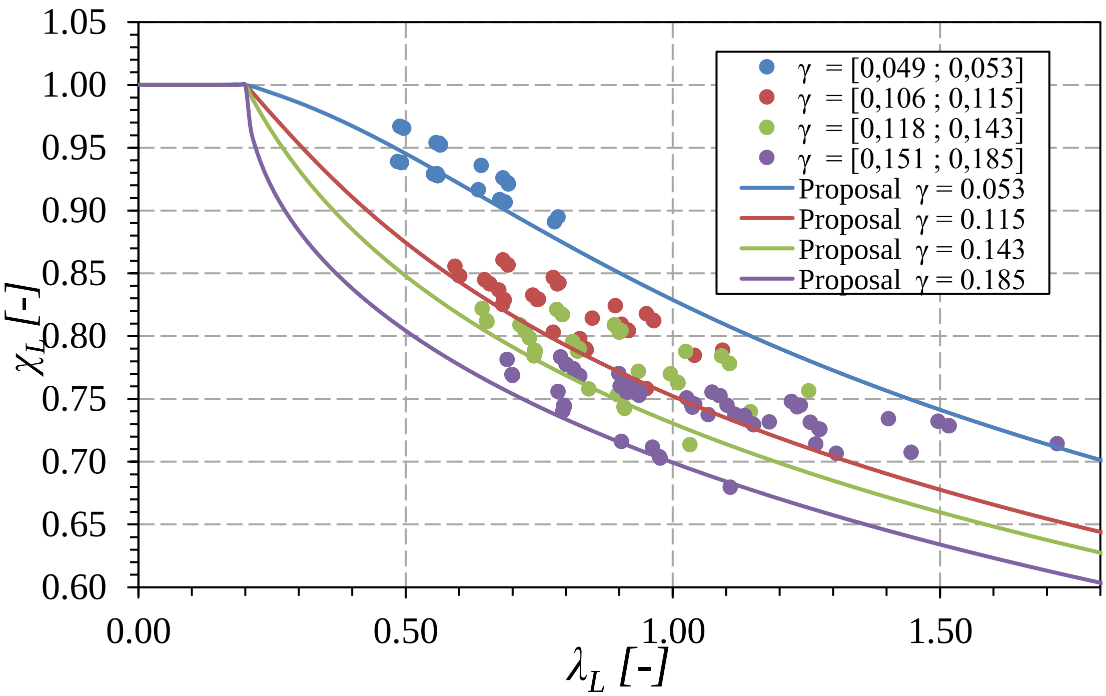

Figure 85 : Design proposal for hot-rolled sections under pure compression

5.3.1.2 Equation for major-axis bending

Table 31 presents the proposed O.I.C. design for major-axis bending.

Table 31 : Design proposal for major-axis bending

<table>
<tr><td>For $\lambda_{L,My} \leq \lambda_0$</td><td colspan="3">For $\lambda_{L,My} > \lambda_0$</td></tr>
<tr><td rowspan="4">$\chi_{L,My} = 1.0$</td><td colspan="3">$\phi = 0.5 \cdot \left(1 + \alpha_L \cdot \left(\lambda_{L,My} - \lambda_0\right) + \lambda_{L,My}{}^{\delta}\right)$</td></tr>
<tr><td colspan="3">$\chi_{L,My} = \dfrac{1}{\phi + \sqrt{\phi^2 - \lambda_{L,My}{}^{\delta}}}$</td></tr>
<tr><td>λ_0</td><td>α_L</td><td>δ</td></tr>
<tr><td>0.3</td><td>$0.02 + 0.59 \cdot \gamma$</td><td>$1.34 - 7.02 \cdot \gamma$</td></tr>
</table>

Figure 86 presents the results from numerical simulations and design curves obtained for different values of the leading parameter γ.

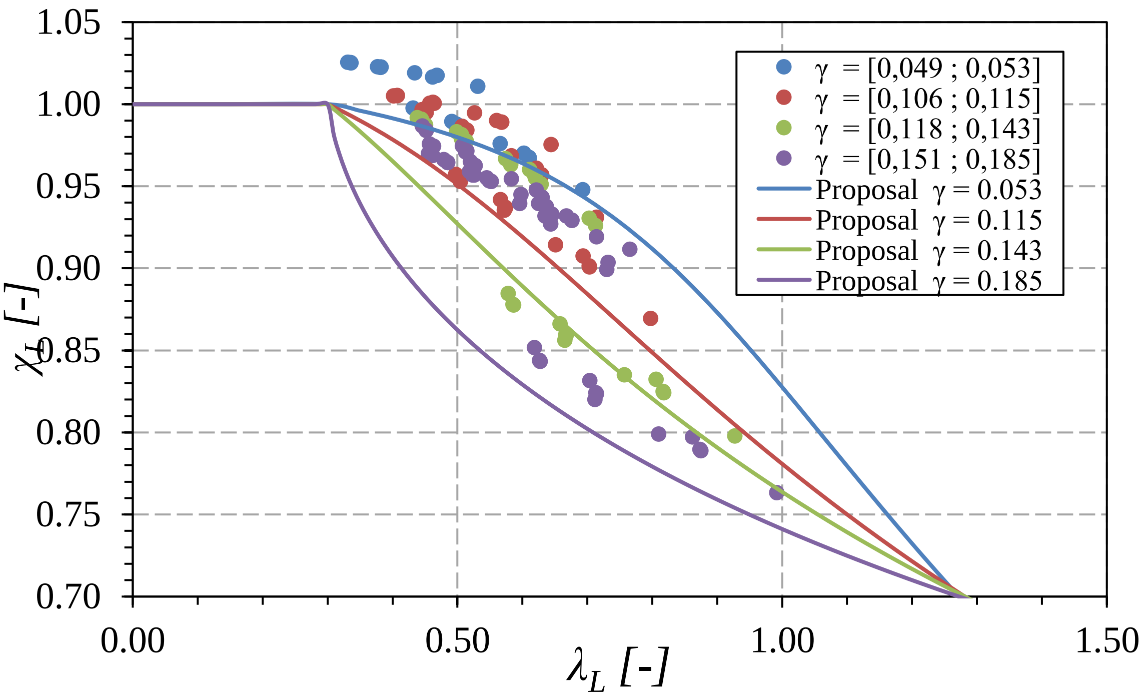

Figure 86 : Design proposal for hot-rolled sections under pure major-axis bending

5.3.1.3 Equation for minor-axis bending

Table 32 presents the proposed O.I.C. design for minor-axis bending.

Table 32 : Design proposal for minor-axis bending

<table>
<tr><td>For $\lambda_{L,Mz} \le \lambda_0$</td><td colspan="3">For $\lambda_{L,Mz} > \lambda_0$</td></tr>
<tr><td rowspan="4">$\chi_{L,Mz} = 1.0$</td><td colspan="3">$\phi = 0.5 \cdot \left(1 + \alpha_L \cdot \left(\lambda_{L,Mz} - \lambda_0\right) + \lambda_{L,Mz}{}^{\delta}\right)$</td></tr>
<tr><td colspan="3">$\chi_{L,Mz} = \dfrac{1}{\phi + \sqrt{\phi^2 - \lambda_{L,Mz}{}^{\delta}}}$</td></tr>
<tr><td>λ_0</td><td>α_L</td><td>δ</td></tr>
<tr><td>0.3</td><td>$-0.023 + 0.88 \cdot \gamma$</td><td>$0.71 - 2.24 \cdot \gamma$</td></tr>
</table>

Figure 87 presents the results from numerical simulations and design curves obtained for different values of the leading parameter γ.

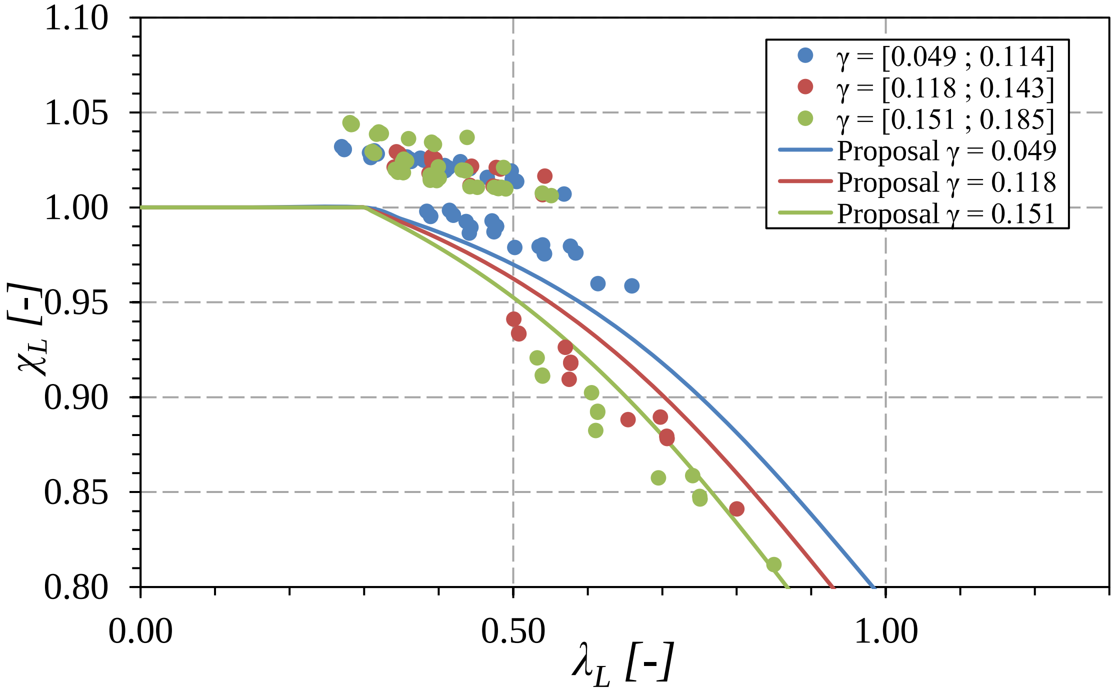

Figure 87 : Design proposal for hot-rolled sections under pure minor-axis bending

5.3.1.4 Equation for combined load cases

As explained previously, for combined load cases, the reduction factor is obtained by combining the reduction factors obtained for simple load cases. For hot-rolled section, the local reduction factor is obtained with Equation (159).

$$\chi_L = \left[\left(\chi_{L,N}\cdot\cos(\phi)^{0.3}\right)^3 + \left(\chi_{L,My}\cdot\sin(\phi)^{1.5}\cdot\cos(\theta)^{0.18}\right)^3 + \left(\chi_{L,Mz}\cdot\sin(\phi)^4\cdot\sin(\theta)^7\right)^3\right]^{(1/3)} \quad (161)$$

5.3.2 Performance of the proposal

To assess the performance of the proposed approach, graphs are presented hereafter. In those graphs, values are represented as the ratio between $\chi_{L\_O.I.C.}$ and χ_{L_FE}. A value of 1.0 means that the calculation method can predict exactly the resistance. A value over 1.0 means that the prediction by the proposal is unconservative while a value lower than 1.0 means that the prediction by the proposal is conservative. The first graph presented on Figure 88 is an histogram of all results obtained for the proposal.

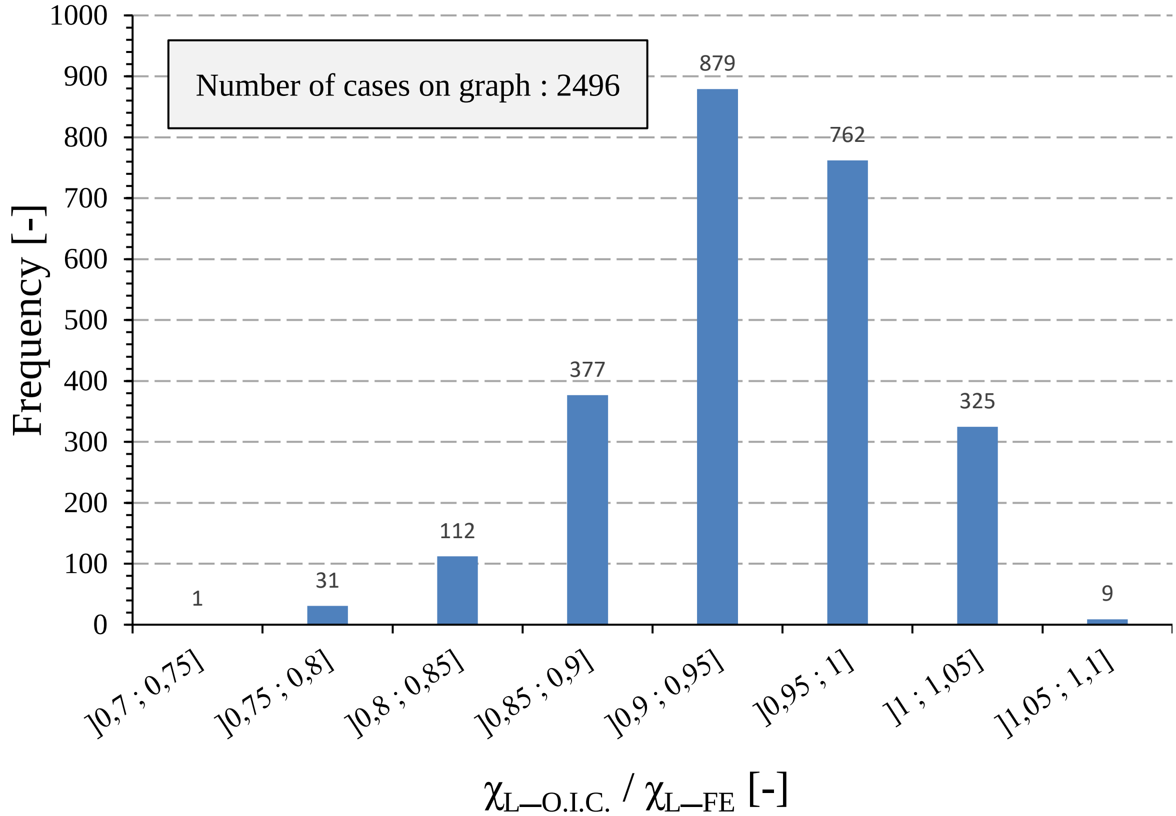

Figure 88 : Accuracy of O.I.C. proposal for hot-rolled sections

The graph shows that the overall performance of the model is good to very good. Effectively, most results are between 0.85 and 1.05 with the biggest portion between of the results between 0.9 and 1.0. Moreover, very few results have over 5% of insecurity. Finally, only 5.7 % of the results are below 0.85 which means that the proposal does not predict overconservative results. This aspect will be discussed in the following sections.

Figure 89 presents the performance of the O.I.C. proposal for different load combinations.

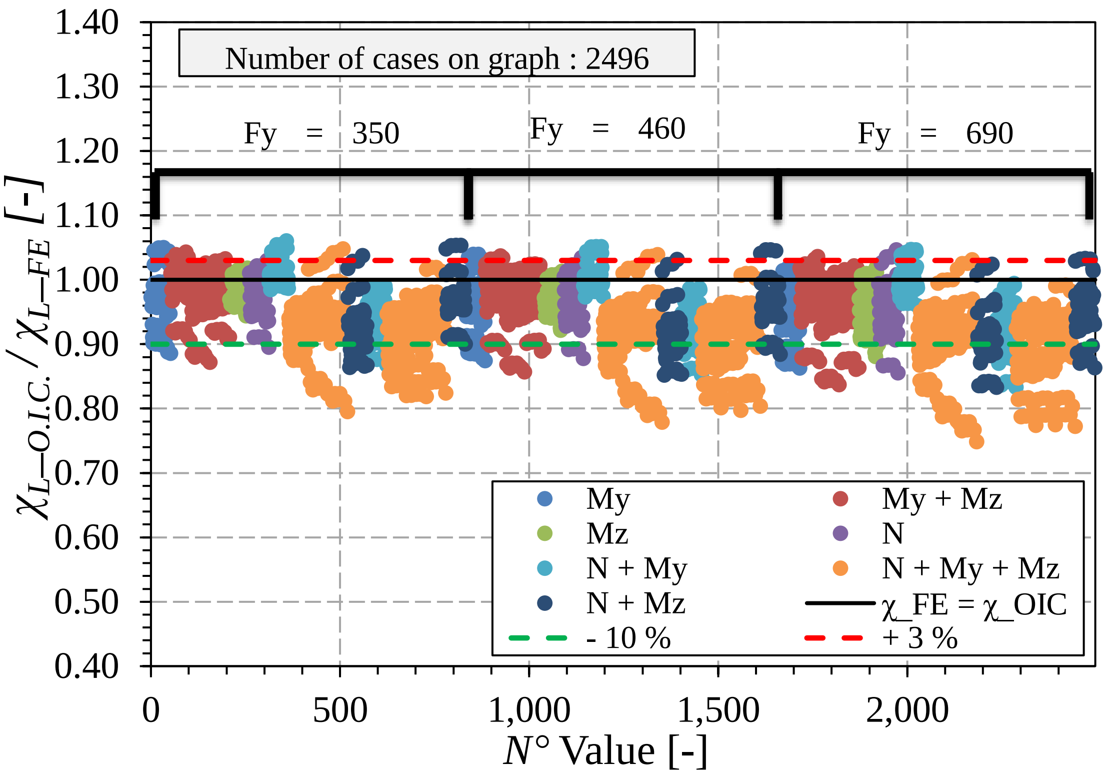

Figure 89 : Performance of proposal for hot-rolled sections based on the load combination

On the graph, two lines are displayed to show the targeted upper (1.03) and lower (0.90) limits. The red line indicates that a unconservative results of maximum 3 % are desirable while the green line indicates that conservative results of maximum 10 % are desirable. The black line indicates a perfect prediction.

This graph shows that the overall performance of the model is good as most of the results lie between the fixed limits. Moreover, the results that do not fall in the fixed interval mostly are on the conservative side. The results on the unconservative side are in the worst cases 6% too high which is considered acceptable. Table 33 presents the statistics of the results based on the different load combinations.

Table 33 : Statistical study of O.I.C. proposal for hot-rolled sections for all load cases

Load combination	N	M_y	M_z	N+M_y	N+M_z	M_y+M_z	N+M_y+M_z	All
Mean	0.97	0.95	0.96	0.96	0.94	0.97	0.91	0.94
Max.	1.05	1.05	1.02	1.06	1.05	1.04	1.05	1.06
Min.	0.86	0.86	0.88	0.83	0.83	0.84	0.75	0.75
C.O.V.	0.043	0.051	0.031	0.052	0.050	0.045	0.055	0.057
Values < 0.8	0	0	0	0	0	0	1	1
Values < 0.9	9	34	4	44	68	45	317	521
Values > 1.0	32	22	25	79	32	115	29	334
Values > 1.03	9	8	0	23	13	12	8	73
Values > 1.1	0	0	0	0	0	0	0	0
Values > 1.25	0	0	0	0	0	0	0	0
Total number of cases	156	156	156	312	312	468	936	2496

First, the table shows that proposal is very accurate for simple load cases. Effectively, the means of those load cases vary between 0.95 and 0.97 which is slightly lower then 1.0. Moreover, the C.O.V. for those load cases is small (max 5.1%), which indicates that all obtained results are very close to the mean. It is possible to see that some results are over 1.0. However, only a hand full of results are over 1.03 with a maximum value of 1.05, which is considered to be more than acceptable. Effectively, as a safety factor will be used with the proposal, the slightly unconservative results will become very close to 1.0. Moreover, for simple load cases, the minimal value is 0.86 which is very good.

As for the combined load cases, the load cases $N + M_y$ and $M_y + M_z$ are the ones with the best performances. Effectively, both load cases respectively have means of 0.96 and 0.97 and small coefficient of variation (5.2% and 4.5%). These load cases do however have a non negligeable number of values over 1.0 (25% of results). As the maximum value is 1.06, the performance of both load cases is still considered very good. Then, when all types of loads are present ($N + M_y + M_z$), the results are more conservative. Effectively, the mean of this set of data is much lower than for other load combinations (0.91) and it is also the load combination with the minimal prediction (0.75) and the smallest proportion of results over 1.0. It also has a significative number of results under 0.9. It is however still considered accurate as most results are still between 0.85 and 0.97.

Even if the performance is not the same for all load cases, the table shows that the overall performance of the model is good as the mean of the values is 0.94 with a coefficient of variation of 5.7 % and only a few results over the upper limit of 3% (3% of results). These statistics indicate that most results are between 0.88 and 1.0, all load cases considered, which is more than acceptable.

Figure 90 shows the same graph as Figure 89 but with points identified based on the section types.

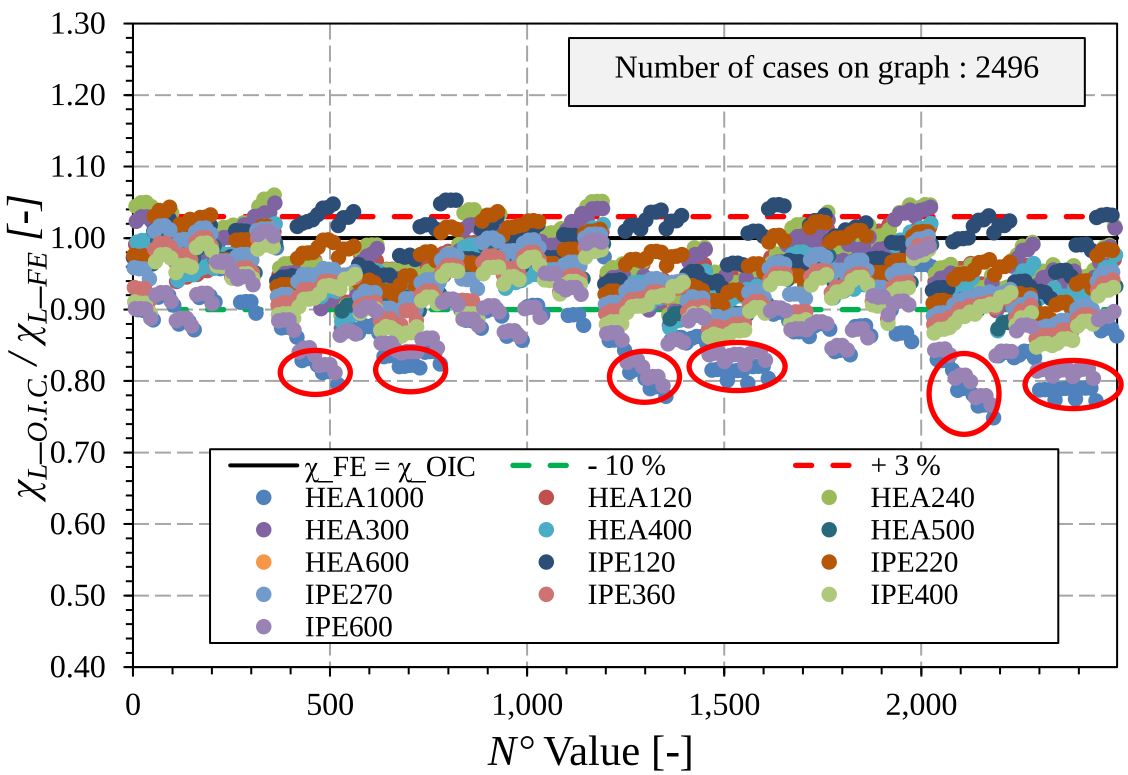

Figure 90 : Performance of proposal for hot-rolled sections based on the section types

This figure shows that the most conservative results obtained for the combined load case N+M_y+M_z are the predictions for two specific sections: IPE600 and HEA1000. Those results are circled in red. These two sections are the ones with the highest webs. As presented previously, the chosen length for the numerical simulations is three times the average between the web high and the flange width. As both these sections have a very high web, the length of the section is to long to avoid global instability effects such as flexural buckling and lateral-torsional buckling. Simulations were therefore redone to try and eliminate those stability problems. For the load cases without minor-axis bending, supports were added along the middle of each flange to prevent global buckling. It was however not possible to add those supports in cases with minor-axis bending. The length was therefore reduced to three times the flange width for those cases. As the width of the flanges is significantly smaller than the height of the web in those sections, the length of the tested specimen was lower which allowed to avoid global stability issues. However, other problems arose from this modification. Effectively, even thought the length is smaller, geometrical imperfections are still incorporated in the model as three half waves along the web. However, at this short length, the natural deformation is no longer three half waves. Therefore, the failure of the cross-sections is potentially not governed by the right failure mode which can lead to results that are not representative of the reality. The result is that the prediction from the O.I.C. proposal is compared to resistance predicted by the finite element model which might not be accurate in those particular cases which can explain why the proposed model is so conservative for those two sections.

Figure 89, presented previously, also shows the results obtained with the different values of F_y. As can be seen in the figure, the value of F_y does not significantly impact the performance of the model. Table 34 presents the statistics of the results based on the value of F_y.

Table 34 : Statistical study of O.I.C. proposal for hot-rolled sections for different value of F_y

F_y (MPa)	355	460	690
Mean	0.95	0.94	0.93
Min	0.80	0.78	0.75
Max	1.06	1.05	1.05
C.O.V.	0.052	0.055	0.061
Values > 1	164	133	110
Values > 1.03	28	25	20
Values > 1.1	0	0	0
Values > 1.25	0	0	0
Total number of cases	832	832	832

The table shows that results obtained with F_y = 355 MPa are slightly more precise as the mean is closer to 1.0 and the coefficient of variation is slightly lower. However, the most unsafe results are also obtained with this value of F_y. On the other side, the most conservative results are obtained with F_y = 690 MPa. However, results are very similar, and it can be concluded that the proposal is adequate for all values of F_y.

This study focuses on the response of open cross sections at high temperature. Figure 91 presents the influence of the temperature on the accuracy of the proposed model.

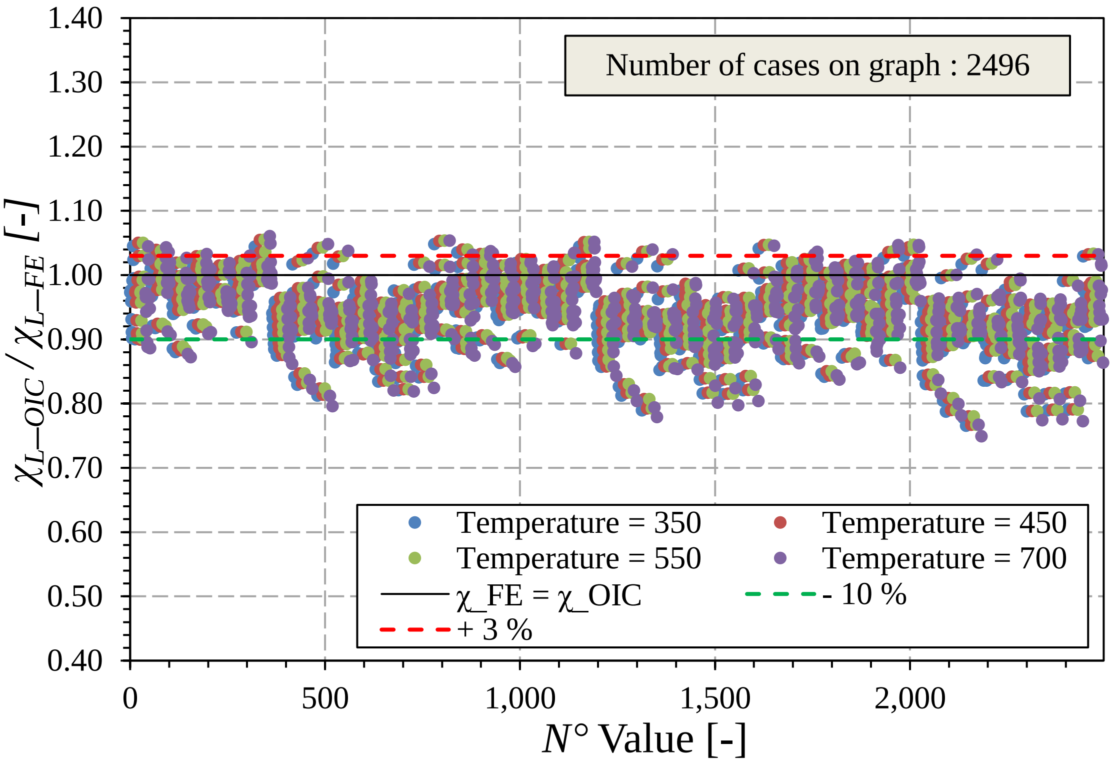

Figure 91 : Performance of proposal for hot-rolled sections based on the temperature

Based on the results, it can be concluded that the temperature does not affect the precision of the model. Effectively, no general tendencies related to the temperature can be noticed.

Chapter 6 : Comparison of proposal with current codes

The performance of both O.I.C. proposals has been demonstrated in the previous chapter. The intent of the current chapter is to compare the performance of the proposal with existing standards. The European standards, the Canadian standards and the American standards are studied in the following sections.

The different standards will be compared using the O.I.C. format used in the previous sections. This means that the ratio between the reduction factor predicted by the calculation method (χ_{method}) and the reduction factor obtained by finite elements (χ_{FE}) is used to evaluate the performance of the standards. A value of 1.0 means that the model can predict exactly the resistance. A value over 1.0 means that the prediction by the model is unconservative while a value lower than 1.0 means that the prediction by the model is conservative. As a reminder, this factor is obtained with the following equation:

$$\chi_L = \frac{R_{b,L}}{R_{pl}} \tag{162}$$

In this equation, the value of $R_{b,L}$ is the ultimate multiplier by which the initial loading must be multiplied to reach the ultimate load according to the standards' calculation method. As for the value of R_{pl}, which is the load multiplier needed to reach the full plastic resistance, it can be calculated in two ways. First, it can be calculated according to the equations provided by the standards. In that case, the equations for Class 1 or 2 sections (or compact sections in the case of the American standards) are used. The multiplier can also be calculated using numerical tools to get the exact results instead of an approximated value.

When calculating the resistance according to standards, typical O.I.C. reduction factors are never calculated. Effectively, the ultimate load is calculated for each simple load case and, for combined load cases, the resistances are then combined with interaction formulas. Consequently, the ultimate load previsions must be compared to the ultimate load obtained with finite elements. As the R_{pl} calculated with the standards' equations is an approximation and is different for all standards, using this value could lead to false conclusions on the performance of the standards. The plastic multiplier used for the comparison must therefore be the exact multiplier obtained with numerical tools.

Two types of graphs are used in the following sections. First, histograms are used to compare the performance of the standards with the O.I.C. proposals. Then, graphs with all the results predicted by the studied standards are used to evaluate the performance of the standards. On these graphs, two lines are displayed to show the targeted upper and lower limits. The red line indicates that a unconservative results of maximum 3 % are desirable while the green line indicates that conservative results of maximum 10 % are desirable. The black line indicates a perfect prevision.

6.1 Comparison with the European standards

This section presents the comparison of the performance of the EC3 with the O.I.C. proposals.

6.1.1 Compression

Figure 92 is an histogram of the results for sections under pure compression. In this histogram, predictions from the Eurocode 3 and from the O.I.C. proposals are compared to the results obtained with the finite element simulations.

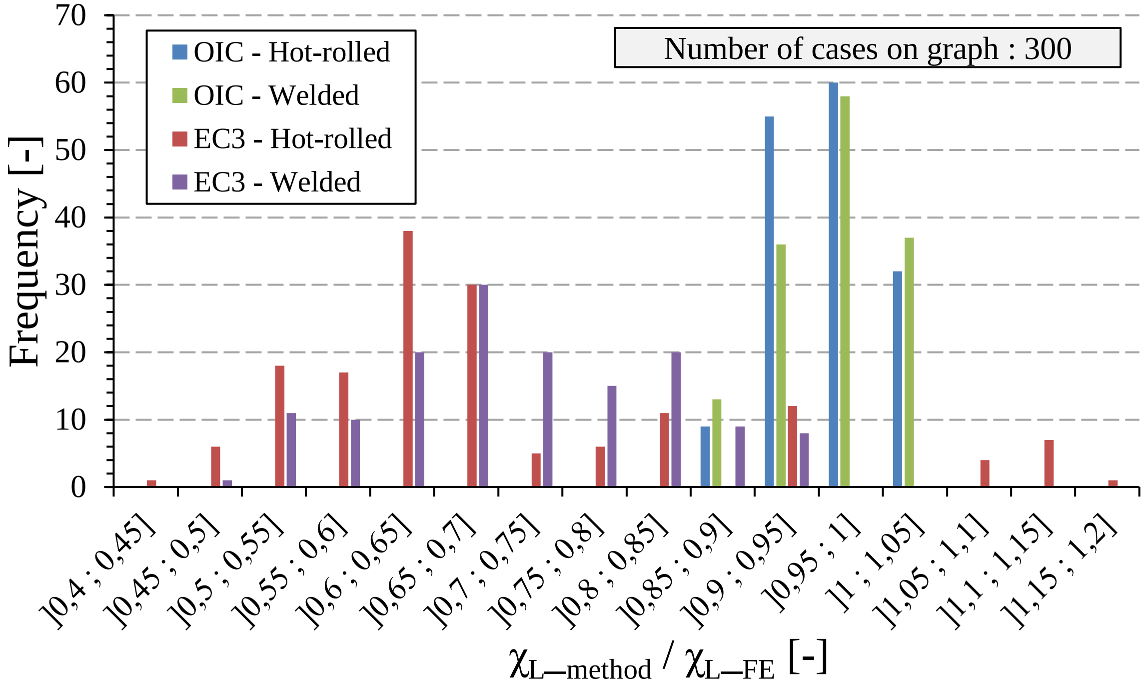

Figure 92 : Accuracy of the results obtained by the O.I.C. proposals and the EC3 for compression

This figure shows that the O.I.C. proposals lead to much more accurate results than the Eurocode 3 for cross-sections under pure compression. Effectively, most of the resistances predicted by the standards are very unconservative with predictions up to 56 % under the finite element results.

Results obtained with the Eurocode 3 for sections under compression are shown on Figure 93. This figure shows the results obtained for both hot-rolled and welded sections and for the three values of F_y studied.

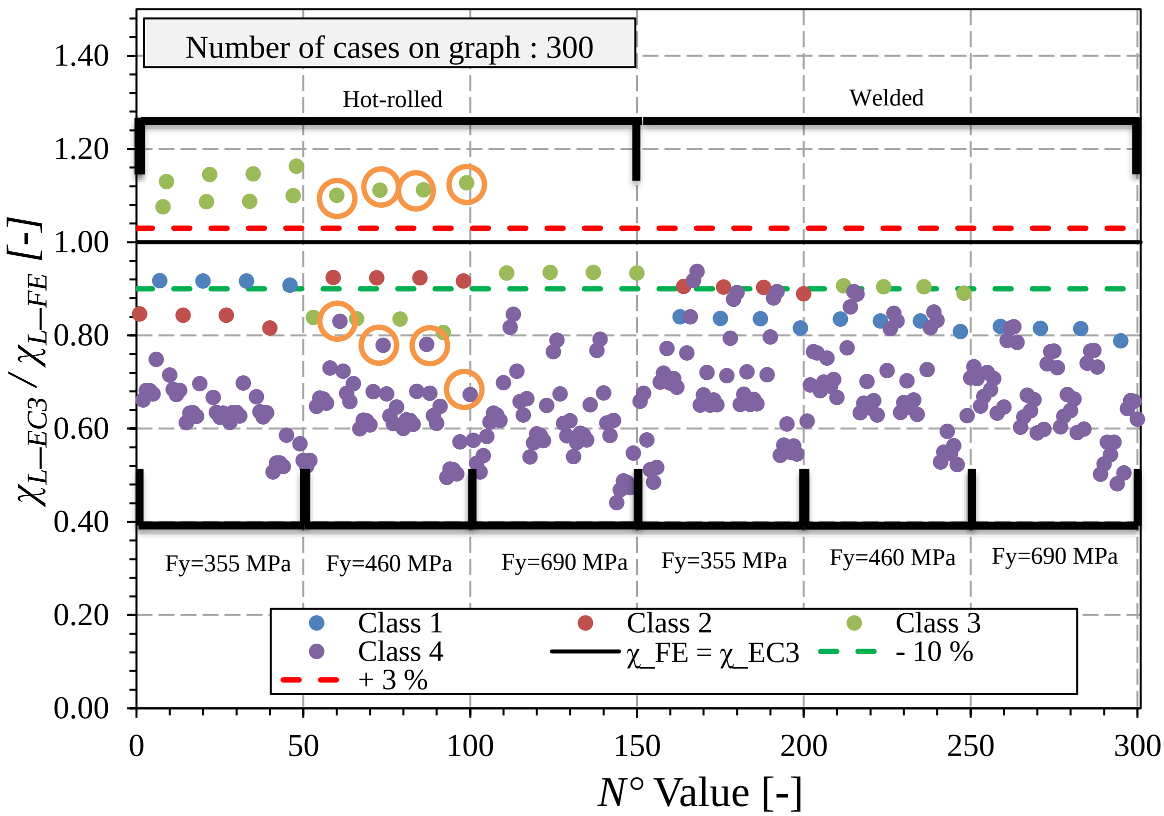

Figure 93 : Performance of the EC3 for sections under compression

The graph shows that most sections are classified as class 4 by the Eurocode 3. This can be explained by the fact that Eurocode 3 considers the increased slenderness at high temperature when classifying cross-sections. All the predictions obtained for that class are on the conservative side. Moreover, they can be considered too conservative which can lead to uneconomical design. The fact that most of the results are too conservative can be explained by two reasons. First, for class 4 sections, the Eurocode 3 uses the 0.2 % proof stress to calculate the resistance instead of the 2 % proof stress which is used for other section classes. This significantly reduces the predicted resistance for class 4 sections which leads to very conservative results. Then, the buckling curve used to calculate the resistance to flexural buckling does not considered a plastic plateau for very small slenderness which means that the resistance is reduced even for very short elements.

As for the temperature, it does not have a significant impact on the accuracy on the predictions for sections from class 1 to 3. Effectively, the orange circles around the green points show that, for a specific cross-section, the predictions present sensibly the same accuracy for all temperatures. However, for class 4 sections, the temperature greatly impacts the accuracy. The purple points with orange circles show that the accuracy is variable for a specific section subjected to different temperatures. Therefore, the results show that the reduction factors to obtain the 0.2% proof strength might not be accurate.

The figure finally shows that results become more conservative as the yield limit increases. Effectively, as F_y increases, the slenderness increases. As a result, the section's class can change between different value of F_y. If a section passes from a class 3 to a class 4, the accuracy of the prediction drastically drops. Moreover, for sections that are considered Class 4 for all values of F_y, the results also become more conservative with the increase in yield limit which indicates that the increase in F_y leads to a bigger reduction in the effective area which is not proportional to the actual decrease in resistance.

6.1.2 Major-axis bending

Figure 94 is a histogram of the results for sections under major-axis bending. In this histogram, predictions from the Eurocode 3 and from the O.I.C. proposals are compared to the results obtained with the finite element simulations.

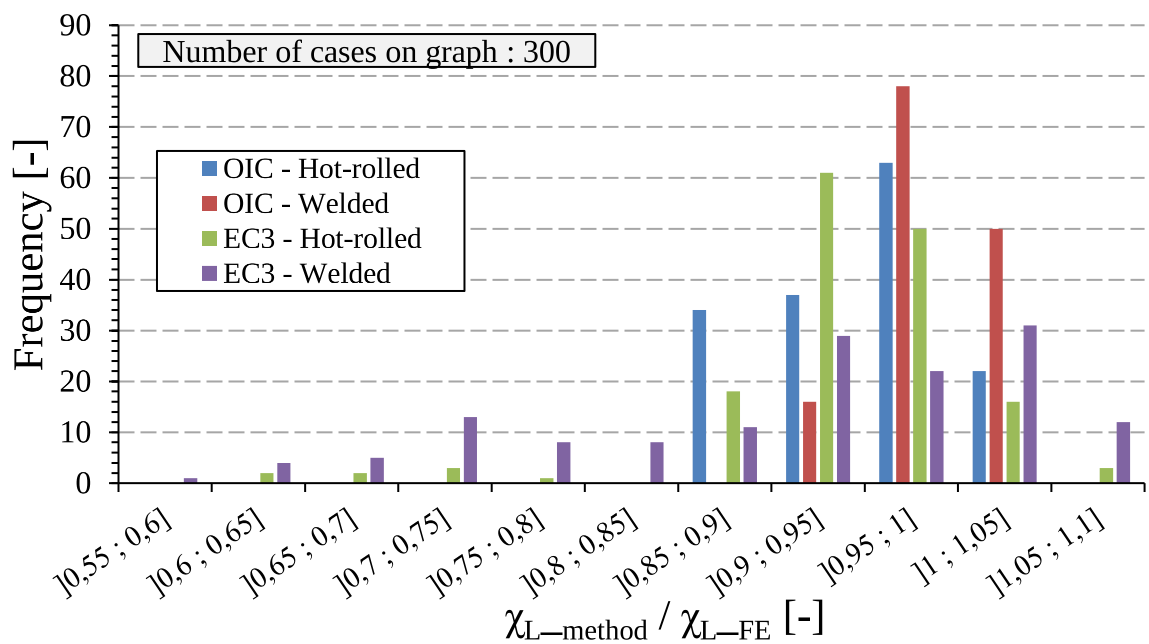

Figure 94 : Accuracy of the results obtained by the O.I.C. proposals and the EC3 for major-axis bending

The graph shows that O.I.C. proposals again have a better overall performance than the Eurocode 3. However, the Eurocode 3 also presents a good performance. Effectively, most of the predicted results are between 0.85 and 1.05. However, the Eurocode 3 also leads to some very conservative results.

Results obtained with the Eurocode 3 for sections under major-axis bending are shown on Figure 95. This figure shows the results obtained for both hot-rolled and welded sections and for the three values of F_y studied.

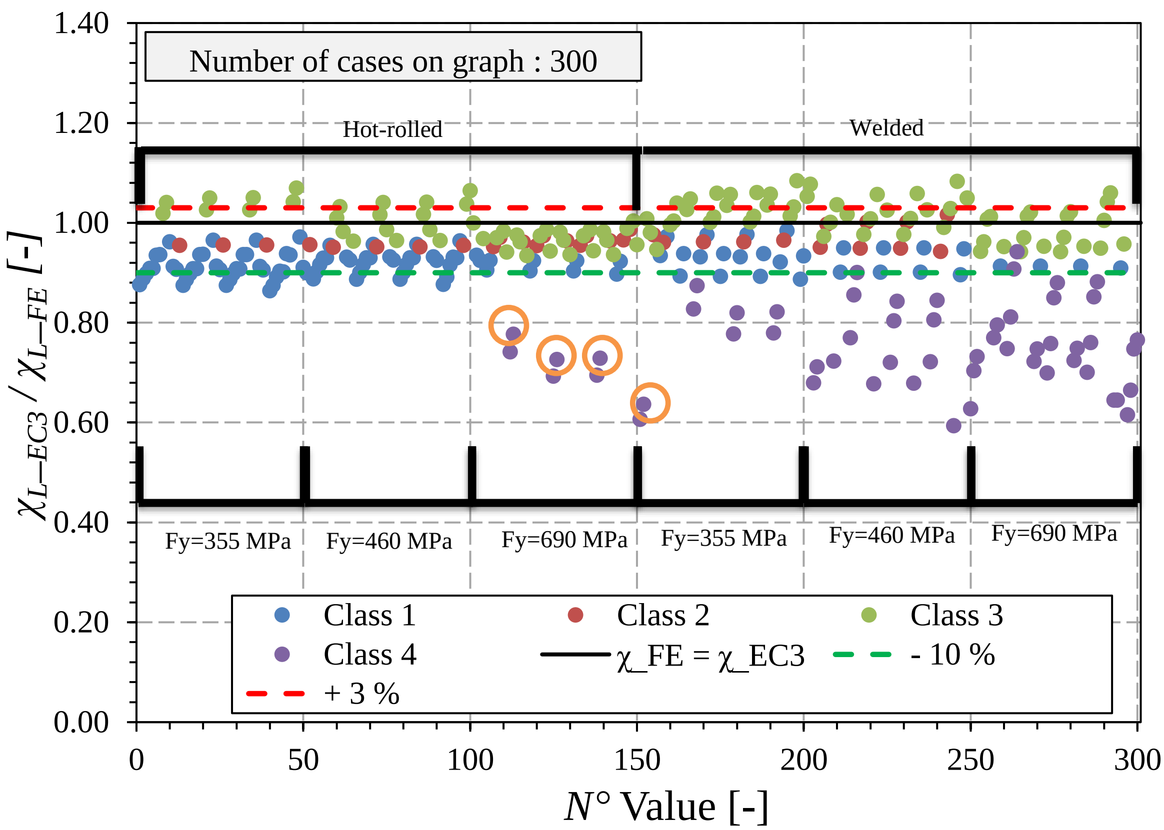

Figure 95 : Performance of the EC3 for sections under major-axis bending

The figure shows that the predictions are very good for sections of classes 1 to 3. In most standards, the elastic resistance is used for class 3 sections which leads to conservative results. However, Eurocode 3, like the O.I.C., considers that the resistance of class 3 sections is between the elastic and the plastic resistance which explains why the predictions are accurate. However, the figure shows that results are too conservative for class 4 sections. As explained previously, this indicates that the use of the 0.2 % proof strength does not allow to predict accurately the resistance. Moreover, the orange circle shows that as for the sections under compression, the temperature has an impact on the precision for class 4 sections.

In the case of major-axis bending, the influence of the yield strength on the results depends on the section's class. Effectively, for sections that are considered class 1 for all values of F_y, the increase in yield limit leads to less conservative results. On the contrary, for sections that are considered class 3 for all yield limit, the increase in F_y leads to more conservative results. The impact of the yield limit on the accuracy of the results is not pronounced for class 2 and class 4 sections.

6.1.3 Minor-axis bending

Figure 96 is a histogram of the results for sections under minor-axis bending. In this histogram, predictions from the Eurocode 3 and from the O.I.C. proposals are compared to the results obtained with the finite element simulations.

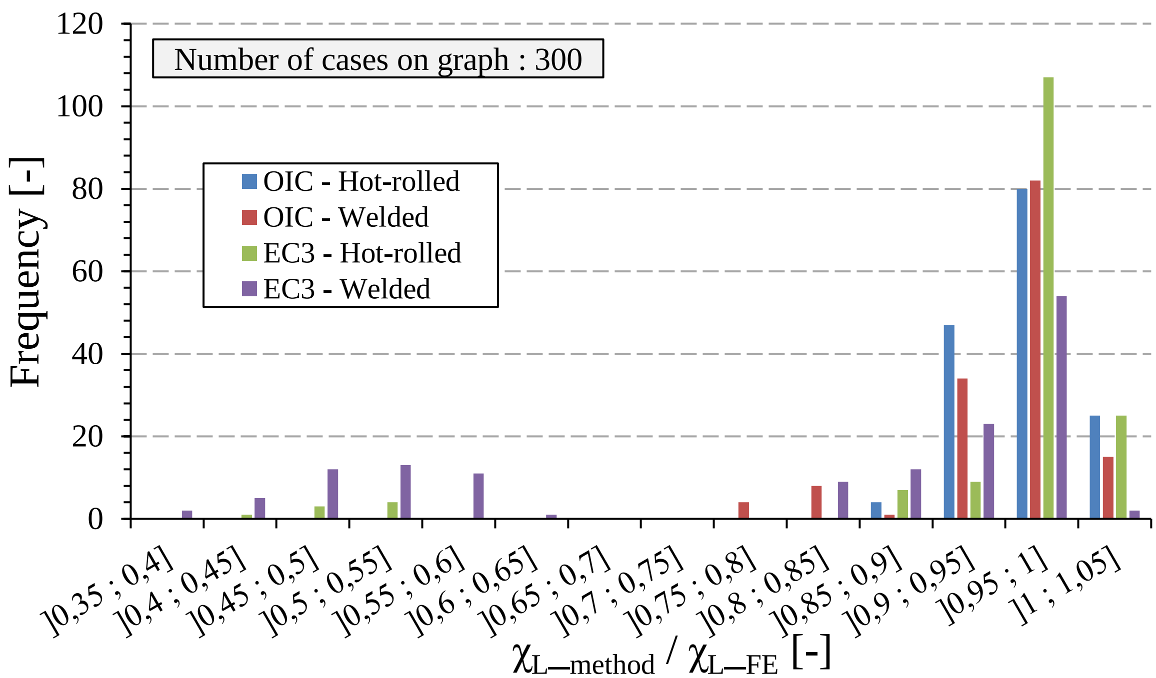

Figure 96 : Accuracy of the results obtained by the O.I.C. proposals and the EC3 for minor-axis bending

This figure shows that both the Eurocode 3 and the O.I.C. proposals lead to a large number of very good predictions for both hot-rolled and welded sections. However, the Eurocode 3 leads to a significant number of very conservative results that can be up to 62 % too conservative.

Results obtained with the Eurocode 3 for sections under minor-axis bending are shown on Figure 97. This figure shows the results obtained for both hot-rolled and welded sections and for the three values of F_y studied.

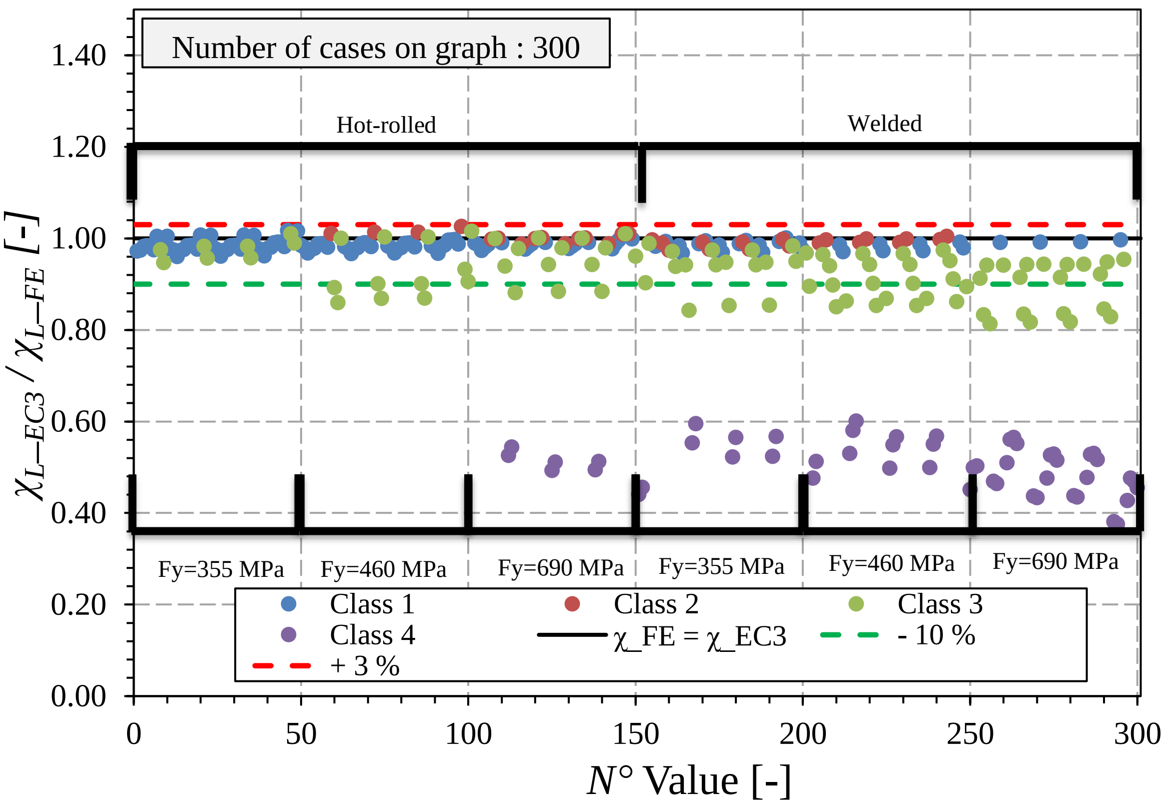

Figure 97 : Performance of the EC3 for sections under minor-axis bending

The figure shows that the results are very accurate for class 1 and 2 sections for which the plastic resistance is calculated. Then, the resistance calculated for class 3 sections is generally good, although some of the results are on the conservative side. The good performance of the EC3 for class 3 sections can be explained by the fact the code uses a resistance that is intermediate between the plastic and the elastic resistance instead of the elastic resistance which is used by many other codes. Finally, the prediction for class 4 sections is again too conservative.

6.1.4 Combined load cases

The performance of the Eurocode 3 and of the O.I.C. proposals for simple load cases has been compared in the previous sections. In all cases, the O.I.C. proposals have proven to be more accurate than the EC3. Figure 98 is an histogram showing the performance of the O.I.C. proposals and of the EC3 for combined load cases. The performance for both hot-rolled and welded sections is shown on the figure.

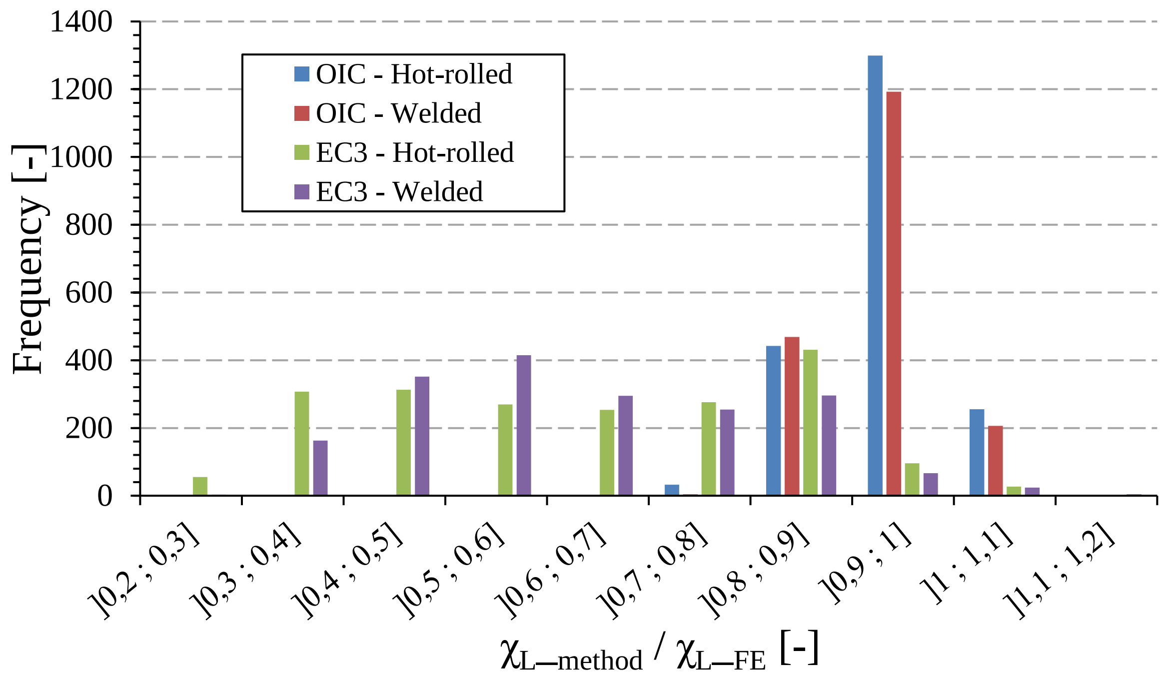

Figure 98 : Accuracy of the results obtained by the O.I.C. proposals and the EC3 for combined load cases

The histogram shows that the performance of the O.I.C. proposals is much better than the performance of the European standards. Effectively, most of the results are between 0.9 and 1.0. The figure also shows that although the performance of the Eurocode 3 for simple load cases was not so bad, the accuracy of the results when it comes to combined load cases is very poor. Effectively, the standards predicts results that are too conservative for both hot-rolled and welded sections.

Figure 99 shows the performance of the Eurocode 3 for hot-rolled sections and welded sections.

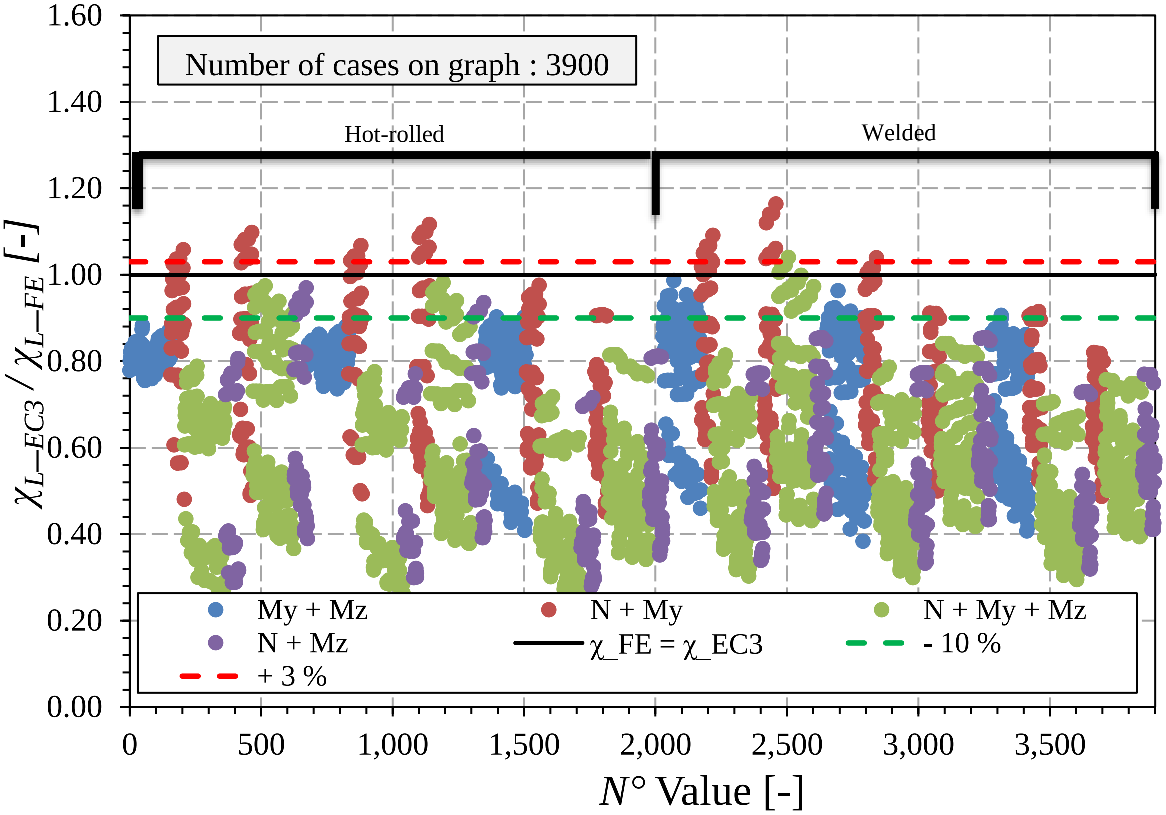

Figure 99 : Performance of the EC3 under combined loading

The figure shows that the predictions of the Eurocode 3 for combined load cases is too conservative for all different cases. The best predictions are obtained for the combination $N + M_y$ but the overall performance is very bad. These results could be explained by the fact that the interaction equations proposed for the fire situation contain some incoherency. Effectively, the equation used for the comparison are the ones provided in Part 1-2 of Eurocode 3. However, the French Annex to the standards proposes corrections for some coefficients used in the equations and specifies that a demand was made for the correction to be introduced in the standards. This can explain why the predictions are so bad.

6.2 Comparison with the Canadian standards

This section presents the comparison of the performance of the Canadian standards to the O.I.C. proposals.

6.2.1 Compression

Figure 100 is a histogram of the results for sections under pure compression. In this histogram, predictions from the Canadian standards and from the O.I.C. proposals are compared to the results obtained with the finite element simulations.

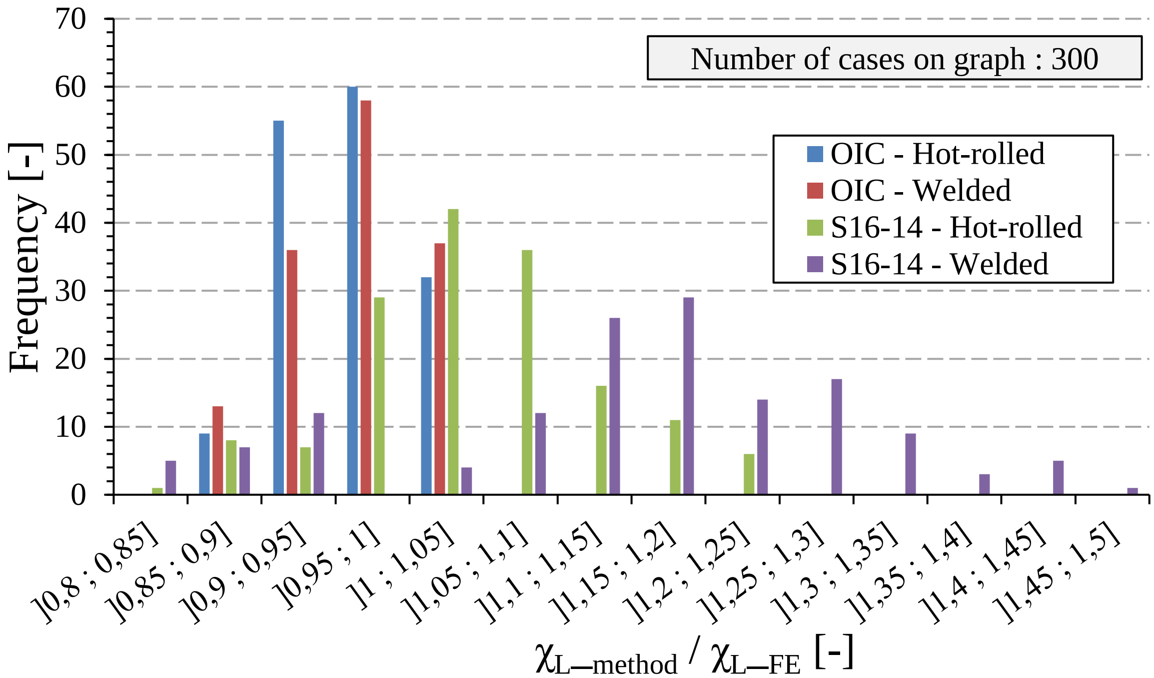

Figure 100 : Accuracy of the results obtained by the O.I.C. proposals and the standard S16-14 for compression

This figure shows that the O.I.C. proposals lead to much more accurate results than the Canadian standards for cross-sections under compression. Moreover, most of the results obtained by the standards are over 1.0 which means that they are unconservative. Some of them are even very unconservative with predictions up to 46 % over the finite element results. The graph also shows that the accuracy of the O.I.C. proposals is similar for both section types while the Canadian standards leads to much less conservative results for welded sections.

Results obtained with the Canadian standards for sections under compression are shown on Figure 101. This figure shows the results obtained for both hot-rolled and welded sections and for the three values of F_y studied.

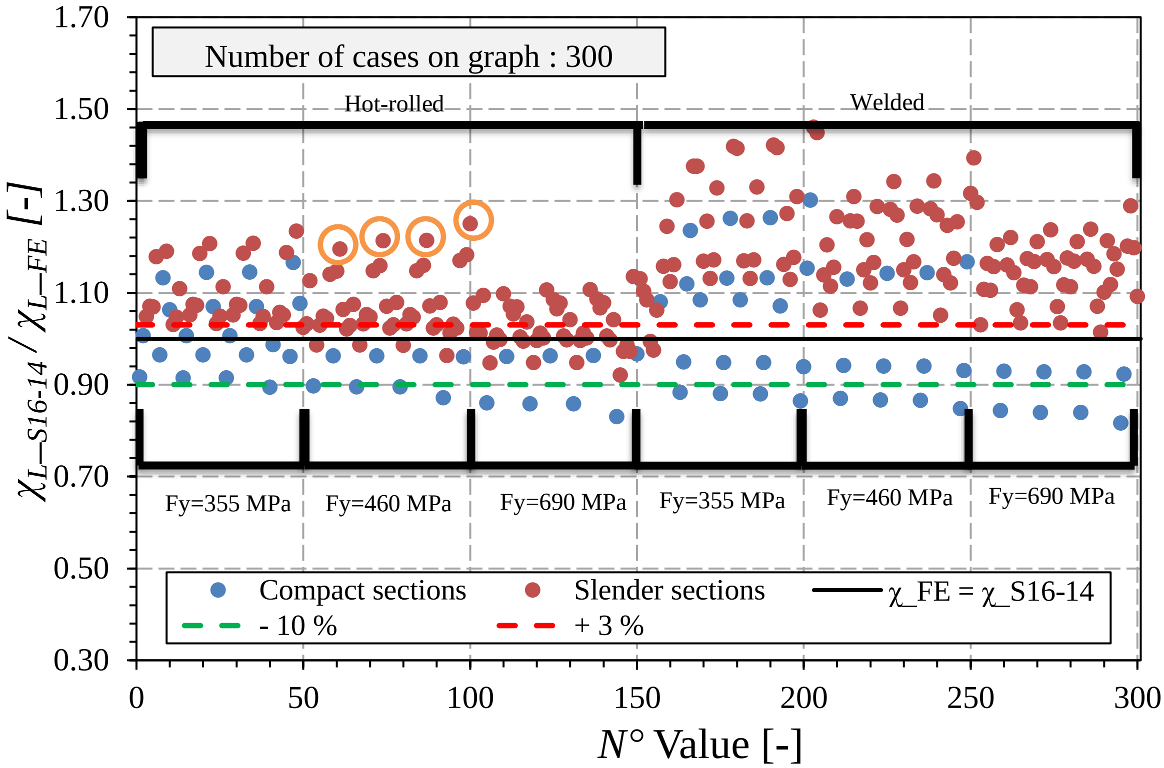

Figure 101 : Performance of the Canadian standards for sections under compression

This figure first shows that the results obtained for hot-rolled sections are generally more accurate than the ones obtained for welded sections. This can be explained by the fact that the same equation is used to calculate the resistance for both type of sections. However, for the same dimensions, hot-rolled sections are more resistant than welded sections for the three following reasons :

1) The area of hot-rolled sections is slightly higher than the area of welded sections because of the radius;
2) The radius present on hot-rolled sections provide more restraint between the web and the flanges which increases the stability of the plates that compose the sections and therefore increases the resistance;
3) Residual stresses are less important in hot-rolled sections which leads to higher resistance.

The first aspect, the area of the section, is considered in the equation. However, the two other aspects are not considered, which leads to unconservative predictions for the welded sections.

Then, the figure shows that most of the very unconservative results are obtained for slender sections. In the Canadian standards, for the fire situation, the resistance is either governed by the cross-section's resistance calculated with the effective area or by the resistance for flexural buckling, which is calculated with the full area for all section classes. Therefore, when flexural buckling governs the resistance, the resistance is overestimated as local buckling is not considered. The equation for flexural buckling presented in the standard S16-14 is the result of the work of Takagi and Deirerlein [48]. In the article presenting this new equation, the authors address the case of slender sections. Effectively, they state the equation leads to unconservative results for slender sections of very short member. However, they explain that the influence of the slender sections on the overall resistance of the member diminishes as the length of the member increases. As unconservative results are obtained for short lengths that are not used in real construction project, the equation was judged adequate. In the case of the present study, cross-sections are studied and therefore very short lengths are considered which explains why so many unconservative results are obtained.

Finally, the value of F_y seams to have an impact on the previsions. For sections that are compact for all values of F_y, the accuracy of the prediction is similar no matter what yield strength is considered. This means that the equation for flexural buckling adequately captures the effect of the increase in yield limit. However, for slender sections, higher values of F_y lead to more conservative results for the same studied sections. This can be explained by the fact that, in the case of compression, the effective area of a slender section is calculated by using the limit between compact and slender sections to reduce the length of the plates. This limit is calculated with the value of F_y. Therefore, the effective area is much smaller for higher value of F_y. In those cases, the resistance the cross-section's resistance is much lower and closer to the real resistance of the section.

As for the temperature, it seems to have a small impact on the performance of the standards. The impact is more pronounced for slender sections. For example, points circled in orange on Figure 101 are results obtained for the same section but at temperature varying from 350°C to 700°C. As the temperature increases, the prediction by the standards become more unconservative. This can be explained by the fact that when classifying the section and when calculating the effective area, properties at ambient temperature are used. Therefore, the increase in slenderness caused by the increase in temperature is not considered which leads to unconservative results.

6.2.2 Major-axis bending

Figure 102 is an histogram of the results for sections under major-axis bending. In this histogram, predictions from the Canadian standards and from the O.I.C. proposals are compared to the results obtained with the finite element simulations.

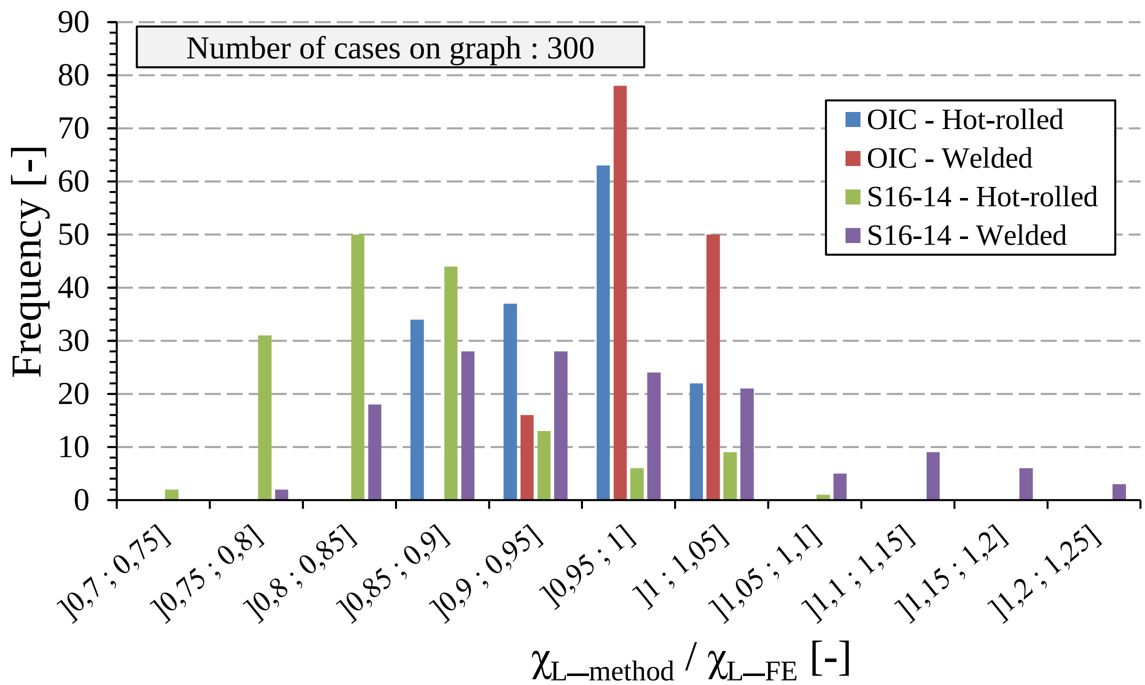

Figure 102 : Accuracy of the results obtained by the O.I.C. proposals and the standard S16-14 for major-axis bending

The graph shows that the O.I.C. proposals are more accurate than the Canadian standards and that the proposal for welded sections is the most performant. Effectively, Figure 102 shows that the predictions by the S16-14 are on the conservative side as most of the results are under 1.0. Moreover, the performance of the standards is very different for hot-rolled and welded sections. Most of the results obtained for the hot-rolled sections are on the conservative side while the standards predict a non negligeable amount of unconservative results for the welded sections.

Results obtained with the Canadian standards for sections under major-axis bending are shown on Figure 103. This figure shows the results obtained for both hot-rolled and welded sections and for the three values of F_y studied.

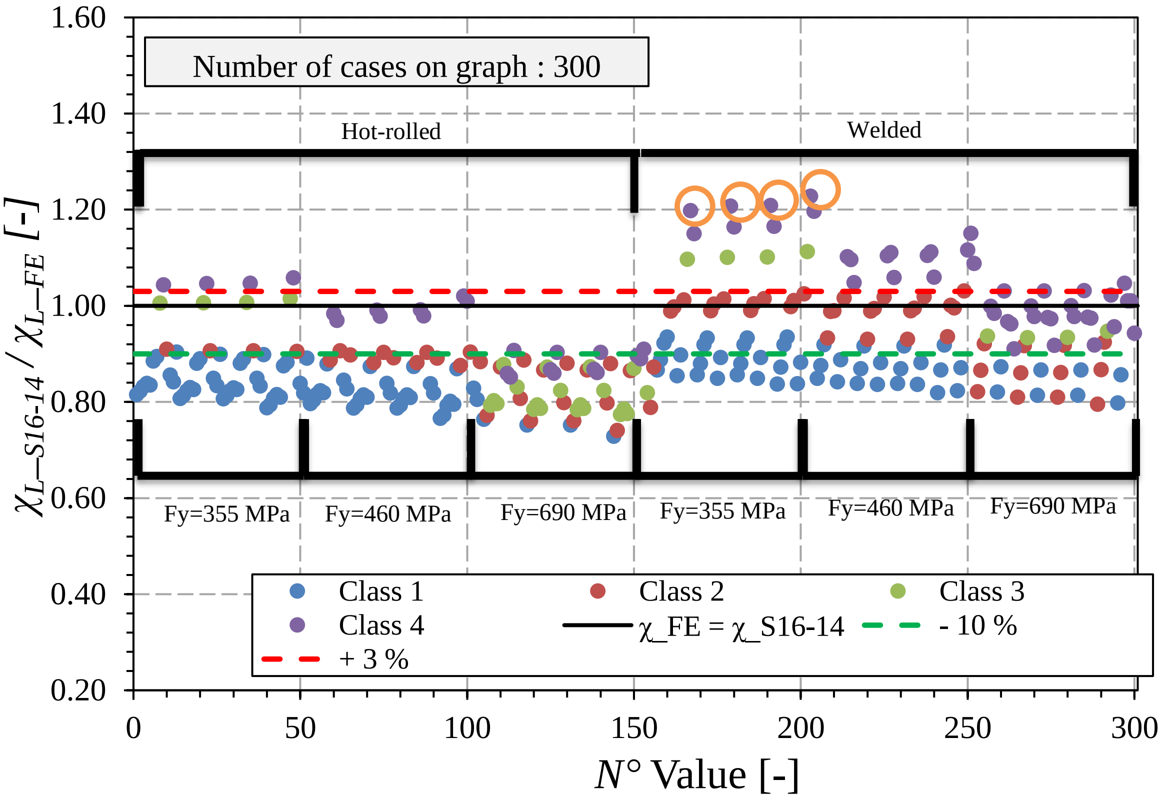

Figure 103 : Performance of the Canadian standards for sections under major-axis bending

The figure shows that the most conservative results are mostly obtained for class 1 cases. The resistance calculated with the Canadian standards is either governed by the cross-section's resistance or by the resistance to lateral torsional buckling. In the case of fire, the cross-section's resistance depends on the cross-section's class. However, the proposed equation for lateral torsional buckling at high temperatures, which calculates a reduction factor for the plastic capacity, is the same for all cross-section's classes. Even at very small lengths and for very compact sections, the reduction factor is significant which explains why such conservative results are obtained for sections that are considered of class 1. As the section's class increases, the formula continues to govern over the cross-section's resistance and progressively becomes less conservative. For class 4 sections, the cross-section's resistance eventually governs over the torsional-lateral buckling. In that case, the predictions become much more conservative.

The value of the yield limit also has a small impact on the accuracy of the results. Effectively, predictions are the most conservative for a yield limit of 690 MPa. As the yield limit increases, the reduction factor in the lateral-torsional buckling equation increases faster than the real reduction in resistance observed in the finite elements results. Therefore, the predictions become more conservative.

Figure 103 also shows that the results are less conservative and even in some case unconservative for the welded sections. As for the sections under compression, this can be explained by the fact that the resistance for both section types is calculated with one equation while hot-rolled sections are in fact more resistant than welded sections as explained in section 6.2.1.

In the case of major-axis bending, the temperature has almost no impact on the accuracy of the results (see orange circles on the figure).

6.2.3 Minor-axis bending

Figure 104 is an histogram of the results for sections under minor-axis bending. In this histogram, predictions from the Canadian standards and from the O.I.C. proposals are compared to the results obtained with the finite element simulations.

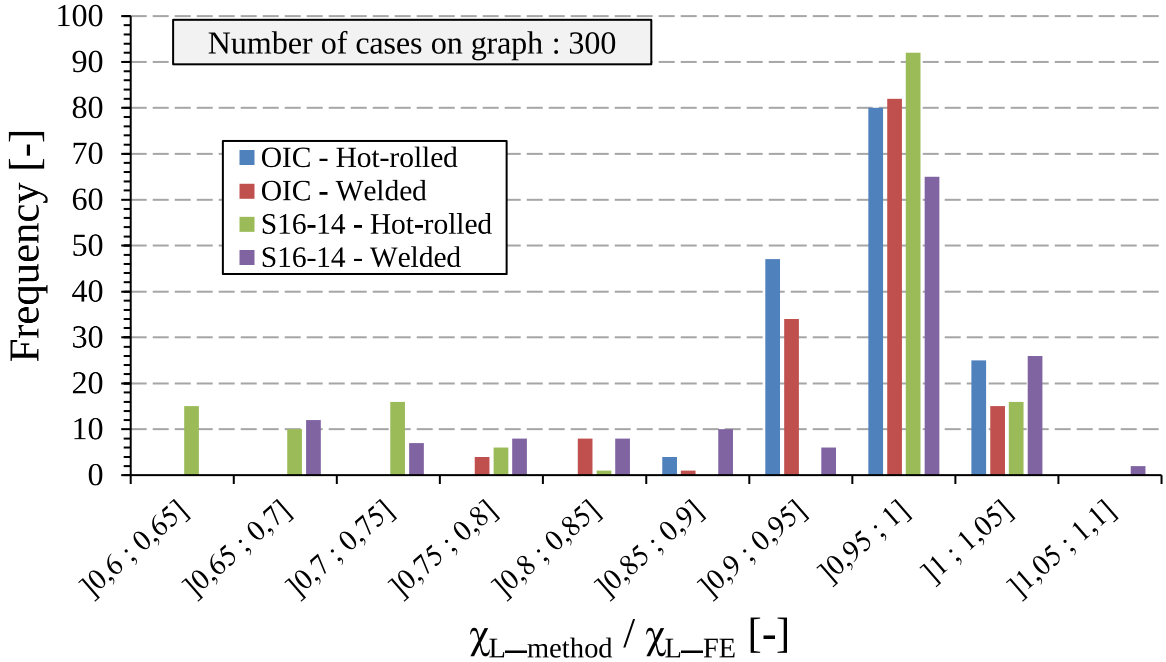

Figure 104 : Accuracy of the results obtained by the O.I.C. proposals and the standard S16-14 for minor-axis bending

This figure shows that both the Canadian standards and the O.I.C. proposals lead to a large number of very good predictions for both hot-rolled and welded sections. However, the Canadian standards leads to more conservative results than the proposal. Those results can be up to 35% too conservative which can lead to uneconomical designs.

Results obtained with the Canadian standards for sections under minor-axis bending are shown on Figure 105. This figure shows the results obtained for both hot-rolled and welded sections and for the three values of F_y studied.

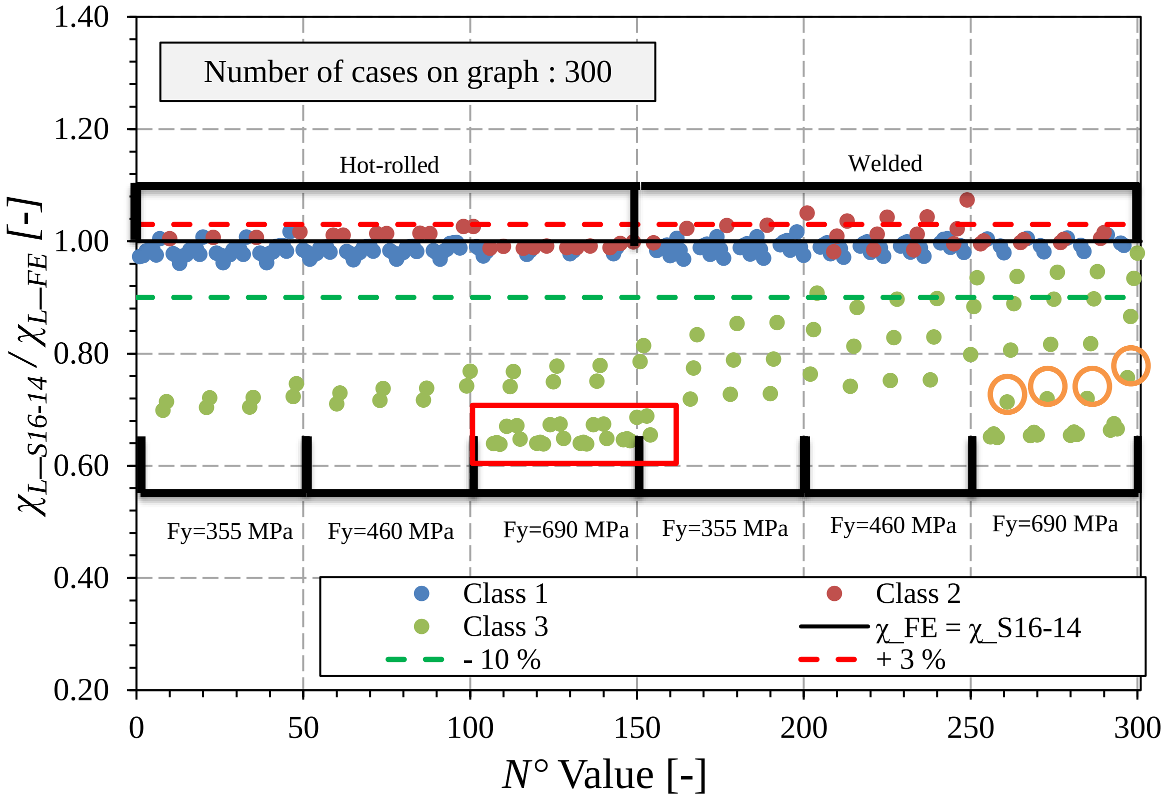

Figure 105 : Performance of the Canadian standards for sections under minor-axis bending

The figure shows that the resistances predicted by the standards for class 1 and 2 sections is very close to the resistances obtained with the finite element model. Those sections are the ones for which it is considered that the full plastic capacity can be reached.

However, the resistance predictions for class 3 sections are overconservative. The resistance for class 3 sections is calculated using elastic properties instead of the plastic properties. However, when a section is very close to the limit between class 2 and 3, the real resistance does not suddenly drop from the plastic resistance to the elastic resistance. Therefore, using elastic properties for class 3 sections leads to conservative results. This drop in resistance can be seen for the sections in the red rectangle on the figure. Those sections are considered of class 1 or 2 for yield limits of 355 MPa and 460 MPa but of class 3 for a yield limit of 690 MPa. Therefore, the prediction of resistance for those sections is very good for lower yield limits but much too conservative for the upper yield limit. The accuracy of the predicted resistance for class 3 sections increases as the sections get closer to the limit for class 4 sections. Effectively, the figure shows that the prediction for sections that are of class 3 for all values of F_y becomes more accurate with the increase of F_y. This can be explained by the fact that sections with higher yield limits are slenderer and their real resistance is therefore closer to the elastic resistance. As no sections considered in this study are of class 4 under minor-axis bending, it was not possible to evaluate the performance of the standards for this type of section.

As for sections under compression presented in section 6.2.1, Figure 105 shows that the results are less conservative for welded sections than for hot-rolled sections. This can again be explained by the fact the same equation is used for both types of section while resistance for welded sections is in fact lower than the resistance of hot-rolled sections as presented in section 6.2.1.

Finally, the figure also shows that, especially for class 3 sections, the results become less conservative as the temperature increases (see orange circles). This can be explained by the fact that the slenderness increases with the increase in temperature which means that the real resistance of the section gets closer to the elastic resistance.

6.2.4 Combined load cases

The performance of the Canadian standards and the O.I.C. proposals for simple load cases has been compared in the previous sections. In all cases, the O.I.C. proposals have proven to be more accurate than the Canadian standards which leads to either too conservative or unconservative predictions for most of the studied sections. The performance of the Canadian standards is therefore expected to be bad for combined load cases as it is based on the combination of the predicted resistances for simple load cases. Figure 106 is an histogram showing the performance of the O.I.C. proposals and of the S16-14 for combined load cases. The performance for both hot-rolled and welded sections is shown on the figure.

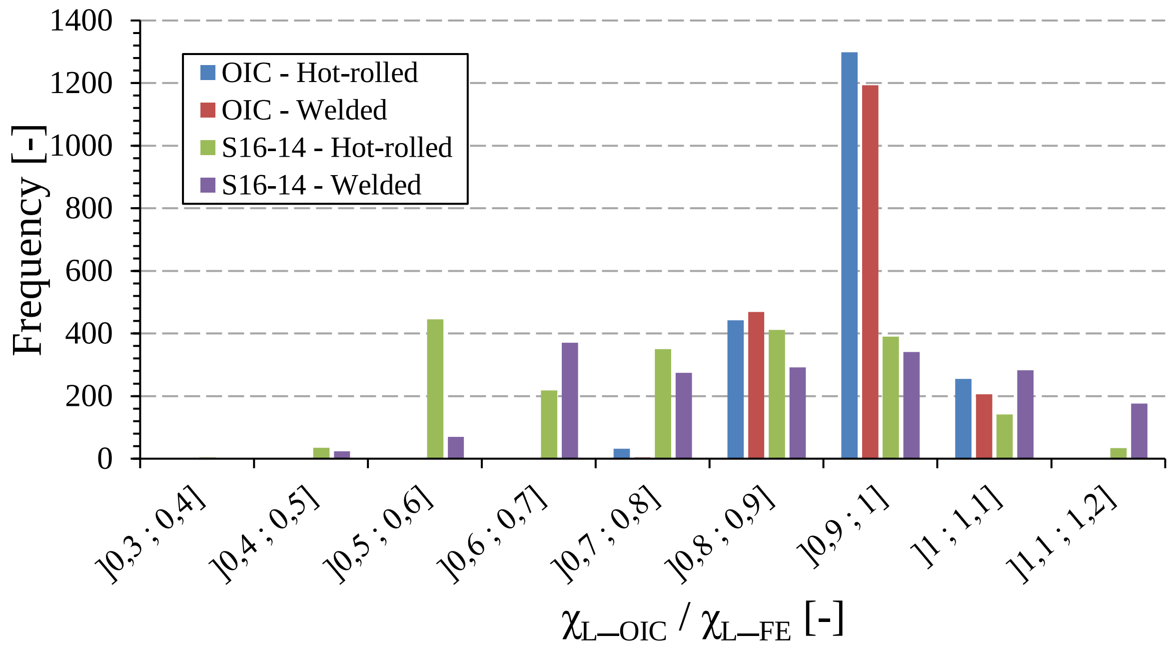

Figure 106 : Accuracy of the results obtained by the O.I.C. proposals and the standard S16-14 for combined load cases

The histogram shows that the performance of the O.I.C. proposals is much better than the performance of the Canadian standards. Effectively, most of the results are between 0.9 and 1.0. The graph also shows that the performance of the proposal is similar for both hot-rolled and welded sections. On the other side, the figure shows that the Canadian standards predict mostly too conservative results for hot-rolled section. As for the welded sections, the standards are more accurate but predicts a large number of unconservative results. Figure 107 shows the performance of the Canadian standards for hot-rolled sections and welded sections.

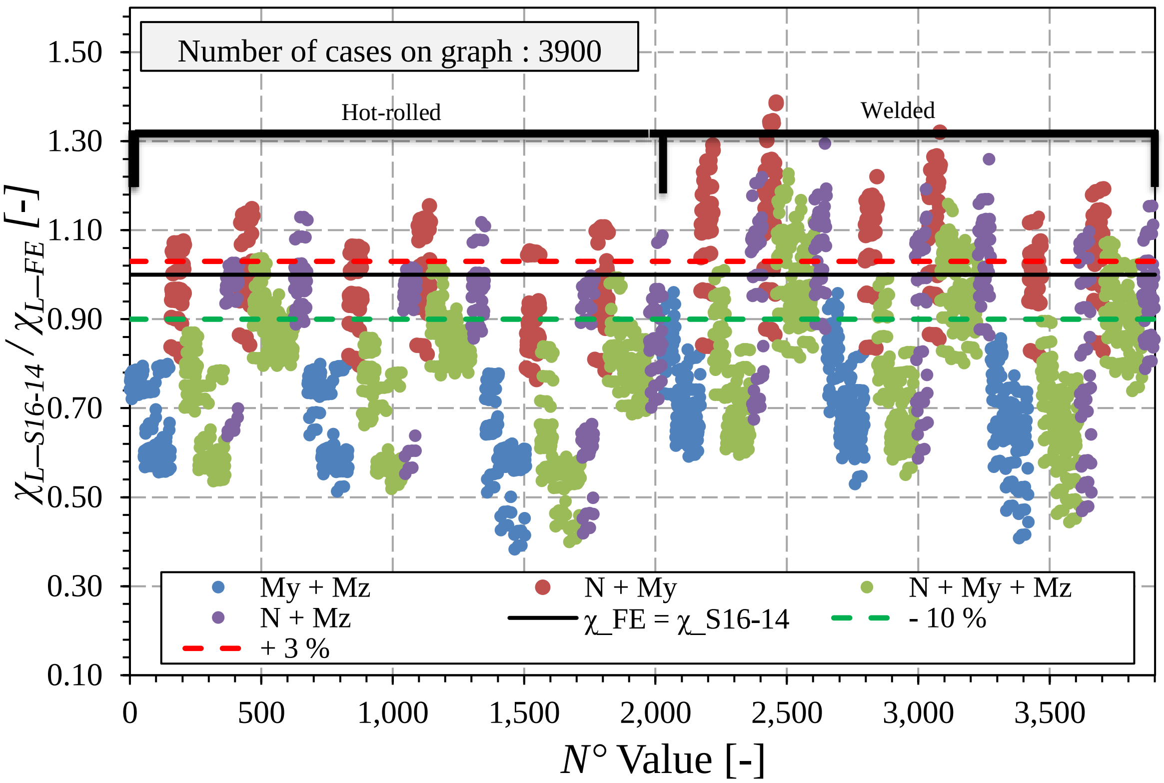

Figure 107 : Performance of the Canadian standard for welded sections under combined loading

The figures confirm that the hot-rolled sections lead to more conservative results than the welded sections which can be explained by the fact that, for the simple load cases studied previously, the prediction is more conservative for hot-rolled sections. In all cases, the results become less conservative for higher values of axial compression with the most conservative results obtained for the $M_y + M_z$ load cases. Moreover, the section's class has an influence on the performance of the standards. Although it is not visible on the presented graph, in most cases, the results obtained for class 3 and 4 sections are more conservative. Effectively, the equation to verify the resistance of sections under combined load cases is more conservative for those classes.

6.3 Comparison with the American standards

This section presents the comparison of the performance of the American standards to the O.I.C. proposals.

6.3.1 Compression

Figure 108 is an histogram of the results for sections under compression. In this histogram, predictions from the American standards and from the O.I.C. proposals are compared to the results obtained with the finite element simulations.

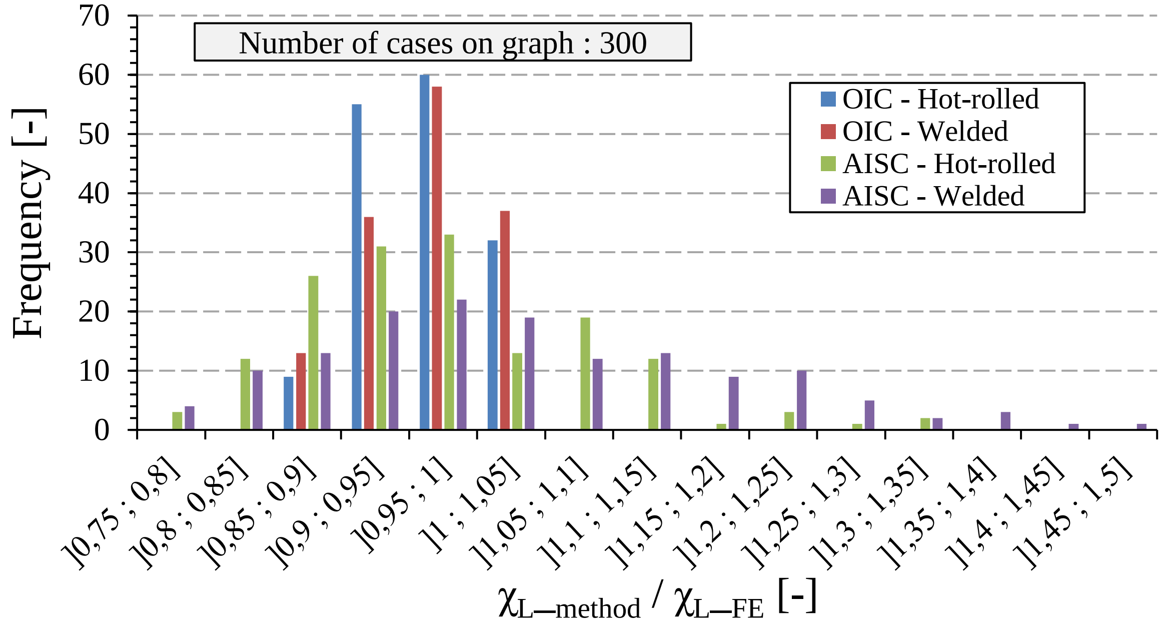

Figure 108 : Accuracy of the results obtained by the O.I.C. proposals and the standard AISC for compression

The figure shows that the O.I.C. proposal leads to more accurate results for both section types. Effectively, the histogram shows that although the mean of the results obtained with the American standards is close to 1.0, the results are very scattered and a lot of results are on the unconservative side.

Results obtained with the American standards for sections under compression are shown on Figure 109. This figure shows the results obtained for both hot-rolled and welded sections and for the three values of F_y studied.

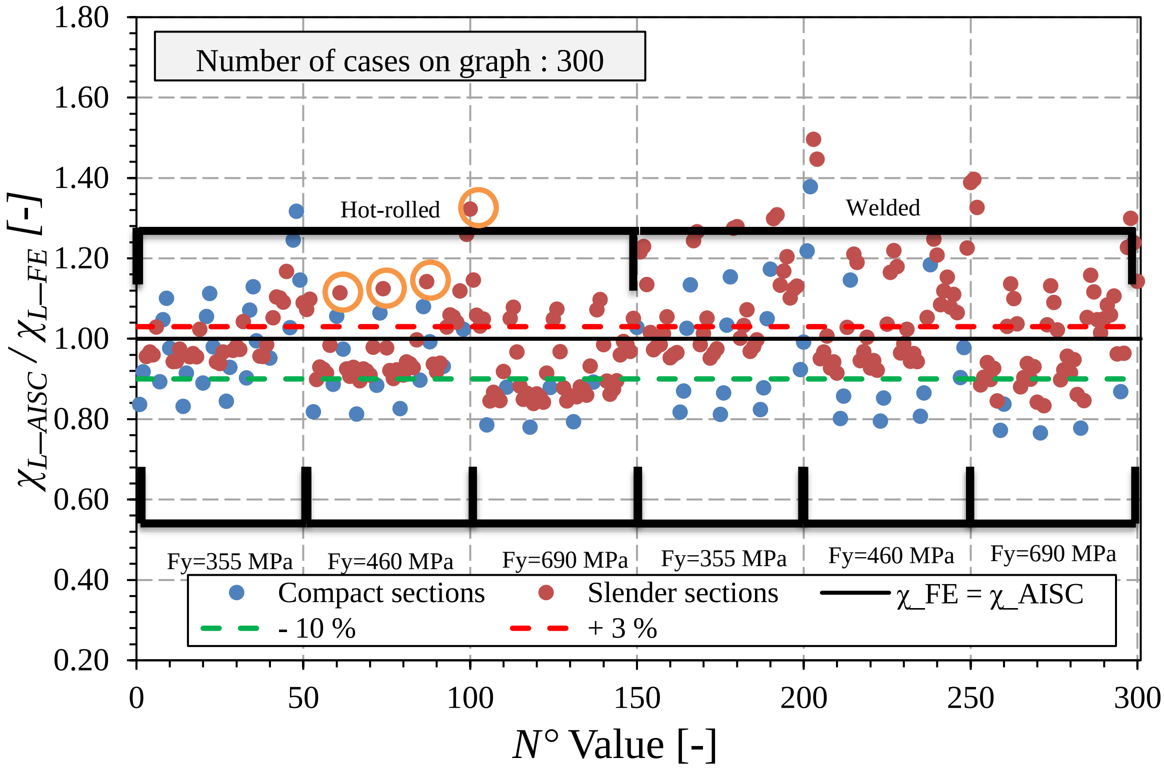

Figure 109 : Performance of the American standards for sections under compression

As for the results obtained with the Canadian standards, this figure first shows that the results obtained for hot-rolled sections are more accurate than the ones obtained for welded sections. This can be again explained by the fact that the same equation is used to calculate the resistance for both types of sections even though the resistance of hot-rolled sections is higher than the resistance of welded sections as explained in section 6.2.1.

The figure also shows that no correlation can be made between the accuracy of the standards and the section's class. Effectively, even though the most conservative results are obtained for compact sections, the results are distributed similarly for both compact and slender sections.

As for the effect of temperature, it can be studied by looking at the results circled in orange. It can be first noticed that the prediction is very similar for the 3 first results that correspond to the temperatures 350°C, 450°C and 550°C. However, the prediction suddenly becomes very much less conservative when the considered temperature is 700°C. For the other standards, the influence of temperature was negligible even at this last high temperature. The bad performance of the Americans standards can be explained by the fact that the reduction factor in the AISC rules are not the same as in the Canadian and European Standards. Table 35 shows the reduction factor used on the yield limit for all considered standards.

Table 35 : Reduction factors for the yield limit ($k_{y,\theta}$) at different temperatures according to all standards

Temperature	EC3 and S16-14	AISC
350°C	1.000	1.000
450°C	0.890	0.889
550°C	0.625	0.632
700°C	0.230	0.264

The table shows that the reduction factors are very similar for temperatures up to 550°C. However, the reduction factor at 700°C, the reduction factor used in the American standards is 15% smaller than the one used in the European and Canadian standards. Therefore, it can be concluded that the reduction factor from the American standards should be modified.

6.3.2 Major-axis bending

Figure 110 is a histogram of the results for sections under major-axis bending. In this histogram, predictions from the American standards and from the O.I.C. proposals are compared to the results obtained with the finite element simulations.

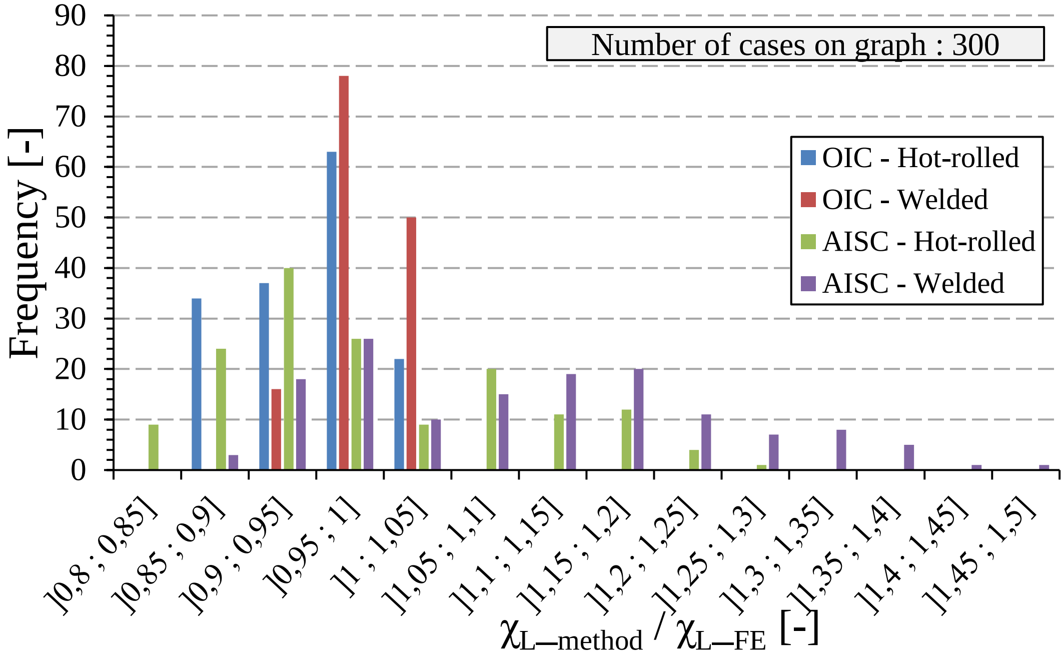

Figure 110 : Accuracy of the results obtained by the O.I.C. proposals and the standard S16-14 for major-axis bending

The graph shows that the O.I.C. proposals are much more accurate than the American standards. Effectively, the American standards leads to some very unconservative results, especially for welded sections.

Results obtained with the American standards for sections under major-axis bending are shown on Figure 111. This figure shows the results obtained for both hot-rolled and welded sections and for the three values of F_y studied. In the American standards, the resistance for major-axis bending is determined based on the classification of both the web and the flanges. In the legend of the figure, C stands for compact while NC means non-compact.

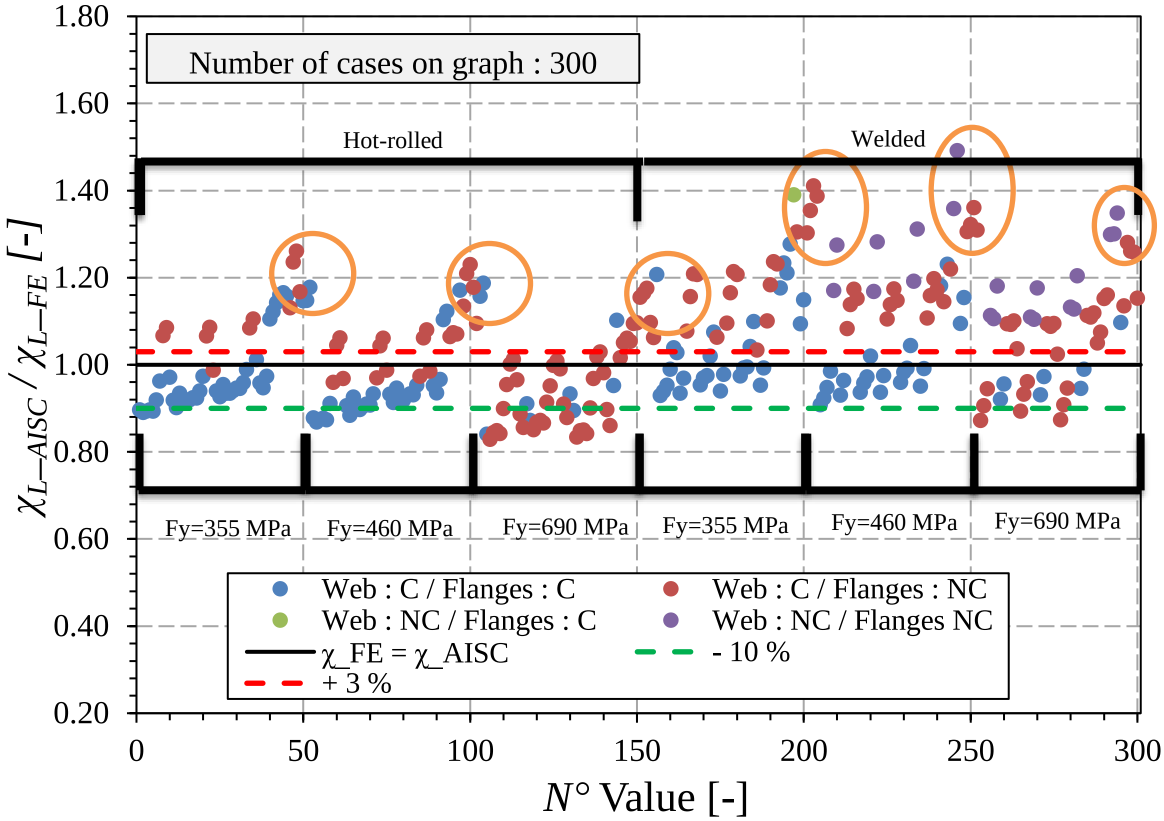

Figure 111 : Performance of the American standards for sections under major-axis bending

The figure first shows that the standard leads to better and more conservative results for hot-rolled sections. Again, this can be explained by the fact that the same equations are used for both section types while hot-rolled section are more resistant. Then, as for the sections under compression, the temperature has an impact on the performance of the standards. Effectively, the results circled in orange are the results for sections at 700°C. As explained in the previous section, the reduction factor for the yield limit at this temperature seams not to be accurate which leads to those unconservative results. The yield limit also has a small impact on the predictions. Effectively, results obtained with higher values of F_y are more conservative.

6.3.3 Minor-axis bending

Figure 112 is a histogram of the results for sections under minor-axis bending. In this histogram, predictions from the American standards and from the O.I.C. proposals are compared to the results obtained with the finite element simulations.

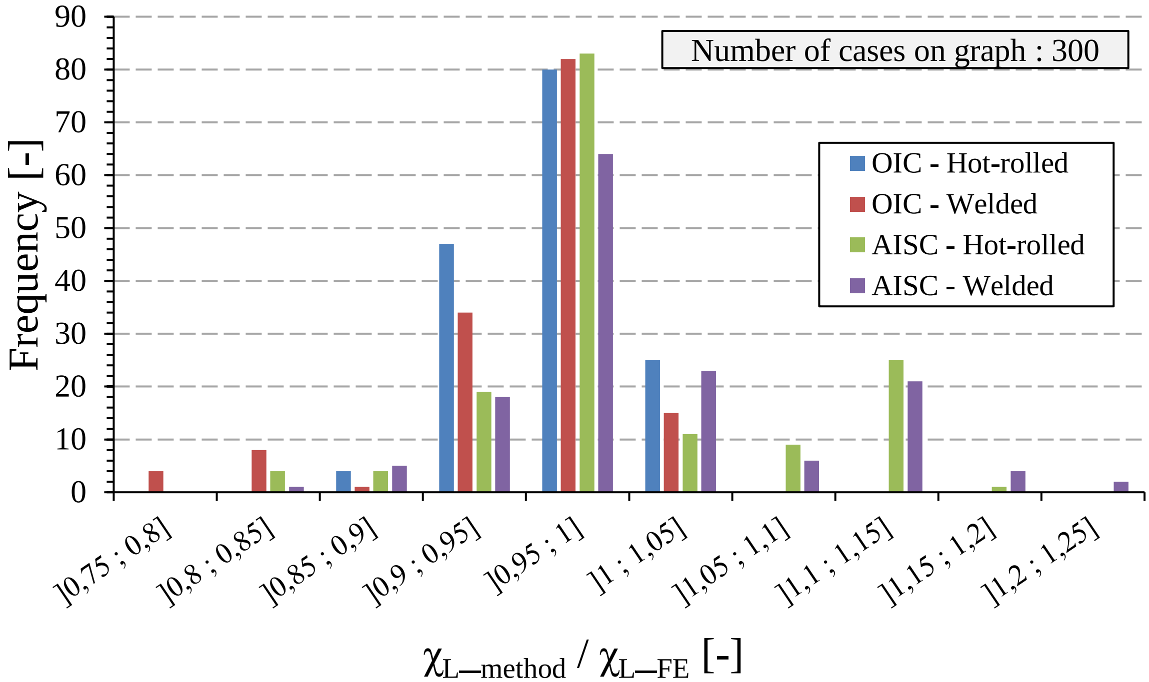

Figure 112 : Accuracy of the results obtained by the O.I.C. proposals and the standard AISC for minor-axis bending

This figure shows that both the American standards and the O.I.C. proposals lead to a large number of very good predictions for both hot-rolled and welded sections. However, the American standards lead to more unconservative results than the O.I.C. proposals.

Results obtained with the American standards for sections under minor-axis bending are shown on Figure 113. This figure shows the results obtained for both hot-rolled and welded sections and for the three values of F_y studied.

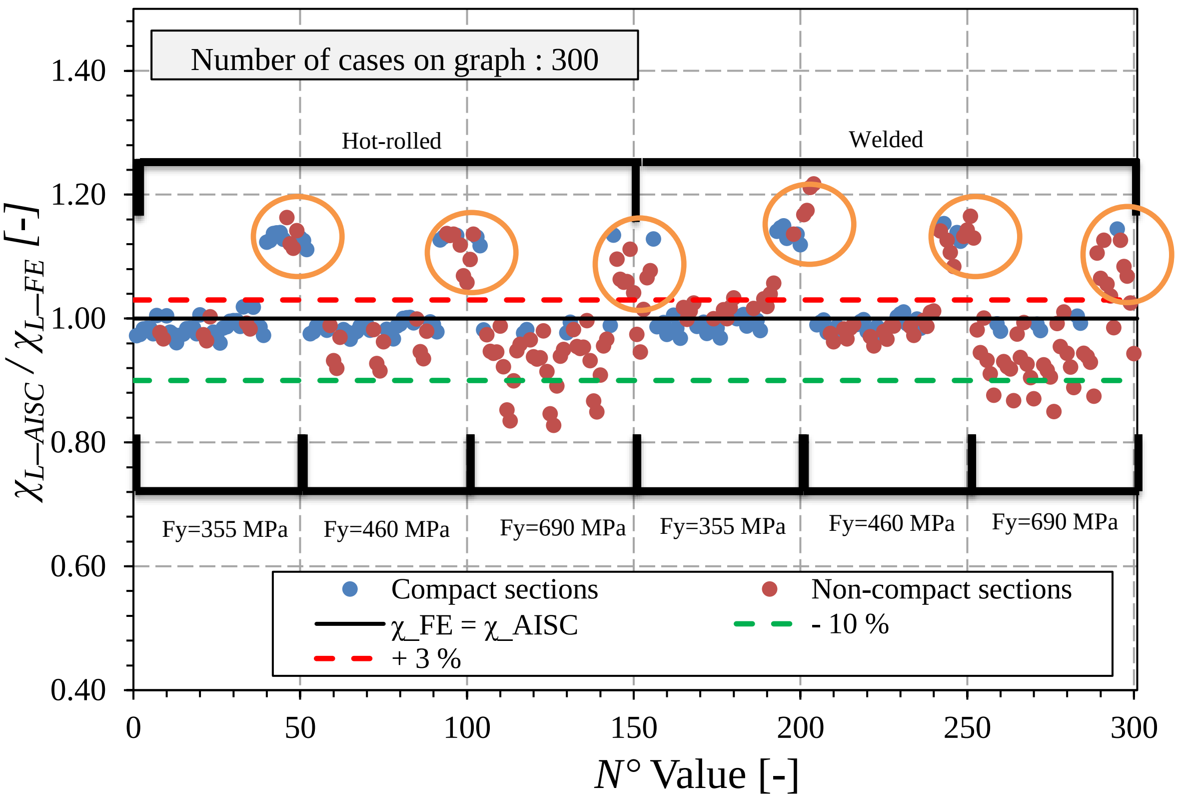

Figure 113 : Performance of the American standards for sections under minor-axis bending

The figure shows that the overall performance of the American standards for sections under minor axis bending is not bad. The standards do however lead to a few unconservative results which are circled in orange. Those results are obtained for sections at 700°C. As explained in section 6.3.1, the reduction factor for the yield limit should be closer to the one found in the European and Canadian standards. The one provided in the American standards does not reduce the yield limit enough at 700°C, which leads to unconservative results. For other temperatures, the prediction of the standards for compact sections is very close to the finite element prediction as in this case the section is able to reach its full plastic capacity. For non-compact sections, the performance is variable. In the American standards, the resistance for non-compact sections is calculated by considering a transition between the plastic resistance and the elastic resistance. For sections that are very close to the limit between compact and non-compact sections, the resistance predictions are very good as they are very close to the plastic capacities. However, as the section becomes slenderer, the prevision becomes more conservative. The prediction is still better than if the sole elastic resistance was considered.

6.3.4 Combined load cases

The performance of the American standards and the O.I.C. proposals for simple load cases has been compared in the previous sections. In all cases, the O.I.C. proposals have proven to be more accurate than the American standards. Figure 114 is a histogram showing the performance of the O.I.C. proposals and of the American standards for combined load cases. The performance for both hot-rolled and welded sections is shown on the figure.

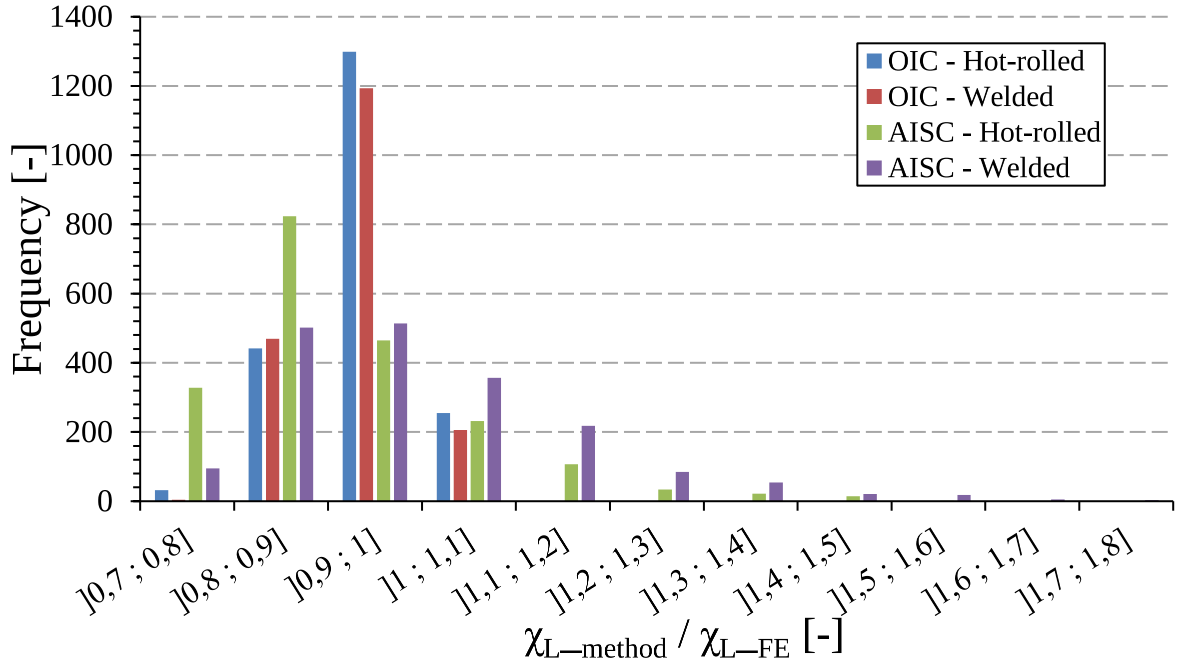

Figure 114 : Accuracy of the results obtained by the O.I.C. proposals and the standard AISC for combined load cases

The histogram shows that, for combined load cases, the performance of the O.I.C. proposals is better than the performance of the American standards. Effectively, most of the results are between 0.9 and 1.0. The graph also shows that the performance of the proposal is similar for both hot-rolled and welded sections. On the other side, the American standards leads to more unconservative results. Some of them are even 80% unconservative which is unacceptable.

Figure 115 shows the performance of the American standards for hot-rolled sections and welded sections.

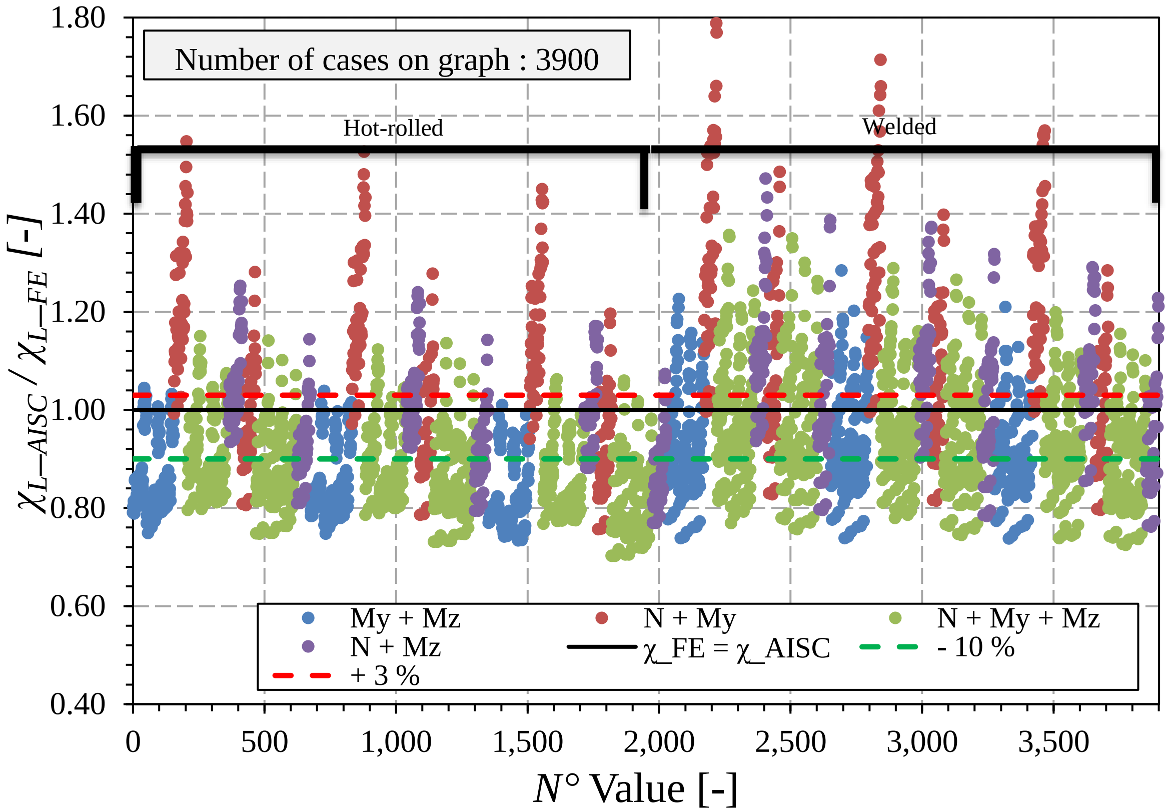

Figure 115 : Performance of the American standards for welded sections under combined loading

The figure confirms that the hot-rolled sections lead to much more conservative results than the welded sections which can be explained by the fact that, for the simple load cases studied previously, the prediction is more conservative for hot-rolled sections. Then, the figure shows that the standard leads to many unconservative results for the combined load cases. However, most of the unconservative results are obtained for sections at 700°C. Therefore, if those results are not considered, the predictions of the American standards for combined load cases present a good accuracy.

Figures also show that the most unconservative results are obtained for the combinations $N + M_y$ and $N + M_z$. However, the predictions for load cases where both bending moments are present a good accuracy.

6.4 Conclusion

In conclusion, the comparisons made allowed to identify many problems with the predictions made by currently used standards and to conclude that the O.I.C. proposals have a much better overall performance. Effectively, even though some standards can provide some accurate predictions for some cases where simple loading is considered, they can lead to either very conservative or very unconservative results. Moreover, the performance of the studied standard is greatly dependant on the load case. On the contrary, both O.I.C. proposals lead to much more accurate results and the good accuracy of the prediction is much more consistent between load cases.

Chapter 7 : Worked examples

The purpose of this section is to compare resistance calculations by means of the O.I.C. proposals with predictions from actual code equations to show the improvement in efficiency and accuracy. The chapter is divided in two parts. First, the cross-section resistance is calculated with the O.I.C. and with different standards. The intent of this part is to show the improvement in efficiency. Then, as the different standards consider the influence of the global behaviour at very short lengths, the calculations are made by considering the overall resistance. The intent of this second part is to show the improvement in accuracy. In all examples, no safety factors are considered which allows to compare the precision of the equations.

The chosen section is a hot-rolled HEA300 with a yield limit of 690 MPa and at a temperature of 700°C. This example was chosen as it considers a slender section (class 4) which requires more tedious calculations. In each part, two examples are presented. First, an example is made for a load case of pure compression. Then, an example is made for the same section under compression and biaxial bending.

7.1 General information and basic data

First, this section presents the dimensions of the considered cross-section. Figure 116 shows the definition of the dimensions.

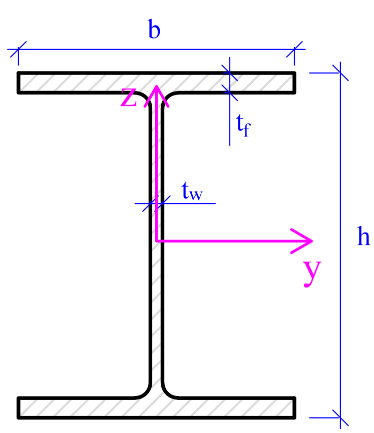

Figure 116 : Definition of the sections' dimensions

All dimensions are presented in Table 36.

Table 36 : Dimensions of the hot-rolled section HEA600

h [mm]	290
b [mm]	300
t_w [mm]	8.5
t_f [mm]	14
r [mm]	27

Table 37 then presents the loading acting on the cross-section.

Table 37 : Loading on the cross-section

	Example 1: compression	Example 2: combined loading
Compression	283.73 kN	408.19 kN
Major-axis bending	-	7.95 kNm
Minor-axis bending	-	2.13 kNm

7.2 Cross-section resistance

As explained previously, this section presents the calculations of the cross-section's resistance with the O.I.C. proposal and with the existing standards.

7.2.1 Example 1: section under compression

7.2.1.1 Cross-section resistance to compression according to the O.I.C. proposal

The steps presented in Chapter 5 are used here to determine the local resistance according to the O.I.C. proposal

1) **Determine the loading acting on the section**

   The loading is presented in Table 37.

2) Calculate n, m_y and m_z using Equations (148), (149) and (150)

For a simple load case, this step is not necessary.

3) Calculate angles ϕ and Θ using Equations (151), (152) and (153)

For a simple load case, this step is not necessary.

4) Determine all required load multipliers

The required load multipliers are the plastic multiplier and the critical multiplier. The plastic multiplier can either be obtained by dividing the plastic resistance by the initial loads or with numerical tool. The critical multiplier is determined using L.B.A. simulations.

Table 38 : Required load multipliers

R_{pl} [-]	R_{cr} [-]
6.293	5.132

5) Calculate reduction factors for simple load cases

The leading parameter γ must first be calculated.

$$\gamma = \frac{\left(\frac{h}{t_w}\right)^2 \cdot \left(\frac{b}{t_f}\right) \cdot \left(\frac{t_w}{t_f}\right)}{100000} = \frac{\left(\frac{290}{8.5}\right)^2 \cdot \left(\frac{300}{14}\right) \cdot \left(\frac{8.5}{14}\right)}{100000} = 0.1514$$

Then, the local relative slenderness λ_L is calculated using the following equation.

$$\lambda_L = \sqrt{\frac{R_{pl}}{R_{cr,L}}} = \sqrt{\frac{6.293}{5.132}} = 1.107$$

Finally, the reduction factor χ_L is calculated with the buckling curve equations.

$$\lambda_0 = 0.2$$

$$\alpha_L = -0.003 + 0.89 \cdot \gamma = -0.003 + 0.89 \cdot 0.1514 = 0.132$$

$$\delta = 0.41 - 2.18 \cdot \gamma = 0.41 - 2.18 \cdot 0.1514 = 0.080$$

$$\phi = 0.5 \cdot \left(1 + \alpha_L \cdot (\lambda_L - \lambda_0) + \lambda_L{}^{\delta}\right) = 0.5 \cdot \left(1 + 0.132 \cdot (1.107 - 0.2) + 1.107^{0.080}\right) = 1.064$$

$$\chi_L = \frac{1}{\phi + \sqrt{\phi^2 - \lambda_L{}^{\delta}}} = \frac{1}{1.064 + \sqrt{1.064^2 - 1.107^{0.080}}} = 0.706$$

Once the reduction factor is calculated, it is possible to calculate the ultimate load multiplier R_b and the ultimate load N_{max}.

$R_b = \chi_L \cdot R_{pl} = 0.706 \cdot 6.293 = 4.44$

$N_{\max} 4.44 \cdot 283.73 = 1259.76 kN$

The result indicates that according to the O.I.C. the initial loading must be multiplied by 4.44 to reach failure.

6) Calculate the reduction factor for the combined load case studied

For a simple load case, this step is not necessary.

7.2.1.2 Cross-section resistance to compression according to the European standards

1) Cross-section classification

Eurocode 3 considers the effect of the temperature when classifying the section by modifying the material parameter ε.

$$\varepsilon = 0.85\left(\frac{235}{f_y}\right)^{0.5} = 0.85\left(\frac{235}{690}\right)^{0.5} = 0.496$$

Web:

$$\frac{c}{t} = \frac{h - 2\cdot t_f - 2\cdot r}{t_w} = \frac{290 - 2\cdot 14 - 2\cdot 27}{8.5} = 24.47 > 38\cdot\varepsilon = 38\cdot 0.496 = 18.848 \rightarrow \text{Class 4}$$

Flanges:

$$\frac{c}{t} = \frac{\frac{b - t_w - 2\cdot r}{2}}{t_f} = \frac{\frac{300 - 8.5 - 2\cdot 27}{2}}{14} = 8.48 > 14\cdot\varepsilon = 14\cdot 0.496 = 6.944 \rightarrow \text{Class 4}$$

The overall section class is 4.

2) Cross-section resistance

In the case of class 4 sections, the European standards propose to calculate effective section properties using the effective width method and the properties at ambient temperature.

$$\varepsilon = \left(\frac{235}{f_y}\right)^{0.5} = \left(\frac{235}{690}\right)^{0.5} = 0.584$$

Web:

$k_\sigma = 4.0$ (uniform stress distribution $\psi = 1.0$)

$$\bar{\lambda}_p = \frac{\frac{\bar{b}}{t}}{28.4\cdot\varepsilon\cdot\sqrt{k_\sigma}} = \frac{\frac{h-2\cdot t_f-2\cdot r}{t_w}}{28.4\cdot\varepsilon\cdot\sqrt{k_\sigma}} = \frac{\frac{290-2\cdot 14-2\cdot 27}{8.5}}{28.4\cdot 0.584\cdot\sqrt{4}} = 0.738$$

$$\rho = \frac{\bar{\lambda}_p - 0.055(3+\psi)}{\bar{\lambda}_p^{\,2}} = \frac{0.738-0.055(3+1)}{0.738^2} = 0.951$$

$$h_{eff} = \rho\cdot\bar{b} = \rho\cdot\left(h-2\cdot t_f-2\cdot r\right) = 0.951\cdot\left(290-2\cdot 14-2\cdot 27\right) = 197.808mm$$

Flanges:

$k_\sigma = 0.43$ (Uniform stress distribution $\psi = 1.0$)

$$\bar{\lambda}_p = \frac{\frac{\bar{b}}{t}}{28.4\cdot\varepsilon\cdot\sqrt{k_\sigma}} = \frac{\frac{\frac{b-t_w-2\cdot r}{2}}{t_f}}{28.4\cdot\varepsilon\cdot\sqrt{k_\sigma}} = \frac{\frac{\frac{300-8.5-2\cdot 27}{2}}{14}}{28.4\cdot 0.584\cdot\sqrt{0.43}} = 0.780$$

$$\rho = \frac{\bar{\lambda}_p - 0.188}{\bar{\lambda}_p^{\,2}} = \frac{0.780-0.188}{0.780^2} = 0.973$$

$$b_{eff} = \rho\cdot\bar{b} = \rho\cdot\frac{b-t_w-2\cdot r}{2} = 0.973\cdot\frac{300-8.5-2\cdot 27}{2} = 115.544mm$$

Effective area and resistance:

$$\begin{aligned} A_{eff} &= 2\cdot\left(\left(2\cdot b_{eff}+t_w+2\cdot r\right)\cdot t_f\right)+\left(h_{eff}+2\cdot r\right)\cdot t_w + r^2\cdot(4-\pi) \\ &= 2\cdot\left(\left(2\cdot 115.544+8.5+2\cdot 27\right)\cdot 14\right)+\left(197.808+2\cdot 27\right)\cdot 8.5+27^2\cdot(4-\pi) \\ &= 10984mm^2 \end{aligned}$$

In Eurocode 3, the 0.2% proof stress is used to calculate the resistance of class 4 sections.

$$N_{fi,\theta,Rd} = A_{eff}\cdot k_{p0.2,\theta}\cdot f_y = 10984\cdot 0.13\cdot 690 = 985kN$$

This resistance corresponds to an ultimate multiplier of 3.47 which means that the initial loading must be multiplied by 3.47 to reach failure according to the European standards.

7.2.1.3 Cross-section resistance to compression according to the Canadian standards

1) Cross-section classification

The classification is made with the properties at ambient temperature.

Web:

$$\frac{h}{w} = \frac{290-2\cdot 14}{8.5} = 30.82 > \frac{670}{\sqrt{F_y}} = \frac{670}{\sqrt{690}} = 25.51 \quad \rightarrow \text{Class 4}$$

Flanges:

$$\frac{b_{el}}{t} = \frac{300/2}{14} = 10.71 > \frac{200}{\sqrt{F_y}} = \frac{200}{\sqrt{690}} = 7.61 \quad \rightarrow \text{Class 4}$$

The overall section class is 4.

2) Cross-section resistance

In the case of class 4 sections under compression, the Canadian standards propose the calculation of an effective area using the reduced flange width and web height according to the maximum width-to-thickness ratio.

$$h_{eff} = \frac{670}{\sqrt{F_y}} \cdot w = \frac{670}{\sqrt{690}} \cdot 8.5 = 216.84mm$$

$$b_{eff} = 2 \cdot \left(\frac{200}{\sqrt{F_y}} \cdot t_f \right) = 2 \cdot \left(\frac{200}{\sqrt{690}} \cdot 14 \right) = 213.08mm$$

$$A_{eff} = 2 \cdot b_{eff} \cdot t_f + h_{eff} \cdot t_w + r^2 \cdot (4 - \pi) = 2 \cdot 213.08 \cdot 14 + 216.84 \cdot 8.5 + 27^2 \cdot (4 - \pi)$$
$$= 8438mm^2$$

The reduced value of F_y at 700°C is calculated using the reduction factor k_y.

$$F_y(T) = F_y \cdot k_y = 690 \cdot 0.23 = 158.7MPa$$

$$C_r(T) = A_{eff} \cdot F_y(T) = 8438 \cdot 158.7 = 1339kN$$

This resistance corresponds to an ultimate multiplier of 4.72 which means that the initial loading must be multiplied by 4.72 to reach failure according to the Canadian standards.

7.2.1.4 Cross-section resistance to compression according to the American standards

1) Cross-section classification

The classification is made with the properties at elevated temperatures.

The reduced value of F_y at 700°C is calculated using the reduction factor k_y.

$$F_y(T) = F_y \cdot k_y = 690 \cdot 0.264 = 182.16MPa$$

The reduced value of E at 700°C is calculated using the reduction factor k_E.

$$E(T) = E \cdot k_E = 210000 \cdot 0.17 = 35700MPa$$

Web:

$$\frac{h}{w}=\frac{290-2\cdot 14-2\cdot 27}{8.5}=24.47>1.49\cdot\sqrt{\frac{E(700)}{F_y(700)}}=1.49\cdot\sqrt{\frac{35700}{182.16}}=20.86\rightarrow\text{Slender}$$

Flanges:

$$\frac{b}{t}=\frac{300/2}{14}=10.71>0.56\cdot\sqrt{\frac{E(700)}{F_y(700)}}=0.56\cdot\sqrt{\frac{35700}{182.16}}=7.84\quad\rightarrow\text{Slender}$$

The section is slender.

2) Cross-section resistance

For slender sections, an effective area must be calculated.

Web:

$$\lambda=\frac{h}{w}=\frac{290-2\cdot 14-2\cdot 27}{8.5}=24.47$$

$$\lambda_r=1.49\cdot\sqrt{\frac{E(700)}{F_y(700)}}=1.49\cdot\sqrt{\frac{35700}{182.16}}=20.86$$

$$c_1=0.18\qquad c_2=1.31$$

$$F_{el}(T)=\left(c_2\cdot\frac{\lambda_r}{\lambda}\right)^2\cdot F_y(T)=\left(1.31\cdot\frac{20.86}{24.47}\right)^2\cdot 182.16=226.42MPa$$

For the cross-section resistance, no length is considered and the critical stress is therefore equal to the yield stress.

$$F_{cr}(T)=F_y(T)=182.16MPa$$

$$h_e=h\left(1-c_1\cdot\sqrt{\frac{F_{el}(T)}{F_{cr}(T)}}\right)\cdot\sqrt{\frac{F_{el}(T)}{F_{cr}(T)}}=208\left(1-0.18\cdot\sqrt{\frac{226.42}{182.16}}\right)\cdot\sqrt{\frac{226.42}{182.16}}=185.36mm$$

Flange:

$$\lambda=\frac{b}{t}=\frac{300/2}{14}=10.71$$

$$\lambda_r=0.56\cdot\sqrt{\frac{E(T)}{F_y(T)}}=0.56\cdot\sqrt{\frac{35700}{182.16}}=7.84$$

$$c_1=0.22\qquad c_2=1.49$$

$$F_{el}(T)=\left(c_2\cdot\frac{\lambda_r}{\lambda}\right)^2\cdot F_y(T)=\left(1.49\cdot\frac{7.84}{10.71}\right)^2\cdot 182.16=215.19MPa$$

For the cross-section resistance, no length is considered and the critical stress is therefore equal to the yield stress.

$$F_{cr}(700) = F_y(700) = 182.16MPa$$

$$b_e = b\left(1 - c_1 \cdot \sqrt{\frac{F_{el}(T)}{F_{cr}(T)}}\right) \cdot \sqrt{\frac{F_{el}(T)}{F_{cr}(T)}} = 300\left(1 - 0.22 \cdot \sqrt{\frac{226.42}{182.16}}\right) \cdot \sqrt{\frac{226.42}{182.16}} = 252.43mm$$

$$A_e = 2 \cdot b_e \cdot t_f + h_e \cdot t_w + r^2 \cdot (4 - \pi) = 2 \cdot 252.43 \cdot 14 + 185.36 \cdot 8.5 + 27^2 \cdot (4 - \pi)$$
$$= 9572mm^2$$

$$P_n(T) = A_e \cdot F_{cr}(T) = 9572 \cdot 182.16 = 1744kN$$

This resistance corresponds to an ultimate multiplier of 6.15 which means that the initial loading must be multiplied by 6.15 to reach failure according to the American standards.

7.2.2 Example 2: section under combined loading

7.2.2.1 Cross-section resistance to combined loading according to the O.I.C. proposal

The steps presented in Chapter 5 are used here to determine the local resistance according to the O.I.C. proposal

1) **Determine the loading on the section**

   The loading is presented in Table 37.

2) **Calculate *n*, m_y and m_z using Equations (148), (149) and (150)**

   To calculate the values of *n*, m_y, and m_z, the plastic resistances must be calculated for all simple load cases. The reduced value of F_y at 700°C is calculated using the reduction factor $k_{y,\theta}$ from Eurocode 3.

   $$F_{y,\theta} = F_y \cdot k_{y,\theta} = 690 \cdot 0.23 = 158.7MPa$$

   The plastic resistances can then be calculated.

   $$N_{pl} = F_{y,\theta} \cdot A = 158.7 \cdot 11253 = 1785.85kN$$

   $$M_{y,pl} = F_{y,\theta} \cdot W_{y,pl} = 158.7 \cdot 1383272 = 219.53kNm$$

   $$M_{z,pl} = F_{y,\theta} \cdot W_{z,pl} = 158.7 \cdot 641166 = 101.75kNm$$

   The values of *n*, m_y and m_z can then be calculated. As explained previously, as the ultimate loads are not yet known, the initial loads are used.

   $$n = \frac{N_i}{N_{pl}} = \frac{408.19}{1785.85} = 0.2286$$

$$m_y = \frac{M_{y,i}}{M_{y,pl}} = \frac{7.95}{219.53} = 0.0362$$

$$m_z = \frac{M_{z,i}}{M_{z,pl}} = \frac{2.13}{101.75} = 0.0209$$

3) Calculate angles ϕ and θ using Equations (151), (152) and (153)

$$\theta = \tan^{-1}\left(\frac{m_z}{m_y}\right) = \tan^{-1}\left(\frac{0.0209}{0.0362}\right) = 30°$$

$$\phi = \tan^{-1}\left(\frac{m_y}{n \cdot \cos(\theta)}\right) = \tan^{-1}\left(\frac{0.0362}{0.2286 \cdot \cos(30)}\right) = 10.37°$$

4) Determine all required load multipliers

The required load multipliers are the plastic multipliers and the critical multipliers for all 3 simple load cases. The plastic multipliers can either be obtained by dividing the plastic resistance by the initial loads or with numerical tool. The critical multipliers are determined using performing L.B.A. simulations. The plastic multiplier for the combined load case is also needed. In this case, for more precision, the multiplier is obtained with numerical tools. Table 38 presents the required load multipliers.

Table 39 : Required load multipliers

Loading	R_{pl} [-]	R_{cr} [-]
N	4.375	3.567
M_y	27.614	28.068
M_z	47.770	65.591
$N + M_y + M_z$	3.839	-

5) Calculate reduction factors for simple load cases;

The leading parameter must first be calculated.

$$\gamma = \frac{\left(\frac{h}{t_w}\right)^2 \cdot \left(\frac{b}{t_f}\right) \cdot \left(\frac{t_w}{t_f}\right)}{100000} = \frac{\left(\frac{290}{8.5}\right)^2 \cdot \left(\frac{300}{14}\right) \cdot \left(\frac{8.5}{14}\right)}{100000} = 0.1514$$

Then, the relative slenderness are calculated using the following equation.

$$\lambda_L = \sqrt{\frac{R_{pl}}{R_{cr,L}}}$$

Figure 51 presents the relative slenderness for all load case.

Table 40 : Relative slenderness for all load cases

Loading	λ_L
N	1.107
M_y	0.992
M_z	0.850

Finally, the reduction factor for each simple load case is calculated with the buckling curve equations. The equations are presented in Figure 52.

Table 41 : Buckling curve equations for all simple load cases

Loading	N	M_y	M_z
λ_0	0.2	0.3	0.3
α_L	$-0.003+0.89\cdot\gamma$	$0.02+0.59\cdot\gamma$	$-0.023+0.88\cdot\gamma$
δ	$0.41-2.18\cdot\gamma$	$1.34-7.02\cdot\gamma$	$0.71-2.24\cdot\gamma$
ϕ	$0.5\cdot\left(1+\alpha_L\cdot\left(\lambda_L-\lambda_0\right)+\lambda_L{}^{\delta}\right)$		
χ_L	$\dfrac{1}{\phi+\sqrt{\phi^2-\lambda_L{}^{\delta}}}$		

The results of the calculation are presented in Table 42.

Table 42 : Calculated parameters

Loading	N	M_y	M_z
λ_0	0.2	0.3	0.3
α_L	0.132	0.109	0.110
δ	0.080	0.277	0.371
ϕ	1.064	1.037	1.001
χ_L	0.706	0.761	0.802

It is important to note here that calculations were redone for the reduction factor for the compression. However, the value had already been calculated in the first example.

6) Calculate the reduction factor for the combined load case studied

Finally, the interaction formula is used to determine the reducing factor for the combined load case.

$$\chi_L = \left[\left(\chi_{L,N}\cdot\cos(\phi)^{0.3}\right)^3 + \left(\chi_{L,My}\cdot\sin(\phi)^{1.5}\cdot\cos(\theta)^{0.18}\right)^3 + \left(\chi_{L,Mz}\cdot\sin(\phi)^4\cdot\sin(\theta)^7\right)^3\right]^{(1/3)}$$

$$= \begin{bmatrix} \left(0.706\cdot\cos(10.37)^{0.3}\right)^3 + \left(0.761\cdot\sin(10.37)^{1.5}\cdot\cos(30)^{0.18}\right)^3 \\ +\left(0.802\cdot\sin(10.37)^4\cdot\sin(30)^7\right)^3 \end{bmatrix}^{(1/3)}$$

$$= 0.703$$

Once the reduction factor is calculated, it is possible to calculate the ultimate multiplier.

$$R_b = \chi_L\cdot R_{pl} = 0.703\cdot 3.839 = 2.70$$

The result indicates that the initial loading must be multiplied by 2.70 to reach failure.

7.2.2.2 Cross-section resistance to combined loading according to the European standards

1) Cross-section classification

Eurocode 3 considers the effect of the temperature when classifying the section by modifying the material parameter ε.

$$\varepsilon = 0.85\left(\frac{235}{f_y}\right)^{0.5} = 0.85\left(\frac{235}{690}\right)^{0.5} = 0.496$$

When the section is subjected to combined loading, the stress distribution is considered when classifying the section.

Web:

$$\sigma_1 = \frac{N_{fi,\theta,Ed}}{A} + \frac{M_{y,fi,\theta,Ed} \cdot \left(h/2 - t_f - r \right)}{I_y}$$

$$= \frac{408.19 \times 10^3}{11253} + \frac{7.95 \times 10^6 \cdot \left(290/2 - 14 - 27 \right)}{183273500} = 40.79$$

$$\sigma_2 = \frac{N_{fi,\theta,Ed}}{A} - \frac{M_{y,fi,\theta,Ed} \cdot \left(h/2 - t_f - r \right)}{I_y}$$

$$= \frac{408.19 \times 10^3}{11253} - \frac{7.95 \times 10^6 \cdot \left(290/2 - 14 - 27 \right)}{183273500} = 31.76$$

$$\psi = \frac{\sigma_2}{\sigma_1} = \frac{31.76}{40.79} = 0.779$$

$$\frac{c}{t} = \frac{h - 2 \cdot t_f - 2 \cdot r}{t_w} = \frac{290 - 2 \cdot 14 - 2 \cdot 27}{8.5} = 24.47$$

$$> \frac{38 \cdot \varepsilon}{0.608 + 0.343 \cdot \psi + 0.049 \cdot \psi^2} = \frac{38 \cdot 0.496}{0.608 + 0.343 \cdot 0.779 + 0.049 \cdot 0.779^2} = 20.83$$

→ Class 4

Flanges:

$$\frac{c}{t} = \frac{\frac{b - t_w - 2 \cdot r}{2}}{t_f} = \frac{\frac{300 - 8.5 - 2 \cdot 27}{2}}{14} = 8.48 > 14 \cdot \varepsilon = 14 \cdot 0.496 = 6.944 \rightarrow \text{Class 4}$$

The overall section class is 4.

2) Cross-section resistance

In the case of class 4 sections, the European standards propose to calculate effective section properties using the effective width method and the properties at ambient temperature. According to the standards, the effective properties must be calculated for each load case separately.

a) Resistance to compression

The cross-section resistance to compression was calculated in the first example.

$$N_{fi,\theta,Rd} = A_{eff} \cdot k_{p0.2,\theta} \cdot f_y = 10984 \cdot 0.13 \cdot 690 = 985kN$$

b) Resistance to major-axis bending

$$\varepsilon = \left(\frac{235}{f_y}\right)^{0.5} = \left(\frac{235}{690}\right)^{0.5} = 0.584$$

The width of the compression flange is first reduced.

Compression flange:

$k_\sigma = 0.43$ (uniform stress distribution $\psi = 1.0$)

$$\bar{\lambda}_p = \frac{\frac{\bar{b}}{t}}{28.4 \cdot \varepsilon \cdot \sqrt{k_\sigma}} = \frac{\frac{\frac{b - t_w - 2 \cdot r}{2}}{t_f}}{28.4 \cdot \varepsilon \cdot \sqrt{k_\sigma}} = \frac{\frac{\frac{300 - 8.5 - 2 \cdot 27}{2}}{14}}{28.4 \cdot 0.584 \cdot \sqrt{0.43}} = 0.780$$

$$\rho = \frac{\bar{\lambda}_p - 0.188}{\bar{\lambda}_p^{\,2}} = \frac{0.780 - 0.188}{0.780^2} = 0.973$$

$$b_{eff} = \rho \cdot \bar{b} = \rho \cdot \frac{b - t_w - 2 \cdot r}{2} = 0.973 \cdot \frac{300 - 8.5 - 2 \cdot 27}{2} = 115.544mm$$

Then, the new centroid of the section must be calculated with the reduced flange.

$$\begin{aligned} A_{eff,cf} &= 2 \cdot \left(\left(2 \cdot b_{eff} + t_w + 2 \cdot r\right) \cdot t_f\right) + \left(h - 2 \cdot t_f\right) \cdot t_w + r^2 \cdot (4 - \pi) \\ &= 2 \cdot \left(\left(2 \cdot 115.544 + 8.5 + 2 \cdot 27\right) \cdot 14\right) + \left(290 - 2 \cdot 14\right) \cdot 8.5 + 27^2 \cdot (4 - \pi) \\ &= 11162mm^2 \end{aligned}$$

$$z_{eff,cf} = \frac{\left(\left(2 \cdot b_{eff} + t_w + 2 \cdot r\right) \cdot t_f\right) \cdot \left(h - \frac{t_f}{2}\right) + \left(\left(h - 2 \cdot t_f\right) \cdot t_w\right) \cdot \left(\frac{\left(h - 2 \cdot t_f\right)}{2} + t_f\right) + \frac{r^2 \cdot (4 - \pi) \cdot h}{2}}{A_{eff,cf}}$$

$$= \frac{\left(\left(2 \cdot 115.544 + 8.5 + 2 \cdot 27\right) \cdot 14\right) \cdot \left(290 - \frac{14}{2}\right) + \left(\left(290 - 2 \cdot 14\right) \cdot 8.5\right) \cdot \left(\frac{\left(290 - 2 \cdot 14\right)}{2} + 14\right) + \frac{27^2 \cdot (4 - \pi) \cdot 290}{2}}{11162}$$

$$= 143.88mm$$

With the position of the new centroid, the stress distribution can be calculated in the web.

Web:

$$\psi = \frac{\sigma_2}{\sigma_1} = \frac{\dfrac{-M_{y,fi,\theta,Ed} \cdot \left(z_{eff,cp} - t_f - r\right)}{I_{y,eff,cf}}}{\dfrac{M_{y,fi,\theta,Ed} \cdot \left(h - t_f - r - z_{eff,cp}\right)}{I_{y,eff,cf}}} = -\frac{z_{eff,cp} - t_f - r}{h - t_f - r - z_{eff,cp}}$$

$$= -\frac{143.88 - 14 - 27}{290 - 14 - 27 - 143.88} = -0.979$$

$$k_\sigma = 7.81 - 6.29 \cdot \psi + 9.78 \cdot \psi^2 = 7.81 - 6.29 \cdot -0.979 + 9.78 \cdot -0.979^2 = 23.33$$

$$\bar{\lambda}_p = \frac{\dfrac{\bar{b}}{t}}{28.4 \cdot \varepsilon \cdot \sqrt{k_\sigma}} = \frac{\dfrac{h - 2 \cdot t_f - 2 \cdot r}{t_w}}{28.4 \cdot \varepsilon \cdot \sqrt{k_\sigma}} = \frac{\dfrac{290 - 2 \cdot 14 - 2 \cdot 27}{8.5}}{28.4 \cdot 0.584 \cdot \sqrt{23.33}} = 0.306$$

$$\rho = \frac{\bar{\lambda}_p - 0.055\left(3 + \psi\right)}{\bar{\lambda}_p^{\,2}} = \frac{0.306 - 0.055\left(3 - 0.979\right)}{0.306^2} = 2.08 > 1 \rightarrow \rho = 1.0$$

Therefore, there is no reduction in the web. The centroid previously calculated can be used to calculate the effective inertia of the cross-section and the effective section modulus.

$$I_{y,eff} = 4 \cdot r^4 \cdot \left(\frac{1}{3} - \frac{\pi}{16} - \left(\frac{1}{9 \cdot \left(4 - \pi\right)}\right)\right) + \frac{r^2 \cdot \left(4 - \pi\right)}{2} \cdot \left(\left(h - t_f - z_{eff}\right) - \left(r - \frac{4 \cdot r}{6 \cdot \left(4 - \pi\right)}\right)\right)^2$$

$$+ \frac{r^2 \cdot \left(4 - \pi\right)}{2} \cdot \left(\left(z_{eff} - t_f\right) - \left(r - \frac{4 \cdot r}{6 \cdot \left(4 - \pi\right)}\right)\right)^2 + \frac{t_w \cdot \left(h - 2 \cdot t_f\right)^3}{12} + h \cdot t_w \cdot \left(\left(\frac{h}{2} - z_{eff}\right)\right)^2$$

$$+ \frac{\left(2 \cdot b_{eff} + t_w + 2 \cdot r\right) \cdot t_f^{\,3}}{12} + \left(2 \cdot b_{eff} + t_w + 2 \cdot r\right) \cdot t_f \cdot \left(h - \frac{t_f}{2} - z_{eff}\right)^2$$

$$+ \frac{b \cdot t_f^{\,3}}{12} + b \cdot t_f \cdot \left(z_{eff} - \frac{t_f}{2}\right)^2$$

$$= 4\cdot 27^4\cdot\left(\frac{1}{3}-\frac{\pi}{16}-\left(\frac{1}{9\cdot(4-\pi)}\right)\right)+\frac{27^2\cdot(4-\pi)}{2}\cdot\left(\begin{array}{l}(290-14-143.88)-\\ \left(27-\frac{4\cdot 27}{6\cdot(4-\pi)}\right)\end{array}\right)^2$$

$$+\frac{27^2\cdot(4-\pi)}{2}\cdot\left((143.88-14)-\left(27-\frac{4\cdot 27}{6\cdot(4-\pi)}\right)\right)^2+\frac{8.5\cdot(290-2\cdot 14)^3}{12}$$

$$+290\cdot 8.5\cdot\left(\left(\frac{290}{2}-143.88\right)\right)^2+\frac{(2\cdot 115.544+8.5+2\cdot 27)\cdot 14^3}{12}$$

$$+(2\cdot 115.544+8.5+2\cdot 27)\cdot 14\cdot\left(290-\frac{14}{2}-143.88\right)^2$$

$$+\frac{300\cdot 14^3}{12}+300\cdot 14\cdot\left(143.88-\frac{14}{2}\right)^2=182634978mm^4$$

$$W_{eff,y}=\frac{I_{y,eff}}{h-z_{eff}}=\frac{182634978}{290-143.88}=1259552mm^3$$

In Eurocode 3, the 0.2% proof stress is used to calculate the resistance of class 4 sections.

$$M_{y,fi,\theta,Rd}=W_{eff,y}\cdot k_{p0.2,\theta}\cdot f_y=1259552\cdot 0.13\cdot 690=113kNm$$

c) Resistance to minor-axis bending

For minor-axis bending, the cross-section reduction is only calculated for the flanges as there is almost no stresses in the web.

$$\psi=\frac{\sigma_2}{\sigma_1}=\frac{\dfrac{M_{z,fi,\theta,Ed}\cdot\left(t_w/2+r\right)}{I_{z,eff,cf}}}{\dfrac{M_{z,fi,\theta,Ed}\cdot\left(b/2\right)}{I_{z,eff,cf}}}=-\frac{t_w/2+r}{b/2}=\frac{8.5/2+27}{300/2}=0.208$$

$$k_\sigma=0.57-0.21\cdot\psi+0.07\cdot\psi^2=0.57-0.21\cdot 0.208+0.07\cdot 0.208^2=0.53$$

$$\bar{\lambda}_p=\frac{\dfrac{\bar{b}}{t}}{28.4\cdot\varepsilon\cdot\sqrt{k_\sigma}}=\frac{\dfrac{\frac{b-t_w-2\cdot r}{2}}{t_f}}{28.4\cdot\varepsilon\cdot\sqrt{k_\sigma}}=\frac{\dfrac{\frac{300-8.5-2\cdot 27}{2}}{14}}{28.4\cdot 0.584\cdot\sqrt{0.208}}=0.703$$

$$\rho = \frac{\bar{\lambda}_p - 0.188}{\bar{\lambda}_p^{\;2}} = \frac{0.703 - 0.188}{0.703^2} = 1.04 > 1.0 \rightarrow \rho = 1.0$$

Therefore, there is no reduction and the elastic modulus is used to calculate the resistance.

$$M_{z,fi,\theta,Rd} = W_{el,z} \cdot k_{p0.2,\theta} \cdot f_y = 420637 \cdot 0.13 \cdot 690 = 37.7kNm$$

d) Interaction equation

For the cross-section resistance of a class 4 section, the following interaction equation is used.

$$\frac{N_{fi,\theta,Ed}}{N_{fi,\theta,Rd}} + \frac{M_{y,fi,\theta,Ed}}{M_{y,fi,\theta,Rd}} + \frac{M_{z,fi,\theta,Ed}}{M_{z,fi,\theta,Rd}} = \frac{408.19}{985} + \frac{7.95}{113} + \frac{2.13}{37.7} = 0.54 \leq 1$$

Since the interaction equation is linear, the ultimate multiplier can be obtained by reversing the result obtained with the interaction formulae. This resistance corresponds to an ultimate multiplier of 1.85 which means that the initial loading must be multiplied by 1.85 to reach failure according to the European standards.

7.2.2.3 Cross-section resistance to combined loading according to the Canadian standards

1) Cross-section classification

The classification is made with the properties at ambient temperature.

Verification to decide which class limits to use for the web:

$$\frac{M_{f,z}}{W_{z,el}} = \frac{2.13 \times 10^6}{424466} = 5.02 \leq 0.9 \cdot \frac{7.95 \times 10^6}{1263955} = 5.66$$

The limits for elements subjected to combined axial compression and major-axis bending must be used.

Web:

$$\frac{h}{w} = \frac{290 - 2 \cdot 14}{8.5} = 30.82 \leq \frac{1100}{\sqrt{F_y}} \cdot \left(1 - 0.39 \cdot \frac{N_f}{N_{pl}}\right) = \frac{1100}{\sqrt{690}} \cdot \left(1 - 0.39 \cdot \frac{408.19}{1785.85}\right) = 38.14$$

→ Class 1

Flanges:

$$\frac{b_{el}}{t}=\frac{300/2}{14}=10.71>\frac{200}{\sqrt{F_y}}=\frac{200}{\sqrt{690}}=7.61 \qquad \rightarrow \text{Class 4}$$

The overall section class is 4.

2) Cross-section resistance

The reduced value of F_y at 700°C needed to calculate the resistance was calculated in the previous example.

a) Resistance to compression

The cross-section resistance to compression was calculated in the first example.

$$C_r(T)=A_{eff}\cdot F_y(T)=8438\cdot 158.7=1339kN$$

b) Resistance to major-axis bending

Since only the flanges are both in compression due to the compression load and are classified as class 4, the Canadian standards recommends reducing the flange width according to the width-to-thickness ratio.

$$b_{eff}=2\cdot\left(\frac{200}{\sqrt{F_y}}\cdot t_f\right)=2\cdot\left(\frac{200}{\sqrt{690}}\cdot 14\right)=213.08mm$$

$$I_{y,eff}=4\cdot r^4\cdot\left(\frac{1}{3}-\frac{\pi}{16}-\left(\frac{1}{9\cdot(4-\pi)}\right)\right)+r^2\cdot(4-\pi)\cdot\left(\left(\frac{h-2\cdot t_f}{2}\right)-\left(r-\frac{4\cdot r}{6\cdot(4-\pi)}\right)\right)^2$$
$$+\frac{t_w\cdot(h-2\cdot t_f)^3}{12}+2\cdot\left(\frac{b_{eff}\cdot t_f^{\,3}}{12}+b_{eff}\cdot t_f\cdot\left(\frac{h-t_f}{2}\right)^2\right)$$

$$=4\cdot 27^4\cdot\left(\frac{1}{3}-\frac{\pi}{16}-\left(\frac{1}{9\cdot(4-\pi)}\right)\right)+27^2\cdot(4-\pi)\cdot\left(\left(\frac{290-2\cdot 14}{2}\right)-\left(27-\frac{4\cdot 27}{6\cdot(4-\pi)}\right)\right)^2$$
$$+\frac{8.5\cdot(290-2\cdot 14)^3}{12}+2\cdot\left(\frac{213.08\cdot 14^3}{12}+213.08\cdot 14\cdot\left(\frac{290-14}{2}\right)^2\right)=136304530mm^4$$

$$W_{y,eff}=\frac{I_{y,eff}}{h/2}=\frac{136304530}{290/2}=940031mm^3$$

$$M_{ry}(T)=W_{y,eff}\cdot F_y(T)=940031\cdot 158.7=149kNm$$

c) **Resistance to minor-axis bending**

Again, since only the flanges are classified as class 4, the Canadian standards recommends reducing the flange width according to the width-to-thickness ratio.

$$b_{eff} = 2\cdot\left(\frac{200}{\sqrt{F_y}}\cdot t_f\right) = 2\cdot\left(\frac{200}{\sqrt{690}}\cdot 14\right) = 213.08mm$$

$$I_{z,eff} = 4\cdot r^4\cdot\left(\frac{1}{3}-\frac{\pi}{16}-\left(\frac{1}{9\cdot(4-\pi)}\right)\right)+r^2\cdot(4-\pi)\cdot\left(\left(\frac{t_w}{2}\right)-\left(r-\frac{4\cdot r}{6\cdot(4-\pi)}\right)\right)^2$$
$$+\frac{t_w^{\ 3}\cdot\left(h-2\cdot t_f\right)}{12}+2\cdot\left(\frac{b_{eff}^{\ 3}\cdot t_f}{12}\right)$$

$$= 4\cdot 27^4\cdot\left(\frac{1}{3}-\frac{\pi}{16}-\left(\frac{1}{9\cdot(4-\pi)}\right)\right)+27^2\cdot(4-\pi)\cdot\left(\left(\frac{8.5}{2}\right)-\left(27-\frac{4\cdot 27}{6\cdot(4-\pi)}\right)\right)^2$$
$$+\frac{8.5^3\cdot(h-2\cdot 14)}{12}+2\cdot\left(\frac{213.08^3\cdot 14}{12}\right) = 22639697mm^4$$

$$W_{z,eff} = \frac{I_{z,eff}}{b_{eff}/2} = \frac{22639697}{213.08/2} = 212391mm^3$$

$$M_{rz}(T) = W_{z,eff}\cdot F_y(T) = 530546\cdot 158.7 = 33.7kNm$$

d) **Interaction equation**

For the cross-section resistance of a class 4 section, the following interaction equation is used.

$$\frac{C_f}{C_r(T)}+\frac{U_{1y}\cdot M_{fy}}{M_{ry}(T)}+\frac{U_{1z}\cdot M_{fz}}{M_{rz}(T)}\leq 1$$

For the cross-section resistance, the length is considered to be equal to 0. Therefore:

$$U_{1y} = U_{1z} = 1.0$$

$$\frac{408.19}{1339}+\frac{7.95}{149}+\frac{2.13}{33.7} = 0.42$$

Since the interaction equation is linear, the ultimate multiplier can be obtained by reversing the result obtained with the interaction formulae. This resistance corresponds to an ultimate multiplier of 2.38 which means that the initial loading must be multiplied by 2.38 to reach failure according to the Canadian standards.

7.2.2.4 Cross-section resistance to combined loading according to the American standards

1) Cross-section classification

The classification is made with the properties at elevated temperatures.

The reduced value of F_y at 700°C is calculated using the reduction factor k_y.

$$F_y(T) = F_y \cdot k_y = 690 \cdot 0.264 = 182.16 MPa$$

The reduced value of E at 700°C is calculated using the reduction factor k_E.

$$E(T) = E \cdot k_E = 210000 \cdot 0.17 = 35700 MPa$$

a) Compression

Web: Slender

Flanges: Slender

b) Major-axis bending

Web:

$$\frac{h}{w} = \frac{290 - 2 \cdot 14 - 2 \cdot 27}{8.5} = 24.47 < 3.76 \cdot \sqrt{\frac{E(700)}{F_y(700)}} = 3.76 \cdot \sqrt{\frac{35700}{182.16}} = 52.64 \rightarrow$$

Compact

Flanges:

$$\frac{b}{t} = \frac{300/2}{14} = 10.71 < 1 \cdot \sqrt{\frac{E(700)}{F_y(700)}} = 1 \cdot \sqrt{\frac{35700}{182.16}} = 14.00 \quad \rightarrow \text{Non-compact}$$

c) Minor-axis bending

Flanges:

$$\frac{b}{t} = \frac{300/2}{14} = 10.71 < 1 \cdot \sqrt{\frac{E(700)}{F_y(700)}} = 1 \cdot \sqrt{\frac{35700}{182.16}} = 14.00 \quad \rightarrow \text{Non-compact}$$

2) Cross-section resistance

a) Compression

$$P_n(T) = A_e \cdot F_{cr}(T) = 9572 \cdot 182.16 = 1744 kN$$

b) Major-axis bending

For a cross-section with a compact web and non-compact flanges, two resistances must be calculated: The resistance to flexural-torsional buckling and the resistance to the compression flange local buckling. For the cross-section resistance, the considered length is 0.

i) Lateral-torsional buckling

When no length is considered, the resistance to lateral-torsional buckling is given by the plastic resistance.

$$M_n(700) = M_p(700) = 252kNm$$

ii) Compression flange local buckling

$$\lambda = \frac{b}{t} = \frac{300/2}{14} = 10.71$$

$$\lambda_{pf} = 0.38 \cdot \sqrt{\frac{E(T)}{F_y(T)}} = 0.38 \cdot \sqrt{\frac{35700}{182.16}} = 5.32$$

$$\lambda_{rf} = 1 \cdot \sqrt{\frac{E(700)}{F_y(700)}} = 1 \cdot \sqrt{\frac{35700}{182.16}} = 14.00$$

$$M_n(T) = M_p(T) - (M_p(T) - 0.7 \cdot F_y(T) \cdot S_x) \cdot \left(\frac{\lambda - \lambda_{pf}}{\lambda_{rf} - \lambda_{pf}} \right)$$

$$= 252 - (252 - 0.7 \cdot 182.16 \cdot 1259552) \cdot \left(\frac{10.71 - 5.32}{14 - 5.32} \right) = 195kNm$$

c) Minor-axis bending

For a cross-section with non-compact flanges, the resistance is either governed by the yielding or by the flange local buckling.

i) Yielding

$$M_n(700) = M_p(700) = 117kNm$$

ii) Flange local buckling

$$\lambda = \frac{b}{t} = \frac{300/2}{14} = 10.71$$

$$\lambda_{pf} = 0.38 \cdot \sqrt{\frac{E(T)}{F_y(T)}} = 0.38 \cdot \sqrt{\frac{35700}{182.16}} = 5.32$$

$$\lambda_{rf} = 1 \cdot \sqrt{\frac{E(T)}{F_y(T)}} = 1 \cdot \sqrt{\frac{35700}{182.16}} = 14.00$$

$$M_n(T) = M_p(T) - (M_p(T) - 0.7 \cdot F_y(T) \cdot S_y) \cdot \left(\frac{\lambda - \lambda_{pf}}{\lambda_{rf} - \lambda_{pf}} \right)$$

$$= 252 - (252 - 0.7 \cdot 182.16 \cdot 420210) \cdot \left(\frac{10.71 - 5.32}{14 - 5.32} \right) = 77.5 kNm$$

3) Interaction equation

$$\frac{P_r}{P_n(T)} = \frac{408.19}{1744} = 0.23 \geq 0.2$$

$$\frac{P_r}{P_n(T)} + \frac{8}{9} \cdot \left(\frac{M_{rx}}{M_{nx}(T)} + \frac{M_{ry}}{M_{ny}(T)} \right) = \frac{408.19}{1744} + \frac{8}{9} \cdot \left(\frac{7.95}{195} + \frac{2.13}{77.5} \right) = 0.29 \leq 1.0$$

Since the interaction equation is linear, the ultimate multiplier can be obtained by inversing the result obtained with the interaction formulae. This resistance corresponds to an ultimate multiplier of 3.39 which means that the initial loading must be multiplied by 3.39 to reach failure according to the American standards.

7.2.3 Analysis and comparison of the results

The main purpose of this first section was to compare the improvement in efficiency and simplicity. The examples show that the length of resolution is variable from one calculation method to the other. However, the calculations with the O.I.C. proposal are significantly more efficient than the calculations with other standards. First, the equations used are simpler that the ones used in the different standards. Effectively, the equations are very short, and the parameters used in the equation are small numbers which helps prevent errors. Then, the great advantage of the O.I.C. proposal is that the calculation of the resistance is done in the same way for all load cases. Effectively, the equations for all load cases are very similar. The calculation process is therefore much easier to follow.

This first section also allows to compare the prediction of various standards for the cross-section resistance with the O.I.C. proposal. As the length used in the numerical simulation is very short, the ultimate resistance obtained is effectively the cross-section resistance and it is therefore expected for the cross-section resistance calculated with the standards to be close to the ones obtained numerically. Table 43 presents the ultimate multiplier obtained with all calculation methods.

Table 43 : Ultimate load multiplier according to the finite elements simulations and to the various calculation methods

	F.E.	O.I.C.	EC3	S16-14	AISC
N	4.27	4.44	3.47	4.72	6.15
$N + M_y + M_z$	2.82	2.70	1.85	2.38	3.39

The results show that there is a lot of variability between the results. It also shows that the multiplier obtained with the O.I.C. is much more precise than the ones obtained with other standards. Table 44 shows the ratio between the multipliers obtained with the calculation methods and the multiplier obtained numerically which allows to compare efficiently the precision of each calculation method.

Table 44 : Ratio between the ultimate multiplier calculated by the various calculation method and the ultimate multiplier obtained by finite elements simulations

	O.I.C./F.E.	EC3/F.E.	S16-14/F.E.	AISC/F.E.
N	1.04	0.81	1.11	1.44
$N + M_y + M_z$	0.96	0.66	0.84	1.20

Results show that the O.I.C. is the most precise calculation method as it gives predictions only 4% away from the real value. Although the prediction is on the unsafe side, it is judged adequate as it is only 4% on the unconservative side and as no safety factor was used in the calculations. Eurocode 3 gives predictions that are very conservative (up to 34%), the S16-14 gives either too unconservative results or too conservative results and AISC provides results that are way too unconservative (up to 44%). However, as explained previously, overall equations that consider the length must be used to adequately compare the precision as the standards consider the influence of global instabilities even at very short lengths.

7.3 Resistance by considering the global resistance equations

As explained previously, this section presents the calculations of the overall resistance with the existing standards. For the O.I.C. proposals the resistance is the same as the one calculated in the previous section. Effectively, Figure 117 presents the failure mode of the section for both load cases. In both cases, the figure shows that global instabilities do not occur, and that failure is due to local buckling of the plates which indicates that the length does not have an influence on the cross-section resistance.

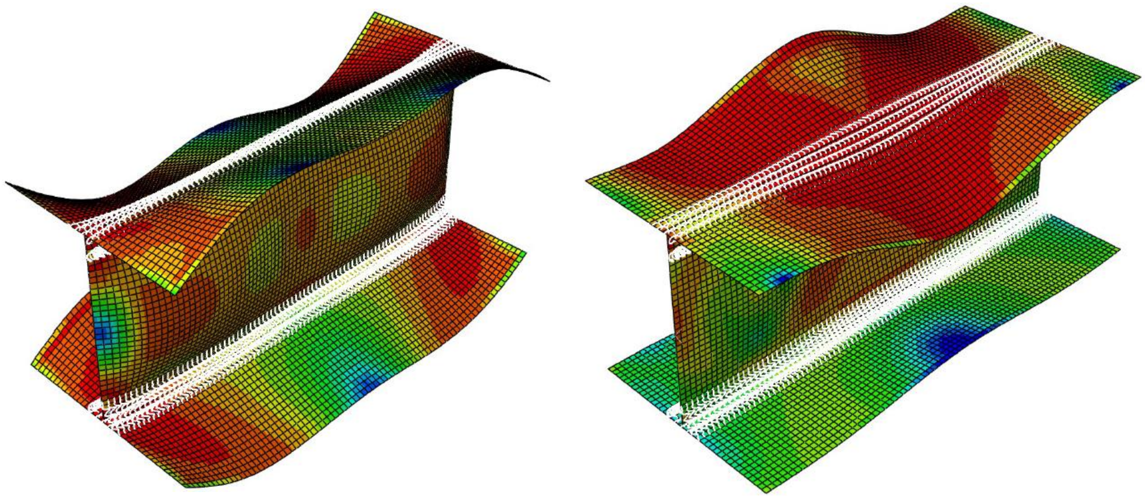

a) b)

Figure 117 : Failure mode of the cross-section under a) compression and b) combined loading

It is however necessary to consider the length when calculating the resistance according to several standards as the equations are formulated to consider global instabilities even at very short lengths. Considering the member resistance therefore allows for an accurate comparison of the precision between standards and the O.I.C. proposal.

7.3.1 Example 1: section under pure compression

7.3.1.1 Resistance according to the European standards

1) **Cross-section classification**

   The classification was made in the previous section.

   Web: Class 4

   Flanges: Class 4

   The overall section class is 4.

2) **Cross-section resistance**

   The cross-section resistance was calculated in the previous section.

$$N_{fi,\theta,Rd} = A_{eff} \cdot k_{p0.2,\theta} \cdot f_y = 10984 \cdot 0.13 \cdot 690 = 985kN$$

This resistance corresponds to an ultimate multiplier of 3.47 which means that the initial loading must be multiplied by 3.47 to reach failure according to the European standards.

3) Member resistance

$$\alpha = 0.65 \cdot \sqrt{\frac{235}{f_y}} = 0.65 \cdot \sqrt{\frac{235}{690}} = 0.221$$

$$\lambda_1 = \pi \cdot \sqrt{\frac{E}{f_y}} = \pi \cdot \sqrt{\frac{210000}{690}} = 54.80$$

$$\bar{\lambda}_{z,\theta} = \bar{\lambda} \cdot \sqrt{\frac{k_{y,\theta}}{k_{E,\theta}}} = \sqrt{\frac{A_{eff} \cdot f_y}{N_{cr}}} \cdot \sqrt{\frac{k_{y,\theta}}{k_{E,\theta}}} = \frac{L_{cr} \cdot \sqrt{\frac{A_{eff}}{A}}}{i_z \cdot \lambda_1} \cdot \sqrt{\frac{k_{y,\theta}}{k_{E,\theta}}} = \frac{864 \cdot \sqrt{\frac{10984}{11253}}}{74.84 \cdot 54.80} \cdot \sqrt{\frac{0.23}{0.13}} = 0.28$$

$$\phi_{z,\theta} = 0.5 \cdot \left(1 + \alpha \cdot \bar{\lambda}_{z,\theta} + \bar{\lambda}_{z,\theta}^{\ 2}\right) = 0.5 \cdot \left(1 + 0.221 \cdot 0.28 + 0.28^2\right) = 0.57$$

$$\chi_{z,fi} = \frac{1}{\phi_{z,\theta} + \sqrt{\phi_{z,\theta}^{\ 2} - \bar{\lambda}_{z,\theta}^{\ 2}}} = \frac{1}{0.57 + \sqrt{0.57^2 - 0.28^2}} = 0.83 \leq 1.0$$

$$\bar{\lambda}_{y,\theta} = \bar{\lambda} \cdot \sqrt{\frac{k_{y,\theta}}{k_{E,\theta}}} = \sqrt{\frac{A_{eff} \cdot f_y}{N_{cr}}} \cdot \sqrt{\frac{k_{y,\theta}}{k_{E,\theta}}} = \frac{L_{cr} \cdot \sqrt{\frac{A_{eff}}{A}}}{i_y \cdot \lambda_1} \cdot \sqrt{\frac{k_{y,\theta}}{k_{E,\theta}}} = \frac{864 \cdot \sqrt{\frac{10984}{11253}}}{127.40 \cdot 54.80} \cdot \sqrt{\frac{0.23}{0.13}} = 0.16$$

$$\phi_{y,\theta} = 0.5 \cdot \left(1 + \alpha \cdot \bar{\lambda}_{y,\theta} + \bar{\lambda}_{y,\theta}^{\ 2}\right) = 0.5 \cdot \left(1 + 0.221 \cdot 0.16 + 0.16^2\right) = 0.53$$

$$\chi_{y,fi} = \frac{1}{\phi_{y,\theta} + \sqrt{\phi_{y,\theta}^{\ 2} - \bar{\lambda}_{y,\theta}^{\ 2}}} = \frac{1}{0.53 + \sqrt{0.53^2 - 0.16^2}} = 0.92 \leq 1.0$$

$$N_{b,fi,\theta,Rd} = \chi_{z,fi} \cdot A_{eff} \cdot k_{p0.2,\theta} \cdot f_y = 0.83 \cdot 10984 \cdot 0.13 \cdot 690 = 818kN$$

This resistance corresponds to an ultimate multiplier of 2.88 which means that the initial loading must be multiplied by 2.88 to reach failure according to the European standards.

7.3.1.2 Resistance according to the Canadian standards

1) Cross-section classification

The classification was made in the previous section.

Web: Class 4

Flanges: Class 4

The overall section class is 4.

2) Cross-section resistance

The cross-section resistance was calculated in the previous section.

$$C_r(T) = A_{eff} \cdot F_y(T) = 8438 \cdot 158.7 = 1339kN$$

This resistance corresponds to an ultimate multiplier of 4.72 which means that the initial loading must be multiplied by 4.72 to reach failure according to the Canadian standards.

3) Member resistance

The reduced value of F_y at 700°C needed to calculate the resistance was calculated in the previous section. The reduced value of E at 700°C is calculated using the reduction factor k_E.

$$E(T) = E \cdot k_E = 210000 \cdot 0.13 = 27300MPa$$

Annex K of the standards propose the same equation for all cross-section class to calculate the resistance to flexural buckling.

$$\lambda_z(700) = \frac{K \cdot L}{r_z} \cdot \sqrt{\frac{F_{ym}}{\pi^2 \cdot E_m}} = \frac{1 \cdot 864}{74.84} \cdot \sqrt{\frac{158.7}{\pi^2 \cdot 27300}} = 0.28$$

$$\lambda_y(700) = \frac{K \cdot L}{r_y} \cdot \sqrt{\frac{F_{ym}}{\pi^2 \cdot E_m}} = \frac{1 \cdot 864}{127.40} \cdot \sqrt{\frac{158.7}{\pi^2 \cdot 27300}} = 0.16$$

$$C_{r,z}(700) = \frac{A \cdot F_{ym}}{\left(1 + \lambda_z(700)^{2 \cdot d \cdot n}\right)^{\frac{1}{d \cdot n}}} = \frac{11253 \cdot 158.7}{\left(1 + 0.28^{2 \cdot 0.6 \cdot 1.34}\right)^{\frac{1}{0.6 \cdot 1.34}}} = 1535kN$$

$$C_{r,y}(700) = \frac{A \cdot F_{ym}}{\left(1 + \lambda_y(700)^{2 \cdot d \cdot n}\right)^{\frac{1}{d \cdot n}}} = \frac{11253 \cdot 158.7}{\left(1 + 0.16^{2 \cdot 0.6 \cdot 1.34}\right)^{\frac{1}{0.6 \cdot 1.34}}} = 1671kN$$

In this case, the cross-section resistance is smaller than the resistance to flexural buckling. This is explained by the fact that the equation for flexural buckling does not consider that the section is considered as slender. This resistance corresponds to an ultimate multiplier of 4.72 which means that the initial loading must be multiplied by 4.72 to reach failure according to the Canadian standards.

7.3.1.3 Resistance according to the American standards

1) Cross-section classification

The classification is made with the properties at elevated temperatures.

The reduced value of F_y at 700°C is calculated using the reduction factor k_y.

$$F_y(T) = F_y \cdot k_y = 690 \cdot 0.264 = 182.16MPa$$

The reduced value of E at 700°C is calculated using the reduction factor k_E.

$$E(T) = E \cdot k_E = 210000 \cdot 0.17 = 35700MPa$$

Web: Slender

Flanges: Slender

The section is slender.

2) Member resistance

For slender sections, an effective area must be calculated.

Web:

$$\lambda = \frac{h}{w} = \frac{290 - 2 \cdot 14 - 2 \cdot 27}{8.5} = 24.47$$

$$\lambda_r = 1.49 \cdot \sqrt{\frac{E(T)}{F_y(T)}} = 1.49 \cdot \sqrt{\frac{35700}{182.16}} = 20.86$$

$$c_1 = 0.18 \qquad c_1 = 0.131$$

$$F_{el}(T) = \left(c_2 \cdot \frac{\lambda_r}{\lambda}\right)^2 \cdot F_y(T) = \left(1.31 \cdot \frac{20.86}{24.47}\right)^2 \cdot 182.16 = 226.42MPa$$

$$F_e(T) = \frac{\pi^2 \cdot E(T)}{\left(\frac{L}{r}\right)^2} = \frac{\pi^2 \cdot 35700}{\left(\frac{864}{74.84}\right)^2} = 2643.9MPa$$

$$F_{cr}(T) = \left(0.42^{\sqrt{\frac{F_y(T)}{F_e(T)}}}\right) \cdot F_y(T) = \left(0.42^{\sqrt{\frac{182.16}{2643.9}}}\right) \cdot 182.16 = 145.0MPa$$

$$h_e = h\left(1 - c_1 \cdot \sqrt{\frac{F_{el}(T)}{F_{cr}(T)}}\right) \cdot \sqrt{\frac{F_{el}(T)}{F_{cr}(T)}} = 208\left(1 - 0.18 \cdot \sqrt{\frac{226.42}{145.0}}\right) \cdot \sqrt{\frac{226.42}{145.0}} = 201.42mm$$

Flange:

$$\lambda = \frac{b}{t} = \frac{300/2}{14} = 10.71$$

$$\lambda_r = 0.56 \cdot \sqrt{\frac{E(T)}{F_y(T)}} = 0.56 \cdot \sqrt{\frac{35700}{182.16}} = 7.84$$

$$c_1 = 0.22 \qquad c_1 = 0.149$$

$$F_{el}(700) = \left(c_2 \cdot \frac{\lambda_r}{\lambda}\right)^2 \cdot F_y(700) = \left(1.49 \cdot \frac{7.84}{10.71}\right)^2 \cdot 182.16 = 215.19 MPa$$

$$b_e = b\left(1 - c_1 \cdot \sqrt{\frac{F_{el}(T)}{F_{cr}(T)}}\right) \cdot \sqrt{\frac{F_{el}(T)}{F_{cr}(T)}} = 300\left(1 - 0.22 \cdot \sqrt{\frac{226.42}{145.0}}\right) \cdot \sqrt{\frac{226.42}{145.0}} = 267.48 mm$$

$$A_e = 2 \cdot b_e \cdot t_f + h_e \cdot t_w + r^2 \cdot (4 - \pi) = 2 \cdot 213.08 \cdot 14 + 216.84 \cdot 8.5 + 27^2 \cdot (4 - \pi)$$
$$= 10286 mm^2$$

$$P_n(T) = A_e \cdot F_{cr}(T) = 10286 \cdot 145.0 = 1492 kN$$

This resistance corresponds to an ultimate multiplier of 5.26 which means that the initial loading must be multiplied by 5.26 to reach failure according to the American standards.

7.3.2 Example 2: section under combined loading

7.3.2.1 Resistance according to the European standards

1) Cross-section classification

The classification was made in the previous section.

Web: Class 4

Flanges: Class 4

The overall section class is 4.

2) Cross-section resistance

The cross-section resistances were calculated in the first example.

a) Resistance to compression

$$N_{fi,\theta,Rd} = A_{eff} \cdot k_{p0.2,\theta} \cdot f_y = 10984 \cdot 0.13 \cdot 690 = 985 kN$$

b) Resistance to major-axis bending

$$M_{y,fi,\theta,Rd} = W_{y,eff} \cdot k_{p0.2,\theta} \cdot f_y = 1259552 \cdot 0.13 \cdot 690 = 113 kNm$$

c) Resistance to minor-axis bending

$$M_{z,fi,\theta,Rd} = W_{z,el} \cdot k_{p0.2,\theta} \cdot f_y = 420637 \cdot 0.13 \cdot 690 = 37.7 kNm$$

3) Member resistance

a) Resistance to compression

The resistance to flexural buckling was calculated in the previous section.

$$\chi_{z,fi} = \frac{1}{\phi_{z,\theta} + \sqrt{\phi_{z,\theta}^{2} - \bar{\lambda}_{z,\theta}^{2}}} = \frac{1}{0.57 + \sqrt{0.57^2 - 0.28^2}} = 0.83 \le 1.0$$

$$\chi_{y,fi} = \frac{1}{\phi_{y,\theta} + \sqrt{\phi_{y,\theta}^{2} - \bar{\lambda}_{y,\theta}^{2}}} = \frac{1}{0.53 + \sqrt{0.53^2 - 0.16^2}} = 0.92 \le 1.0$$

$$N_{b,fi,\theta,Rd} = \chi_{z,fi} \cdot A_{eff} \cdot k_{p0.2,\theta} \cdot f_y = 0.83 \cdot 10984 \cdot 0.13 \cdot 690 = 818 kN$$

b) Resistance to major-axis bending

$$\alpha = 0.65 \cdot \sqrt{\frac{235}{f_y}} = 0.65 \cdot \sqrt{\frac{235}{690}} = 0.221$$

$$M_{cr} = \frac{\pi}{L} \cdot \sqrt{E \cdot I_z \cdot G \cdot I_t + I_z \cdot I_w \cdot \left(\frac{\pi \cdot E}{L}\right)^2}$$

$$= \frac{\pi}{864} \cdot \sqrt{210000 \cdot 63031432 \cdot 80769 \cdot 847130 + 63031432 \cdot 12.0 \times 10^{11} \cdot \left(\frac{\pi \cdot 210000}{864}\right)^2}$$

$$= 24391 kNm$$

$$\bar{\lambda}_{LT,\theta} = \bar{\lambda}_{LT} \cdot \sqrt{\frac{k_{y,\theta}}{k_{E,\theta}}} = \sqrt{\frac{W_{eff} \cdot f_y}{M_{cr}}} \cdot \sqrt{\frac{k_{y,\theta}}{k_{E,\theta}}} = \sqrt{\frac{1259552 \cdot 690}{24391 \times 10^6}} \cdot \sqrt{\frac{0.23}{0.13}} = 0.25$$

$$\phi_{LT,\theta} = 0.5 \cdot \left(1 + \alpha \cdot \bar{\lambda}_{LT,\theta} + \bar{\lambda}_{LT,\theta}^{2}\right) = 0.5 \cdot \left(1 + 0.221 \cdot 0.25 + 0.25^2\right) = 0.56$$

$$\chi_{LT,fi} = \frac{1}{\phi_{LT,\theta} + \sqrt{\phi_{LT,\theta}^{2} - \bar{\lambda}_{LT,\theta}^{2}}} = \frac{1}{0.56 + \sqrt{0.56^2 - 0.25^2}} = 0.94 \le 1.0$$

$$M_{b,fi,\theta,Rd} = \chi_{LT,fi} \cdot W_{y,eff} \cdot k_{p0.2,\theta} \cdot f_y = 0.94 \cdot 1259552 \cdot 0.13 \cdot 690 = 107 kNm$$

c) Resistance to minor-axis bending

For minor-axis bending, the local and global resistances are the same.

$$M_{z,fi,\theta,Rd} = W_{z,el} \cdot k_{p0.2,\theta} \cdot f_y = 420637 \cdot 0.13 \cdot 690 = 37.7 kNm$$

4) **Interaction equation**

The following equations are used to verify the resistance to combined loading.

$$\frac{N_{fi,Ed}}{\chi_{\min,fi}\cdot A_{eff}\cdot k_{p0.2,\theta}\cdot f_y}+\frac{k_y\cdot M_{y,fi,Ed}}{W_{y,eff}\cdot k_{p0.2,\theta}\cdot f_y}+\frac{k_z\cdot M_{z,fi,Ed}}{W_{z,eff}\cdot k_{p0.2,\theta}\cdot f_y}\leq 1.0$$

$$\frac{N_{fi,Ed}}{\chi_{z,fi}\cdot A_{eff}\cdot k_{p0.2,\theta}\cdot f_y}+\frac{k_{LT}\cdot M_{y,fi,Ed}}{\chi_{LT,fi}\cdot W_{y,eff}\cdot k_{p0.2,\theta}\cdot f_y}+\frac{k_z\cdot M_{z,fi,Ed}}{W_{z,eff}\cdot k_{p0.2,\theta}\cdot f_y}\leq 1.0$$

$$\beta_{M,LT}=\beta_{M,y}=\beta_{M,z}=1.8-0.7\cdot\psi=1.8-0.7\cdot 1=1.1$$

$$\mu_{LT}=0.15\cdot\bar{\lambda}_{z,\theta}\cdot\beta_{M,LT}-0.15=0.15\cdot 0.28\cdot 1.1-0.15=-0.104<0.9$$

$$k_{LT}=1-\frac{\mu_{LT}\cdot N_{fi,Ed}}{\chi_{z,fi}\cdot A_{eff}\cdot k_{p,0.2,\theta}\cdot f_y}=1-\frac{-0.104\cdot 408.19\times 10^3}{0.83\cdot 10984\cdot 0.13\cdot 690}=1.05>1.0\rightarrow k_{LT}=1.0$$

$$\mu_y=\left(1.2\cdot\beta_{M,y}-3\right)\cdot\bar{\lambda}_{y,\theta}+0.44\cdot\beta_{M,y}-0.29$$
$$=\left(1.2\cdot 1.1-3\right)\cdot 0.16+0.44\cdot 1.1-0.29=-0.079<0.8$$

$$k_y=1-\frac{\mu_y\cdot N_{fi,Ed}}{\chi_{y,fi}\cdot A_{eff}\cdot k_{p,0.2,\theta}\cdot f_y}=1-\frac{-0.079\cdot 408.19\times 10^3}{0.92\cdot 10984\cdot 0.13\cdot 690}=1.04<3.0$$

$$\mu_z=\left(2\cdot\beta_{M,y}-5\right)\cdot\bar{\lambda}_{z,\theta}+0.44\cdot\beta_{M,z}-0.29$$
$$=\left(2\cdot 1.1-3\right)\cdot 0.28+0.44\cdot 1.1-0.29=-0.58<0.8$$

$$k_z=1-\frac{\mu_z\cdot N_{fi,Ed}}{\chi_{z,fi}\cdot A_{eff}\cdot k_{p,0.2,\theta}\cdot f_y}=1-\frac{-0.58\cdot 408.19\times 10^3}{0.83\cdot 10984\cdot 0.13\cdot 690}=1.29<3.0$$

$$\frac{N_{fi,Ed}}{\chi_{\min,fi}\cdot A_{eff}\cdot k_{p0.2,\theta}\cdot f_y}+\frac{k_y\cdot M_{y,fi,Ed}}{W_{y,eff}\cdot k_{p0.2,\theta}\cdot f_y}+\frac{k_z\cdot M_{z,fi,Ed}}{W_{z,eff}\cdot k_{y,\theta}\cdot k_{p0.2,\theta}}\leq 1.0$$

$$\frac{N_{fi,Ed}}{\chi_{z,fi}\cdot A_{eff}\cdot k_{p0.2,\theta}\cdot f_y}+\frac{k_{LT}\cdot M_{y,fi,Ed}}{\chi_{LT,fi}\cdot W_{y,eff}\cdot k_{p0.2,\theta}\cdot f_y}+\frac{k_z\cdot M_{z,fi,Ed}}{W_{z,eff}\cdot k_{p0.2,\theta}\cdot f_y}\leq 1.0$$

$$\frac{408.19\times 10^3}{0.83\cdot 10984\cdot 0.13\cdot 690}+\frac{1.04\cdot 7.95\times 10^6}{1259552\cdot 0.13\cdot 690_y}+\frac{1.29\cdot 2.13\times 10^6}{420637\cdot 0.13\cdot 690}=0.643\leq 1.0$$

$$\frac{408.19\times 10^3}{0.83\cdot 10984\cdot 0.13\cdot 690}+\frac{1.0\cdot 7.95\times 10^6}{0.94\cdot 1259552\cdot 0.13\cdot 690_y}+\frac{1.29\cdot 2.13\times 10^6}{420637\cdot 0.13\cdot 690}=0.645\leq 1.0$$

This resistance corresponds to an ultimate multiplier of 1.55 which means that the initial loading must be multiplied by 1.55 to reach failure according to the European standards.

7.3.2.2 Resistance according to the Canadian standards

1) Cross-section classification

The classification was made previously.

Web: Class 1

Flanges: Class 4

The overall section class is 4.

2) Cross-section resistance

The cross-section resistances were calculated in the previous section

a) Resistance to compression

$$C_r(T) = A_{eff} \cdot F_y(T) = 8438 \cdot 158.7 = 1339 kN$$

b) Resistance to major-axis bending

$$M_{ry}(T) = W_{y,eff} \cdot F_y(T) = 940031 \cdot 158.7 = 149 kNm$$

c) Resistance to minor-axis bending

$$M_{rz}(T) = W_{z,eff} \cdot F_y(T) = 530546 \cdot 158.7 = 33.7 kNm$$

3) Overall resistance

a) Resistance to compression

The resistance to flexural buckling was calculated in the previous section.

$$C_{r,z}(T) = \frac{A \cdot F_y(T)}{\left(1+\lambda_z(700)^{2 \cdot d \cdot n}\right)^{\frac{1}{d \cdot n}}} = \frac{11253 \cdot 158.7}{\left(1+0.28^{2 \cdot 0.6 \cdot 1.34}\right)^{\frac{1}{0.6 \cdot 1.34}}} = 1535 kN$$

$$C_{r,y}(T) = \frac{A \cdot F_y(T)}{\left(1+\lambda_y(700)^{2 \cdot d \cdot n}\right)^{\frac{1}{d \cdot n}}} = \frac{11253 \cdot 158.7}{\left(1+0.16^{2 \cdot 0.6 \cdot 1.34}\right)^{\frac{1}{0.6 \cdot 1.34}}} = 1671 kN$$

b) Resistance to major-axis bending

Annex K of the standards propose the same equation for all cross-section class to calculate the resistance to lateral-torsional buckling.

$$C_z(T) = \frac{700+800}{500} = 3 > 2.4 \rightarrow C_z(700) = 2.4$$

$$M_p(T) = W_{y,pl} \cdot F_y(T) = 1383272 \cdot 158.7 = 219.5 kNm$$

$$M_u(T) = \frac{\omega_2 \cdot \pi}{L} \cdot \sqrt{E_m \cdot I_z \cdot G(T) \cdot J + I_z \cdot C_w \cdot \left(\frac{\pi \cdot E(T)}{L}\right)^2}$$

$$= \frac{1 \cdot \pi}{864} \cdot \sqrt{27300 \cdot 63031432 \cdot 10500 \cdot 847130 + 63031432 \cdot 12.0 \times 10^{11} \cdot \left(\frac{\pi \cdot 27300}{864}\right)^2}$$

$$= 3171 kNm$$

$$M_{r,y}(T) = C_K \cdot M_p(T) + \left(1 - C_K\right) \cdot M_p(T) \cdot \left(1 - \left(\frac{C_K \cdot M_p(T)}{M_u(T)}\right)^{0.5}\right)^{C_z(700)}$$

$$= 0.12 \cdot 219.5 + \left(1 - 0.12\right) \cdot 219.5 \cdot \left(1 - \left(\frac{0.12 \cdot 219.5}{3171}\right)^{0.5}\right)^{2.4}$$

$$= 180 kNm$$

c) Resistance to minor-axis bending

For minor-axis bending, the local and global resistances are the same.

$$M_{rz}(T) = W_{z,eff} \cdot F_y(T) = 530546 \cdot 158.7 = 33.7 kNm$$

4) Interaction equations

The interaction equation to use for Class 4 sections is the following.

$$\frac{C_f}{C_r(T)} + \frac{U_{1y} \cdot M_{fy}}{M_{ry}(T)} + \frac{U_{1z} \cdot M_{fz}}{M_{rz}(T)} \leq 1$$

Three verifications must be made: cross-sectional strength, overall strength and lateral-torsional buckling strength.

The following interaction equation must also be satisfied :

$$\frac{M_{fy}}{M_{ry}(T)} + \frac{M_{fz}}{M_{rz}(T)} \leq 1$$

$$C_{e,z} = \frac{\pi^2 \cdot E \cdot I_z}{L^2} = \frac{\pi^2 \cdot 27300 \cdot 63031432}{864^2} = 22751 kN$$

$$C_{e,y} = \frac{\pi^2 \cdot E \cdot I_y}{L^2} = \frac{\pi^2 \cdot 27300 \cdot 182634978}{864^2} = 65920 kN$$

$$U_{1z} = \frac{\omega_1}{1 - \frac{C_f}{C_{e,z}}} = \frac{1}{1 - \frac{408.19}{22751}} = 1.018$$

$$U_{1y} = \frac{\omega_1}{1-\frac{C_f}{C_{e,y}}} = \frac{1}{1-\frac{408.19}{65920}} = 1.006$$

a) Cross-sectional strength

$$\frac{408.19}{1339} + \frac{1.006 \cdot 7.95}{149} + \frac{1.018 \cdot 2.13}{33.7} = 0.42$$

b) Overall strength

$$\frac{408.19}{1535} + \frac{1.0 \cdot 7.95}{149} + \frac{1.0 \cdot 2.13}{33.7} = 0.38$$

c) Lateral-torsional buckling strength

$$\frac{408.19}{1535} + \frac{1.0 \cdot 7.95}{180} + \frac{1.0 \cdot 2.13}{33.7} = 0.37$$

d) Bi-axial bending

$$\frac{7.95}{149} + \frac{2.13}{33.7} = 0.12 \qquad \frac{7.95}{180} + \frac{2.13}{33.7} = 0.11$$

The most critical verification is verification a). The local behaviour is not considered in the calculation of the flexural buckling resistance nor in the calculation of the lateral-torsional buckling resistance. In the considered case, the cross-section resistance is more critical than the member resistance. Since the interaction equation is linear, the ultimate multiplier can be obtained by reversing the result obtained with the interaction formulae. This resistance corresponds to an ultimate multiplier of 2.38 which means that the initial loading must be multiplied by 2.38 to reach failure according to the Canadian standards.

7.3.2.3 Resistance according to the American standards

1) Cross-section classification

The classification is made with the properties at elevated temperatures.

The reduced value of F_y at 700°C is calculated using the reduction factor k_y.

$$F_y(T) = F_y \cdot k_y = 690 \cdot 0.264 = 182.16 MPa$$

The reduced value of E at 700°C is calculated using the reduction factor k_E.

$$E(T) = E \cdot k_E = 210000 \cdot 0.17 = 35700 MPa$$

a) Compression

Web: Slender

Flanges: Slender

b) Major-axis bending

Web: Compact

Flanges: Non-compact

c) Minor-axis bending

Flanges: Non-compact

2) Member resistance

a) Compression

$$P_n(T) = A_e \cdot F_{cr}(T) = 10286 \cdot 145.0 = 1492kN$$

b) Major-axis bending

For a cross-section with a compact web and non-compact flanges, two resistances must be calculated: the resistance to flexural-torsional buckling and the resistance to compression flange local buckling.

iii) Lateral-torsional buckling

$$h_0 = h - t_f = 290 - 14 = 276mm$$

$$r_{ts} = \sqrt{\frac{\sqrt{I_y \cdot C_w}}{S_x}} = \sqrt{\frac{\sqrt{63031432 \cdot 12 \times 10^{11}}}{1259552}} = 83.1mm$$

$$F_L(700) = F_y \cdot \left(k_p - 0.3 \cdot k_y\right) = 690 \cdot \left(0.098 - 0.3 \cdot 0.264\right) = 13.10MPa$$

$$L_r(T) = 1.95 \cdot r_{ts} \cdot \frac{E(T)}{F_L(T)} \cdot \sqrt{\frac{J}{S_x \cdot h_0} + \sqrt{\left(\frac{J}{S_x \cdot h_0}\right)^2 + 6.76 \cdot \left(\frac{F_L(T)}{E(T)}\right)^2}}$$

$$= 1.95 \cdot 83.1 \cdot \frac{35700}{13.10} \cdot \sqrt{\frac{847130}{1259552 \cdot 276} + \sqrt{\left(\frac{847130}{1259552 \cdot 276}\right)^2 + 6.76 \cdot \left(\frac{13.10}{35700}\right)^2}}$$

$$= 31396mm$$

$$L_b < L_r(T)$$

$$C_x = 0.6 + \frac{700}{250} = 3.4 > 3.0 \qquad C_x = 3.0$$

$$M_r(T) = F_L(T) \cdot S_x = 13.10 \cdot 1259552 = 16.5kNm$$

$$M_n(T) = C_b \cdot \left(M_r(T) + \left(M_p(T) - M_r(T) \right) \cdot \left(1 - \frac{L_b}{L_r(T)} \right)^{C_z} \right)$$

$$= 1 \cdot \left(16.5 + \left(252 - 16.5 \right) \cdot \left(1 - \frac{864}{31396} \right)^3 \right) = 233 kNm$$

iv) Compression flange local buckling

$$\lambda = \frac{b}{t} = \frac{300/2}{14} = 10.71$$

$$\lambda_{pf} = 0.38 \cdot \sqrt{\frac{E(T)}{F_y(T)}} = 0.38 \cdot \sqrt{\frac{35700}{182.16}} = 5.32$$

$$\lambda_{rf} = 1 \cdot \sqrt{\frac{E(700)}{F_y(700)}} = 1 \cdot \sqrt{\frac{35700}{182.16}} = 14.00$$

$$M_n(T) = M_p(T) - (M_p(T) - 0.7 \cdot F_y(T) \cdot S_x) \cdot \left(\frac{\lambda - \lambda_{pf}}{\lambda_{rf} - \lambda_{pf}} \right)$$

$$= 252 - (252 - 0.7 \cdot 182.16 \cdot 1259552) \cdot \left(\frac{10.71 - 5.32}{14 - 5.32} \right) = 195 kNm$$

c) Minor-axis bending

For a cross-section with non-compact flanges, the resistance is either governed by yielding or by the flange local buckling.

iii) Yielding

$$M_n(T) = M_p(T) = 117 kNm$$

iv) Flange local buckling

$$M_n(T) = M_p(T) - (M_p(T) - 0.7 \cdot F_y(T) \cdot S_y) \cdot \left(\frac{\lambda - \lambda_{pf}}{\lambda_{rf} - \lambda_{pf}} \right)$$

$$= 252 - (252 - 0.7 \cdot 182.16 \cdot 420210) \cdot \left(\frac{10.71 - 5.32}{14 - 5.32} \right) = 77.5 kNm$$

3) Interaction equation

$$\frac{P_r}{P_n} = \frac{408.19}{1744} = 0.23 \geq 0.2$$

$$\frac{P_r}{P_2} + \frac{8}{9} \cdot \left(\frac{M_{rx}}{M_{nx}} + \frac{M_{ry}}{M_{ny}} \right) = \frac{408.19}{1492} + \frac{8}{9} \cdot \left(\frac{7.95}{195} + \frac{2.13}{77.5} \right) = 0.33 \leq 1.0$$

Since the interaction equation is linear, the ultimate multiplier can be obtained by reversing the result obtained with the interaction formulae. This resistance corresponds to an ultimate multiplier of 3.00 which means that the initial loading must be multiplied by 3.00 to reach failure according to the American standards.

7.3.3 Analysis and comparison of the results

The intent of this section was to adequately compare the prediction of the different calculation methods by considering the length of the sections in the calculations made with the standards. Table 47 shows that, as for the cross-section resistance, there is a lot of variability between the results which is explained by the fact that all standards propose very different approaches.

Table 45 : Ultimate load multiplier according to the finite elements simulations and to the various calculation methods with overall equations

	F.E.	O.I.C.	EC3	S16-14	AISC
N	4.27	4.44	2.88	4.72	5.26
$N + M_y + M_z$	2.82	2.70	1.55	2.38	3.00

As for the cross-section resistance the ratio between the calculated ultimate multipliers and the finite elements ultimate multiplier is shown in the following table to adequately compare the precision of the different methods.

Table 46 : Ratio between the ultimate multiplier calculated by the various calculation method with overall equations and the ultimate multiplier obtained by finite elements simulations

	O.I.C./F.E.	EC3/F.E.	S16-14/F.E.	AISC/F.E.
N	1.04	0.67	1.11	1.23
$N + M_y + M_z$	0.96	0.55	0.84	1.06

Again, the O.I.C. proposal proves to be the more accurate of all calculation methods. In the case of the European standards, the results that were already conservative when considering only the cross-section resistance are even more conservative as the standards considers an additional reduction in resistance due to global instabilities (up to 45%). The results, which are much too conservative, can lead to very uneconomical designs. Effectively, in the case of combined loading, the real resistance of the section is almost twice the predicted resistance. In the case of the Canadian standards, the results are the same as the ones obtained for the cross-section resistance as it was the governing case. This can be explained by the fact that the equations that consider the global instabilities in the case of fire disregard the local resistance. At very short lengths, the cross-section resistance is therefore more conservative than the global resistance. Finally, in the case of the American standards, the use of global equations improves the precision by giving more conservative results. However, those are still on the unconservative side (up to 23%). Even though in this case the use of global formulas improves the results, the standards can still be considered unprecise as the results for the cross-section resistance are corrected by equations that considered the global behaviour which does not have an effect on the resistance at such small lengths.

Chapter 8 : Observations on the influence of increasing temperature on section capacity

For this numerical study, finite element simulations where initially done with five different temperatures: 20°C, 350°C, 450°C, 550°C and 700°C. Figure 70 and Figure 71, presented previously, respectively show the influence of the temperature on the results for hot-rolled and welded sections. With these figures, it was concluded that, for both section types, it was possible to identify tendencies between the results obtained at various high temperatures, but that the behaviour at room temperature was very different from the behaviour at high temperature. It was therefore decided to make a proposal for hot temperatures different form the existing proposal at room temperature that was made in another study. The performance of the proposal at high temperature was proven to be very accurate for the studied high temperatures by the evaluation made in Chapter 5.

However, the simulations made did not allow to evaluate the proposal at smaller temperatures, between 20°C and 350°C. Additional simulations were therefore performed for compression load cases with three other temperatures: 100°C, 150°C and 250°C. Both proposals, the proposal at room temperature and the proposal at high temperature, were then used to predict the resistance in compression of sections at temperatures varying from 20°C to 700°C. The proposal at 20°C was made by Liya Li, a PhD student and is present in Appendix 2. The performances of the proposals at room temperature and at high temperatures are respectively presented on Figure 118 and Figure 119.

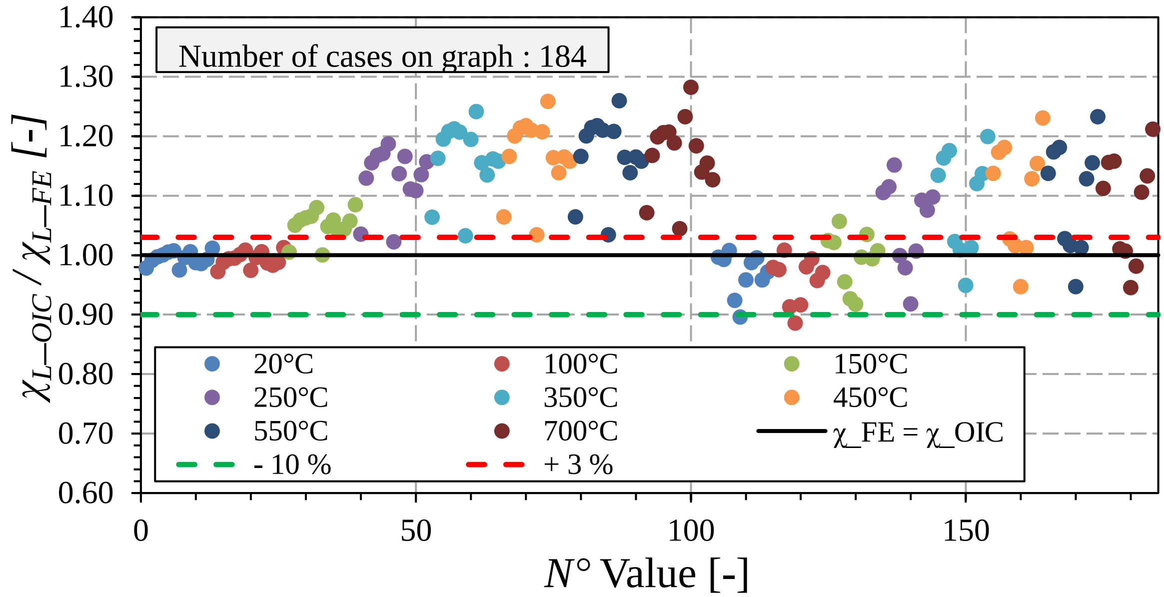

Figure 118 : Performance of the 20°C proposal for various temperatures

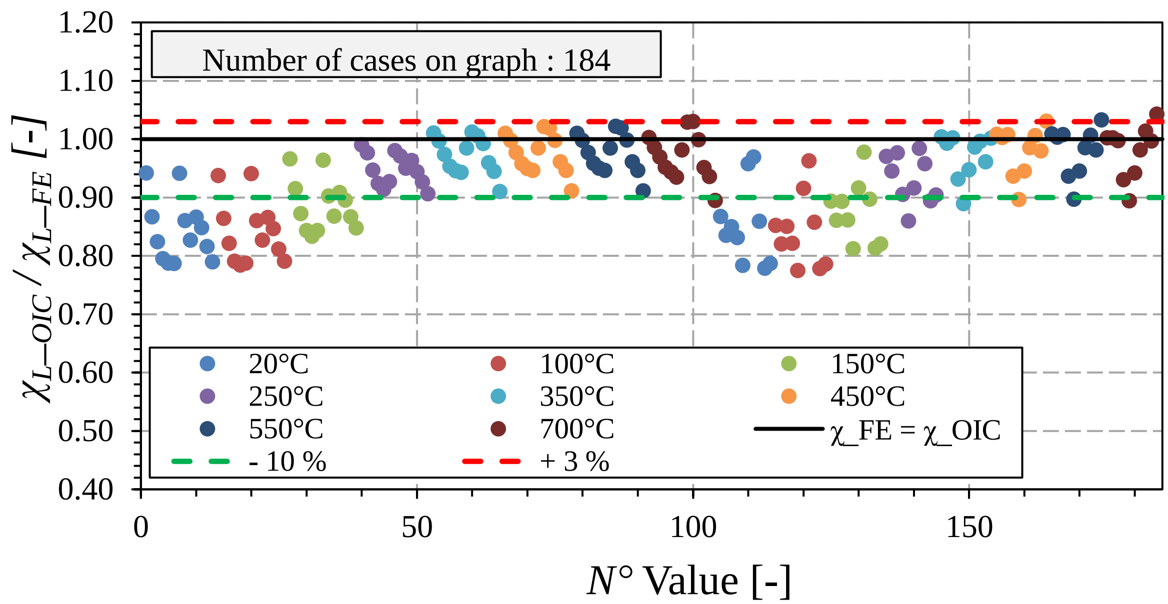

Figure 119 : Performance of the high temperatures proposal for various temperatures

Figure 118 shows that the proposal at room temperature is very good for cross-sections at 20°C and at 100°C. However, the proposal is not accurate for temperatures over 100°C with particularly bad performance for temperatures over 250°C. Effectively, at those temperatures, predicted resistances are more than 10% higher than the real resistances. The use of this proposal at such temperatures could therefore lead to unsafe designs. Then, Figure 119 shows that the proposal at high temperature is good for temperatures 250°C and over. At lower temperatures, the proposal leads to too conservative predictions. The different performances between both proposals indicate that there is no continuity between both proposals. It could be considered acceptable to have two different proposals, but it would be preferable and simpler to have one proposal that gives accurate results for all temperatures.

To understand why there is no continuity between a good proposal at room temperature and a good proposal at high temperature, the evolution of the behaviour with the increase in temperature was studied and is presented on Figure 120 and Figure 121.

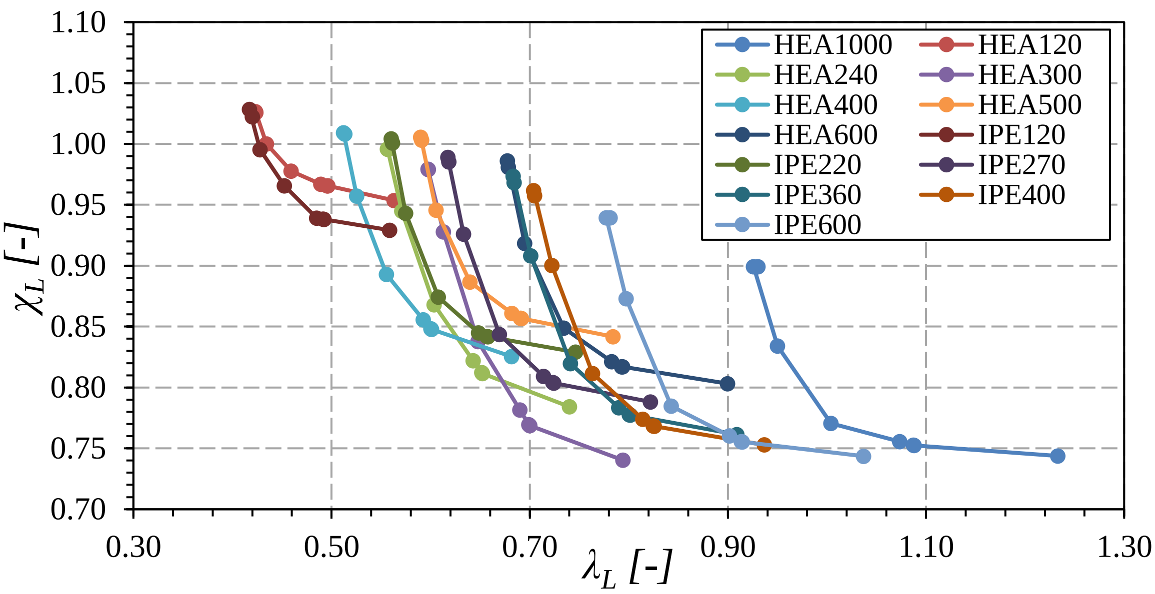

Figure 120 : Evolution of resistance with the increase in temperature for hot-rolled sections

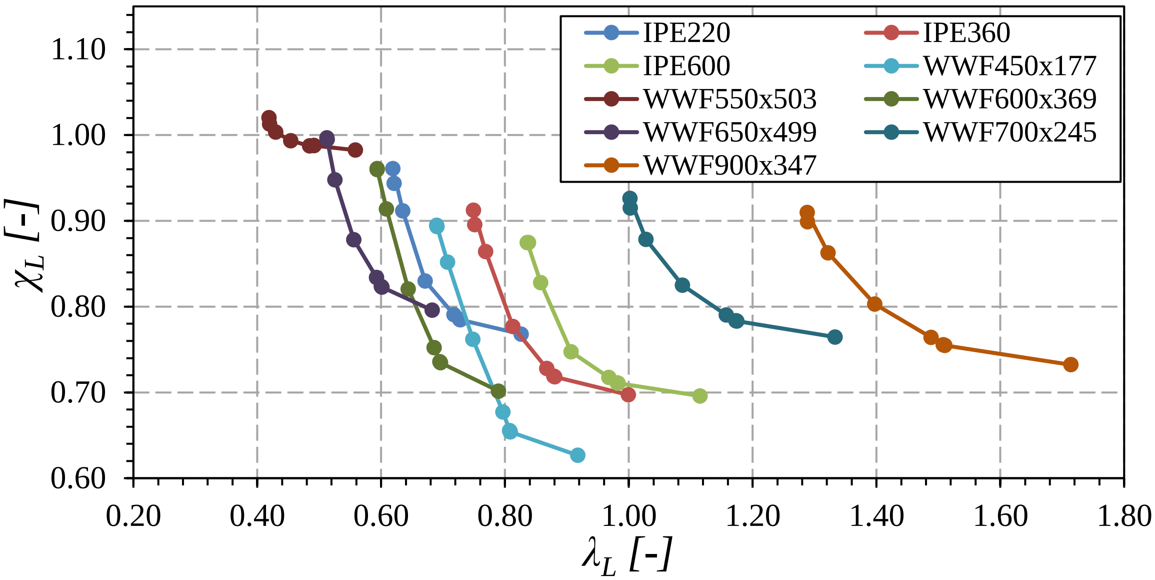

Figure 121 : Evolution of resistance with the increase in temperature for welded sections

The figures show the evolution of the reduction factor χ and of the local slenderness λ with the increase in temperature. It is first possible to see that the evolution is not the same for all sections, which means that the geometry has an impact on the evolution of the behaviour. The difference can mostly be seen between very compact sections for which the resistance is very close to the plastic resistance (χ close to 1.0) and the sections for which the reduction factor drastically diminishes with the increase in temperature. Then, both figures show that the reduction factor decreases more rapidly between the smaller temperatures than between the higher temperatures. This could probably be explained by the shape of the material law. Based on the material laws provided by Eurocode 3 and used in the finite element simulations, it is possible to see that as the temperature increases, the length of the elastic branch decreases. However, the deformation at which the plastic plateau begins is the same for all temperatures. This means that as the temperature increases, the non-linear part of the material law becomes more important. In order to have a proposal that is continuous at all temperatures, the proportionality limit should therefore be included in the proposal. This aspect was however not studied further in this study. Further research would be necessary to see if it is possible to find a proposal suitable for all temperatures.

Conclusion

Main conclusions

The main objective of this study was to develop a new design method for the cross-section capacity of steel open sections at high temperatures. Currently, fire protection in structures is mostly ensured by the use of certified protective materials which can greatly increase the costs. In the past years, most codes have opened the possibility to performance-based approaches which allow the incorporation of the fire considerations directly in the design. However, current calculations methods for steel at high temperatures proposed by codes need improvements to ensure the accuracy of the predictions and the efficiency of the calculations. This study therefore proposes to rely on the Overall Interaction Concept (O.I.C.), a new design method continuously developed since 2012, to make a new proposal at high temperatures.

The first chapter of this thesis presents a state-of-the art review in which relevant information was collected and studied. It presents a review on the behaviour of steel at high temperatures, on local buckling at normal and at high temperatures, on geometrical imperfections, on residual stresses at normal and high temperatures and on current design methods used in standards. This literature review provides important information needed to conduct the current study and allows to highlight the need for a new design method.

Then, Chapter 2 gives a detailed description of the finite element model used to perform the numerical simulations. Information about the element's type, material behaviour, geometrical imperfection, residual stresses, support conditions and loading are provided. Then, the sub-study on mesh density made to find the best compromise between accuracy and computation time is presented. Finally, a validation of the finite element model against experimental results is presented, which confirms that the use of the numerical model is adequate.

With the finite element model validated, Chapter 3 provides information about the considered parameters in the numerical study. It gives information about the type of numerical analysis conducted, the chosen cross-sections dimensions, the considered load cases and on the studied temperatures and yield limits. The study focuses on the bi-symmetric sections subjected to a uniform temperature.

Once all numerical simulations were done, results were gathered and studied to identify leading parameters. Those parameters are needed to group the results that follow the same tendencies therefore allowing to formulate an O.I.C. proposal. Chapter 4 presents the studied parameters and the chosen ones. First, the study of the temperature showed that a distinct proposal was needed at elevated temperatures. Then, two geometrical leading parameters were identified: one for the hot-rolled sections and one for the welded sections. Those parameters are considered adequate for all load cases and all temperatures over 350°C, therefore ensuring the continuity of the proposals.

Then, Chapter 5 presents the O.I.C. proposals at high temperatures. Two proposals are presented: one for the hot-rolled sections and one for the welded sections. Both proposals rely on modified Ayrton-Perry equations that depend on the chosen leading parameter, to define the buckling curves. Those equations allow to determine the reduction factors for all three simple load cases. Then, an interaction formula based on a 3-dimensional loading space is used to combine the reduction factors obtained for simple load cases and to determine the reduction factors for combined load cases. The chapter then presents an evaluation of the performance of the model based on the temperature, the load case and the yield limit. The results show that the proposed models have a very good overall performance.

Chapter 6 presents a comparison between the performance of the O.I.C. proposals and the performance of the European, Canadian and American standards. In all cases, the O.I.C. proposal proves to be much more precise than the current design methods.

Chapter 7 then presents several worked examples in which the resistance of a cross-section under compression and under combined loading is calculated using the O.I.C. proposal and the current standards. Those examples show that the O.I.C. proposal, in addition to being more accurate, is significantly simpler. Effectively, less variables and calculations are necessary, the equations are simpler and the calculation method is the same for all load cases.

Finally, Chapter 8 presents a brief study on the evolution of the behaviour between room temperature and high temperatures. It first shows that the O.I.C. proposals made at room temperature and the ones suggested for high temperatures in the current study are not continuous. It also shows that the evolution of the behaviour with the increase in temperature is not the same for all sections and therefore highlights the need for more research on the subject.

Future developments

The objective of the study, which was to propose a new design method for the cross-section capacity of steel open sections at high temperatures, has been reached. However, the work done is only the first contribution in the field of fire resistance. As mentioned previously, future research works could include the study of the evolution of the behaviour of steel with the increase in temperature to allow for a continuous design proposal for all temperatures. Then, as this study focused on the cross-sectional resistance, more research needs to be done to extent the proposal to global resistance as members used in structures are affected by both local and global instabilities. Then, for the proposal to eventually be used in codes, a safety factor must be identified and coupled with the proposals. Also, the study only considered sections subjected to uniform temperatures. More research could therefore be done to quantify the impact of the temperature gradient and to include its effect in the proposals.

In a more global context, the O.I.C. has the advantage of being suitable for all geometries and material. Research could therefore be made in order to make O.I.C. proposal at high temperatures for other steel shapes and even other materials.

Bibliography

[1] L. T. Phan, T. P. McAllister, J. L. Gross, and M. J. Hurley, “Best practice guidelines for structural fire resistance design of concrete and steel buildings,” National Institute of Standards and Technology, NIST TN 1681, Nov. 2010. doi: 10.6028/NIST.TN.1681.

[2] J. Zhuang, V. M. Payyappalli, A. Behrendt, and K. Lukasiewicz, “Total Cost of Fire in the United States,” p. 55, 2017.

[3] L. Gérard, “Contribution to the design of steel I and H-sections members by means of the Overall Interaction Concept,” Université Laval, Québec, Canada, 2019.

[4] M. Knobloch and M. Fontana, “Strain-based approach to local buckling of steel sections subjected to fire,” *Journal of Constructional Steel Research*, vol. 62, no. 1–2, pp. 44–67, Jan. 2006, doi: 10/fsq8z3.

[5] V. Kodur, M. Dwaikat, and R. Fike, “High-Temperature Properties of Steel for Fire Resistance Modeling of Structures,” *J. Mater. Civ. Eng.*, vol. 22, no. 5, pp. 423–434, May 2010, doi: 10/bh4vv5.

[6] M. Knobloch, “Local Buckling Behaviour of Steel Sections Subjected to Fire,” *Fire Science and Technology*, vol. 26, no. 2, pp. 61–66, 2007, doi: 10.3210/fst.26.61.

[7] M. Knobloch, J. Pauli, D. Somaini, and M. Fontana, “Stress–strain response and cross-sectional capacity of steel sections in fire,” *Proceedings of the Institution of Civil Engineers - Structures and Buildings*, vol. 166, no. 8, pp. 444–455, Sep. 2013, doi: 10/gg3wxw.

[8] M. Knobloch, J. Pauli, and M. Fontana, “Influence of the strain-rate on the mechanical properties of mild carbon steel at elevated temperatures,” *Materials & Design*, vol. 49, pp. 553–565, Aug. 2013, doi: 10.1016/j.matdes.2013.01.021.

[9] CEN, Comité Européen de normalisation, “Eurocode 3 : Calcul des structures en acier - Partie 1-2 : Règles générales - Calcul du comportement au feu,” *Bruxelle, Belgique*, p. 79, 2005.

[10] M. Knobloch, J. Pauli, D. Somaini, and A. Frangi, “Cross-sectional capacity and flexural buckling resistance under fire conditions: An experimental study,” *Stahlbau*, vol. 83, no. 9, pp. 657–667, Sep. 2014, doi: 10/f2tv5t.

[11] W. Wang, V. Kodur, X. Yang, and G. Li, “Experimental study on local buckling of axially compressed steel stub columns at elevated temperatures,” *Thin-Walled Structures*, vol. 82, pp. 33–45, Sep. 2014, doi: 10/f6b9th.

[12] M. Knobloch, D. Somaini, J. Pauli, and M. Fontana, “Numerical Analysis and Comparative Study of the Cross-Sectional Capacity of Structural Steel Members in Fire,” *Journal of Structural Fire Engineering*, vol. 3, no. 1, pp. 19–36, Mar. 2012, doi: 10/gg3wxz.

[13] M. Knobloch, “Stability of steel structures in fire: State-of-the-art, recent studies in Switzerland and future trends,” *Stahlbau*, vol. 83, no. 4, pp. 257–264, Apr. 2014, doi: 10/f2q8gq.

[14] S. P. Timoshenko, *History of strength of materials*, vol. 2. Mc Graw Hill International Book Company, 1953.

[15] R. M. Jones, *Deformation theory of plasticity*. Blacksburg, Va: Bull Ridge Pub, 2009.

[16] R. Maquoi and J. Rondal, “Mise en équation des nouvelles courbes européennes de flambement,” *Construction métallique*, no. 1, 1978.

[17] F. Engesser, “Über die Knickfestigkeit Stäbe,” *Zeitschr. des Arch. u. Ing. Vereins*, vol. 35, 1889.
[18] A. Considere, “Résistance des pièces comprimées,” presented at the Congrès International des Procédés de Construction, Paris, 1889.
[19] F. Jasinski, “Recherche sur la flexion des pièces comprimées,” *Annales des Ponts et Chaussées*, vol. 8, 1894.
[20] F. R. Shanley, “Inelastic column theory,” *Journal of Aeronautical Science*, vol. 14, no. 5, 1947.
[21] T. Young, *A course of lectures on natural philosophy and the mechanicals arts*. London: J. Johnson, 1807.
[22] ECCS Technical Committe 8, “Behaviour and design of steel plated structues,” *Publication No.44*, 1986.
[23] C. Arsenault, “Development of a new design method for the cross-section capacity of steel slender I-sections,” Université Laval, Québec, Canada, 2018.
[24] S. P. Timoshenko and J. M. Gere, *Theory of Elastic Stability*, 2nd ed. Mc Graw Hill International Book Company, 1963.
[25] M. Bruneau, C.-M. Uang, and R. Sabelli, *Ductile design of steel structures*. McGraw Hill, 2011.
[26] European Committee for Standardization, *Eurocode 3 -Design of steel structures. Part 1-1 : General rules and rules for buildings.* Brussels, 2005.
[27] CSA Group, *S16-14 : Design of steel structures*. Toronto, Canada, 2014.
[28] American institute of steel construction, *ANSI/AISC 360-16 : Specification for structural steel buildings*. Chicago, USA, 2016.
[29] X. Cheng, Y. Chen, and L. Pan, “Experimental study on steel beam–columns composed of slender H-sections under cyclic bending,” *Journal of Constructional Steel Research*, vol. 88, pp. 279–288, Sep. 2013, doi: 10/gg6chm.
[30] E. Saloumi, “Development of a new design method to define the rotation capacity of steel hollow sections.” 2016.
[31] N. S. Trahair, M. A. Bradford, D. A. Nethercot, and L. Gardner, *The Behaviour and Design of Steel Structures to EC3*, Fourth Edition. London ; New York: Taylor & Francis, 2008.
[32] D. Camotim and A. Reis, *Estabilidade e Dimensionamento de Estructuras*. Orion, 2012.
[33] H. H. Bleich, *Buckling Strength of Metal Structure*. New York, NY: McGraw-Hill Book Company, Inc., 1952.
[34] M. Seif and B. W. Schafer, “Local buckling of structural steel shapes,” *Journal of Constructional Steel Research*, vol. 66, no. 10, pp. 1232–1247, Oct. 2010, doi: 10/d8m64t.
[35] T. Von Karman, E. Sechler, and L. Donel, *Strength of thin plates in compression*, Society of Mechanical Engineers-Transactions-Applied Mechanics., vol. 54. 1932.
[36] G. Winter, “Strength of Thin Steel Compression Flanges,” *Transaction ASCE*, vol. 112.
[37] European Committee for Standardization, *Eurocode 3 - Design of steel structures. Part 1-5 : Plated structural elements*. Brussel, 2006.
[38] S. E. Quiel and M. E. M. Garlock, “Calculating the buckling strength of steel plates exposed to fire,” *Thin-Walled Structures*, vol. 48, no. 9, pp. 684–695, Sep. 2010, doi: 10/cgmdhj.
[39] J.-M. Franssen and P. Vila Real, *Fire Design of Steel Structures*. Weinheim, Germany: Wiley-VCH Verlag GmbH & Co. KGaA, 2012.

[40] C. Couto, P. Vila Real, N. Lopes, and B. Zhao, "Effective width method to account for the local buckling of steel thin plates at elevated temperatures," *Thin-Walled Structures*, vol. 84, pp. 134–149, Nov. 2014, doi: 10/f6mfzm.
[41] X. Yun, J. Nseir, L. Gardner, and N. Boissonnade, "Experimental and numerical investigation into the local imperfection sensitivity of hot-rolled steel I-sections," p. 18, 2016.
[42] B. W. Schafer and T. Peköz, "Computational modeling of cold-formed steel: characterizing geometric imperfections and residual stresses," *Journal of Constructional Steel Research*, vol. 47, no. 3, pp. 193–210, Sep. 1998, doi: 10/dn29qv.
[43] A.-S. Gagné, L. Gérard, and N. Boissonnade, "Design of stainless steel cross-sections for simple load cases with the O.I.C.," *Journal of Constructional Steel Research*, vol. 168, p. 105936, May 2020, doi: 10/gg3w2g.
[44] M. Hayeck, "Development of a new design method for steel hollow section members resistance," 2016.
[45] J. Nseir, "Development of a new design method for the cross-section capacity of steel hollow sections," Université de Liège, Liège, Belgique, 2015.
[46] L. Gérard, L. Li, M. Kettler, and N. Boissonnade, "Recommendations on the geometrical imperfections definition for the resistance of I-sections," *Journal of Constructional Steel Research*, vol. 162, p. 105716, Nov. 2019, doi: 10.1016/j.jcsr.2019.105716.
[47] ECCS Technical Committe 8, "Ultimate Limit state Calculation of Sway Frames with Rigid Joint," *Publication No.33*, 1984.
[48] T. V. Galambos and R. L. Ketter, "Columns under combined bending and thrust, Proc. ASCE, 85 (EM2), p. 1, (1959), (also ASCE Trans. Vol. 126, (1961), Reprint No. 136 (61-22)," p. 49.
[49] B. W. Young, "Residual stresses in hot rolled members," 1975, doi: 10/gg3wxn.
[50] N. Boissonnade and H. Somja, "Influence of imperfections in FEM modeling of lateral torsional buckling," in *Proceedings of the Annual Stability Conference, Structural Stability Research Council, Grapevine, Texas, April 18*, 2012, vol. 21, Accessed: May 26, 2017. [Online]. Available: https://www.researchgate.net/profile/Nicolas_Boissonnade/publication/263657511_Influence_of_Imperfections_in_FEM_Modeling_of_Lateral_Torsional_Buckling/links/53fed5210cf21edafd152681.pdf.
[51] Y.-B. Wang, G.-Q. Li, S.-W. Chen, and F.-F. Sun, "Experimental and numerical study on the behavior of axially compressed high strength steel columns with H-section," *Engineering Structures*, vol. 43, pp. 149–159, Oct. 2012, doi: 10/f37f2c.
[52] Y. D. Kim, "Behavior and design of metal building frames using general prismatic and web-tapered steel I-Section members," Georgia Institute of Technology, Georgia, USA, 2010.
[53] S. P. Prawel, M. L. Morrel, and G. C. Lee, "Bending and Buckling Strength of Tapered Structural Members," *Welding Research Supplement*, pp. 75–84, 1974.
[54] W. Wang, G.-Q. Li, and Y. Ge, "Residual stress study on welded section of high strength Q460 steel after fire exposure," 2015, doi: 10/gg5jqg.
[55] W. Wang and S. Qin, "Experimental investigation of residual stresses in thin-walled welded H-sections after fire exposure," *Thin-Walled Structures*, vol. 101, pp. 109–119, Apr. 2016, doi: 10/f8chk5.
[56] J.-M. Franssen, "Residual stresses in steel profiles submitted to the fire. An analogy," 1996.

[57] P. M. M. Vila Real, R. Cazeli, L. Simões da Silva, A. Santiago, and P. Piloto, "The effect of residual stresses in the lateral-torsional buckling of steel I-beams at elevated temperature," *Journal of Constructional Steel Research*, vol. 60, no. 3–5, pp. 783–793, Mar. 2004, doi: 10/crcrrj.
[58] C. Couto, P. Vila Real, N. Lopes, and B. Zhao, "Numerical investigation of the lateral–torsional buckling of beams with slender cross sections for the case of fire," *Engineering Structures*, vol. 106, pp. 410–421, Jan. 2016, doi: 10/f74srx.
[59] J. Takagi and G. Deierlein, "Proposed design equations for CAN/CSA S16 Appendix K provisions for steel members at high temperatures," p. 22, 2009.
[60] C. Maraveas, T. Gernay, and J.-M. Franssen, "An equivalent stress method for considering the local buckling in beam finite elements in the fire situation," *Steel Structures*, p. 8, 2018.
[61] M. Kettler, "Elastic-plastic cross-sectional resistance of semi-compact H- and hollow sections," Graz University of Technology, Styria, Austria, 2008.
[62] M. Kettler, "Influence of warping on the cross-section resistance," Québec, Canada, 2017.
[63] J. Pauli, "The behavior of steel columns in fire," ETH Zurich, Zurich, Switzerland, 2013.

Appendix A : Model validation

This appendix first presents the comparison between the numerical and experimental stress-strain relationship for all specimens studied for the model validation. On all figures, the red line is the load displacement curve obtained numerically while the black line is the load-displacement curve obtained experimentally.

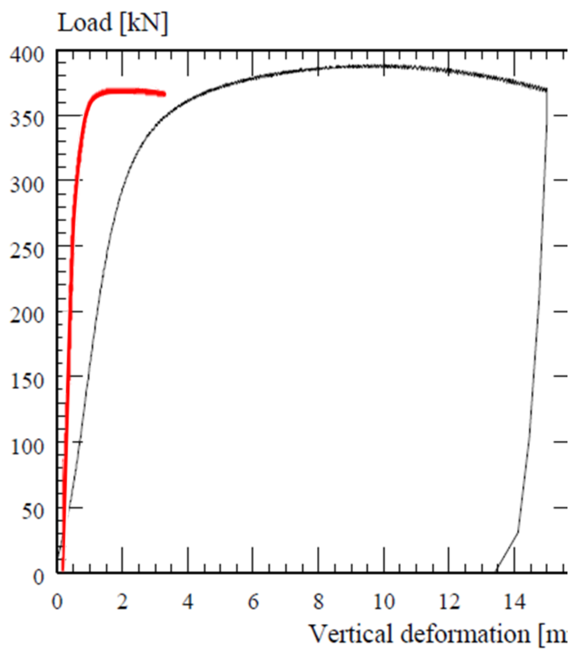

S02 – 550 °C – N+M_y

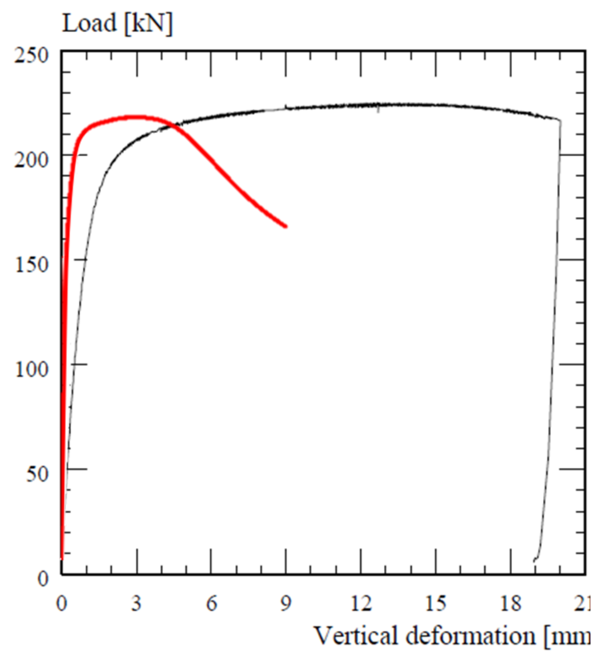

S03 – 550 °C – N+M_y

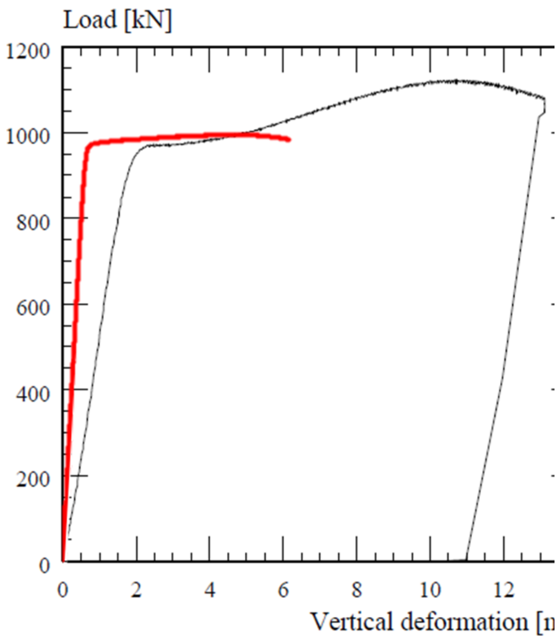

S04 – 20 °C – *N*

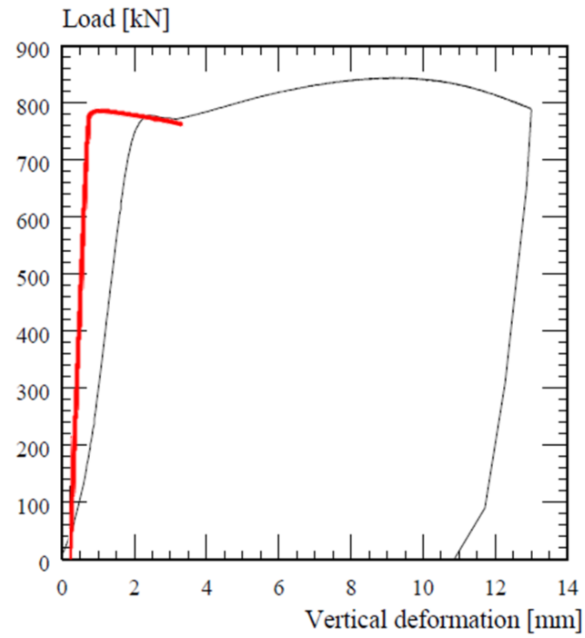

S05 – 20 °C – $N+M_y$

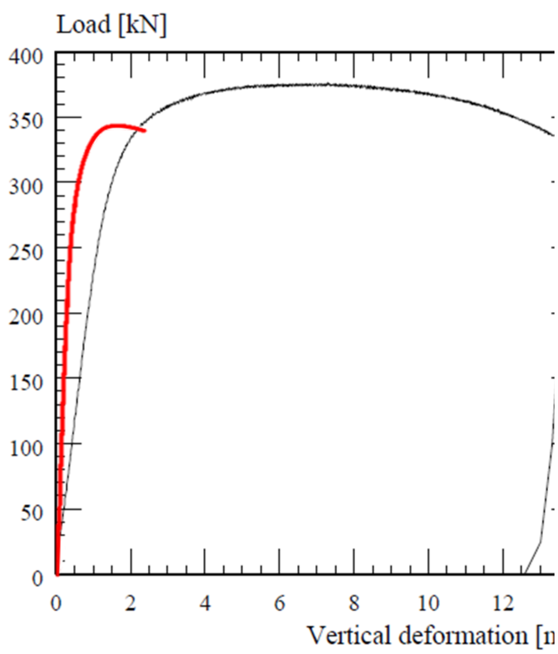

S06 – 550 °C – $N+M_z$

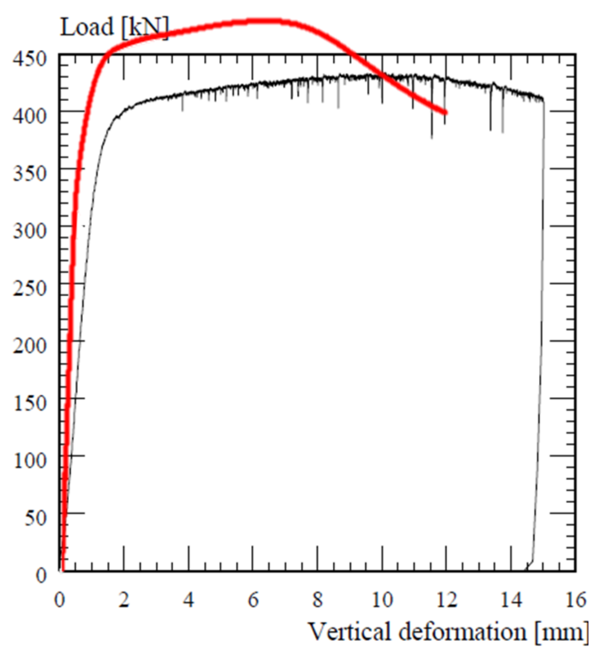

S07 – 550 °C - *N*

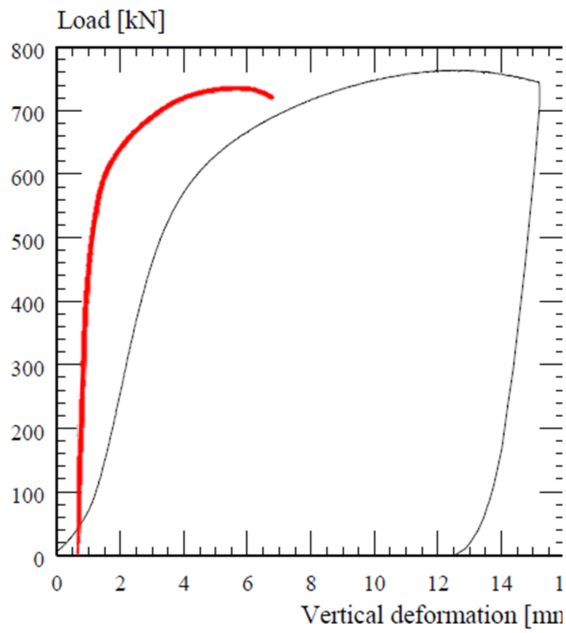

S08 – 400 °C – $N{+}M_y$

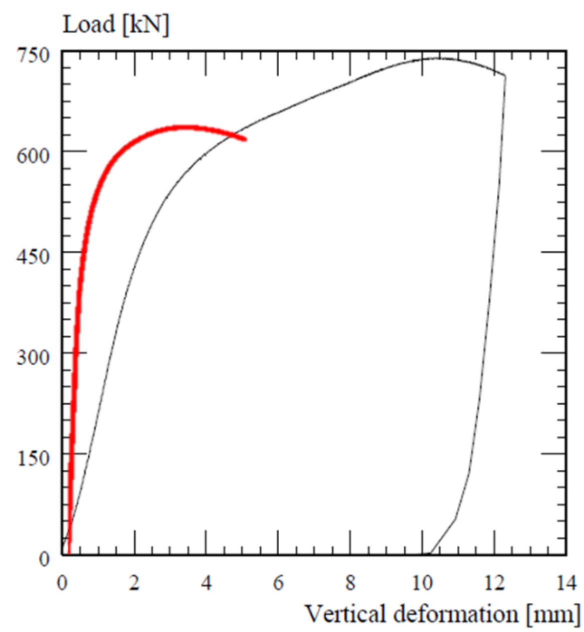

S09 – 400 °C – $N{+}M_z$

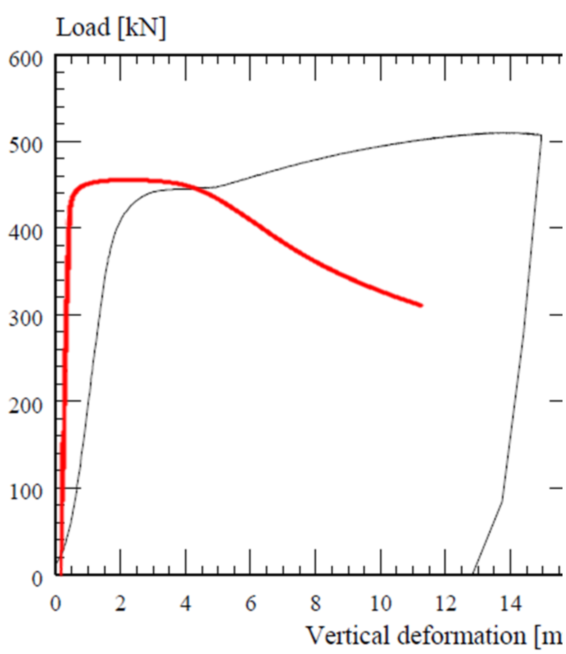

S10 – 20 °C – $N{+}M_y$

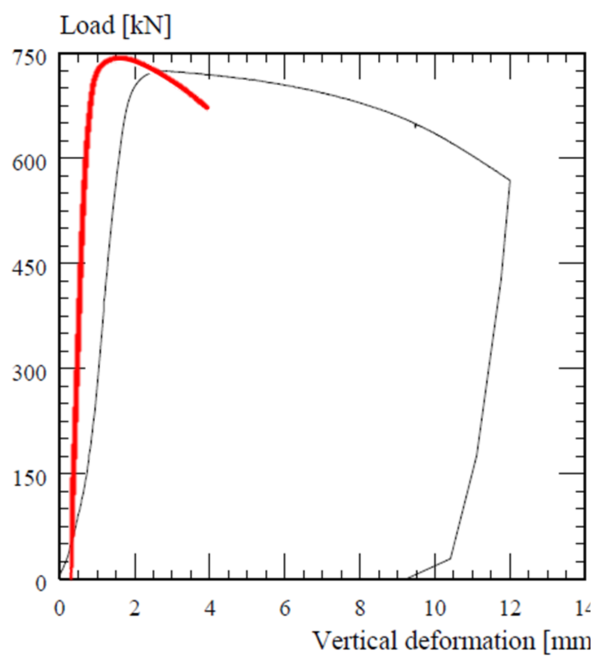

S12 – 20 °C – $N{+}M_z$

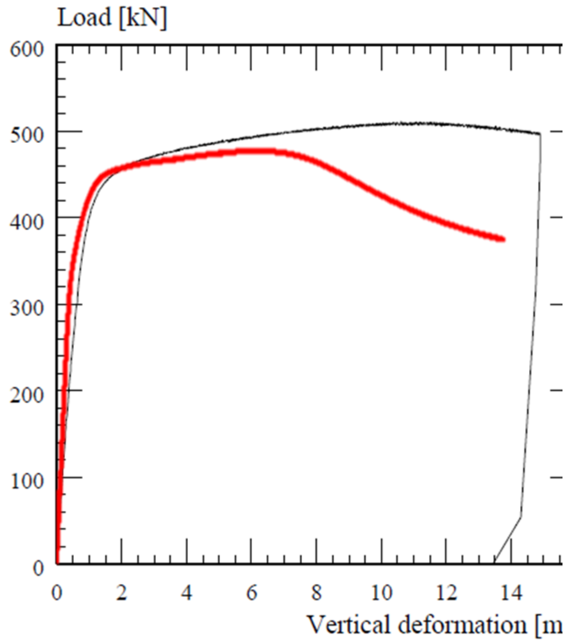

S13 – 550 °C - N

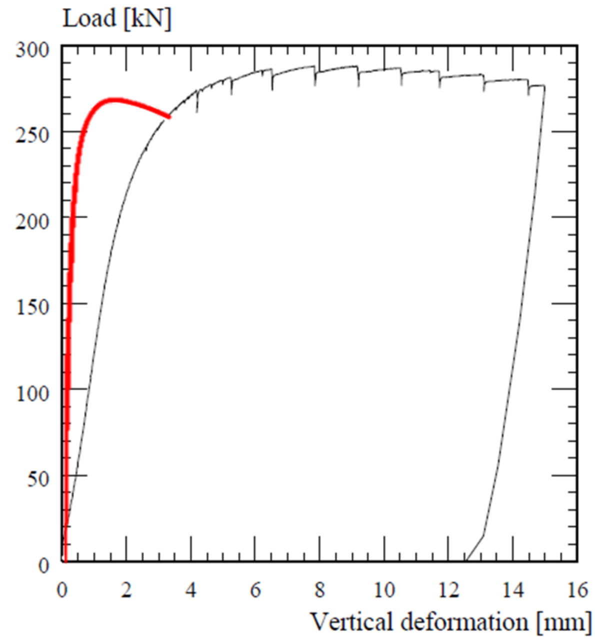

S14 – 400 °C – N+M_z

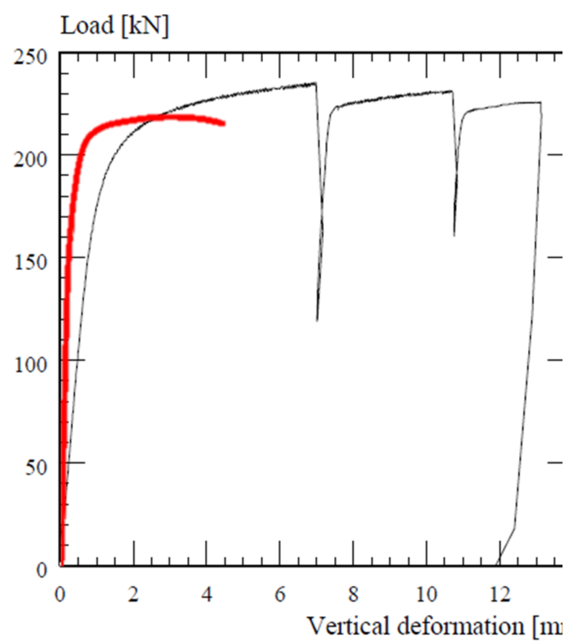

S15 – 550 °C – N+M_y

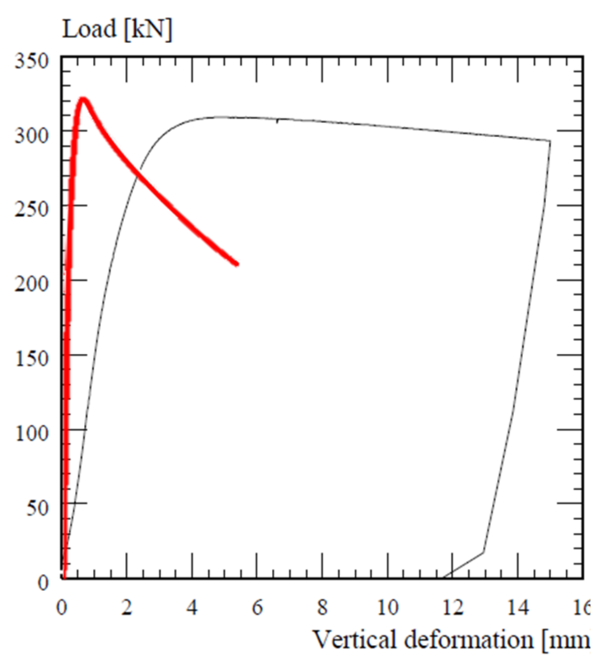

S16 – 20 °C – N+M_z

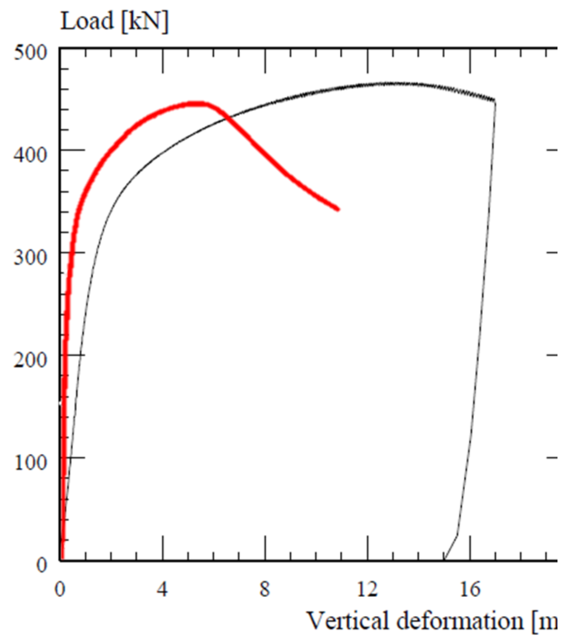

S17 – 400 °C – N+M_y

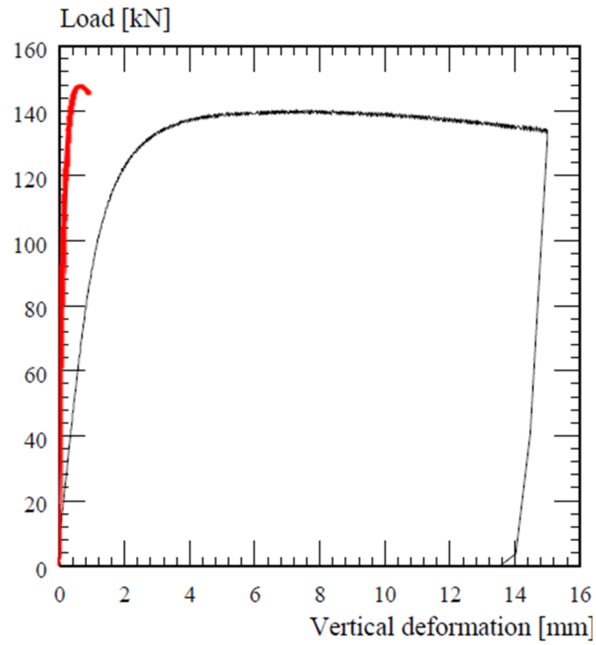

S18 – 550 °C – N+M_z

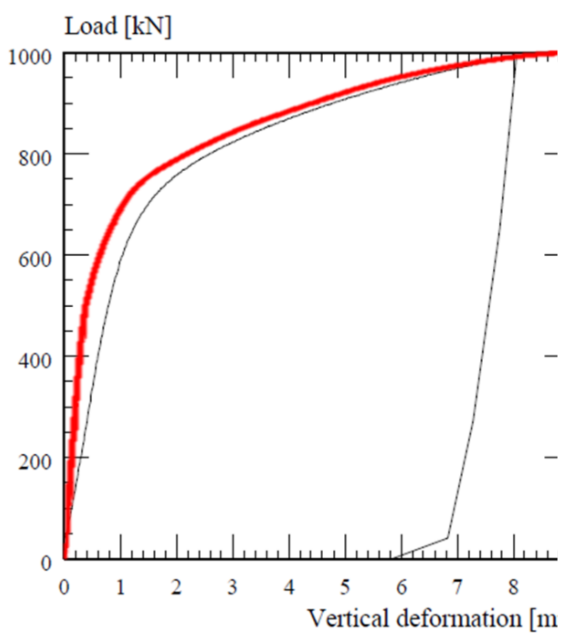

S19 – 400 °C – N

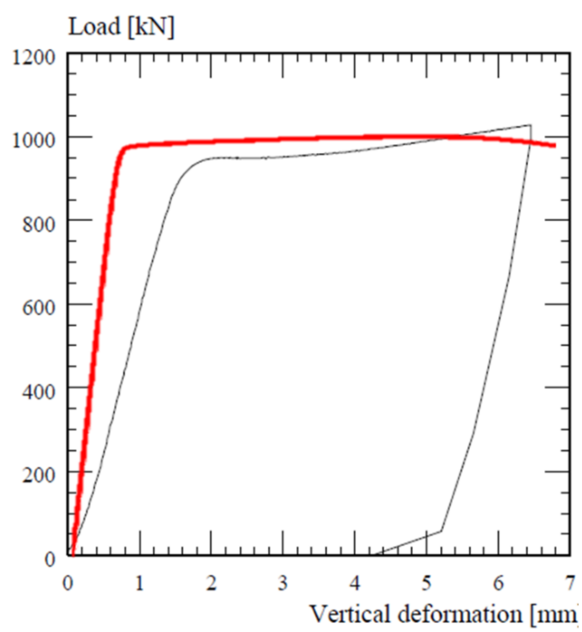

S20 – 20 °C – N

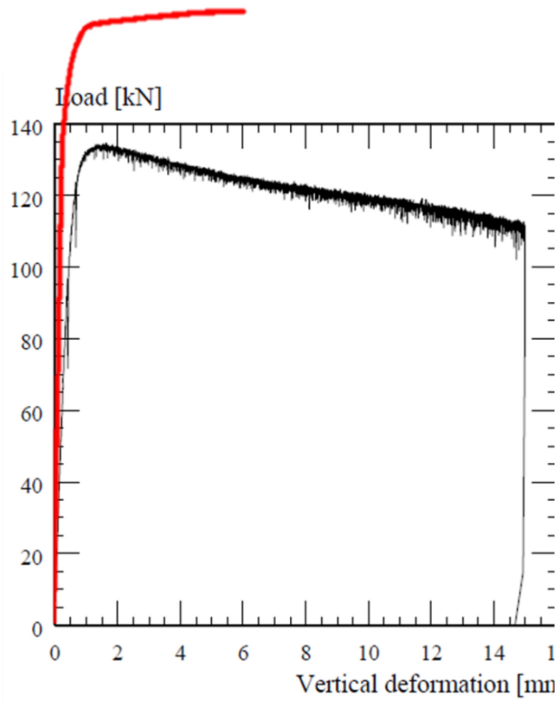

S21 – 700 °C - *N*

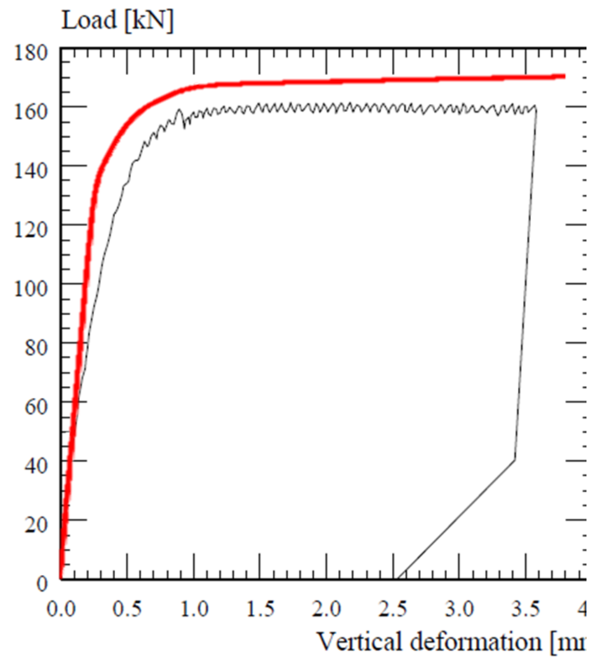

S22 – 700 °C - *N*

Then, all failure modes for experimental and numerical specimens are compared.

S02 – 550 °C – N+M_y

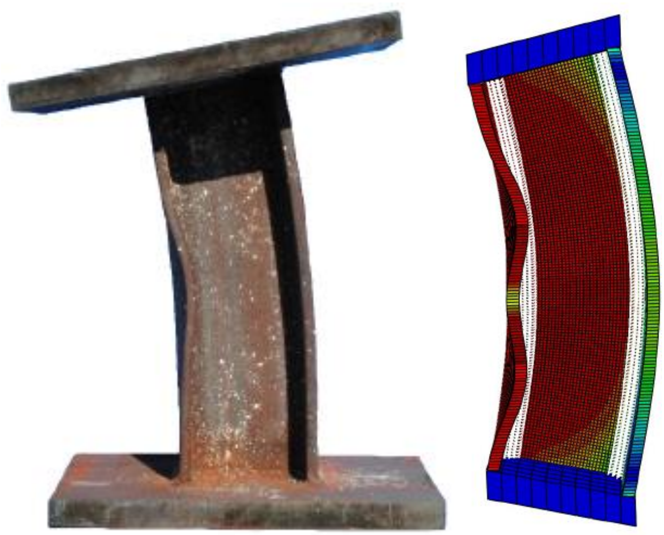

S03 – 550 °C – N+M_y

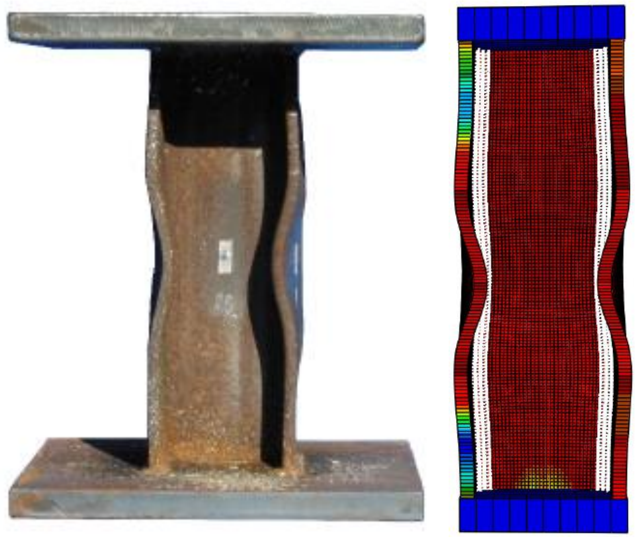

S04 – 20 °C – N

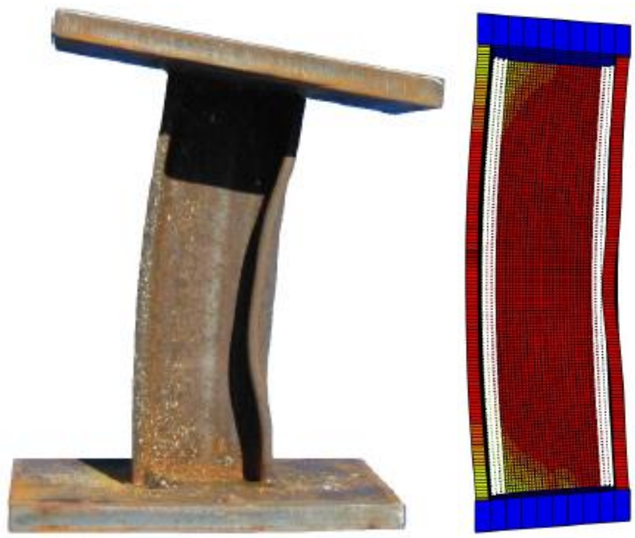

S05 – 20 °C – N+M_y

S06 – 550 °C – N+M_z

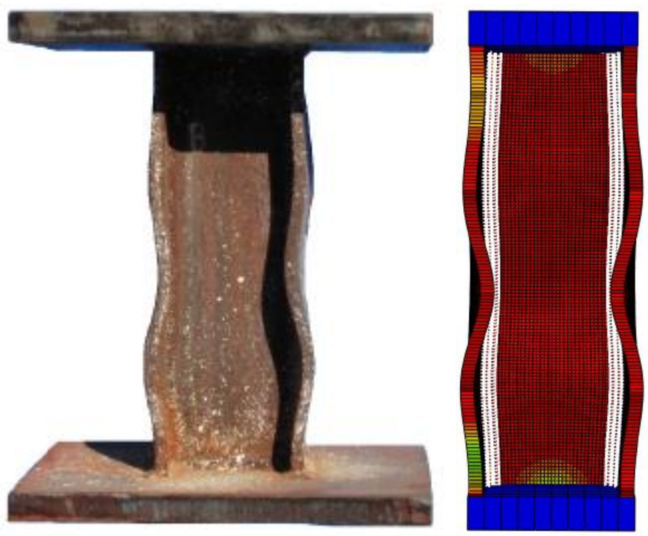

S07 – 550 °C - N

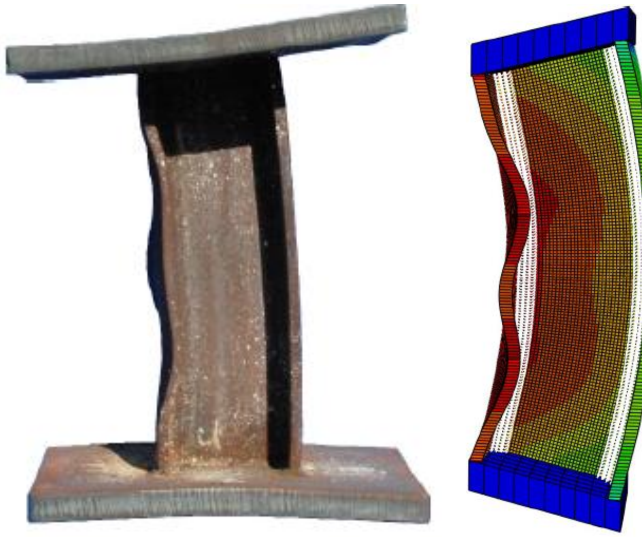

S08 – 400 °C – $N+M_y$

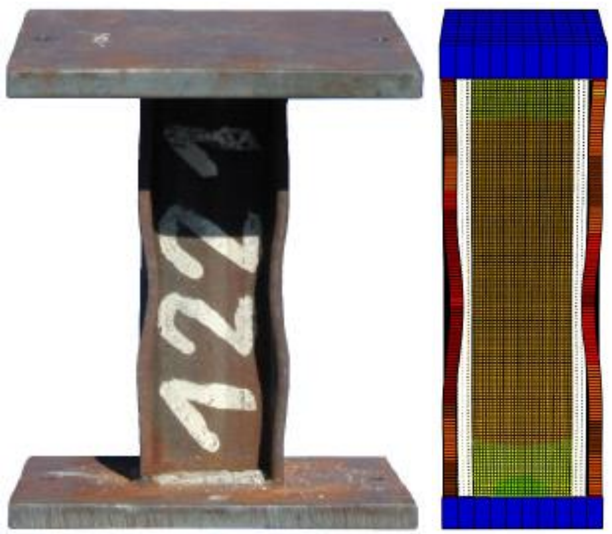

S09 – 400 °C – $N+M_z$

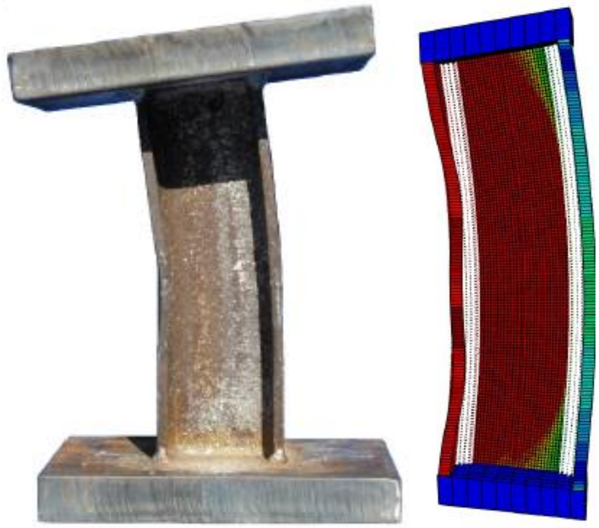

S10 – 20 °C – $N+M_y$

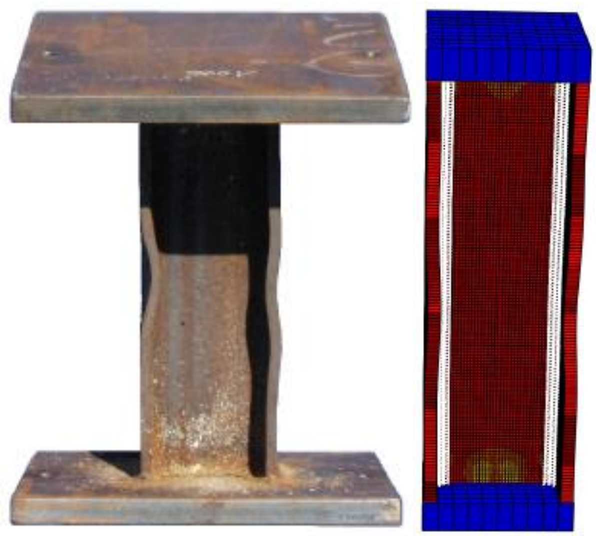

S12 – 20 °C – $N+M_z$

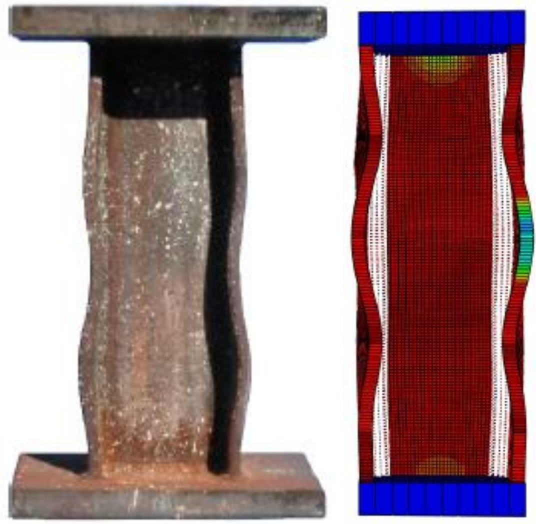

S13 – 550 °C - *N*

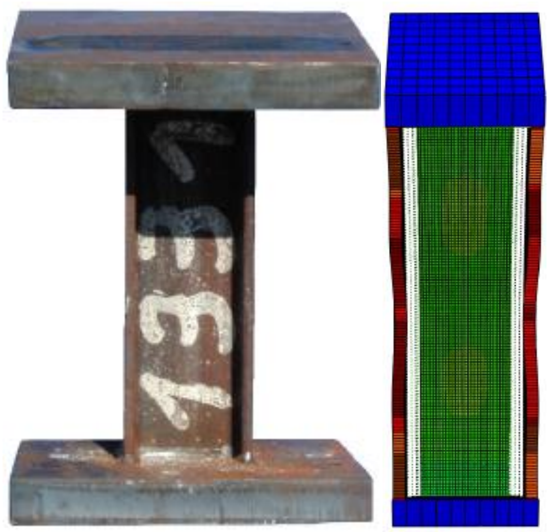

S14 – 400 °C – N+M_z

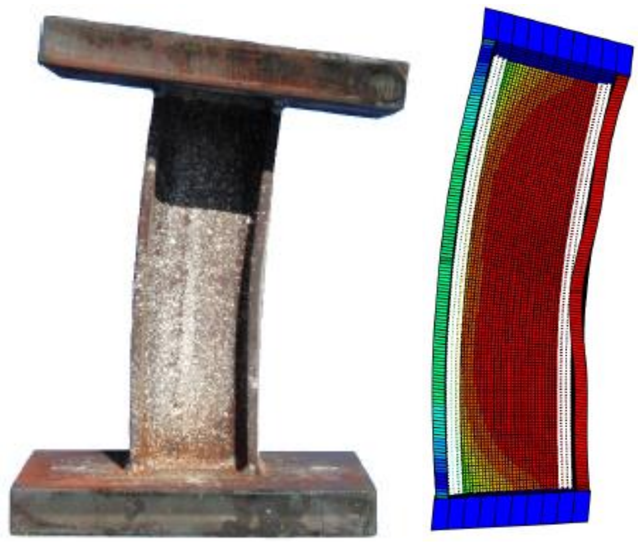

S15 – 550 °C – $N+M_y$

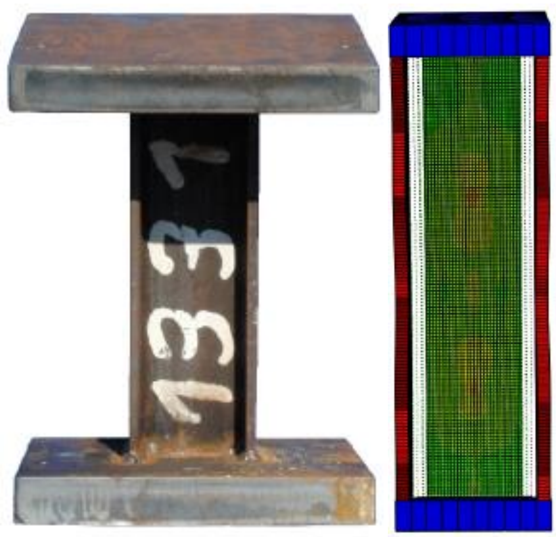

S16 – 20 °C – $N+M_z$

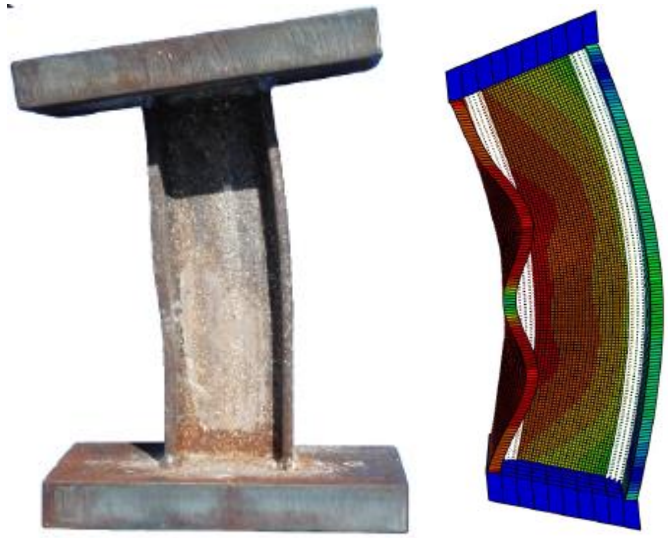

S17 – 400 °C – $N+M_y$

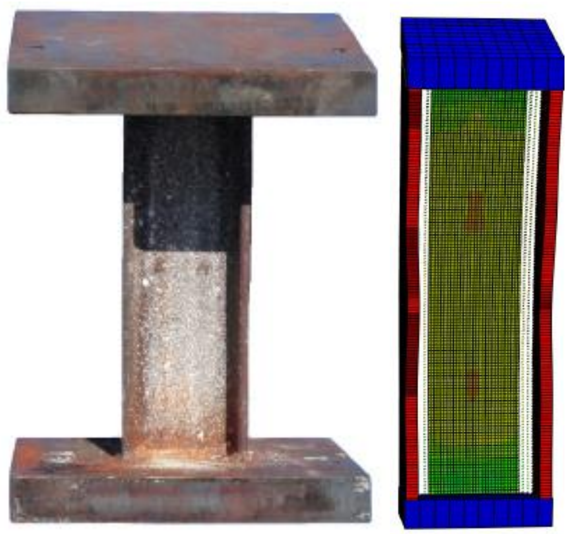

S18 – 550 °C – $N+M_z$

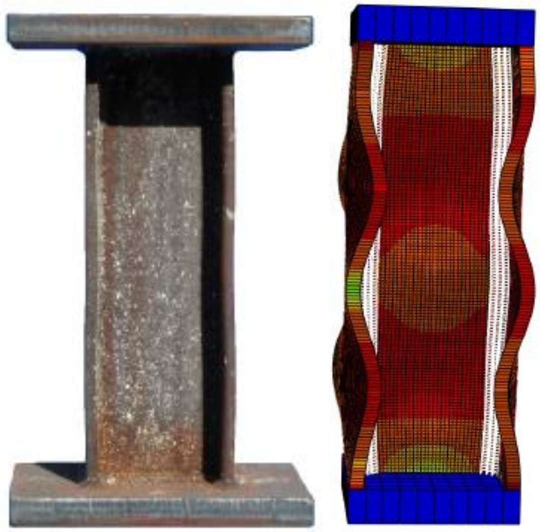

S19 – 400 °C – *N*

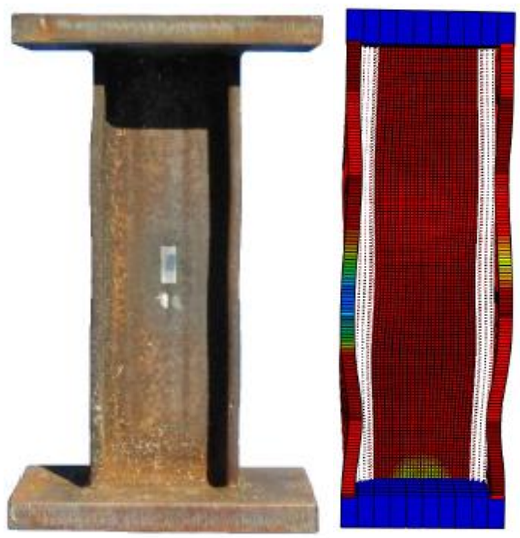

S20 – 20 °C – *N*

S21 – 700 °C - *N*

S22 – 700 °C - *N*

Appendix B : O.I.C. proposal for the cross-section resistance of open-sections at room temperature

The O.I.C. proposal for the cross-section resistance of open sections at room temperature was made by Liya Li, a current PhD student. The proposal is presented in this appendix. Similarly to the proposals at high temperature, a proposal is made for hot-rolled sections and another proposal is made for welded sections. The same modified Ayrton-Perry buckling curves are used.

For hot-rolled sections, the chosen leading parameter is the same as the one at high temperature :

$$\gamma = \left(\frac{h}{t_w}\right)^2 \cdot \left(\frac{b}{t_f}\right) \cdot \left(\frac{t_w}{t_f}\right)$$

The different parameters needed to calculate the reduction factor for simple load cases are presented in Table 47.

Table 47 : Equations for the calculation of the reduction factor for simple load cases for hot-rolled sections

Loading case	λ_0	α_L	δ
N	0.45	$0.005 + 0.1 \cdot \gamma$	$0.31 + \dfrac{0.01}{\gamma}$
M_y	0.4	$0.02 + 0.26 \cdot \gamma - 0.3 \cdot \gamma^2$	$2.11 - 3.64 \cdot \gamma^2$
M_z	0.35	$0.08 + 0.3 \cdot \gamma$	$3.23 - \dfrac{0.05}{\gamma}$

The following equation is used to calculate the reduction factor for combined load cases:

$$\chi_L = \left[\left(\chi_{L,N} \cdot \cos(\phi)^{0.15}\right)^{7.65} + \left(\chi_{L,My} \cdot \sin(\phi) \cdot \cos(\theta)^{0.29}\right)^{7.65} + \left(\chi_{L,Mz} \cdot \sin(\phi) \cdot \sin(\theta)^{0.33}\right)^{7.65}\right]^{(1/7.65)}$$

For welded sections, the chosen leading parameter is presented is the following equation:

$$\gamma = \left(\frac{b}{h}\right) \cdot \left(\frac{t_w}{t_f}\right)$$

The different parameters needed to calculate the reduction factor for simple load cases are presented in Table 48.

Table 48 : Equations for the calculation of the reduction factor for simple load cases for hot-rolled sections

Loading case	λ_0	α_L	δ
N	0.5	$-0.034+0.43\cdot\gamma$	$0.23-0.32\cdot\gamma$
M_y	0.5	$-0.26+1.15\cdot\gamma^{0.5}-0.84\cdot\gamma$	0.40
M_z	0.5	0.25	0.35

The following equation is used to calculate the reduction factor for combined load cases:

$$\chi_L = \left[\left(\chi_{L,N}\cdot\cos(\phi)^{0.15}\right)^9 + \left(\chi_{L,My}\cdot\sin(\phi)\cdot\cos(\theta)^{1.2}\right)^9 + \left(\chi_{L,Mz}\cdot\sin(\phi)\cdot\sin(\theta)^{0.04}\right)^9\right]^{(1/9)}$$